CONTINUUM DISLOCATION DYNAMICS MODELING OF MESOSCALE CRYSTAL PLASTICITY AT FINITE DEFORMATION

by

Kyle Starkey

A Dissertation

Submitted to the Faculty of Purdue University

In Partial Fulfillment of the Requirements for the degree of

Doctor of Philosophy

School of Materials Engineering

West Lafayette, Indiana

May 2022

THE PURDUE UNIVERSITY GRADUATE SCHOOL
STATEMENT OF COMMITTEE APPROVAL

Dr. Anter El-Azab, Chair

School of Materials Engineering

Dr. David Johnson

School of Materials Engineering

Dr. Michael Titus

School of Materials Engineering

Dr. Ghadir Haikal

School of Civil Engineering

Approved by:

Dr. David F. Bahr

ACKNOWLEDGMENTS

It is a genuine pleasure to express my gratitude to my mentor, advisor, and friend Prof. Anter El-Azab. His persistent pursuit for knowledge is infectious and inspirational. Your patience and insightful feedback pushed me to refine my thinking and brought my work to a higher level.

I want to express my gratitude to my committee members Prof. David Johnson, Dr. Ghadir Haikal, and Dr. Michael Titus, for their help and suggestions. I would also like to thank Prof. Haiyan Wang for a very productive research collaboration. I want to thank the Materials Engineering staff, specifically Rosemary Son and Yuan-Yu Karen Morgan, for their guidance. Thanks also to all of my fellow group members who provided both stimulating conversations that helped my research tremendously and happy distractions that have turned into great friendships. I want to thank Professor Grethe Winther of The Technical University of Denmark for her guidance during the testing of the finite-deformation formalism of continuum dislocation dynamics. Her expertise in deformation microstructure was crucial for the successful design of the test problems. I also wish to thank Professor Thomas Hochrainer of Graz University for beneficial discussions on using de Rham currents to develop the reaction closure of the dislocation transport equations.

A special and most sincere thanks goes to my wife, Haley; this dissertation would not have been possible without your help, love, and unwavering support. I would also like to thank my parents and family for their care and sacrifices that made me the person I am today.

TABLE OF CONTENTS

LIST OF TABLES

LIST OF FIGURES

ABSTRACT

Over the past two decade, there have been renewed interests in the use of continuum models of dislocation to predict the plastic strength of metals from basic properties of dislocations. Such interests have been motivated by the unique self-organized dislocation microstructures that develop during plastic deformation of metals and the need to understand their origin and connection with strength of metals. This thesis effort focuses on the theoretical development of a vector-density based representation of dislocation dynamics on the mesoscale accounting for the kinematics of finite deformation. This model consists of two parts, the first is the development of the transport-reaction equations governing dislocation dynamics within the finite deformation setting, and the second focuses on the computational solution of the resulting model. The transport-reaction equations come in the form of a set of hyperbolic curl type transport equations, with reaction terms that nonlinearly couple these equations. The equations are also geometrically non-linear due to finite deformation kinematics and by their constitutive closure. The solution of the resulting model consists of two parts that are coupled in a staggered fashion, the crystal mechanics equations are lumped in the stress equilibrium equations, and the dislocation transport-reactions equations. The two sets of equations are solved by the Galerkin and First-Order System Least-Squares (FOSLS) finite element methods. A special attention is given to the accurate modeling of glissile dislocation junctions using de Rahm currents and graph theory ideas. The introduction of these measures requires the derivation of further transport relations. Using homogenization theory, we specialize the proposed model to a mean deformation gradient driven bulk plasticity model. Lastly, we simulate bulk plasticity behavior and compare our results against experiments.

1. INTRODUCTION

Dislocations are line defects that cause irreversible distortion to the crystal from the breaking of atomic bonds, otherwise known as plastic distortion. They were theorized to exist to account for the discrepancy between the theoretical yield strength of materials and experimentally observed value. To account for this discrepancy [184], [155], and [150] simultaneously suggested the existence of dislocations. They suggested that the perfect crystal can handle large stresses, but the observed weakness in the material were due to dislocations, which introduced a localized stress relaxation mechanism. Dislocations are also the boundary of slip surfaces of which demarcate regions of relatively displaced atoms. The amount of relative displacement between the atoms above and below these surfaces is known as the Burgers vector [80]. When the line direction of the dislocation line is aligned with the Burgers vector, the dislocation is called a screw dislocation, and when they are perpendicular, an edge dislocation. In general, the line direction can be in any direction, and the dislocation is said to be of mixed character. The measurement of the Burgers vector can be performed by introducing a Burgers circuit in a deformed crystal. This Burgers circuit is shown in Fig. 1.1. The closure failure of this circuit transferred to an ideal crystal gives the Burgers vector

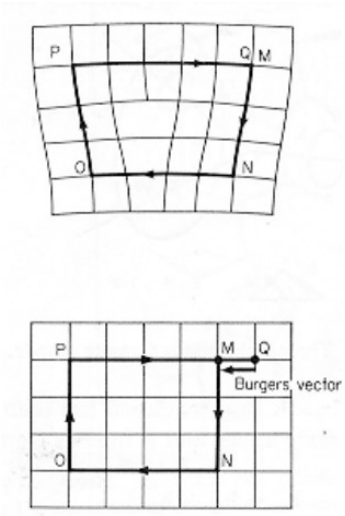

Figure 1.1. Burgers circuit introduced in the deformed crytal (top) that is transferred to an ideal crystal (bottom). The circuit is no longer closed in the ideal crystal due to the relative motion of atoms caused by the dislocation. Figure modified from [95].

[95]. A perfect dislocation has a Burgers vector corresponding to a translation vector of the material's lattice; otherwise, it is a partial dislocation. The slip plane, on which the slip surface resides, is the plane that the dislocation glides on. In crystalline materials, the Burgers vector and slip plane define a slip system. In face-centered cubic (FCC) materials there are twelve distinct families of slip systems denoted by {111}<110> where the curly brackets denote families of slip planes of the (111) type and the angle brackets denote families of the slip vectors which are of the [110] type [31] .

The introduction of dislocation into the crystal brings with it residual stress, which decays with one over the distance away from the dislocation line. This long-range residual stress field leads to interactions among pairs of dislocations and gives rise to the network's complex dynamics. When two dislocations are close to each other, they can react and (when it is energetically favorable) form a third dislocation segment called a junction segment. The common method to determine if this is energetically favorable is the Frank's criteria [9] which approximately compares the energy of the configuration before and after the reaction and deems the reaction is favorable if the energy is lowered after the reaction. If the reaction is such that the junction segment is on a slip system, the segment can move and is called glissile; otherwise, it is called sessile. These interactions increase the complexity of the dislocation networks, which further impede the motion of dislocations. Screw dislocations can also change their slip system through the process of cross slip [95].

Dislocation were thought of as hypothetical objects until they were first observed using Transmission Electron Microscopy (TEM) technology in the 1950's [78]. These techniques are still used to study complex problems involving dislocations like their interactions with various types of interfaces [101, 122], their interactions with point defects [30, 158], their interactions with other dislocations [27, 134], their interactions with various volume defects [49, 135], and dislocation nucleation [35, 129] to name a few.

As dislocations cross slip and react, they form a complex evolving network that takes on many different structures. For example, under monotonic loading, cell structures were found present in both FCC and body-centered cubic (BCC) materials in [143]. Under cyclic loading, vein and ladder structures can be observed [201, 58]. [91] found the dislocation structure to be dependent on the loading orientation of the crystal. This is shown in Fig. 1.2 These

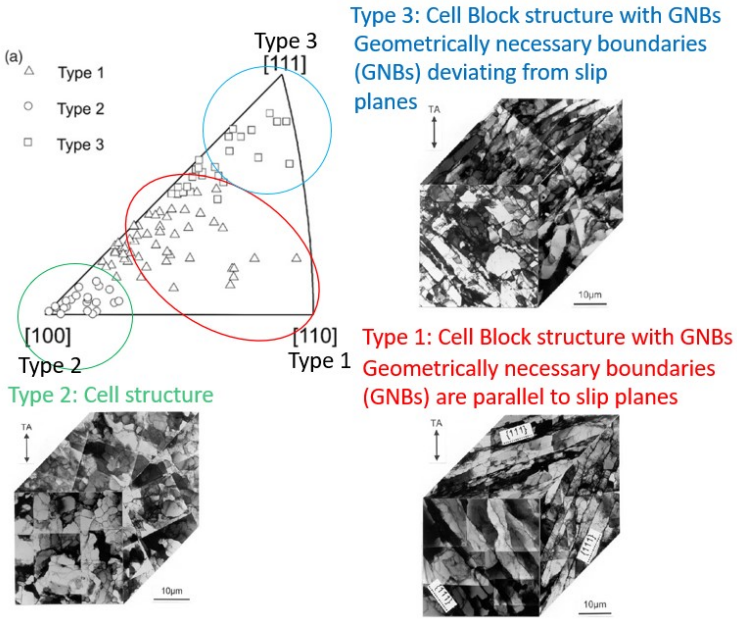

Figure 1.2. Depiction of the orientation dependence on the resulting dislocation structure. Three types of distinct structures formed depending on the orientation of the crystal compared to the loading axis. Modified from [91].

structures are typically characterized by their geometrically necessary boundaries (GNB) which separate regions with different slip system activity and cell boundaries which are believed to originate from statistically trapped dislocations; dislocations in close proximity which are oriented differently. It was shown in [91] that the type I structures shown in Fig.1.2 had GNBs aligned with slip planes whereas type III structures aligned with other crystolographic directions. In the type II experiments, cell structures were shown to form. It is believed that these structures formed according to the principle of Low-Energy Dislocation Structures (LEDS) where dislocation structure form based on configurations that lead to dislocations screening each other's elastic strain fields [111].

Plasticity models have existed for some time now to study the morphology of the dislocation network and the behavior of materials. Traditional crystal plasticity models [77, 14, 15] have been able to capture the hardening effect of dislocations through the use of local hardening rules. However, these models fail to capture the evolving microstructure of dislocations due to the local nature of the evolution equations. Discrete dislocation dynamics (DDD) models were created to study the dislocation networks and their evolution more faithfully. These models date back to the late 80's [119], and in more recent models of this type, dislocations are discretized into line segments connected by nodes in the network. The line segments are then evolved based on dislocation physics [24, 175]. The drawback of these models is the computational effort needed to obtain solutions at increasing strain due to the workload scaling by the number of dislocation segments squared. State of the art codes exist to minimize this computational burden see [25, 46, 152] to name a few. Continuum models of dislocations that include transport relations for dislocations are introduced to address the shortcomings of both the DDD and conventional crystal plasticity models. In these models, the transport of dislocations is accounted for in partial differential equations (PDE). These PDEs are obtained from various averaging operations applied to the discrete dislocation system. Because of these averaging operations, these continuum models contain less information than their discrete counterparts but require less computational effort to solve. Compared to DDD, these models require a constant computational effort at increasing strain which is proportional to the discretization resolution used in obtaining a solution. This

dissertation is focused on the study and development of a continuum vector density model of dislocations on the mesoscale.

Despite knowing the dislocation physics at the discrete level, there is still a lack of understanding of the emergent properties of dislocation networks such as patterning, hardening of metals, strain localization, and finite deformation-related phenomena, to name a few. This research serves as a stepping stone towards studying these complex phenomena. In this work, a finite deformation model of dislocations is developed to study various large strain effects such as the rotation of the crystal lattice. In developing this model, a lack of understanding in the continuum literature on how to incorporate dislocation-dislocation reactions into continuum models was noticed. A more fundamental introduction of dislocation reactions is lacking in the literature. The introduction of a junction point density aims to fill this gap. Interestingly the junction points may be viewed as markers in the material to denote when reactions reactions have occurred. It is believed that this work will aid our understanding of the hardening of the material and patterning of the dislocation network.

This dissertation is arranged as follows. Chapter 2 presents a review of previous continuum dislocation dynamics (CDD) models. Then in Chapter 3, a vector density continuum model for dislocations at finite deformation is introduced. This model will set the foundation for later models in studying the behavior of dislocations at finite deformation. A numerical algorithm for solving this model using the finite element method is developed in Chapter 4. This algorithm uses a staggered approach for solving the coupled system of dislocation transport equations and crystal mechanics. Numerical solutions to single slip system problems are presented to illustrate various aspects of the model. In Chapter 5, integral currents and graph theory are used to introduce dislocation reactions in the vector density representation of dislocations. A set of junction point densities are introduced to more accurately represent the dislocation network in the continuum model.The kinematics and transport equations for both the dislocation line densities on each slip system and junction point densities are the primary focus of this chapter. Chapter 6 is devoted to obtaining a mean velocity field for the junction point densities and obtaining a closed form set of coupled transport equations for the vector densities and junction point densities. In this chapter, the forces on individual dislocation junction points are developed and with the help of a velocity mobility law they

are related to junction point velocities. The mean velocity is then obtained via averaging. Lastly in Chapter 7, we end with a summary and discussion of future work.

2. CONTINUUM DISLOCATION DYNAMICS: BACKGROUND

2.1 Classical theory of dislocations

The derivation of the static theory of dislocations can be traced back to [100],[146],[17] and [106] where the concept of the geometrically necessary dislocations (GND) are introduced and are used as a measure of the incompatibilities in the displacement gradient. In the classical theory of dislocations the displacement gradient is decomposed into an elastic and plastic part as

$$\boldsymbol{\beta} = \boldsymbol{\beta}^{\mathrm{e}} + \boldsymbol{\beta}^{\mathrm{p}} \tag{2.1}$$

where $\boldsymbol{\beta}^{\mathrm{p}}$ is the plastic distortion of the crystal accounting for the plastic slip of the crystal due to dislocations, and $\boldsymbol{\beta}^{\mathrm{e}}$ is the elastic distortion which accounts for the distortions due to elastic fields and is responsible for stresses. $\boldsymbol{\beta}^{\mathrm{p}}$ and $\boldsymbol{\beta}^{\mathrm{e}}$ both contain the incompatibility that is created by the dislocation. The dislocation density tensor, sometimes named the Kroner-Nye tensor, measures this incompatibility. It is derived from the continuum version of the definition of the Burgers vector

$$\mathbf{b} = -\int_c \boldsymbol{\beta}^{\mathrm{e}} \mathrm{d}\boldsymbol{x} = \int_c \boldsymbol{\beta}^{\mathrm{p}} \mathrm{d}\boldsymbol{x}. \tag{2.2}$$

In the last expression, c is a closed loop known as the Burgers circuit. Then, using Stokes Theorem, the Kroner-Nye tensor is introduced over the surface which bounds the Burgers circuit. Locally, the Kroner-Nye tensor takes the form

$$\boldsymbol{\alpha} = -\mathrm{Curl}\boldsymbol{\beta}^{\mathrm{e}} = \mathrm{Curl}\boldsymbol{\beta}^{\mathrm{p}}. \tag{2.3}$$

For a single dislocation loop, $\boldsymbol{\alpha}$ takes the form [102]

$$\alpha_{\mathrm{ij}} = \xi_{\mathrm{i}} b_k \delta_c \tag{2.4}$$

where ξ is the unit tangent to the dislocation line and δ_c is a dirac delta function over the dislocation line.

The static theory was further developed into a dynamic theory by Mura et al [144] and Kosevich et al [103]. Disclinations were also added into the dynamic theory by a series of papers by DeWit [41, 47, 42, 39]. In this dynamic theory, a dislocation flux across the burgers circuit is introduced in one form or another in the previously stated models. This flux can be viewed as an incompatibility introduced by the movement of dislocations.

The next question is how the dislocation density tensor varies over time. Mura addressed this question in [144, 145]. In these works, the time rate of change of the dislocation density tensor is equated to the flux of dislocations across the burgers circuit. This is shown in the figure below, Mura describes the dislocation flux through the third order tensor $\boldsymbol{V}$.

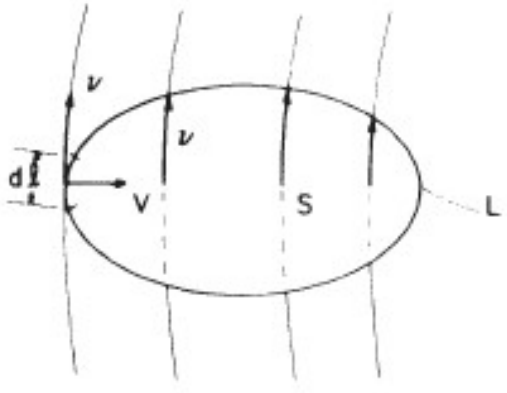

Figure 2.1. Burgers vector content increases due to dislocations threading a surface S by passing through circuit L, where v is the dislocation direction, V is the dislocation velocity, and dl is the infinitesimal line element of the circuit L. Taken from [145].

The net increase in Burgers vector content within the Burgers circuit is obtained as

$$\int_S \frac{\mathrm{d}}{\mathrm{d}t}\alpha_{hl}n_h\mathrm{d}S = \int_L \epsilon_{lh\mathrm{j}}V_{lh\mathrm{i}}\mathrm{d}l_{\mathrm{j}} \tag{2.5}$$

$$V_{lh\mathrm{i}} \equiv \sum_n \xi_h^n v_l^n b_{\mathrm{i}}^n$$

where n is summing over all dislocations with unit line tangent ξ, Burgers vector $\mathbf{b}$, and d$\boldsymbol{l}$ denotes an infinitesimal line segment.

The development of a continuum model fundamentally requires a choice of scale. This choice of scale impacts the accuracy of the density measures used to describe the dislocation system. For instance, the definition of the dislocation density tensor can be viewed as measuring the signed intersections of dislocations with the plane bounding the Burgers circuit. This interpretation illuminates the fact that the dislocation density tensor is ignorant of the statistically stored dislocations which link the circuit. This inadequacy of the dislocation density tensor is increased by using the dislocation density at larger length scales. This is depicted in the figure below, In the subsequent sections of this chapter, the focus is shifted

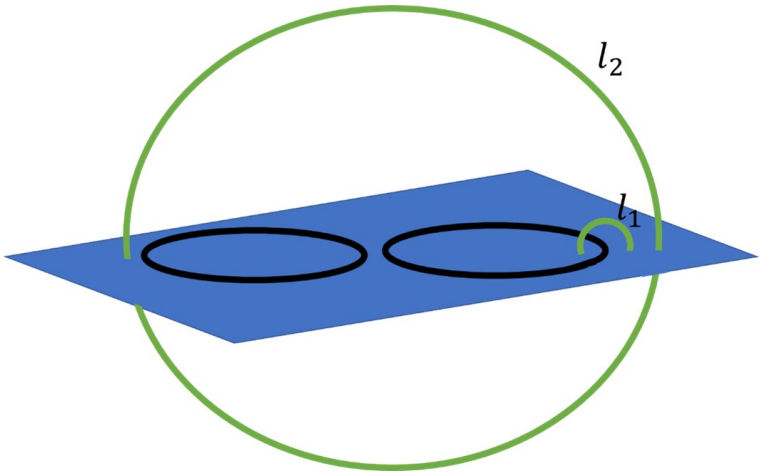

Figure 2.2. Length scale visualization. The comparison of two length scales l_1 and l_2 which represent the size of the burgers circuit in green used to measure dislocations.

onto how various authors solve this fundamental modeling problem associated with a choice of modeling scale.

2.2 Statistical models of dislocations

In the earlier statistical models, only 2D models were analyzed. In these models, dislocations are viewed as particles so that classical statistical methods can be applied. Because they are treated as point particles, an ensemble average of the defect density is

relatively easy to define. However, in 3D dislocations models, dislocations are treated as space curves, adding a layer of complexity in describing the dislocation system. For the 2D derivations, a discrete system of edge dislocations piercing the plane are considered. For over-damped dislocation motion, the dynamic equations governing each of the dislocation's motion can be written in the form:

$$\begin{aligned} \mathbf{v}_{\mathrm{i}} &= B\left(\sum_{\mathrm{j}\neq\mathrm{i}}^{N}\mathbf{F}(\mathbf{r}_{\mathrm{i}}-\mathbf{r}_{\mathrm{j}})+\mathbf{b}\tau_{\mathrm{ext}}\right) \\ \mathbf{F}(\mathbf{r}_{\mathrm{i}}-\mathbf{r}_{\mathrm{j}}) &\equiv \mathbf{b}\tau_{\mathrm{ind}}. \end{aligned} \tag{2.6}$$

In the previous expression, $\mathbf{v}_{\mathrm{i}}$ is the vector representing the velocity of the ith dislocation, τ_{ext} is the externally applied shear stress, $\mathbf{F}(\mathbf{r}_{\mathrm{i}}-\mathbf{r}_{\mathrm{j}})$ is the force on dislocation i due to incompatible elastic field on dislocation j, τ_{ind} is the stress field caused by an edge dislocation at the point $\mathbf{r}$, and B is the dislocation drag coefficient. The stress field τ_{ind} is given by

$$\tau_{\mathrm{ind}}(\mathbf{r}) = \frac{b\mu}{2\pi(1-\nu)}\frac{x\left(x^2-y^2\right)}{\left(x^2+y^2\right)^2}. \tag{2.7}$$

In [62] Groma utilizes ideas from statistical mechanics to show that the dynamics of the system of 2D edge dislocations can be cast into transport equations of the form:

$$\begin{aligned} \frac{\partial\rho_{+}}{\partial t} &= \int\frac{\partial}{\partial\mathbf{r}_1}\left\{\rho_{+,-}-\rho_{+,+}\right\}\mathbf{F}\left(\mathbf{r}_1-\mathbf{r}_2\right)d\mathbf{r}_2 \\ \frac{\partial\rho_{-}}{\partial t} &= \int\frac{\partial}{\partial\mathbf{r}_1}\left\{\rho_{-,+}-\rho_{-,-}\right\}\mathbf{F}\left(\mathbf{r}_1-\mathbf{r}_2\right)d\mathbf{r}_2. \end{aligned} \tag{2.8}$$

In the above, ρ_{+} and ρ_{-} are the one-particle density functions and $\rho_{+,+}, \rho_{+,-}, \rho_{-,+}$ and $\rho_{-,-}$ are the two-particle density functions. To close the set of equations the two particle density functions are approximated using pair correlation functions $d_{\mathrm{i,j}}$ as

$$\rho_{\mathrm{i,j}}\left(r_1,r_2\right) \approx \rho_{\mathrm{i}}\left(r_1\right)\rho_{\mathrm{i}}\left(r_2\right)\left[1+d_{\mathrm{i,j}}\right] \quad \mathrm{i,j}=+,-. \tag{2.9}$$

In [62], higher-order pair correlations are neglected and the following transport equations are found:

$$\begin{aligned} \frac{\partial \rho}{\partial t} + \frac{\partial}{\partial \mathbf{r}} \{B\mathbf{b}\tau_{\text{int}} k\} &= 0 \\ \frac{\partial k}{\partial t} - \frac{\partial}{\partial \mathbf{r}} \{B\mathbf{b}\tau_{\text{int}} \rho\} &= 0. \end{aligned} \tag{2.10}$$

In the above, $\rho = \rho_- + \rho_+$ is the total dislocation density, $k = \rho_+ - \rho_-$ is the GND dislocation density, and τ_{int} is the nonlocal stress due to interacting dislocations and external stress given by

$$\tau_{\text{int}} = \int \tau_{\text{ind}} \left(\mathbf{r} - \mathbf{r}'\right) \{\rho_+ - \rho_-\} \, d\mathbf{r}' + \tau_{\text{ext}} \, . \tag{2.11}$$

In a subsequent work, [204] investigate the higher-order pair correlation functions that were neglected in [62]. These pair correlation terms will prove to be essential for modeling the short-range interactions for dislocations and providing hardening behavior for these models. In the work [204], the pair correlation functions are computed using discrete dislocation dynamics simulations. The correlation functions are found to scale with the average dislocation spacing $\sqrt{\rho}$ and exhibit a 1/r singularity at short distances. This is shown Fig. 2.3.

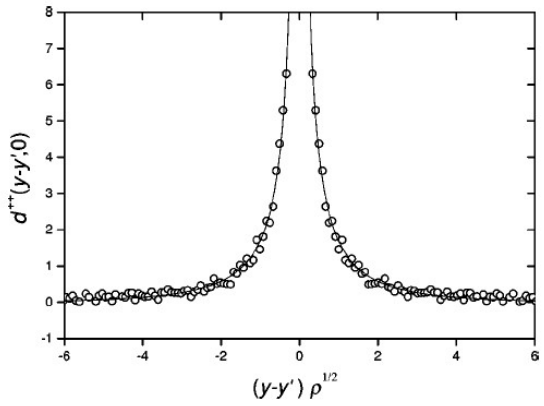

Figure 2.3. Decay of correlation function of dislocations of the same sign [204].

In a later paper, [63] introduces the correlation functions into their model in (2.9). In the next few years, the effects of new stress terms that arise due to the pair correlation functions are studied. In particular, the effects that the new terms have on the patterning of

2D single slip dislocation systems are analyzed. In [64] additional stress terms are included which come from a more detailed expansion of pair correlation terms. This leads to the transport equations

$$\frac{\partial \rho}{\partial t} + M_0 b \frac{\partial}{\partial x}\left\{k\left[\tau_{sc} + \tau_{ext}\right] + k\tau_b + \rho\widetilde{\tau}_b\right\} = 0 \tag{2.12}$$
$$\frac{\partial k}{\partial t} + M_0 b \frac{\partial}{\partial x}\left\{\rho\left[\tau_{sc} + \tau_{ext}\right] + \rho\tau_b - \rho\tau_f + \frac{k^2}{\rho}\tau_f + k\widetilde{\tau}_b\right\} = 0$$

where the flow stress τ_f, the back stress τ_b, and the diffusion stress $\widetilde{\tau}_b$ are additional terms derived from the correlation functions. They can be approximated as:

$$\tau_f \approx -\mu b C\sqrt{\rho}\left(1 + \frac{\partial^2 \rho}{\partial x \partial x}\right) \tag{2.13}$$

$$\tau_b \approx -\frac{GbD}{\rho}\frac{\partial k}{\partial x} \tag{2.14}$$

$$\widetilde{\tau}_b \approx -\frac{GbA}{\rho}\frac{\partial \rho}{\partial x}. \tag{2.15}$$

In the previous relations A, C and D are nondimemsional constants and G is the shear modulus. In [64] it is shown that the primary source of the instability that leads to pattern formation for 2D dislocation systems is the $\sqrt{\rho}$ dependence on the flow stress. It is also noted that the $\sqrt{\rho}$ dependence of the flow stress alone does not account for the introduction of a length scale. The addition of the diffusion term, $\frac{\partial^2 \rho}{\partial x \partial x'}$, associated with the flow stress leads to the length scale of the dislocations patterning. Since this paper is only for a single slip system this term can be thought as coming from the dipole interactions of dislocations. Also, the hardening behavior that comes from τ_b,$\widetilde{\tau}_b$ and $\tau_f$should only resemble stage 1 hardening considering that short range interaction of junction formation and forest hardening are not being considered.

2.3 Hochrainer's higher dimensional model

The theory developed by Hochrainer and coworkers [88] was designed to address an issue with the inadequacy of the geometrically necessary dislocation density's ability to represent the total dislocation density of the dislocation network at increasing length scales.

The dislocations are represented in a higher dimensional configuration space consisting of the regular spatial coordinates and additional coordinates that account for the description of the dislocation line direction. For this reason it is named higher dimensional Continuum Dislocation Dynamics (hdCDD). In this description, the dislocation density is obtained by taking ensemble averages over "lifted curves". To illustrate this formulation, a simple 2D example with only one slip system is considered. In this space, the generalized "lifted" line direction is defined as

$$\boldsymbol{L} = (\cos(\phi), \sin(\phi), k(\mathbf{x}\phi)) \tag{2.16}$$

$$\tag{2.17}$$

where the first two components of $\boldsymbol{L}$ represent the regular line direction on the glide plane and ϕ is the angle that parametrizes the line direction relative to the Burgers vector. The third component of this generalized line direction is the local line curvature. In this formulation, at a single point, two different dislocation lines with parallel line directions originating from separate loops will be distinguishable due to their differing curvature in the 3rd component of the generalized line direction. A pictorial depiction is shown in Fig. 2.4

The addition of the angular dependence on the model is important for considering length scales where the Burgers circuit used to measure dislocations is larger than l_1 in Fig. 2.2 and one still wishes for the density variables to accurately represent dislocations. With the generalized line direction in (2.16), the higher order dislocation density tensor, denoted by α^{II}, takes the form

$$\boldsymbol{\alpha}^{II}(\boldsymbol{x}, \phi) = \rho^{II}(\boldsymbol{x}, \phi)\boldsymbol{L}(\boldsymbol{x}, \phi) \otimes \boldsymbol{b}. \tag{2.18}$$

The Kroner-Nye tensor used by the previous works can be recovered by integrating over the line orientation

$$\boldsymbol{\alpha} = \int_0^{2\pi} \rho^{II}(\boldsymbol{x}, \phi)\boldsymbol{L}(\boldsymbol{x}, \phi) d\phi \otimes \boldsymbol{b}. \tag{2.19}$$

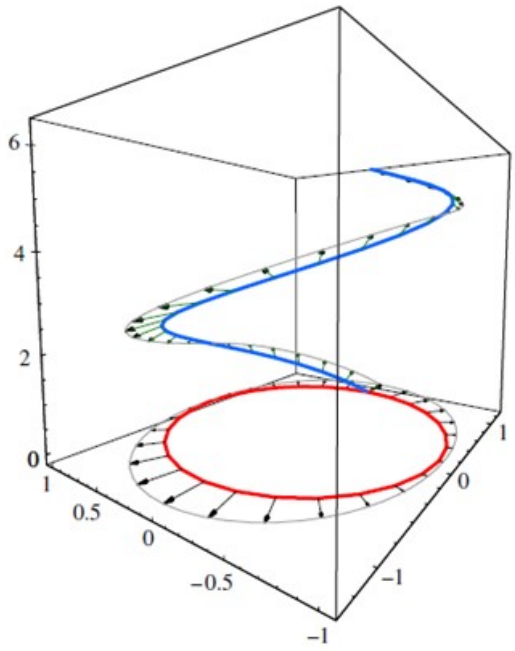

Figure 2.4. A dislocation (in red) with its line direction parametrized by the value in the vertical direction of the blue curve. The lifted blue curve represents the loop with extra information about the orientation of the red curve. The arrows attached to the blue and red curves correspond to the rotational and dislocation velocity respectively [88].

The transport relations for this model read:

$$\partial_t \rho = -\hat{\nabla} \cdot (\rho \mathbf{V}) + qv \tag{2.20}$$

$$\partial_t q = -\hat{\nabla} \cdot (q \mathbf{V}) - \rho \hat{\nabla}_{\mathbf{L}} \hat{\nabla}_{\mathbf{L}} v \tag{2.21}$$

where $\boldsymbol{V}$ is a generalized velocity in the higher dimensional space and v is the scalar normal velocity. In the previous expression, $\hat{\nabla} = \nabla + \partial_\phi$ is a generalized derivative operator consisting of a normal spatial derivative and a derivative for the angular coordinate.

Since these equations are expressed in a higher dimensional space they are numerically difficult to solve. To reconcile this, the equations are averaged over the orientation space to reduce the dimensionality of the problem. Since these dislocation measures are based on kinematics alone and not directly tied to the plastic distortion, these densities represent the total dislocation density and not just the GND's. A numerical implementation of these simplified CDD (sCDD) equations are derived in [165] where the model is compared to DDD simulations. Back-stress type terms similar to the ones in (2.13) are added to account for dislocation interactions. It is important to note also that on smaller length scales, like l_1 in Fig. 2.2, averages over the orientation space reduce to the line bundle approximation of dislocations which is discussed in the next subsection.

2.4 Vector density model of dislocations

In the paper [197], a mesoscale model is derived using the vector density representation of dislocations. The assumption for this models length scale is that it is considerably shorter than the length of the average dislocation loop radius but larger than the average dislocation spacing. On this length scale, all dislocations are GNDs and can be viewed as an averaged bundle of dislocations with the same line orientation. The velocity of this bundle is the average velocity of the individual dislocations. This is represented below,

The dislocation density tensor is represented as a sum of dislocation density tensors on each slip system l

$$\boldsymbol{\alpha} = \sum_l \boldsymbol{\alpha}^{(l)} = \sum_l \boldsymbol{\rho}^{(l)} \otimes \boldsymbol{b}^{(l)}. \tag{2.22}$$

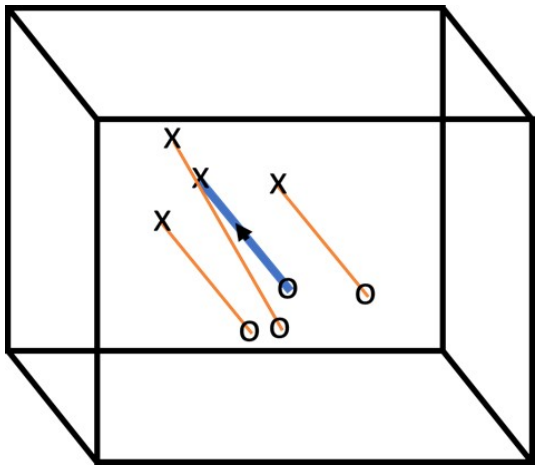

Figure 2.5. Depiction of a continuum point with a line bundle (blue) representation. It is obtained by the average of the orientations of dislocations (orange) in the representative volume.

The dislocations on the slip system are then represented as a vector density,$\boldsymbol{\rho}^{(l)} = \rho^{(l)}\boldsymbol{\xi}^{(l)}$ where $\boldsymbol{\xi}^{(l)}$ is the average unit line tangent of the dislocation bundle. The evolution equations for this density follow from the transport equations for the total dislocation density tensor. By adding networking terms, the transport equations for each vector density become

$$\dot{\boldsymbol{\rho}}^{(l)} = \boldsymbol{\nabla} \times \left(\boldsymbol{v}^{(l)} \times \boldsymbol{\rho}^{(l)}\right) + \dot{\boldsymbol{\rho}}^{CS}_{l^* \to l} + \dot{\boldsymbol{\rho}}^{CS}_{l \to l^*} \tag{2.23}$$

where only cross slip networking terms have been added. In more recent works interaction terms for junction formation have also been considered, see [125, 188]. The glide component of the Peach-Koehler force and a velocity mobility law can be used to calculate the dislocation bundle velocity as

$$\mathbf{v}^{(l)} = \mathrm{M}|b|\tau^{(l)}\left(\boldsymbol{\xi}^{(l)} \times \boldsymbol{n}^{(l)}\right) \tag{2.24}$$

where $\boldsymbol{n}^{(l)}$ is the slip system unit normal vector and $\tau^{(l)}$ is the resolved shear stress on slip system l.

2.5 Field dislocation mechanics model

Field Dislocation Mechanics (FDM) is a continuum theory of dislocation dynamics that was developed in the finite deformation setting by Acharya and coworkers [1, 2]. It was designed as a continuum microscopic theory of dislocation dynamics with the free energy dependent on the elastic strain. In the small deformation theory and neglecting boundary conditions, the FDM equations read:

$$\begin{aligned} \operatorname{curl}(\boldsymbol{\chi}) &= \boldsymbol{\alpha} \\ \operatorname{div}(\boldsymbol{\chi}) &= \mathbf{0} \\ \operatorname{div}(\operatorname{grad}(\dot{\mathbf{z}}) &= \operatorname{div}(\boldsymbol{\alpha} \times \boldsymbol{V}) \\ \operatorname{div}(\boldsymbol{C} : \{\operatorname{grad}(\boldsymbol{u} - \mathbf{z}) + \boldsymbol{\chi}\}) &= \mathbf{0} \\ \dot{\boldsymbol{\alpha}} &= -\operatorname{curl}(\boldsymbol{\alpha} \times \boldsymbol{V}) + \boldsymbol{s} \end{aligned} \tag{2.25}$$

where $\boldsymbol{\chi}$ is the incompatible part of the plastic distortion, $\text{grad}(\mathbf{z})$ is its compatible part, $\mathbf{V}$ is the average dislocation velocity, $\text{grad}(\mathbf{u}-\mathbf{z})+\boldsymbol{\chi}$ is the elastic distortion tensor, and $\boldsymbol{s}$ represents a source term for dislocations. The first two equations are the field equations for the incompatible field $\boldsymbol{\chi}$, in terms of a given dislocation density tensor. Using the Helmholtz decomposition for second-order tensors, the plastic distortion is written as

$$\boldsymbol{\beta}^p = \text{grad}(\mathbf{z}) + \boldsymbol{\chi} \tag{2.26}$$

where $\boldsymbol{\chi}$ is the incompatibility that represents dislocations. Then the third equation in (2.25) comes from taking the divergence of Orowans equation in tensor form

$$\text{div}\left(\dot{\boldsymbol{\beta}}^p\right) = \text{div}(\boldsymbol{\alpha}\times\boldsymbol{V}). \tag{2.27}$$

The next set of equations in (2.25) comes from the mechanical equilibrium equations after applying Hooke's law. The last equation comes from a balance law of the change in the Burgers vector content contained within a Burgers circuit where an additional source term is added.

In subsequent papers, this theory is developed into the Phenomenological Mesoscopic Field Dislocation Mechanics (PMFDM) from space-time averaging of the FDM equations in [4, 163] with the averaging procedure performed in [5]. The space-time averaged equations are written below:

$$\begin{aligned}
\text{curl}(\bar{\boldsymbol{\chi}}) &= \overline{\boldsymbol{\alpha}} \\
\text{div}(\bar{\boldsymbol{\chi}}) &= \mathbf{0} \\
\text{div}\left(\text{grad}(\overline{\mathbf{z}}\right) &= \text{div}\left(\overline{\boldsymbol{\alpha}}\times\overline{\boldsymbol{V}} + \boldsymbol{L}^p\right) \\
\text{div}(\boldsymbol{C} : \{\text{grad}(\overline{\boldsymbol{u}}-\overline{\mathbf{z}}) + \bar{\boldsymbol{\chi}}\}) &= \mathbf{0} \\
\overline{\boldsymbol{\alpha}} &= -\,\text{curl}\left(\overline{\boldsymbol{\alpha}}\times\overline{\boldsymbol{V}} + \boldsymbol{L}^p\right) + \overline{\boldsymbol{s}}
\end{aligned} \tag{2.28}$$

where the averaged quantities are denoted with a bar. $\boldsymbol{L}^p$ is interpreted as the rate of plastic flow due to statistically stored dislocations (SSD) and is introduced to account for the fact

that $\overline{\alpha \times \mathbf{V}} \neq \overline{\alpha} \times \overline{\mathbf{V}}$ at increasing length scales. In the paper the claim is that this term should be obtained from phenomenological constitutive laws. $\mathbf{L}^p$,$\overline{s}$ and $\overline{\mathbf{V}}$ are introduced and to get a closed set of equations these will need to be expressed in terms of the field variables $\bar{\boldsymbol{\alpha}}, \bar{\boldsymbol{\chi}}, \bar{\mathbf{z}}$, and $\bar{\mathbf{u}}$. These terms can be closed by stochastic terms to account for statistically stored dislocations and for short range interactions.

3. CONTINUUM DISLOCATION DYNAMICS AT FINITE DEFORMATION

A portion of this chapter is previously published in the Journal of the Mechanics and Physics of Solids by Kyle Starkey, Grethe Winther, Anter El-Azab as "Theoretical development of continuum dislocation dynamics for finite-deformation crystal plasticity at the mesoscale", 139, 103926. https://doi.org/10.1016/j.jmps.2020.103926

3.1 Abstract

The equations of dislocation transport at finite crystal deformation were developed, with a special emphasis on a vector density representation of dislocations. A companion thermodynamic analysis yielded a generalized expression for the driving force of dislocations that depend on Mandel (Cauchy) stress in the reference (spatial) configurations and the contribution of the dislocation core energy to the free energy of the crystal. Our formulation relied on several dislocation density tensor measures linked to the incompatibility of the plastic distortion in the crystal. While previous works develop such tensors starting from the multiplicative decomposition of the deformation gradient, we developed the tensor measures of the dislocation density and the dislocation flux from the additive decomposition of the displacement gradient and the crystal velocity fields. The two-point dislocation density measures defined by the referential curl of the plastic distortion and the spatial curl of the inverse elastic distortion and the associate dislocation currents were found to be more useful in deriving the referential and spatial forms of the transport equations for the vector density of dislocations. A few test problems showing the effect of finite deformation on the static dislocation fields are presented, with a particular attention to lattice rotation. The framework developed provides the theoretical basis for investigating crystal plasticity and dislocation patterning at the mesoscale, and it bears the potential for realistic comparison with experiments upon numerical solution.

3.2 Introduction

A theoretical development of continuum dislocation dynamics for finite deformation mesoscale crystal plasticity is presented in this communication. This development is motivated by the progress made in modeling crystal deformation at the mesoscale using dislocation dynamics, with both discrete [13, 46, 154, 175, 191] and continuum [54] representations of the dislocations. This progress showed that a direct coupling of the dislocation theory and continuum mechanics of crystals to study metal plasticity is feasible. Now, an important goal is to extend the dislocation dynamics approach to model finite crystal deformation, which can help us understand the collective dislocation mechanisms of plasticity at experimentally relevant plastic strains. Above few to several percent strain, dislocations self-organize in patterns that influence the flow strength of crystals. Such patterns are associated with significant lattice misorientation across dislocation walls or boundaries of various types [92].

Continuum dislocation dynamics represent dislocations by density fields governed by transport equations that are solved concurrently with crystal mechanics. Some models within this framework that use a tensor representation of the dislocation density were developed by developed by [1, 2], [4], and [163] see also a recent development in which a finite deformation formalism was presented [11]. Formalisms that distinguish dislocations based upon their slip systems but utilize scalar or vector representations of the dislocation fields were developed by other authors [44, 45, 53, 52, 86, 153, 171, 196, 197, 203]. In the latter models, the line direction of dislocations is preserved in the density representation so as to facilitate the incorporation of processes such as cross slip, annihilation, and junction reactions [139, 196, 179]. However, most of the latter models, the ones of interest here, lack the kinematics of finite deformation, which is intimately tied to the dislocation patterns in crystals deforming in multiple slip up to strains exceeding few percent. In such strain ranges, crystals develop dislocation microstructures with dislocation dense boundaries. Three characteristic types of such boundaries were observed under monotonic loading: extended planar boundaries aligned with slip planes, microstructures with shorter and more randomly oriented boundaries forming cells, and extended planar boundaries on planes slightly deviating from the slip plane; see Fig. 3.1. In between the extended planar boundaries cells are also found.

All three types of microstructures are observed independent of the deformation mode, e.g., tension [90], compression [115] and rolling [128]. In all modes, however, the type of microstructure found exhibits a strong dependence on the crystallographic orientation of the load. The microstructures in single crystals of aluminium [98, 183], nickel [208] and copper [99] exhibit the same type of orientation dependence. It was also observed that grains in polycrystals develop microstructures with the same orientation dependence and microstructural characteristics as single crystals [75, 90] for grain sizes down to about 1 µm [114]. These characteristics have been clearly observed after true strains of about 0.05-0.8 [91] and strain rates of 10^{-4}-10^{3} [91, 208] at ambient temperatures. At smaller strains, the boundaries are less well-defined but dislocation-rich and dislocation-free domains are formed in multi-slip conditions [97, 178].

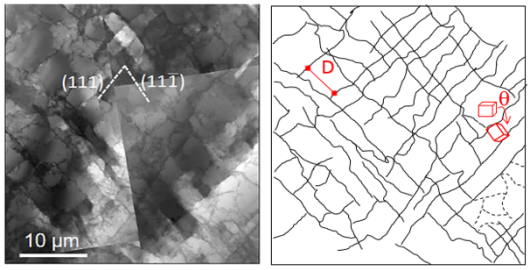

Figure 3.1. A TEM micrograph showing a typical dislocation microstructure in rolled aluminum (adopted from [89]) and a tracing of the extended planar boundaries aligned with {111} slip planes (continuous lines) and cell boundaries (dashed lines) . These boundaries are characterized by lattice misorientation and separation distance that were extensively studied [93].

The goal of the current effort is to develop a mesoscale plasticity formalism capable of predicting the dislocation microstructures of the types discussed above. An important first step in this regard is to generalize our continuum dislocation dynamics [197] to account for the kinematics of finite deformation of crystals. In doing so, it is critical to distinguish the dislocation density measures in the reference, microstructural, and deformed crystal configurations and derive their space-time evolution equations accordingly. Our effort builds upon the classical continuum representation of dislocations. As such, we mention here the early contributions reported in [100], [146], [17], and [106]. In these works, dislocations were measured by the incompatibility of the displacement field using the dislocation density

tensor, $\boldsymbol{\alpha}$. In the case of small deformation, this tensor, which is known as the Kröner-Nye tensor, is derived from the kinematic definition of Burgers vector, $\mathbf{b}$, as follows:

$$-\mathbf{b}=\oint \mathrm{d}\mathbf{u}^{\mathrm{e}}=\oint \boldsymbol{\beta}^{\mathrm{e}}\mathrm{d}\mathbf{x}=\int (\boldsymbol{\nabla}\times\boldsymbol{\beta}^{\mathrm{e}})\mathrm{d}\mathbf{A}=\int \boldsymbol{\alpha}\mathrm{d}\mathbf{A}. \tag{3.1}$$

This yields: $\boldsymbol{\alpha}=-\boldsymbol{\nabla}\times\boldsymbol{\beta}^{\mathrm{e}}=\boldsymbol{\nabla}\times\boldsymbol{\beta}^{\mathrm{p}}$. In the above, $\boldsymbol{\beta}^{\mathrm{e}}$ is the elastic distortion, $\mathrm{d}\mathbf{u}^{\mathrm{e}}$ is a differential elastic displacement over a differential distance $\mathrm{d}\mathbf{x}$ in the crystal, and $\mathrm{d}\mathbf{A}$ is a differential area element [144], [103] and [40] further elaborated the dynamics of dislocations within this framework by introducing a dislocation flux and developing continuity equation for the Kröner-Nye tensor in terms of the dislocation flux [54]. Relatively recently, an invariant form of the second order dislocation density tensor was developed [34] and shown to transform between different crystal configurations in the same way as the stress tensor does. Following that development, gradient plasticity theories making use of the dislocation density tensor were developed [70, 72, 71]. In [82], a formulation of dislocation evolution at finite deformation was introduced in the intermediate space necessitating the use of curvilinear coordinates in a way similar to the works in [18] and [107] but extended this to the language of differential forms and de Rham currents in the finite deformation setting.

In this paper, we present a new formulation of continuum dislocation dynamics for mesoscale plasticity at finite deformation with vector representation of dislocations. The starting point is the kinematics of incompatible crystal deformation. We identify the incompatibility of deformation, i.e., Burgers vector measure, starting with the additive decomposition of the displacement gradient, which was found to be consistent with the definition based on the multiplicative decomposition of the deformation gradient. In deriving the rate form of crystal incompatibility, which is the continuity equations for the dislocation density tensors, we follow an additive decomposition of the material velocity field as well. It is shown that the additive decomposition of the displacement gradient and the compatibility of the total displacement leads to defining multiple dislocation density tensors that were already used by other authors. It is also shown that, the decomposition of the crystal velocity and its compatibility leads to the definition of the dislocation current and transport equations for the dislocation density tensors. In Appendix 3.A, we demonstrate that the latter derivation

is consistent with the transport equations derived in [34] for the microstructure dislocation density tensor. Our formalism is distinctly different from other previous works in that it ends up with the transport equations governing the vector dislocation densities as the basic equations of continuum dislocation dynamics. This required a derivation of a work conjugate driving force for dislocation motion which is similar in form to the Peach-Koehler force. Numerical examples are presented for dislocation fields at finite deformation illustrating the role of the geometric non-linearity and lattice rotation in the context of dislocation mechanics at large deformations. Referential forms of the equations of dislocation statics were used in these examples. However, the continuum dislocation dynamics equations of interest were developed in both referential and spatial forms.

3.3 Notation and preliminary content

Here we follow the tensor notation and convention used by [73]. In the following $\mathbf{T}$ represents a second order tensor field and $\mathbf{v}$ represents a vector field.

$$\mathrm{div}(\mathbf{v}) = \frac{\partial \mathrm{v_i}}{\partial \mathrm{x_i}} \tag{3.2}$$

$$\mathrm{curl(v)_i} = \epsilon_{\mathrm{ijk}} \frac{\partial \mathrm{v_k}}{\partial \mathrm{x_j}} \tag{3.3}$$

$$\mathrm{div(T)_i} = \frac{\partial \mathrm{T_{ij}}}{\partial \mathrm{x_j}} \tag{3.4}$$

$$\mathrm{curl(T)_{ij}} = \epsilon_{\mathrm{ipq}} \frac{\partial \mathrm{T_{jq}}}{\partial \mathrm{x_p}} \tag{3.5}$$

The notation $\mathrm{curl}\,(\mathbf{T})^{\mathrm{T}}$ is used here to denote the transpose of the curl of the second order tensor $\mathbf{T}$.

Some useful identities are shown below ($\mathbf{v}$ and $\mathbf{u}$ are vector fields):

$$\mathrm{curl}(\mathbf{u} \otimes \mathbf{v}) = [\,\mathrm{grad}(\mathbf{u})\mathbf{v} \times\,]^{\mathrm{T}} + \mathrm{curl}(\mathbf{v}) \otimes \mathbf{u} \tag{3.6}$$

$$\mathrm{div}(\mathbf{u} \otimes \mathbf{v}) = \mathrm{div}(\mathbf{v})\mathbf{u} + \mathrm{grad}(\mathbf{u})\mathbf{v} \tag{3.7}$$

$$\mathrm{curl}(\mathbf{u} \times \mathbf{v}) = \mathrm{div}(\mathbf{u} \otimes \mathbf{v} - \mathbf{v} \otimes \mathbf{u}) \tag{3.8}$$

Stokes theorem is expressed in the form:

$$\oint \mathbf{T}\mathrm{d}\mathbf{x}=\int \mathrm{curl}(\mathbf{T})^{\mathrm{T}}\mathbf{n}\mathrm{da}\ , \tag{3.9}$$

which follows from the well-known Stokes theorem for vector fields,

$$\oint \mathbf{v}\cdot\mathrm{d}\mathbf{x}=\int \mathbf{n}\cdot\mathrm{curl}\,(\mathbf{v})\,\mathrm{da}\ , \tag{3.10}$$

with the substitution $\mathbf{v}=\mathbf{T}\mathbf{c}$ for an arbitrary constant vector $\mathbf{c}$ that can be factored out to give (3.9). In the above $\mathbf{n}$da is an oriented area element with unit normal $\mathbf{n}$ and magnitude da. We refer to the material time derivative operator with the usual superposed dot notation,

$$\dot{(\ \ )}=\frac{\partial}{\partial \mathrm{t}}(\ \ )_{\mathbf{X}},$$

with $\mathbf{X}$ being the position vector in the reference configuration. The definitions (3.2)-(3.5) are written with respect to the coordinates $\mathbf{x}$ in the deformed configuration. The spatial differential operators with respect to referential coordinate $\mathbf{X}$ will be denoted by upper case; for example, the divergence of a vector field $\mathbf{v}$ is

$$\mathrm{Div}\,(\mathbf{v})=\frac{\partial \mathrm{v_i}}{\partial \mathrm{X_i}}. \tag{3.11}$$

We will also use the following tensor identities for the double inner product of two second order tensors $\mathbf{A}$ and $\mathbf{B}$:

$$\mathbf{A}:\mathbf{B}=\mathrm{A_{ij}B_{ij}}, \tag{3.12}$$

from which the identities below follow:

$$\mathbf{A}:\mathbf{B}=\mathbf{A}^{\mathrm{T}}:\mathbf{B}^{\mathrm{T}} \tag{3.13}$$

$$\mathbf{A}:(\mathbf{B}\mathbf{C})=\left(\mathbf{B}^{\mathrm{T}}\mathbf{A}\right):\mathbf{C}=\left(\mathbf{A}\mathbf{C}^{\mathrm{T}}\right):\mathbf{B}. \tag{3.14}$$

3.4 Incompatible crystal deformation and dislocation density measures

In this section, we introduce several dislocation density measures associated with plastic deformation of crystals, including two two-point tensors in addition to that introduced by [34]. Unlike these and other authors, we do so by working with the displacement gradient and its elastic and plastic components.

3.5 Decomposition of deformation gradient and displacement gradient

In the finite deformation setting for single crystal plasticity, the Kröner-Lee multiplicative decomposition of the deformation gradient [105, 116] is used,

$$\mathbf{F} = \text{Grad } = \mathbf{F}^{\text{e}}\mathbf{F}^{\text{p}}, \tag{3.15}$$

where $\mathbf{F}$ is the referential gradient of the deformation mapping $\mathbf{x} = \mathbf{(X}, \text{t}\mathbf{)}$, with $\mathbf{X}$ and $\mathbf{x}$ being the position vectors in the reference and deformed configurations of the crystal, respectively, and t is time. The elastic distortion $\mathbf{F}^{\text{e}}$ and the plastic distortion $\mathbf{F}^{\text{p}}$ are generally incompatible and do not generally represent gradients of a deformation mapping as does $\mathbf{F}$ itself. $\mathbf{F}^{\text{e}}$ holds the information of the rotation and stretch of the crystal lattice while $\mathbf{F}^{\text{p}}$ holds the information of the deformation due to the creation and motion of defects, mainly dislocations in our case. The decomposition (3.15) is understood in the sense that $\text{d}\mathbf{x} = \mathbf{F}\text{d}\mathbf{X}$, $\text{d}\mathbf{y} = \mathbf{F}^{\text{p}}\text{d}\mathbf{X}$, and $\text{d}\mathbf{x} = \mathbf{F}^{\text{e}}\text{d}\mathbf{y}$, with $\text{d}\mathbf{X}$ and $\text{d}\mathbf{x}$ being differential vector distances in the reference and deformed configurations of the crystal, respectively, and $\text{d}\mathbf{y}$ is a corresponding distance in the microstructure (intermediate) space. The latter space is not a continuous configuration of the material that is obtained by the gradient of a mapping from the reference configuration [74]. With this decomposition, the velocity gradient can be written as,

$$\mathbf{L} = \text{grad } \mathbf{v} = \mathbf{L}^{\text{e}} = \mathbf{F}^{\text{e}}\mathbf{L}^{\text{p}}\mathbf{F}^{\text{e}-1}, \tag{3.16}$$

where we define the elastic velocity gradient in deformed configuration

$$\mathbf{L}^{\text{e}} = \dot{\mathbf{F}}^{\text{e}}\mathbf{F}^{\text{e}-1} \tag{3.17}$$

and the plastic velocity gradient in the microstructure space is

$$\mathbf{L}^{\mathrm{p}} = \dot{\mathbf{F}}^{\mathrm{p}}\mathbf{F}^{\mathrm{p}-1}. \tag{3.18}$$

The kinematic argument that plasticity happens due to slip on specific slip planes manifests itself in the relationship [157],

$$\begin{aligned} \mathbf{L}^{\mathrm{p}} &= \sum_{l} \dot{\gamma}^{l}\mathbf{S}^{l} \\ \mathbf{S}^{l} &= \mathbf{s}^{l} \otimes \mathbf{m}^{l} \\ \mathbf{m}^{l} \cdot \mathbf{s}^{l} &= 0, |\mathbf{s}^{l}| = |\mathbf{m}^{l}| = 1 \end{aligned} \tag{3.19}$$

with $\mathbf{S}^{l}$ being the Schmid tensor of the l^{th}slip system, $\mathbf{s}^{l}$is the slip direction and $\mathbf{m}^{l}$ is the slip plane normal in the microstructure space. The term $\mathbf{F}^{\mathrm{e}}\mathbf{L}^{\mathrm{p}}\mathbf{F}^{\mathrm{e}-1}$in (3.16) represents the push forward of the plastic velocity gradient in the microstructure space to the deformed configuration. From the multiplicative decomposition the total Lagrangian strain can be decomposed into elastic and plastic parts,

$$\mathbf{E} = \mathbf{F}^{\mathrm{p}\mathrm{T}}\mathbf{E}^{\mathrm{e}}\mathbf{F}^{\mathrm{p}} = \mathbf{E}^{\mathrm{p}} \tag{3.20}$$

where

$$\begin{aligned} \mathbf{E}^{\mathrm{p}} &= \frac{1}{2}\left(\mathbf{F}^{\mathrm{p}\mathrm{T}}\mathbf{F}^{\mathrm{p}} - \mathbf{I}\right) \\ \mathbf{E}^{\mathrm{e}} &= \frac{1}{2}\left(\mathbf{F}^{\mathrm{e}\mathrm{T}}\mathbf{F}^{\mathrm{e}} - \mathbf{I}\right). \end{aligned} \tag{3.21}$$

We may also write (3.20) as $\mathbf{E} = \mathbf{E}^{\mathrm{e}}_{\mathrm{R}} = \mathbf{E}^{\mathrm{p}}$, with$\mathbf{E}^{\mathrm{e}}_{\mathrm{R}} \equiv \mathbf{F}^{\mathrm{p}\mathrm{T}}\mathbf{E}^{\mathrm{e}}\mathbf{F}^{\mathrm{p}}$ being the pullback of the elastic strain in the microstructure space to the reference configuration.

We propose to additively decompose the differential displacement $\mathrm{d}\mathbf{u} = \mathbf{u}(\mathbf{X} = \mathrm{d}\mathbf{X}) = \mathbf{u}(\mathbf{X}) = \mathbf{u}(\mathbf{x} = \mathrm{d}\mathbf{x}) = \mathbf{u}(\mathbf{x})$ along a differential element $\mathrm{d}\mathbf{X}$ into plastic and elastic parts in the form,

$$\mathrm{d}\mathbf{u} = \boldsymbol{\beta}\mathrm{d}\mathbf{X} = \boldsymbol{\beta}^{\mathrm{p}}\mathrm{d}\mathbf{X} + \boldsymbol{\beta}^{\mathrm{e}}\mathrm{d}\mathbf{x} \tag{3.22}$$

where,

$$\boldsymbol{\beta}^{p} \equiv \mathbf{F}^{p} - \mathbf{I} \quad \text{and} \quad \boldsymbol{\beta}^{\mathbf{e}} \equiv \mathbf{I} - \mathbf{F}^{\mathbf{e}^{-1}}. \tag{3.23}$$

In the above construction, $\boldsymbol{\beta}^{\mathrm{p}}$ and $\boldsymbol{\beta}^{\mathbf{e}}$ coincide with the elastic and plastic distortions of [105] in the limit of infinitesimal deformation. We now show that this construction is true by making use of the multiplicative decomposition. Using (3.22), (3.23) and (3.15) we get,

$$\begin{aligned}
\boldsymbol{\beta}^{\mathbf{p}}\mathrm{d}\mathbf{X} + \boldsymbol{\beta}^{\mathbf{e}}\mathrm{d}\mathbf{x} &= \left(\mathbf{F}^{\mathbf{p}} - \mathbf{I}\right)\mathrm{d}\mathbf{X} + \left(\mathbf{I} - \mathbf{F}^{\mathbf{e}^{-1}}\right)\mathrm{d}\mathbf{x} \\
&= \left(\mathbf{F}^{\mathbf{p}} - \mathbf{I}\right)\mathrm{d}\mathbf{X} + \left(\mathbf{I} - \mathbf{F}^{\mathbf{e}^{-1}}\right)\mathbf{F}\mathbf{X} \\
&= \left(\mathbf{F}^{\mathbf{p}} - \mathbf{I}\right)\mathrm{d}\mathbf{X} + \left(\mathbf{F} - \mathbf{F}^{\mathbf{p}}\right)\mathrm{d}\mathbf{X} \\
&= (\mathbf{F} - \mathbf{I})\mathrm{d}\mathbf{X} = \boldsymbol{\beta}\mathrm{d}\mathbf{X} = \mathrm{d}\mathbf{u}.
\end{aligned}$$

We also define the plastic and elastic differential displacements by,

$$\begin{aligned}
d\mathbf{u}^{\mathbf{p}} &\equiv \boldsymbol{\beta}^{\mathbf{p}}\mathrm{d}\mathbf{X} \\
d\mathbf{u}^{\mathbf{e}} &\equiv \boldsymbol{\beta}^{\mathbf{e}}\mathrm{d}\mathbf{x}
\end{aligned} \tag{3.24}$$

so that

$$\mathrm{d}\mathbf{u} = d\mathbf{u}^{\mathrm{p}} = d\mathbf{u}^{\mathrm{e}} \tag{3.25}$$

We note that we are distinguishing between the integrable differential $\mathrm{d}\mathbf{u}$ and the non-integrable differentials $d\mathbf{u}^{\mathrm{p}}$ and $d\mathbf{u}^{\mathrm{e}}$ with italicized font. We note here that we can use the Helmholtz decomposition, as was first done in [1] in the context of dislocations and plasticity, for second order tensors to write

$$\boldsymbol{\beta}^{p} = \boldsymbol{\phi}^{p} + \boldsymbol{\chi}^{p} \quad \text{and} \quad \boldsymbol{\beta}^{\mathrm{e}} = \boldsymbol{\phi}^{\mathrm{e}} + \boldsymbol{\chi}^{\mathrm{e}}, \tag{3.26}$$

where,

$$\boldsymbol{\phi}^{\mathrm{p}} = \mathrm{Grad}\ \mathbf{V}^{\mathrm{p}}, \quad \boldsymbol{\phi}^{\mathrm{e}} = \mathrm{grad}\ \mathbf{V}^{\mathrm{e}}$$

$$\boldsymbol{\chi}^{\mathrm{p}} = \mathrm{Curl}(\mathbf{A}^{\mathrm{p}})^{\mathrm{T}}, \boldsymbol{\chi}^{\mathrm{e}} = \mathrm{curl}(\mathbf{A}^{\mathrm{e}})^{\mathrm{T}},$$

with $\mathbf{V}^{\mathrm{p}}$ and $\mathbf{V}^{\mathrm{e}}$ being vector potentials and $\mathbf{A}^{\mathrm{p}}$ and $\mathbf{A}^{\mathrm{e}}$ second order tensor potentials. We note that the Helmholtz decomposition for second order tensors can be traced back to [76] where it was introduced in the context of electromagnetism. A consequence of the decomposition (3.26) for $\boldsymbol{\beta}^{\mathbf{e}}$ and $\boldsymbol{\beta}^{\mathrm{p}}$ is that the elastic and plastic distortions can be written in the form: $\mathbf{F}^{\mathrm{p}} = (\boldsymbol{\phi}^{\mathrm{p}} - \mathbf{I}) + \boldsymbol{\chi}^{\mathrm{p}}$ and $\mathbf{F}^{\mathrm{e}-1} = (\mathbf{I} - \boldsymbol{\phi}^{\mathrm{e}}) + \boldsymbol{\chi}^{\mathrm{e}}$. In turn,

$$\begin{aligned} \operatorname{Curl}(\boldsymbol{\beta}^{p}) &= \operatorname{Curl}(\boldsymbol{\chi}^{p}) = \operatorname{Curl}(\mathbf{F}^{p}) \\ \operatorname{curl}(\boldsymbol{\beta}^{\mathrm{e}}) &= \operatorname{curl}(\boldsymbol{\chi}^{\mathrm{e}}) = -\operatorname{curl}\left(\mathbf{F}^{\mathrm{e}-1}\right) \end{aligned} \tag{3.27}$$

The last equations show that the curl operation isolates the incompatible fields $\boldsymbol{\chi}^{\mathrm{p}}$ and $\boldsymbol{\chi}^{\mathrm{e}}$ which we will relate to the dislocation density in following sections.

3.6 Compatibility conditions and definition of dislocation density tensor

We are now in a position to define the dislocation density tensor by investigating the compatibility of the displacement field and its elastic and plastic contributions. We start with the compatibility condition of the total displacement,

$$\oint \mathrm{d}\mathbf{u} = \oint \boldsymbol{\beta} \mathrm{d}\mathbf{X} = 0 \tag{3.28}$$

where the integral is carried out along a closed path in the crystal. Using (3.22) this becomes,

$$\oint \boldsymbol{\beta} \mathrm{d}\mathbf{X} = \oint \boldsymbol{\beta}^{\mathrm{p}} \mathrm{d}\mathbf{X} + \oint \boldsymbol{\beta}^{\mathrm{e}} \mathrm{d}\mathbf{x} = \mathbf{0}. \tag{3.29}$$

Using Stokes theorem, we reach

$$\int \operatorname{Curl}(\boldsymbol{\beta}^{\mathrm{p}})^{\mathrm{T}} \, \mathrm{d}\mathbf{A}_{\mathrm{R}} + \int \operatorname{curl}(\boldsymbol{\beta}^{\mathrm{e}})^{\mathrm{T}} \, \mathrm{d}\mathbf{a}_{\mathrm{D}} = \mathbf{0}. \tag{3.30}$$

That is,

$$\int \operatorname{Curl}(\boldsymbol{\beta}^{\mathrm{p}})^{\mathrm{T}} \, \mathrm{d}\boldsymbol{A}_{\mathrm{R}} = -\int \operatorname{curl}(\boldsymbol{\beta}^{\mathrm{e}})^{\mathrm{T}} \, \mathrm{d}\mathbf{a}_{\mathrm{D}}. \tag{3.31}$$

with $\mathrm{d}\mathbf{A}_{\mathrm{R}}$ and $\mathrm{d}\mathbf{a}_{\mathrm{D}}$ being differential area elements in the referential and spatial configurations, respectively. We can then define two two-point dislocation density tensors by

$$\begin{aligned}\boldsymbol{\alpha}^{\mathrm{RM}} &\equiv \mathrm{Curl}\left(\boldsymbol{\beta}^{\mathrm{p}}\right) = \mathrm{Curl}\left(\mathbf{F}^{\mathrm{p}}\right)\\ \boldsymbol{\alpha}^{\mathrm{DM}} &\equiv -\,\mathrm{curl}\left(\boldsymbol{\beta}^{\mathrm{e}}\right) = \mathrm{curl}\left(\mathbf{F}^{\mathrm{e}-1}\right),\end{aligned} \tag{3.32}$$

where $\boldsymbol{\alpha}^{\mathrm{DM}}$ is the dislocation density tensor that Acharya uses in his field dislocation mechanics theory [1]. From this point onward, the superscripts and subscripts R, M and D on vector and tensor quantities refer to their measures in the reference, microstructure and deformed configurations, respectively. Double superscripts on two-point tensors refer to the two configurations they are associated with. We note here that since both $\boldsymbol{\alpha}^{\mathrm{RM}}$ and $\boldsymbol{\alpha}^{\mathrm{DM}}$ are defined to be the curl of tensors they must satisfy:

$$\begin{aligned}\mathrm{Div}\left(\boldsymbol{\alpha}^{\mathrm{RMT}}\right) &= \mathbf{0}\\ \mathrm{div}\left(\boldsymbol{\alpha}^{\mathrm{DMT}}\right) &= \mathbf{0}\end{aligned} \tag{3.33}$$

These conditions have the usual interpretation that the dislocations have no free ends inside the crystal. It is to be noted here that, according to the definitions of the curl operator we used, and for a second order tensor $\mathbf{T}$, Div $(\mathrm{Curl}(\mathbf{T})^{\mathrm{T}})$ =$\mathbf{0}$. Hence the transpose in the divergence conditions (3.33). Some authors define the curl operator so that Div $(\mathrm{Curl}\ \mathbf{T})$ =$\mathbf{0}$. In addition to the above relations, we can also write the differential Burgers vector in the microstructure configuration as follows:

$$\mathrm{d}\mathbf{b}_{\mathrm{M}} = \boldsymbol{\alpha}^{\mathrm{RMT}}\mathrm{d}\mathbf{A}_{\mathrm{R}} = \boldsymbol{\alpha}^{\mathrm{DMT}}\mathrm{d}\mathbf{a}_{\mathrm{D}}. \tag{3.34}$$

Nanson's formula can then be used to arrive at the microstructural dislocation density tensor, $\boldsymbol{\alpha}^{\mathrm{M}}$:

$$\boldsymbol{\alpha}^{\mathrm{M}} \equiv \frac{1}{\mathrm{J}^{\mathrm{p}}}\mathbf{F}^{\mathrm{p}}\,\mathrm{Curl}\left(\boldsymbol{\beta}^{\mathrm{p}}\right) = \frac{1}{\mathrm{J}^{\mathrm{p}}}\mathbf{F}^{\mathrm{p}}\,\mathrm{Curl}\left(\mathbf{F}^{\mathrm{p}}\right) = -\mathrm{J}^{\mathrm{e}}\mathbf{F}^{\mathbf{e}-\mathbf{1}}\,\mathrm{curl}\left(\boldsymbol{\beta}^{\mathbf{e}}\right) = \mathrm{J}^{\mathrm{e}}\mathbf{F}^{\mathrm{e}-1}\,\mathrm{curl}\left(\mathbf{F}^{\mathrm{e}-1}\right), \tag{3.35}$$

where the last terms come from (3.27). We note that these are the same definitions that [34] made. The tensor $\boldsymbol{\alpha}^{\mathrm{M}}$ lives in the microstructure space and gives a local measure of Burgers vector $\mathbf{b}_{\mathrm{M}}$ in that space through the relation

$$\mathrm{d}\mathbf{b}_{\mathrm{M}} = \boldsymbol{\alpha}^{\mathrm{MT}}\mathrm{d}\boldsymbol{A}_{\mathrm{M}}. \tag{3.36}$$

It is now possible to derive relations for the referential dislocation density tensor and the deformed dislocation density tensor using the same ideas in [34]. The microstructure Burgers vector $\mathrm{d}\mathbf{b}_{\mathrm{M}}$ can be transformed into either its deformed $\mathrm{d}\mathbf{b}_{\mathrm{D}}$ or referential $\mathrm{d}\mathbf{b}_{\mathrm{M}}$ counterpart via

$$\begin{aligned} \mathrm{d}\mathbf{b}_{\mathrm{R}} &= \mathbf{F}^{\mathrm{p}-1}\ \mathrm{d}\mathbf{b}_{\mathrm{M}} \\ \mathrm{d}\mathbf{b}_{\mathrm{D}} &= \mathbf{F}^{\mathrm{e}}\mathrm{d}\mathbf{b}_{\mathrm{M}} \end{aligned} \tag{3.37}$$

Furthermore, using Nanson's formula, we can transform the microstructure area element into referential and deformed area elements which allows us to write

$$\begin{aligned} \mathrm{d}\mathbf{b}_{\mathrm{M}} &= \boldsymbol{\alpha}^{\mathrm{MT}}\mathrm{J}^{\mathrm{p}}\mathbf{F}^{\mathrm{p}-\mathrm{T}}\mathrm{d}\mathbf{A}_{\mathrm{R}} \\ \mathrm{d}\mathbf{b}_{\mathrm{M}} &= \boldsymbol{\alpha}^{\mathrm{MT}}\frac{1}{\mathrm{J}^{\mathrm{e}}}\mathbf{F}^{\mathrm{eT}}\mathrm{d}\mathbf{a}_{\mathrm{D}}. \end{aligned} \tag{3.38}$$

Combining (3.37) and (3.38) gives us the definition of the dislocation density tensor in the reference and deformed configuration,

$$\begin{aligned} \mathrm{d}\mathbf{b}_{\mathrm{R}} &= \mathbf{F}^{\mathrm{p}-1}\,\mathrm{Curl}\,(\mathbf{F}^{\mathrm{p}})^{\mathrm{T}}\,\mathrm{d}\boldsymbol{A}_{\mathrm{R}} \equiv \boldsymbol{\alpha}^{\mathrm{RT}}\mathrm{d}\boldsymbol{A}_{\mathrm{R}} \\ \mathrm{d}\mathbf{b}_{\mathrm{D}} &= \mathbf{F}^{\mathrm{e}}\,\mathrm{curl}\left(\mathbf{F}^{\mathrm{e}-1}\right)^{\mathrm{T}}\,\mathrm{d}\boldsymbol{A}_{\mathrm{D}} \equiv \boldsymbol{\alpha}^{\mathrm{DT}}\mathrm{d}\boldsymbol{a}_{\mathrm{D}}. \end{aligned} \tag{3.39}$$

From these transformations we get the following relationships:

$$\begin{aligned} \boldsymbol{\alpha}^{\mathrm{R}} &= \mathrm{J}^{\mathrm{p}}\mathbf{F}^{\mathrm{p}-1}\boldsymbol{\alpha}^{\mathrm{M}}\mathbf{F}^{\mathrm{p}-\mathrm{T}} & \boldsymbol{\alpha}^{\mathrm{M}} &= \mathrm{J}^{\mathrm{p}-1}\mathbf{F}^{\mathrm{p}}\boldsymbol{\alpha}^{\mathrm{R}}\mathbf{F}^{\mathrm{pT}} \\ \boldsymbol{\alpha}^{\mathrm{D}} &= \mathrm{J}^{\mathrm{e}-1}\mathbf{F}^{\mathrm{e}}\boldsymbol{\alpha}^{\mathrm{M}}\mathbf{F}^{\mathrm{eT}} & \boldsymbol{\alpha}^{\mathrm{M}} &= \mathrm{J}^{\mathrm{e}}\mathbf{F}^{\mathrm{e}-1}\boldsymbol{\alpha}^{\mathrm{D}}\mathbf{F}^{\mathrm{e}-\mathrm{T}} \\ \boldsymbol{\alpha}^{\mathrm{R}} &= \mathrm{J}\mathbf{F}^{-1}\boldsymbol{\alpha}^{\mathrm{D}}\mathbf{F}^{-\mathrm{T}} & \boldsymbol{\alpha}^{\mathrm{D}} &= \mathrm{J}^{-1}\mathbf{F}\boldsymbol{\alpha}^{\mathrm{R}}\mathbf{F}^{\mathrm{T}} \\ \boldsymbol{\alpha}^{\mathrm{RM}} &= \mathrm{J}^{\mathrm{p}}\mathbf{F}^{\mathbf{p}-1}\boldsymbol{\alpha}^{\mathrm{M}} & \boldsymbol{\alpha}^{\mathrm{M}} &= \mathrm{J}^{\mathrm{p}-1}\mathbf{F}^{\mathrm{p}}\boldsymbol{\alpha}^{\mathrm{RM}} \\ \boldsymbol{\alpha}^{\mathrm{DM}} &= \mathrm{J}^{\mathrm{e}-1}\mathbf{F}^{\mathrm{e}}\boldsymbol{\alpha}^{\mathrm{M}} & \boldsymbol{\alpha}^{\mathrm{M}} &= \mathrm{J}^{\mathrm{e}}\mathbf{F}^{\mathrm{e}-1}\boldsymbol{\alpha}^{\mathrm{DM}}. \end{aligned} \tag{3.40}$$

The connections between $\boldsymbol{\alpha}^{\mathrm{M}}$, $\boldsymbol{\alpha}^{\mathrm{D}}$ and $\boldsymbol{\alpha}^{\mathrm{R}}$ were given by [34]. These dislocation density tensors can be written as compositions of vector dislocation densities in the respective crystal configurations and the corresponding crystallographic Burgers vectors. In order to do so, we assume that the dislocation density on each crystallographic slip system consists of line bundles having single-valued line direction at each point in space. For simplicity, let us assume that we have a single slip system with crystallographic Burgers vector $\mathbf{b}_{\mathrm{R}}$, in the reference configuration, with its images in the microstructure and deformed configurations being $\mathbf{b}_{\mathrm{M}}$ and $\mathbf{b}_{\mathrm{D}}$, respectively. In this case, the dislocation density tensors mentioned above have the form

$$
\begin{aligned}
\boldsymbol{\alpha}^{\mathrm{R}} &= \boldsymbol{\rho}_{\mathrm{R}} \otimes \mathbf{b}_{\mathrm{R}} = \rho_{\mathrm{R}} \mathbf{l}_{\mathrm{R}} \otimes \mathbf{b}_{\mathrm{R}} \\
\boldsymbol{\alpha}^{\mathrm{M}} &= \boldsymbol{\rho}_{\mathrm{M}} \otimes \mathbf{b}_{\mathrm{M}} = \rho_{\mathrm{M}} \mathbf{l}_{\mathrm{M}} \otimes \mathbf{b}_{\mathrm{M}} \\
\boldsymbol{\alpha}^{\mathrm{D}} &= \boldsymbol{\rho}_{\mathrm{D}} \otimes \mathbf{b}_{\mathrm{D}} = \rho_{\mathrm{D}} \mathbf{l}_{\mathrm{D}} \otimes \mathbf{b}_{\mathrm{D}} \\
\boldsymbol{\alpha}^{\mathrm{RM}} &= \boldsymbol{\rho}_{\mathrm{R}} \otimes \mathbf{b}_{\mathrm{M}} = \rho_{\mathrm{R}} \mathbf{l}_{\mathrm{R}} \otimes \mathbf{b}_{\mathrm{M}} \\
\boldsymbol{\alpha}^{\mathrm{DM}} &= \boldsymbol{\rho}_{\mathrm{D}} \otimes \mathbf{b}_{\mathrm{M}} = \rho_{\mathrm{D}} \mathbf{l}_{\mathrm{D}} \otimes \mathbf{b}_{\mathrm{M}},
\end{aligned}
\tag{3.41}
$$

where $\boldsymbol{\rho}_{\mathrm{R}}$, $\boldsymbol{\rho}_{\mathrm{M}}$, and $\boldsymbol{\rho}_{\mathrm{D}}$ are the vector dislocation densities in the reference, microstructure and deformed configurations with their magnitudes ρ_{R}, ρ_{M}, and ρ_{D} and unit tangents $\mathbf{l}_{\mathrm{R}}$, $\mathbf{l}_{\mathrm{M}}$, and $\mathbf{l}_{\mathrm{D}}$, respectively. When multiple slip systems are considered, expressions (3.41) are constructed by summing the contributions from all systems; see section 5.
We also have the transformation relations:

$$
\begin{array}{lll}
\mathbf{l}_{\mathrm{R}} = \mathbf{F}^{\mathrm{p}-1}\mathbf{l}_{\mathrm{M}} & \mathbf{s}_{\mathrm{R}} = \mathbf{F}^{\mathrm{p}-1}\mathbf{s}_{\mathrm{M}} & \mathbf{m}_{\mathrm{R}} = \mathbf{F}^{\mathrm{pT}}\mathbf{m}_{\mathrm{M}} \\
\mathbf{l}_{\mathrm{D}} = \mathbf{F}^{\mathrm{e}}\mathbf{l}_{\mathrm{M}} & \mathbf{s}_{\mathrm{D}} = \mathbf{F}^{\mathrm{e}}\mathbf{s}_{\mathrm{M}} & \mathbf{m}_{\mathrm{D}} = \mathbf{F}^{\mathrm{e}-\mathrm{T}}\mathbf{m}_{\mathrm{M}} \\
\mathbf{l}_{\mathrm{D}} = \mathbf{F}\mathbf{l}_{\mathrm{R}} & \mathbf{s}_{\mathrm{D}} = \mathbf{F}\mathbf{s}_{\mathrm{R}}, & \mathbf{m}_{\mathrm{D}} = \mathbf{F}^{-\mathrm{T}}\mathbf{m}_{\mathrm{R}} \\
\mathbf{b}_{\mathrm{R}} = \mathrm{b}\mathbf{s}_{\mathrm{R}} & \mathbf{b}_{\mathrm{M}} = \mathrm{b}\mathbf{s}_{\mathrm{M}} & \mathbf{b}_{\mathrm{D}} = \mathrm{b}\mathbf{s}_{\mathrm{D}} \\
\boldsymbol{\rho}_{\mathrm{R}} = \mathrm{J}^{\mathrm{p}}\mathbf{F}^{\mathbf{p}-\mathbf{1}}\boldsymbol{\rho}_{\mathbf{M}} & \boldsymbol{\rho}_{\mathrm{D}} = \mathrm{J}^{\mathrm{e}-1}\mathbf{F}^{\mathrm{e}}\boldsymbol{\rho}_{\mathbf{M}} & \boldsymbol{\rho}_{\mathrm{R}} = \mathrm{J}\mathrm{F}^{-\mathbf{1}}\boldsymbol{\rho}_{\mathbf{D}}.
\end{array}
\tag{3.42}
$$

As seen in the following sections, these relations are useful in deriving the transport relations for the dislocation density. Again, the subscripts R, M and D refer to the reference, microstructure and deformed configurations, respectively.

3.7 Dislocation currents and continuity equations for the dislocation density tensors

The crystal displacement field is compatible and so is the corresponding velocity field. This means that

$$\oint \mathrm{d}\mathbf{v} = \oint \dot{\boldsymbol{\beta}}\mathrm{d}\mathbf{X} = \dot{\overline{\oint \boldsymbol{\beta}\mathrm{d}\mathbf{X}}} = 0. \tag{3.43}$$

For $\mathrm{d}\mathbf{v}$, we use the differential definition of the velocity, [156]

$$\mathrm{d}\mathbf{v} = \dot{\overline{\mathrm{d}\mathbf{x}}} = \dot{\overline{\mathbf{F}\mathrm{d}\mathbf{X}}} = \dot{\overline{\boldsymbol{\beta}\mathrm{d}\mathbf{X}}}. \tag{3.44}$$

We now use our additive decomposition of the displacement gradient to show how the incompatible part of the displacement gradient should evolve. To this end, we write

$$\begin{aligned}
\overline{\boldsymbol{\beta}\mathrm{d}\mathbf{X}} &= \overline{\boldsymbol{\beta}^{\mathbf{p}}\mathrm{d}\mathbf{X} + \boldsymbol{\beta}^{\mathbf{e}}\mathbf{d}\mathbf{x}} \\
&= \overline{\boldsymbol{\beta}^{\mathbf{p}}\mathrm{d}\mathbf{X}} + \overline{\boldsymbol{\beta}^{\mathbf{e}}\mathbf{F}\mathbf{F}\mathbf{X}} \\
&= \boldsymbol{\beta}^{\mathbf{p}}\mathrm{d}\mathbf{X} + (\boldsymbol{\beta}^{\mathbf{e}}\mathrm{d}\mathbf{x} + \boldsymbol{\beta}^{\mathbf{e}}\mathbf{L}\mathbf{F}\mathbf{X}\mathbf{X}) \\
&= \boldsymbol{\beta}^{\mathbf{p}}\mathrm{d}\mathbf{X} + \left(\dot{\boldsymbol{\beta}}^{\mathbf{e}} + \boldsymbol{\beta}^{\mathbf{e}}\mathbf{L}\right)\mathrm{d}\mathbf{x}.
\end{aligned} \tag{3.45}$$

We start by simplifying the quantity $(\dot{\boldsymbol{\beta}}^{\mathrm{e}}+\boldsymbol{\beta}^{\mathrm{e}}\mathbf{L})\mathrm{d}\mathbf{x}$ in the above expression. We find the first term to be

$$\dot{\boldsymbol{\beta}}^{\mathrm{e}} = -\dot{\mathbf{F}}^{\mathrm{e}-1} = \mathbf{F}^{\mathrm{e}-1}\mathbf{L}^{\mathrm{e}}, \tag{3.46}$$

and the second term

$$\begin{aligned}
\boldsymbol{\beta}^{\mathrm{e}}\mathbf{L} &= \mathbf{L} - \mathbf{F}^{\mathrm{e}-1}\mathbf{L} \\
&= \mathbf{L} - \mathbf{F}^{\mathrm{e}-1}\mathbf{L}^{\mathrm{e}} - \mathbf{F}^{\mathrm{e}-1}\mathbf{F}^{\mathrm{e}}\mathbf{L}^{\mathrm{p}}\mathbf{F}^{\mathrm{e}-1} = \mathbf{L} - \mathbf{F}^{\mathrm{e}-1}\mathbf{L}^{\mathrm{e}} - \mathbf{L}^{\mathrm{p}}\mathbf{F}^{\mathrm{e}-1}.
\end{aligned} \tag{3.47}$$

Summing (3.46) and (3.47) then gives,

$$\begin{aligned}\boldsymbol{\beta}^{\mathrm{e}}+\boldsymbol{\beta}^{\mathrm{e}}\mathbf{L} &= \mathbf{F}^{\mathrm{e}-1}\mathbf{L}^{\mathrm{e}}+\mathbf{L}-\mathbf{F}^{\mathrm{e}-1}\mathbf{L}^{\mathrm{e}}-\mathbf{L}^{\mathrm{p}}\mathbf{F}^{\mathrm{e}-1}\\ &= \mathbf{L}-\mathbf{L}^{\mathrm{p}}\mathbf{F}^{\mathrm{e}-1}=\mathbf{L}-\mathbf{L}^{\mathrm{p}}\mathbf{F}^{\mathrm{p}}\mathbf{F}^{\mathbf{p}-\mathbf{1}}\mathbf{F}^{\mathrm{e}-1}\\ &= \mathbf{L}-\boldsymbol{\beta}^{\mathrm{p}}\mathbf{F}^{\mathrm{p}-1}\mathbf{F}^{\mathrm{e}-1}=\mathbf{L}-\boldsymbol{\beta}^{\mathrm{p}}\mathbf{F}^{-1}.\end{aligned} \tag{3.48}$$

We now define the plastic and elastic velocity contributions as,

$$\begin{aligned}d\mathbf{v}^{\mathrm{p}} &\equiv \boldsymbol{\beta}^{\mathrm{p}}\mathrm{d}\mathbf{X}\\ d\mathbf{v}^{\mathrm{e}} &\equiv \left(\mathbf{L}-\boldsymbol{\beta}^{\mathrm{p}}\mathbf{F}^{-1}\right)\mathrm{d}\mathbf{x}\end{aligned} \tag{3.49}$$

which yield,

$$\mathrm{d}\mathbf{v}=d\mathbf{v}^{\mathrm{e}}=d\mathbf{v}^{\mathrm{p}}. \tag{3.50}$$

where, again, we used italicized font to refer to the fact that $d\mathbf{v}^{\mathrm{e}}$ and $d\mathbf{v}^{\mathrm{p}}$ are not individually rates of compatible displacement fields. The decomposition (3.50) is used below to derive the dislocation current.

3.8 The dislocation current

In [104] the dislocation current is regarded as a measure of the deviation of the rate of plastic distortion from compatibility. Here, we develop the same idea in the finite deformation setting by obtaining a measure of the incompatibility of the plastic contribution to the crystal velocity. Since the crystal velocity is compatible, it is possible to write

$$\oint \mathrm{d}\mathbf{v}=\oint d\mathbf{v}^{\mathrm{p}}+\oint d\mathbf{v}^{\mathrm{e}}=0. \tag{3.51}$$

That is,

$$\oint d\mathbf{v}^{\mathrm{p}}=-\oint d\mathbf{v}^{\mathrm{e}}. \tag{3.52}$$

Plugging in the definition of $d\mathbf{v}^{\mathrm{p}}$ and $d\mathbf{v}^{\mathrm{e}}$ from (3.49) gives,

$$\oint \dot{\boldsymbol{\beta}}^{\mathrm{p}}\mathrm{d}\mathbf{X}=-\oint \left(\mathbf{L}-\dot{\boldsymbol{\beta}}^{\mathrm{p}}\mathbf{F}^{-1}\right)\mathrm{d}\mathbf{x}. \tag{3.53}$$

Applying Stokes Theorem on both sides we reach,

$$\int \mathrm{Curl}\left(\dot{\boldsymbol{\beta}}^{\mathrm{p}}\right)^{\mathrm{T}} \mathrm{d}\mathbf{A}_{\mathrm{R}} = -\int \mathrm{curl}\left(-\dot{\boldsymbol{\beta}}^{\mathrm{p}}\mathbf{F}^{-1}\right)^{\mathrm{T}} \mathrm{d}\mathbf{a}_{\mathrm{D}} \ , \tag{3.54}$$

where $\mathrm{d}\mathbf{a}_{\mathrm{D}} = \mathbf{n}_{\mathrm{D}}\mathrm{d}a_{\mathrm{D}}$ and $\mathrm{d}\mathbf{A}_{\mathrm{R}} = \mathbf{N}_{\mathrm{R}}\mathrm{d}A_{\mathrm{R}}$, with $\mathbf{n}_{\mathrm{D}}$ and $\mathbf{N}_{\mathrm{R}}$ being the unit normal in the deformed and reference configurations, respectively, and the contribution due to $\mathbf{L}$ is null since it is compatible. We further note that the term on the left-hand (right-hand) side of (3.54) is a measure of the incompatibility of the plastic (elastic) part of the velocity. We interpret the left-hand side of (3.54) as the material time rate of change of the net microstructure Burgers vector $\mathbf{b}_{\mathrm{M}}(\mathrm{A}_{\mathrm{R}})$ of dislocations piercing an area A_{R}. Likewise, the right-hand side of (3.54) defines the same for dislocations piercing an area a_{D} in the deformed configuration, which is the image of A_{R}. This is written as

$$\begin{aligned} \dot{\mathbf{b}}_{\mathrm{M}}\left(A_{\mathrm{R}}\right) &= \int \mathrm{Curl}\left(\boldsymbol{\beta}^{\mathrm{p}}\right)^{\mathrm{T}} \mathrm{d}\boldsymbol{A}_{\mathrm{R}} \\ \dot{\mathbf{b}}_{\mathrm{M}}\left(\mathrm{a}_{\mathrm{D}}\right) &= \int \mathrm{curl}\left(\boldsymbol{\beta}^{\mathrm{p}}\mathbf{F}^{-1}\right)^{\mathrm{T}} \mathrm{d}\mathbf{a}_{\mathrm{D}} \end{aligned} \tag{3.55}$$

In the above, $\dot{\mathbf{b}}_{\mathrm{M}}\left(\mathrm{A}_{\mathrm{R}}\right) = \dot{\mathbf{b}}_{\mathrm{M}}\left(\mathrm{a}_{\mathrm{D}}\right)$.

Now consider the first of (3.55). From the decomposition of $\boldsymbol{\beta}^{\mathrm{p}}$ into compatible and incompatible parts (3.27), we may write,

$$\int \mathrm{Curl}\left(\dot{\boldsymbol{\beta}}^{\mathrm{p}}\right)^{\mathrm{T}} \mathrm{d}\mathbf{A}_{\mathrm{R}} = \int \mathrm{Curl}(\dot{\boldsymbol{\chi}}^{\mathrm{p}})^{\mathrm{T}} \mathrm{d}\mathbf{A}_{\mathrm{R}}. \tag{3.56}$$

We interpret the term $\mathrm{Curl}(\dot{\boldsymbol{\chi}}^{\mathrm{p}})^{\mathrm{T}}$ as coming from motion of dislocations. Using Stokes theorem, we can write this as a flux term $\boldsymbol{\phi}$ of dislocations piercing a Burgers circuit. That is,

$$\int \mathrm{Curl}(\dot{\boldsymbol{\chi}}^{\mathrm{p}})^{\mathrm{T}} \mathrm{d}\mathbf{A}_{\mathbf{R}} = \oint \dot{\boldsymbol{\beta}}^{\mathrm{p}} \mathrm{d}\mathbf{X} \equiv \oint \boldsymbol{\phi} \mathrm{d}\mathbf{X} = \int \mathrm{Curl}(\boldsymbol{\phi})^{\mathrm{T}} \mathrm{d}\mathbf{A}_{\mathrm{R}}. \tag{3.57}$$

The term $\boldsymbol{\phi}$ has been called the dislocation current in [104] and so we stick with this term noting that our case is concerned with finite deformations. For the line bundle representation of dislocations on various slip systems, and at a point the crystal, we may

express the current $\boldsymbol{\phi}$ at a point the crystal in terms of the vector densities of these bundles, their velocities, and Burgers vectors in the form [144]:

$$\boldsymbol{\phi}=\sum_{l}\mathbf{b}_{\mathrm{M}}^{(l)}\otimes\left(\mathbf{v}_{\mathrm{R}}^{(l)}\times\boldsymbol{\rho}_{\mathrm{R}}^{(l)}\right), \tag{3.58}$$

with

$$\mathrm{b}_{\mathrm{M}}^{(l)}\mathbf{v}_{\mathrm{R}}^{(l)}\times\boldsymbol{\rho}_{\mathrm{R}}^{(l)}=\dot{\gamma}^{(l)}\mathbf{m}_{\mathrm{R}}^{(l)}\ , \tag{3.59}$$

where $\dot{\gamma}^{(l)}$ is the slip rate on slip system l, with Burgers vector $\mathbf{b}_{\mathrm{M}}^{(l)}$, velocity $\mathbf{v}_{\mathrm{R}}^{(l)}$, and dislocation density $\boldsymbol{\rho}_{\mathrm{R}}^{(l)}$, respectively. We will now consider the current term that comes from the deformed configuration on the right-hand side of (3.54), $\mathrm{curl}\left(\boldsymbol{\phi}\mathbf{F}^{-1}\right)^{\mathrm{T}}$, which we wish to write in terms of the dislocation density and velocity vectors in the deformed configuration. To this end we expand the term $\boldsymbol{\phi}\mathbf{F}^{-1}$ to get,

$$\boldsymbol{\phi}\mathbf{F}^{-1}=\left[\sum_{l}\mathbf{b}_{\mathrm{M}}^{(l)}\otimes\left(\mathbf{v}_{\mathrm{R}}^{(l)}\times\boldsymbol{\rho}_{\mathrm{R}}^{(l)}\right)\right]\ \mathbf{F}^{-1}=\sum_{l}\mathbf{b}_{\mathrm{M}}^{(l)}\otimes\left(\left(\mathbf{v}_{\mathrm{R}}^{(l)}\times\boldsymbol{\rho}_{\mathrm{R}}^{(l)}\right)\mathbf{F}^{-1}\right). \tag{3.60}$$

In index notation, the terms on the right of the outer product read: $\left[\left(\mathbf{v}_{\mathrm{R}}^{(l)}\times\boldsymbol{\rho}_{\mathrm{R}}^{(l)}\right)\mathbf{F}^{-1}\right]_{\mathrm{o}}=\epsilon_{\mathrm{IJK}}\mathrm{v}_{\mathrm{R}\ \mathrm{I}}^{(l)}\rho_{\mathrm{R}\ \mathrm{J}}^{(l)}\mathrm{F}_{\mathrm{Ko}}^{-1}$. Using the transformation properties of $\rho_{\mathrm{R}\ \mathrm{j}}^{(l)}$ in (3.42) and $\mathrm{v}_{\mathrm{R}\ \mathrm{i}}^{(l)}$ from ($\mathbf{F}\mathbf{v}_{\mathrm{R}}^{(l)}=\mathbf{v}_{\mathrm{D}}^{(l)}$), we can rewrite the flux term in terms of the density and dislocation velocity in the deformed configuration,

$$\epsilon_{\mathrm{IJK}}\mathrm{v}_{\mathrm{R}\ \mathrm{I}}^{(l)}\rho_{\mathrm{R}\ \mathrm{J}}^{(l)}\mathrm{F}_{\mathrm{Ko}}^{-1}=\mathrm{v}_{\mathrm{D}\ \mathrm{i}}^{(l)}\rho_{\mathrm{D}\ \mathrm{j}}^{(l)}\mathrm{J}\epsilon_{\mathrm{IJK}}\mathrm{F}_{\mathrm{Ii}}^{-1}\mathrm{F}_{\mathrm{Jj}}^{-1}\mathrm{F}_{\mathrm{Ko}}^{-1}. \tag{3.61}$$

The transformation property of the permutation symbol from spatial to material coordinates, $\epsilon_{\mathrm{IJK}}=\mathrm{J}^{-1}\epsilon_{\mathrm{lmn}}\mathrm{F}_{\mathrm{lI}}\mathrm{F}_{\mathrm{mJ}}\mathrm{F}_{\mathrm{nK}}$, can now be used in (3.61) to obtain

$$\left[\left(\mathbf{v}_{\mathrm{R}}^{(l)}\times\boldsymbol{\rho}_{\mathrm{R}}^{(l)}\right)\mathbf{F}^{-1}\right]_{\mathrm{o}}=\mathrm{v}_{\mathrm{D}\ \mathrm{i}}^{(l)}\rho_{\mathrm{D}\ \mathrm{j}}^{(l)}\mathrm{J}\mathrm{J}^{-1}\epsilon_{\mathrm{lmn}}\mathrm{F}_{\mathrm{lI}}\mathrm{F}_{\mathrm{mJ}}\mathrm{F}_{\mathrm{nK}}\mathrm{F}_{\mathrm{Ii}}^{-1}\mathrm{F}_{\mathrm{Jj}}^{-1}\mathrm{F}_{\mathrm{Ko}}^{-1}=\mathrm{v}_{\mathrm{D}\ \mathrm{i}}^{(l)}\rho_{\mathrm{D}\ \mathrm{j}}^{(l)}\epsilon_{\mathrm{ijo}}. \tag{3.62}$$

Using this result, we can write the dislocation current term in the deformed configuration as,

$$\mathrm{curl}\left(\boldsymbol{\phi}\mathbf{F}^{-1}\right)^{\mathrm{T}}=\mathrm{curl}\left(\sum_{l}\mathbf{b}_{\mathrm{M}}^{(l)}\otimes\left(\mathbf{v}_{\mathrm{D}}^{(l)}\times\boldsymbol{\rho}_{\mathrm{D}}^{(l)}\right)\right)^{\mathrm{T}}, \tag{3.63}$$

with the corresponding vector form of Orowan's equation in the deformed configuration,

$$\mathrm{b}_{\mathrm{M}}^{(l)}\mathbf{v}_{\mathrm{D}}^{(l)}\times\boldsymbol{\rho}_{\mathrm{D}}^{(l)}=\dot{\gamma}^{(l)}\mathbf{m}_{\mathrm{D}}^{(l)}, \tag{3.64}$$

which is consistent with the transformation rule for $\mathbf{m}_{\mathrm{D}}^{(l)}$ and $\mathbf{m}_{\mathrm{R}}^{(l)}$. The dislocation current is used to describe the time rate of change of Burgers vector content within the body and will be used to get a closed form of transport relations in the following section.

3.9 The rate form of compatibility and the transport equations for the two-point dislocation density tensors

From (3.34) we can write the time rate of change of the Burgers vector measure coming from both the reference and deformed configuration as,

$$\overline{\mathrm{d}\dot{\mathbf{b}}_{\mathrm{M}}}=\overline{\boldsymbol{\alpha}^{\mathrm{RM}\ \mathrm{T}}\mathrm{d}\mathbf{A}_{\mathrm{R}}}^{\cdot}=\dot{\boldsymbol{\alpha}}^{\mathrm{RM}\ \mathrm{T}}\mathrm{d}\mathbf{A}_{\mathrm{R}}, \tag{3.65}$$

and from the deformed configuration we have,

$$\overline{\mathrm{d}\dot{\mathbf{b}}_{\mathbf{M}}}=\overline{\boldsymbol{\alpha}^{\mathrm{DM}\ \mathrm{T}}\mathrm{d}\mathbf{a}_{\mathrm{D}}}^{\cdot}=\dot{\boldsymbol{\alpha}}^{\mathrm{DM}\ \mathrm{T}}\mathrm{d}\mathbf{a}_{\mathrm{D}}+\boldsymbol{\alpha}^{\mathrm{DM}\ \mathrm{T}}\overline{\mathrm{d}\dot{\mathbf{a}}_{\mathrm{D}}}, \tag{3.66}$$

where $\overline{\mathrm{d}\dot{\mathbf{a}}_{\mathrm{D}}}=\left(\mathrm{tr}\left(\mathbf{L}\right)\mathbf{I}=\mathbf{L}^{\mathrm{T}}\right)\mathrm{d}\mathbf{a}_{\mathrm{D}}$, which we get from the material time derivative of Nanson's formula,

$$\begin{aligned}\overline{\mathbf{n}_{\mathrm{D}}\mathrm{d}\dot{\mathrm{a}}_{\mathrm{D}}} &= \overline{\mathrm{J}\mathbf{F}^{-\mathrm{T}}\mathbf{N}\mathrm{d}\mathrm{A}_{\mathrm{R}}}^{\cdot}\\ &= \dot{\mathrm{J}}\mathbf{F}^{-\mathrm{T}}\mathbf{N}\mathrm{d}\mathrm{A}_{\mathrm{R}}+\mathrm{J}\overline{\dot{\mathbf{F}}^{-\mathrm{T}}}\mathbf{N}\mathrm{d}\mathrm{A}_{\mathrm{R}}\\ &= \mathrm{tr}(\mathbf{L})\mathbf{F}^{-\mathrm{T}}\mathbf{N}\mathrm{d}\mathrm{A}_{\mathrm{R}}+\left(-\mathbf{L}^{\mathrm{T}}\mathbf{F}^{-\mathrm{T}}\mathbf{N}\mathrm{d}\mathrm{A}_{\mathrm{R}}\right)\\ &= \left[\mathrm{tr}(\mathbf{L})\mathbf{I}-\mathbf{L}^{\mathrm{T}}\right]\mathbf{F}^{-\mathrm{T}}\mathbf{N}\mathrm{d}\mathrm{A}_{\mathrm{R}}\\ &= \left[\mathrm{tr}(\mathbf{L})\mathbf{I}-\mathbf{L}^{\mathrm{T}}\right]\mathbf{n}\mathrm{d}\mathrm{a}_{\mathrm{D}}.\end{aligned} \tag{3.67}$$

Plugging this back into (3.66) yields,

$$\overline{\mathrm{d}\dot{\mathbf{b}}_{\mathrm{M}}}=\left[\dot{\boldsymbol{\alpha}}^{\mathrm{DM}\ \mathrm{T}}+\boldsymbol{\alpha}^{\mathrm{DM}\ \mathrm{T}}\left(\mathrm{tr}\left(\mathbf{L}\right)\mathbf{I}-\mathbf{L}^{\mathrm{T}}\right)\right]\mathrm{d}\mathbf{a}_{\mathrm{D}}. \tag{3.68}$$

For the total velocity to remain compatible, we must maintain the relations,

$$\overline{\mathrm{d}\dot{\mathbf{b}}_{\mathrm{M}}} = \mathrm{Curl}(\boldsymbol{\phi})^{\mathrm{T}}\mathrm{d}\mathbf{A}_{\mathrm{R}} \tag{3.69}$$

which says that the net change of the burgers vector content is due to the motion of dislocations, or that the time rate of change of the incompatible part of $\boldsymbol{\beta}^{\mathrm{p}}$ is equal to the incompatible part of the plastic velocity. Using the first equation in (3.34) and (3.69) we can write,

$$\int \dot{\boldsymbol{\alpha}}^{\mathrm{RM}\ \mathrm{T}}\mathrm{d}\mathbf{A}_{\mathrm{R}} = \int \mathrm{Curl}(\boldsymbol{\phi})^{\mathrm{T}}\mathrm{d}\mathbf{A}_{\mathrm{R}}. \tag{3.70}$$

Locally we then get,

$$\dot{\boldsymbol{\alpha}}^{\mathrm{RM}} = \mathrm{Curl}(\boldsymbol{\phi}). \tag{3.71}$$

Noting that the rate of plastic distortion, $\dot{\boldsymbol{\beta}}^{\mathrm{p}}$, is equal to the dislocation current, $\boldsymbol{\phi}$, the last equation can be regarded as the rate form of the incompatibility of the plastic distortion, expressed in terms of the two-point tensor $\boldsymbol{\alpha}^{\mathrm{RM}}$. We can also derive a similar equation for $\boldsymbol{\alpha}^{\mathrm{DM}}$ from equating (3.55) and (3.65) and also noting $\dot{\boldsymbol{\beta}}^{\mathrm{p}} = \boldsymbol{\phi}$. This gives,

$$\int \dot{\boldsymbol{\alpha}}^{\mathrm{DM}\ \mathrm{T}} + \boldsymbol{\alpha}^{\mathrm{DM}\ \mathrm{T}}(\mathrm{tr}\,(\mathbf{L})\,\mathbf{I} - \mathbf{L}^{\mathrm{T}})\mathrm{d}\mathbf{a}_{\mathrm{D}} = \int \mathrm{curl}\left(\boldsymbol{\phi}\mathbf{F}^{-1}\right)^{\mathrm{T}}\mathrm{d}\mathbf{a}_{\mathrm{D}} \tag{3.72}$$

and locally we have, by taking the transpose,

$$\dot{\boldsymbol{\alpha}}^{\mathrm{DM}} + (\mathrm{tr}\,(\mathbf{L})\,\mathbf{I} - \mathbf{L}\ )\,\boldsymbol{\alpha}^{\mathrm{DM}} = \mathrm{curl}\left(\boldsymbol{\phi}\mathbf{F}^{-1}\right). \tag{3.73}$$

We note here that the terms involving the velocity gradient came from taking the material time derivative of the area element in the deformed configuration, so these terms correspond to the change in $\boldsymbol{\alpha}^{\mathrm{DM}}$ due to the deforming body itself and not due to dislocation motion. The term on the right-hand side of (3.73) is responsible for the change in $\boldsymbol{\alpha}^{\mathrm{DM}}$ due to dislocation motion. An expression similar to (3.73) can be found in [2]. Equations (3.71) and (3.73) can be regarded as the transport equations for the two-point tensors $\boldsymbol{\alpha}^{\mathrm{RM}}$ and $\boldsymbol{\alpha}^{\mathrm{DM}}$ written in the referential and spatial frames, respectively.

3.10 Transport equations for the vector density of dislocations

We now obtain the transport equations for the vector dislocation density fields. To do so, we start by decomposing $\boldsymbol{\alpha}^{\mathrm{RM}}$ into its slip system contribution in terms of the dislocation density vector and the crystal Burgers vectors,

$$\boldsymbol{\alpha}^{\mathrm{RM}} = \sum_{l} \boldsymbol{\alpha}^{\mathrm{RM}\ (l)} = \sum_{l} \boldsymbol{\rho}_{\mathrm{R}}^{(l)} \otimes \mathbf{b}_{\mathrm{M}}^{(l)}. \tag{3.74}$$

Plugging this into the transport equation (3.71) and using (3.58) for the dislocation current yields

$$\sum_{\mathrm{l}} \dot{\boldsymbol{\rho}}_{\mathrm{R}}^{(l)} \otimes \mathbf{b}_{\mathrm{M}}^{(l)} = \mathrm{Curl}\left(\sum_{l} \mathbf{b}_{\mathrm{M}}^{(l)} \otimes \left(\mathbf{v}_{\mathrm{R}}^{(l)} \times \boldsymbol{\rho}_{\mathrm{R}}^{(l)} \right) \right). \tag{3.75}$$

Using the curl identity (3.6) and the fact that $\mathbf{b}_{\mathrm{M}}^{(\mathrm{l})}$ is constant gives

$$\sum_{\mathrm{l}} \dot{\boldsymbol{\rho}}_{\mathrm{R}}^{(l)} \otimes \mathbf{b}_{\mathrm{M}}^{(l)} = \sum_{\mathrm{l}} \mathrm{Curl}\left(\mathbf{v}_{\mathrm{R}}^{(l)} \times \boldsymbol{\rho}_{\mathrm{R}}^{(l)} \right) \otimes \mathbf{b}_{\mathrm{M}}^{(l)}. \tag{3.76}$$

It is now possible to split (3.76) for the transport equations for individual slip systems

$$\dot{\boldsymbol{\rho}}_{\mathrm{R}}^{(l)} = \mathrm{Curl}\left(\mathbf{v}_{\mathrm{R}}^{(l)} \times \boldsymbol{\rho}_{\mathrm{R}}^{(l)} \right) + \dot{\boldsymbol{\rho}}_{\mathrm{R}}^{\mathrm{N}(l)}, \tag{3.77}$$

where $\dot{\boldsymbol{\rho}}_{\mathrm{R}}^{\mathrm{N}(l)}$ is the rate of network density for slip system l as a result of cross-slip and dislocation junction reactions and annihilation; see [125] for the case of infinitesimal deformation theory. These rates satisfy the condition: $\sum_{\mathrm{l}} \dot{\boldsymbol{\rho}}_{\mathrm{R}}^{\mathrm{N}(l)} \otimes \mathbf{b}_{\mathrm{M}}^{l} = 0$. We neglect the network terms in this paper by assuming that dislocations on each slip system form their own closed network, and dedicate a future publication to their treatment in the case of finite deformation. In this case, the condition that $\boldsymbol{\alpha}^{\mathrm{RM\ T}}$ is divergence free leads to

$$\mathrm{Div}\left(\mathbf{b}_{\mathrm{M}}^{(l)} \otimes \boldsymbol{\rho}_{\mathrm{R}}^{(l)} \right) = 0.$$

Using the divergence identity (3.7) and the fact that $\mathbf{b}_{\mathrm{M}}^{(l)}$ is constant we arrive at,

$$\mathrm{Div}\left(\boldsymbol{\rho}_{\mathrm{R}}^{(l)} \right) = 0. \tag{3.78}$$

Similarly, we can get transport equations for the vector densities in the current configuration by considering the transport equation (3.73) and decomposing $\boldsymbol{\alpha}^{\mathrm{DM}}$ into slip system contributions,

$$\boldsymbol{\alpha}^{\mathrm{DM}} = \sum_l \boldsymbol{\alpha}^{\mathrm{DM}(l)} = \sum_l \boldsymbol{\rho}_{\mathrm{D}}^{(l)} \otimes \mathbf{b}_{\mathrm{M}}^{(l)}. \tag{3.79}$$

Substituting this into the transport equation (3.73) gives

$$\sum_l \dot{\boldsymbol{\rho}}_{\mathrm{D}}^{(l)} \otimes \mathbf{b}_{\mathrm{M}}^{(l)} + (\operatorname{tr}(\mathbf{L})\,\mathbf{I} - \mathbf{L}\,) \sum_l \boldsymbol{\rho}_{\mathrm{D}}^{(l)} \otimes \mathbf{b}_{\mathrm{M}}^{(l)} = \operatorname{curl}\left(\boldsymbol{\phi}\mathbf{F}^{-1}\right).$$

With the use of (3.63), this can be rewritten in the form

$$\sum_l \dot{\boldsymbol{\rho}}_{\mathrm{D}}^{(l)} \otimes \mathbf{b}_{\mathrm{M}}^{(l)} + (\operatorname{tr}(\mathbf{L})\,\mathbf{I} - \mathbf{L}\,) \sum_l \boldsymbol{\rho}_{\mathrm{D}}^{(l)} \otimes \mathbf{b}_{\mathrm{M}}^{(l)} = \operatorname{curl} \sum_l \mathbf{b}_{\mathrm{M}}^{(l)} \otimes \left(\mathbf{v}_{\mathrm{D}}^{(l)} \times \boldsymbol{\rho}_{\mathrm{D}}^{(l)}\right). \tag{3.80}$$

Upon using the curl identity (3.6) and with the addition of network terms, equation (3.80) yields the transport equations for the individual vector densities in the deformed configuration,

$$\dot{\boldsymbol{\rho}}_{\mathrm{D}}^{(l)} + (\operatorname{tr}(\mathbf{L})\,\mathbf{I} - \mathbf{L}\,)\,\boldsymbol{\rho}_{\mathrm{D}}^{(l)} = \operatorname{curl}\left(\mathbf{v}_{\mathrm{D}}^{(l)} \times \boldsymbol{\rho}_{\mathrm{D}}^{(l)}\right) + \dot{\boldsymbol{\rho}}_{\mathrm{D}}^{\mathrm{N}(l)}, \tag{3.81}$$

where, again, a network term is added for completeness.

We remark that the transport equations for the vector densities were derived from the two-point tensors since in these tensors the crystal Burgers vectors in the microstructure configuration are constant. It is also worth noting that these two tensors were considered unimportant by [34] due to the fact that they were not invariant tensors.

Expression (3.81) is the material form of the transport equation of the density measure in the deformed configuration, $\boldsymbol{\rho}_{\mathrm{D}}$, which can be transformed into a spatial of Eulerian form following the usual techniques of continuum mechanics. In contrast to the two-point dislocation density tensors, the referential and spatial density tensors $\boldsymbol{\alpha}^{\mathrm{R}}$ and $\boldsymbol{\alpha}^{\mathrm{D}}$ have two contributions to their material time derivative, a contribution due to dislocation motion and another due to change in the Burgers vector in the respective configurations. For example, for $\boldsymbol{\alpha}^{\mathrm{D}}$ from (40), the material time derivative is $\dot{\boldsymbol{\alpha}}^{\mathrm{D}} = \dot{\boldsymbol{\rho}}_{\mathrm{D}} \otimes \mathbf{b}_{\mathrm{D}} + \boldsymbol{\rho}_{\mathrm{D}} \otimes \dot{\mathbf{b}}_{\mathrm{D}}$. Because of this, it

is not possible to use $\boldsymbol{\alpha}^{\mathrm{D}}$ to isolate an expression for the transport equations for $\boldsymbol{\rho}_{\mathrm{D}}$ because of the additional terms that come from $\dot{\mathbf{b}}_{\mathrm{D}}$. Instead, we start by expanding the material time derivative in (3.81) into the form

$$\dot{\boldsymbol{\rho}}_{\mathrm{D}}^{(l)}=\boldsymbol{\rho}'^{(l)}_{\mathrm{D}}+\mathrm{grad}\left(\boldsymbol{\rho}_{\mathrm{D}}^{(l)}\right)\mathbf{v}, \tag{3.82}$$

with the prime denoting the Eulerian time derivative. Using the identity (3.7) we obtain

$$\mathrm{div}\left(\boldsymbol{\rho}_{\mathrm{D}}^{(l)}\otimes\mathbf{v}\right)=\mathrm{div}\left(\mathbf{v}\right)\boldsymbol{\rho}_{\mathrm{D}}^{(l)}=\mathrm{grad}\left(\boldsymbol{\rho}_{\mathrm{D}}^{(l)}\right)\mathbf{v},$$

which we write as,

$$\mathrm{div}\left(\boldsymbol{\rho}_{\mathrm{D}}^{(l)}\otimes\mathbf{v}\right)=\mathrm{tr}\left(\mathrm{L}\right)\boldsymbol{\rho}_{\mathrm{D}}^{(l)}+\mathrm{grad}\left(\boldsymbol{\rho}_{\mathrm{D}}^{(l)}\right)\mathbf{v}. \tag{3.83}$$

Using the same identity again gives,

$$\mathrm{div}\left(\mathbf{v}\otimes\boldsymbol{\rho}_{\mathrm{D}}^{(l)}\right)=\mathrm{div}\left(\boldsymbol{\rho}_{\mathrm{D}}^{(l)}\right)\mathbf{v}+\mathrm{grad}\left(\mathbf{v}\right)\boldsymbol{\rho}_{\mathrm{D}}^{(l)}.$$

Neglecting again the network terms and using (3.78) we write this as

$$\mathrm{div}\left(\mathbf{v}\otimes\boldsymbol{\rho}_{\mathrm{D}}^{(l)}\right)=0+\mathbf{L}\boldsymbol{\rho}_{\mathrm{D}}^{(l)}. \tag{3.84}$$

Looking at just the left-hand side of the transport equations (3.81) and using (3.82), we get

$$\dot{\boldsymbol{\rho}}_{\mathrm{D}}^{(l)}+\left(\mathrm{tr}\left(\mathbf{L}\right)\mathbf{I}-\mathbf{L}\right)\boldsymbol{\rho}_{\mathrm{D}}^{(l)}=\boldsymbol{\rho}'^{(l)}_{\mathrm{D}}+\mathrm{grad}\left(\boldsymbol{\rho}_{\mathrm{D}}^{(l)}\right)\mathbf{v}+\left(\mathrm{tr}\left(\mathbf{L}\right)\mathbf{I}-\mathbf{L}\right)\boldsymbol{\rho}_{\mathrm{D}}^{(l)}.$$

With the use of (3.83), it becomes: $\boldsymbol{\rho}'^{(l)}_{\mathrm{D}}+\mathrm{div}\left(\boldsymbol{\rho}_{\mathrm{D}}^{(l)}\otimes\mathbf{v}\right)-\mathrm{tr}\left(\mathbf{L}\right)\boldsymbol{\rho}_{\mathrm{D}}^{(l)}+\left(\mathrm{tr}\left(\mathbf{L}\right)\mathbf{I}-\mathbf{L}\right)\boldsymbol{\rho}_{\mathrm{D}}^{(l)}=\boldsymbol{\rho}'^{(l)}_{\mathrm{D}}+\mathrm{div}\left(\boldsymbol{\rho}_{\mathrm{D}}^{(l)}\otimes\mathbf{v}\right)-\mathbf{L}\boldsymbol{\rho}_{\mathrm{D}}^{(l)}$, and with further use of (3.84), it becomes: $\boldsymbol{\rho}'^{(l)}_{\mathrm{D}}+\mathrm{div}\left(\boldsymbol{\rho}_{\mathrm{D}}^{(l)}\otimes\mathbf{v}\right)-\mathrm{div}\left(\mathbf{v}\otimes\boldsymbol{\rho}_{\mathrm{D}}^{(l)}\right)$. Finally, using (3.8), it can be simplified to: $\boldsymbol{\rho}'^{(l)}_{\mathrm{D}}=\mathrm{curl}\left(\mathbf{v}\times\boldsymbol{\rho}_{\mathrm{D}}^{(l)}\right)$. The final

form for the transport equations for the vector densities in the deformed configuration then becomes

$$\boldsymbol{\rho}'^{(l)}_{\mathrm{D}} = \operatorname{curl}\left((\mathbf{v}^{(l)}_{\mathbf{D}} + \mathbf{v}) \times \boldsymbol{\rho}^{(l)}_{\mathrm{D}}\right) + \boldsymbol{\rho}'^{\mathrm{N}(l)}_{\mathrm{D}}, \tag{3.85}$$

where the network term was added. This equation represents the transport of dislocations in the deformed configuration and the velocity term ($\mathbf{v}^{(l)}_{\mathrm{D}} = \mathbf{v}$) can be thought of as the absolute velocity of dislocations, which is the sum of dislocation velocity relative to the crystal, $\mathbf{v}^{(l)}_{\mathrm{D}}$, and the crystal velocity, $\mathbf{v}$. A condition similar to (3.78) does apply to the spatial density $\boldsymbol{\rho}^{(l)}_{\mathrm{D}}$. Again, we hold off on the analysis of the network terms $\boldsymbol{\rho}^{\mathrm{N}(l)}_{\mathrm{D}}$ for a future publication. We can now move on to deriving the driving forces associated with referential and spatial forms (3.77) and (3.85) of the transport equations for the vector density of dislocations. For completeness, thought, we refer the reader to Appendix 3.A where the transport relations for the remaining dislocation density tensors, namely, $\boldsymbol{\alpha}^{\mathrm{R}}$, $\boldsymbol{\alpha}^{\mathrm{M}}$, and $\boldsymbol{\alpha}^{\mathrm{D}}$, are derived.

3.11 Crystal kinetics and constitutive analysis

We now wish to connect the velocity of dislocations to the corresponding driving force. We do so by deriving the force conjugate to the velocity of dislocations, from which the velocities can be fixed using a mobility law.

We begin by introducing the stress equilibrium equations. Neglecting inertia, Cauchy stress, $\boldsymbol{\sigma}$, satisfies the static equilibrium equation with no body forces in the deformed configuration,

$$\operatorname{div}(\boldsymbol{\sigma}) = \mathbf{0}. \tag{3.86}$$

In the reference configuration equilibrium takes on the form,

$$\operatorname{Div}\left(\mathbf{P}^{\mathrm{T}}\right) = \mathbf{0}, \tag{3.87}$$

where $\mathbf{P}$ is the first Piola-Kirchhoff (PK1) stress tensor, which measures the traction in the deformed configuration on an area element in the reference configuration. It is related to the second Piola-Kirchhoff (PK2) stress tensor, $\mathbf{S}$, by $\mathbf{P}^{\mathrm{T}}{=}\mathbf{S}^{\mathrm{T}}\mathbf{F}^{\mathrm{T}}$.

3.12 Power of deformation in reference configuration

The power of deformation in the deformed configuration is $\boldsymbol{\sigma} : \mathbf{D}$, with $\mathbf{D}$ being the symmetric part of the velocity gradient, or the rate-of-strain tensor. This power can be pulled back to give its counterpart in the reference configuration: $\mathrm{J}\boldsymbol{\sigma}{:}\mathbf{D}$. By further using $\mathbf{D}{=}\mathbf{F}^{-1}\dot{\mathbf{E}}\mathbf{F}^{-\mathrm{T}}$ and using the relationships between Cauchy stress and the second Piola-Kirchhoff stress, the referential power density can be written in the form:

$$\mathrm{J}\left(\boldsymbol{\sigma} : \mathbf{D}\right) = \mathbf{S}{:}\dot{\mathbf{E}}. \tag{3.88}$$

Below we show that the power of deformation in the reference configuration can be split into two contributions associated with the dislocation motion and elastic strain rate. By exploiting equation (3.20) for the Lagrangian strain, we can write:

$$\mathbf{S} : \dot{\mathbf{E}} = \mathbf{S} : \left(\dot{\overline{\mathbf{F}^{\mathrm{p}\mathrm{T}}\mathbf{E}^{\mathrm{e}}\mathbf{F}^{\mathrm{p}}}}\right) = \mathbf{S} : \dot{\mathbf{E}}^{\mathrm{p}}, \tag{3.89}$$

which simplifies to

$$\mathbf{S} : \dot{\mathbf{E}}{=}\mathbf{M}{:}\left(\mathbf{F}^{\mathrm{p}-1}\boldsymbol{\phi}\right) = \mathbf{S} : \left(\mathbf{F}^{\mathrm{p}\mathrm{T}}\dot{\mathbf{E}}^{\mathrm{e}}\mathbf{F}^{\mathrm{p}}\right), \tag{3.90}$$

with $\mathbf{M} = \mathbf{C}\mathbf{S}$ being the referential Mandel stress. We refer the reader to Appendix 3.B for the algebra used to rewrite equation (3.89) into (3.90). We note that the quantity $\mathbf{S} : \dot{\mathbf{E}}$ is comprised of a term associated with the motion of dislocations, $\mathbf{M}{:}\left(\mathbf{F}^{\mathrm{p}-1}\boldsymbol{\phi}\right)$, and another corresponding to the elastic energy storage, $\mathbf{S} : \left(\mathbf{F}^{\mathrm{p}\mathrm{T}}\dot{\mathbf{E}}^{\mathrm{e}}\mathbf{F}^{\mathrm{p}}\right)$.

3.13 Constitutive analysis

In this section, we derive the elastic and plastic constitutive relationships from the principles of thermodynamics. As expected, the elastic constitutive relationship corresponds

to that of a hyperelastic solid. The plastic counterpart is associated with dissipation due to dislocation motion and it leads to defining the configurational force acting on dislocations in the reference configuration, which is the Peach-Koehler force in a finite-deformation setting. To achieve this goal, we start with the global referential free energy imbalance ignoring entropic effects,

$$\int \left(\dot{\psi}_R - \mathbf{S}:\dot{\mathbf{E}}\right) \mathrm{dV_R} \leq 0, \tag{3.91}$$

with ψ_{R} being the referential free energy density. We assume that the free energy can be split into contributions, the stored elastic energy plus a second part due to dislocations [84],

$$\psi_{\mathrm{R}} = \psi_{\mathrm{R}}^{\mathrm{e}} + \psi_{\mathrm{R}}^{\mathrm{p}}. \tag{3.92}$$

For a technical reason that will become clear later, the deformed free energy density counterparts, ψ_{D}, $\psi_{\mathrm{D}}^{\mathrm{e}}$ and $\psi_{\mathrm{D}}^{\mathrm{p}}$, are defined per unit mass. We expect these scalars to transform according to,

$$\begin{aligned} \psi_{\mathrm{R}}^{\mathrm{e}} &= \rho_{\mathrm{R}} \psi_{\mathrm{D}}^{\mathrm{e}} \\ \psi_{\mathrm{R}}^{\mathrm{p}} &= \rho_{\mathrm{R}} \psi_{\mathrm{D}'}^{\mathrm{p}} \end{aligned} \tag{3.93}$$

We consider writing (3.92) in an equivalent form,

$$\psi_{\mathrm{R}} = \rho_{\mathrm{R}} \psi_{\mathrm{D}}^{\mathrm{e}} + \psi_{\mathrm{R}}^{\mathrm{p}}. \tag{3.94}$$

Since the referential density does not depend on time, we write the free energy imbalance as [71],

$$\int \left(\rho_{\mathrm{R}} \dot{\psi}_{\mathrm{D}}^{\mathrm{e}} + \dot{\psi}_{\mathrm{P}}^{\mathrm{p}} - \mathbf{S}:\dot{\mathbf{E}}\right) \mathrm{dV_R} \leq 0. \tag{3.95}$$

Let us assume that the elastic and defect free energy contributions in the deformed configuration have the form,

$$\begin{aligned} \psi_{\mathrm{D}}^{\mathrm{e}} &= \widehat{\psi}_{\mathrm{D}}^{\mathrm{e}} \left(\mathbf{F}^{\mathrm{e}}\right) \\ \psi_{\mathrm{R}}^{\mathrm{p}} &= \widehat{\psi}_{\mathrm{R}}^{\mathrm{p}} \left(\boldsymbol{\rho}_{\mathrm{R}}^{(l)}\right) \end{aligned} \tag{3.96}$$

Upon using the chain rule of differentiation with respect to time, (3.96) gives

$$\begin{aligned}\dot{\psi}_{\mathrm{D}}^{\mathrm{e}} &= \frac{\partial \widehat{\Psi}_{\mathrm{D}}^{\mathrm{e}}}{\partial \mathbf{F}^{\mathrm{e}}} : \mathbf{F}^{\mathrm{e}} \\ \dot{\psi}_{\mathrm{P}}^{\mathrm{p}} &= \sum_{1} \frac{\partial \widehat{\psi}_{\mathrm{R}}^{\mathrm{p}}}{\partial \boldsymbol{\rho}_{\mathrm{R}}^{(l)}} \cdot \dot{\boldsymbol{\rho}}_{R}^{(l)}\end{aligned} \tag{3.97}$$

Plugging this into the free energy imbalance equation yields

$$\int \left(\rho_{\mathrm{R}} \frac{\partial \widehat{\psi}_{\mathrm{D}}^{\mathrm{e}}}{\partial \mathbf{F}^{\mathbf{e}}} : \dot{\mathbf{F}}^{\mathbf{e}} - \mathbf{S} : \dot{\mathbf{E}} + \sum_{l} \frac{\partial \widehat{\psi}_{\mathrm{R}}^{\mathrm{p}}}{\partial \boldsymbol{\rho}_{\mathrm{R}}^{(l)}} \cdot \dot{\boldsymbol{\rho}}_{R}^{(l)} \right) \mathrm{dV}_{\mathrm{R}} \leq 0. \tag{3.98}$$

From (3.90) we can write the free energy imbalance as

$$\int \left(\rho_{\mathrm{R}} \frac{\partial \widehat{\psi}_{\mathrm{D}}^{\mathrm{e}}}{\partial \mathbf{F}^{\mathbf{e}}} : \dot{\mathbf{F}}^{\mathbf{e}} - \mathbf{S} : \left(\mathbf{F}^{\mathbf{pT}} \dot{\mathbf{E}}^{\mathbf{e}} \mathbf{F}^{\mathbf{p}} \right) \right) \mathrm{dV}_{\mathrm{R}} + \int \left(\sum_{l} \frac{\partial \widehat{\psi}_{\mathrm{R}}^{\mathrm{p}}}{\partial \boldsymbol{\rho}_{\mathrm{R}}^{(l)}} \cdot \dot{\boldsymbol{\rho}}_{R}^{(l)} - \mathbf{M} : \left(\mathbf{F}^{\mathrm{p}-1} \boldsymbol{\phi} \right) \right) \mathrm{dV}_{\mathrm{R}} \leq 0, \tag{3.99}$$

where we have grouped the terms according to corresponding rate quantities. We further simplify this inequality below to obtain the hyperelastic constitutive relationship and the driving force for dislocation motion.

3.13.1 Elastic constitutive response of the crystal

Let us call the integrals in (3.99) the elastic and plastic terms, respectively. Our strategy now is to write the expression $\mathbf{S} : \left(\mathbf{F}^{\mathbf{pT}} \dot{\mathbf{E}}^{\mathbf{e}} \mathbf{F}^{\mathbf{p}} \right)$ under the first integral in terms of the rate of the elastic distortion so that we can group it with the first term. To this end, using properties of the double inner product we can write

$$\mathbf{S} : \left(\mathbf{F}^{\mathrm{pT}} \dot{\mathbf{E}}^{\mathrm{e}} \mathbf{F}^{\mathrm{p}} \right) = \left(\mathbf{F}^{\mathrm{p}} \mathbf{S} \mathbf{F}^{\mathrm{pT}} \right) : \dot{\mathbf{E}}^{\mathrm{e}}. \tag{3.100}$$

Since $\left(\mathbf{F}^{\mathbf{p}} \mathbf{S} \mathbf{F}^{\mathbf{pT}} \right)$ is symmetric it is possible to express this in the form

$$\left(\mathbf{F}^{\mathrm{p}} \mathbf{S} \mathbf{F}^{\mathrm{pT}} \right) : \dot{\mathbf{E}}^{\mathrm{e}} = \left(\mathbf{F}^{\mathrm{p}} \mathbf{S} \mathbf{F}^{\mathrm{pT}} \right) : \left(\mathbf{F}^{\mathrm{eT}} \dot{\mathbf{F}}^{\mathrm{e}} \right). \tag{3.101}$$

Using the double inner product properties again gives

$$\left(\mathbf{F}^{\mathrm{p}}\mathbf{S}\mathbf{F}^{\mathrm{pT}}\right) : \dot{\mathbf{E}}^{\mathrm{e}} = \left(\mathbf{F}^{\mathrm{e}}\mathbf{F}^{\mathrm{p}}\mathbf{S}\mathbf{F}^{\mathrm{pT}}\right) : \dot{\mathbf{F}}^{\mathrm{e}}. \tag{3.102}$$

With this, the elastic integral in the free energy imbalance (3.98) becomes

$$\int \left(\rho_{\mathrm{R}} \frac{\partial \widehat{\psi}_{\mathrm{D}}^{\mathrm{e}}}{\partial \mathbf{F}^{\mathbf{e}}} - \mathbf{F}^{\mathrm{e}}\mathbf{F}^{\mathrm{p}}\mathbf{S}\mathbf{F}^{\mathrm{pT}}\right) : \dot{\mathbf{F}}^{\mathbf{e}} \mathrm{dV}_{\mathrm{R}}. \tag{3.103}$$

For arbitrary motion of the body and due to the non-dissipative nature of this term we require the integrand to vanish

$$\rho_{\mathrm{R}} \frac{\partial \widehat{\psi}_{\mathrm{D}}^{\mathrm{e}}}{\partial \mathbf{F}^{\mathbf{e}}} - \mathbf{F}^{\mathrm{e}}\mathbf{F}^{\mathrm{p}}\mathbf{S}\mathbf{F}^{\mathrm{pT}} = \mathbf{0}. \tag{3.104}$$

Solving (3.103) for the PK2 stress gives

$$\mathbf{S} = \mathbf{F}^{\mathrm{p}-1}\left(\mathbf{F}^{\mathrm{e}-1}\rho_{\mathrm{R}} \frac{\partial \widehat{\psi}_{\mathrm{D}}^{\mathrm{e}}}{\partial \mathbf{F}^{\mathbf{e}}}\right)\mathbf{F}^{\mathrm{p}-\mathrm{T}}. \tag{3.105}$$

We can now start to talk about elastic materials in this context. If we define the PK1 stress in the microstructure space as,

$$\mathbf{P}^{\mathrm{e}} \equiv \rho_{\mathrm{M}} \frac{\partial \widehat{\psi}_{\mathrm{D}}^{\mathrm{e}}}{\partial \mathbf{F}^{\mathbf{e}}}. \tag{3.106}$$

Assuming there exists a mass density such that $\mathrm{J}^{\mathrm{p}}\rho_{\mathrm{M}}=\rho_{\mathrm{R}}$, then by using the transformation relation for the stresses we obtain $\mathbf{S} = \mathrm{J}^{\mathrm{p}}\mathbf{F}^{-1}\mathbf{P}^{\mathrm{e}}\mathbf{F}^{\mathrm{p}-\mathrm{T}} = \mathbf{F}^{\mathrm{p}-1}\left(\mathbf{F}^{\mathrm{e}-1}\rho_{\mathrm{R}}\frac{\partial \widehat{\psi}_{\mathrm{D}}^{\mathrm{e}}}{\partial \mathbf{F}^{\mathbf{e}}}\right)\mathbf{F}^{\mathrm{p}-\mathrm{T}}$, which corresponds to the constitutive requirement (3.105). Using the transformation between the PK2 and Cauchy stress yields

$$\boldsymbol{\sigma} = \rho_{\mathrm{D}} \frac{\partial \widehat{\psi}_{\mathrm{D}}^{\mathrm{e}}}{\partial \mathbf{F}^{\mathbf{e}}}\mathbf{F}^{\mathrm{eT}}, \tag{3.107}$$

with $\rho_{\mathrm{D}} = J^{-1}\rho_{\mathrm{R}}$ is the mass density in the deformed configuration. The relationship (3.107) is the reminiscent of the standard constitutive law for a hyperelastic solid [71].

3.13.2 The force acting on dislocations and mobility law

We next consider the plastic integral in free energy imbalance (3.99), which is related to the dislocation transport. We want to manipulate these terms so that we get an expression that looks like $\mathbf{v}_{\mathbf{R}}^{l}\cdot\left(-\mathbf{f}\right)\leq 0$, where $\mathbf{f}$ is a force that is rate-of-work conjugate to the dislocation velocity field. Once we have this expression, we can write a velocity mobility law in the form: $\mathbf{v}_{\mathbf{R}}^{l}=\mathbf{v}_{\mathbf{R}}^{l}\left(\mathbf{f}\right)$. To this end we consider the term $\mathbf{M}$: $\left(\mathbf{F}^{\mathrm{p}-1}\boldsymbol{\phi}\right)$,

$$\begin{aligned}\mathbf{M}:\left(\mathbf{F}^{\mathrm{p}-1}\boldsymbol{\phi}\right)&=\mathbf{M}:\sum_{\mathrm{i}}\mathbf{F}^{\mathrm{p}-1}\mathbf{b}_{\mathrm{M}}^{(l)}\otimes\left(\mathbf{v}_{\mathrm{R}}^{(l)}\times\boldsymbol{\rho}_{\mathrm{R}}^{(l)}\right)\\&=\sum_{\mathrm{i}}\mathbf{b}_{\mathrm{R}}^{(l)}\otimes\left(\mathbf{v}_{\mathrm{R}}^{(l)}\times\boldsymbol{\rho}_{\mathrm{R}}^{(l)}\right)=\sum_{\mathrm{i}}\mathbf{M}:\mathbf{b}_{\mathrm{R}}^{(l)}\otimes\left(\mathbf{v}_{\mathrm{R}}^{(l)}\times\boldsymbol{\rho}_{\mathrm{R}}^{(l)}\right)\\&=\sum_{l}^{l}M_{\mathrm{ij}}b_{\mathrm{Ri}}^{(l)}\epsilon_{kmj}v_{\mathrm{R}k}^{(l)}\rho_{\mathrm{R}m}^{(l)}=\sum_{l}v_{\mathrm{R}k}^{(l)}\epsilon_{kmj}M_{\mathrm{ij}}b_{\mathrm{Ri}}^{(l)}\rho_{\mathrm{R}m}^{(l)}\end{aligned}\tag{3.108}$$

Since $\epsilon_{kmj}=\epsilon_{jmk}$, we can write, $\sum_l v_{\mathrm{R}k}^{(l)}\epsilon_{jmk}M_{\mathrm{ij}}b_{\mathrm{Ri}}^{(l)}\rho_{\mathrm{R}m}^{(l)}=\sum_l\mathbf{v}_{\mathrm{R}}^{(l)}\cdot(\mathbf{M}\mathbf{b}_{\mathrm{R}}^{(l)}\times\boldsymbol{\rho}_{\mathrm{R}}^{(l)})$. This yields a simplified expression for the $\mathbf{M}$: $\left(\mathbf{F}^{\mathbf{p}-1}\boldsymbol{\phi}\right)$ as follows:

$$\mathbf{M}:\left(\mathbf{F}^{\mathrm{p}-1}\boldsymbol{\phi}\right)=\sum_{l}\mathbf{v}_{\mathrm{R}}^{(l)}\cdot\left(\left(\mathbf{b}_{\mathrm{R}}^{(l)}\cdot\mathbf{M}^{\mathrm{T}}\right)\times\boldsymbol{\rho}_{\mathrm{R}}^{(l)}\right).\tag{3.109}$$

We will now look at the term $\sum_l\rho_{\mathrm{R}}\frac{\partial\widehat{\psi}}{\partial\boldsymbol{\rho}_{\mathrm{R}}^{l}}\cdot\dot{\boldsymbol{\rho}}_{R}^{(l)}$. We manipulate this term by borrowing the expression for $\dot{\boldsymbol{\rho}}_{R}^{(l)}$ from the transport equation (3.77) while ignoring the network term for simplicity. Prior to inserting the corresponding expression, we manipulate it further by replacing the curl operator with the divergence operator as follows:

$$\mathrm{Curl}\left(\mathbf{v}_{\mathrm{R}}^{(l)}\times\boldsymbol{\rho}_{\mathrm{R}}^{(l)}\right)=\mathrm{Div}\left(\mathbf{v}_{\mathrm{R}}^{(l)}\otimes\boldsymbol{\rho}_{\mathrm{R}}^{(l)}-\boldsymbol{\rho}_{\mathrm{R}}^{(l)}\otimes\mathbf{v}_{\mathrm{R}}^{(l)}\right).$$

With this, the corresponding term in the free energy imbalance becomes

$$\int\sum_{l}\frac{\partial\widehat{\psi}_{\mathrm{R}}^{\mathrm{p}}}{\partial\boldsymbol{\rho}_{\mathrm{R}}^{(l)}}\cdot\mathrm{Div}\left(\mathbf{v}_{\mathrm{R}}^{(l)}\otimes\boldsymbol{\rho}_{\mathrm{R}}^{(l)}-\boldsymbol{\rho}_{\mathrm{R}}^{(l)}\otimes\mathbf{v}_{\mathrm{R}}^{(l)}\right)\mathrm{dV}_{\mathrm{R}}.\tag{3.110}$$

Carrying out integration by parts, with periodic boundary conditions to get rid of surface terms, the last integral can be expressed in the form

$$-\int \sum_l \text{Grad}\left(\frac{\partial \widehat{\psi}_{\text{R}}^{\text{p}}}{\partial \boldsymbol{\rho}_{\text{R}}^{(l)}}\right) : \left(\mathbf{v}_{\text{R}}^{(l)} \otimes \boldsymbol{\rho}_{\text{R}}^{(l)} - \boldsymbol{\rho}_{\text{R}}^{(l)} \otimes \mathbf{v}_{\text{R}}^{(l)}\right) \text{dV}_{\text{R}}. \tag{3.111}$$

which can be further simplified to

$$-\int \sum_l \mathbf{v}_{\text{R}}^{(l)} \cdot \left[\left(\mathbf{A}^{(l)} - \mathbf{A}^{(l)\text{T}}\right) \boldsymbol{\rho}_{\text{R}}^{(l)}\right] \text{dV}_{\text{R}}, \tag{3.112}$$

with $\mathbf{A}^{(l)} \equiv \text{Grad}\left(\frac{\partial \widehat{\psi}_{\text{R}}^{\text{p}}}{\partial \boldsymbol{\rho}_{\text{R}}^{(l)}}\right)$. Since $\left(\mathbf{A}^{(l)} - \mathbf{A}^{(l)\text{T}}\right)$ is antisymmetric, it has an axial vector $\boldsymbol{\omega}^{(l)}$ defined such that $\left(\mathbf{A}^{(l)} - \mathbf{A}^{(l)\text{T}}\right) \boldsymbol{\xi}_{\text{R}}^{(l)} = \boldsymbol{\omega}^{(l)} \times \boldsymbol{\xi}_{\text{R}}^{(l)}$ and given by $\omega_{\text{i}}^{(l)} = -\frac{1}{2}\epsilon_{\text{ijk}}\left(\boldsymbol{A}^{(l)} - \boldsymbol{A}^{(l)\text{T}}\right)_{jk}$. This axial vector can also be expressed in the form: $\boldsymbol{\omega}^{(l)} = \text{Curl}\left(\frac{\partial \widehat{\psi}_{\text{R}}^{\text{p}}}{\partial \boldsymbol{\rho}_{\text{R}}^{(l)}}\right)$. With this, Eq. (3.112) becomes,

$$\int \sum_l \frac{\partial \widehat{\psi}_{\text{R}}^{\text{p}}}{\partial \boldsymbol{\rho}_{\text{R}}^{(l)}} \cdot \dot{\boldsymbol{\rho}}_R^{(l)} \text{dV}_{\text{R}} = -\int \sum_l \rho_{\text{R}}^{(l)} \mathbf{v}_{\text{R}}^{(l)} \cdot \left[\text{Curl}\left(\frac{\partial \widehat{\psi}_{\text{R}}^{\text{p}}}{\partial \boldsymbol{\rho}_{\text{R}}^{(l)}}\right) \times \boldsymbol{\xi}_{\text{R}}^{(l)}\right] \text{dV}_{\text{R}}, \tag{3.113}$$

where $\boldsymbol{\rho}_{\text{R}}^{(l)} = \rho_{\text{R}}^{(l)} \boldsymbol{\xi}_{\text{R}}^{(l)}$. Adding the simplified terms (3.109) and (3.113), the second integral in Eq. (3.98) becomes

$$\int \sum_l \rho_{\text{R}}^{(l)} \mathbf{v}_{\text{R}}^{(l)} \cdot \left[-\left(\mathbf{b}_{\text{R}}^{(l)} \cdot \mathbf{M}^{\text{T}} + \boldsymbol{\omega}^{(l)}\right) \times \boldsymbol{\xi}_{\text{R}}^{(l)}\right] \text{dV}_{\text{R}} \leq 0. \tag{3.114}$$

The quantity between brackets is nothing but the configuration force acting on dislocations. It has the proper dimensions of force per unit length, and the multiplication by the scalar density of dislocation and the velocity yields the contribution to the rate of decline of the free energy per unit volume, with the minus sign taken into consideration. We note here that a similar expression for the driving force for dislocations in the reference configuration was given in [153] where the Mandel stress is used as a driving force with an additional back

stress term coming from the free energy. We may thus define the referential Peach-Koehler force in the case of finite deformation by

$$\mathbf{f}_{\mathrm{R}}^{(l)} = \left(\mathbf{b}_{\mathbf{R}}^{(l)} \cdot \mathbf{M}^{\mathrm{T}} + \boldsymbol{\omega}^{(l)}\right) \times \boldsymbol{\xi}_{\mathrm{R}}^{(l)}. \tag{3.115}$$

A similar procedure can be used to obtain the Peach-Kohler force in the deformed configuration by considering the free energy imbalance in that configuration; this results in the usual expression for the driving force with the Cauchy stress as the driving stress measure

$$\mathbf{f}_{\mathrm{D}}^{(l)} = \left(\mathbf{b}_{\mathrm{D}}^{(l)} \cdot \boldsymbol{\sigma}^{\mathrm{T}} + \boldsymbol{\omega}_{\mathrm{D}}^{(l)}\right) \times \boldsymbol{\xi}_{\mathrm{D}}^{(l)}, \tag{3.116}$$

where $\boldsymbol{\omega}_{\mathrm{D}}^{(l)} \equiv \mathrm{curl}\left(\frac{\partial \widehat{\psi}_{\mathrm{D}}^{\mathrm{p}}}{\partial \boldsymbol{\rho}_{\mathrm{D}}^{(l)}}\right)$. The reader is referred to the Appendix 3.C for relevant details of the derivation. Because the integral in (3.114) is negative, a mobility law can then be postulated to yield the dislocation velocity in terms of the driving force. The simplest form of such a law is

$$\mathbf{v}_{\mathrm{R}}^{(l)} = \mathrm{M}\mathbf{f}_{\mathrm{R}}^{(l)}, \tag{3.117}$$

with M being a positive quantity. Regardless of its form, such a mobility law connects the dislocation velocity to the local stress state and closes the set of equations to be solved once a constitutive function $\psi_{\mathrm{R}}^{\mathrm{p}} = \widehat{\psi}_{\mathrm{R}}^{\mathrm{p}}\left(\boldsymbol{\rho}_{\mathrm{R}}^{l}\right)$ is fixed. These equations are:

$$\begin{cases} \mathrm{Div}\left(\mathbf{P}^{\mathrm{T}}\right) = \mathbf{0} \\ \dot{\boldsymbol{\rho}}_{\mathrm{R}}^{(l)} = \mathrm{Curl}\left(\mathbf{v}_{\mathrm{R}}^{(l)} \times \boldsymbol{\rho}_{\mathrm{R}}^{(l)}\right) + \dot{\boldsymbol{\rho}}_{\mathrm{R}}^{\mathrm{N}(l)} \\ \mathbf{v}_{\mathrm{R}}^{(l)} = \mathrm{M}\mathbf{f}_{\mathrm{R}}^{(\boldsymbol{l})}. \end{cases} \tag{3.118}$$

where the network contribution to the rate of change of the slip system density $\dot{\boldsymbol{\rho}}_{\mathrm{R}}^{(l)}$ has been restored. The numerical treatment of these equations fully coupled with the rest of the equations of finite-deformation crystal mechanics will be the subject of a forthcoming publication. Only a few static solution problems, i.e., when $\mathbf{v}_{\mathrm{R}}^{(l)} = \mathbf{0}$, are presented in the next section to illustrate some of the important relationships.

We remark here that, in the development presented so far the idea of an arbitrary reference configuration is important, and we refer the reader to Appendix 3.D where an attempt is made at defining what this should mean in the case of dislocated crystals.

3.14 Static solutions and discussion

In this section, numerical solutions are presented for a set of finite-eigenstrain problem involving the introduction of plastic distortion into a single crystal and the calculation of the dislocation and elastic fields. The calculations are done for FCC iron with shear modulus of 79.52 GPa, Poisson's ratio of 0.2945, and Burgers vector of 0.254 nm [172]. The domain size was 5 μm on the edge. The governing equations are solved using a total Lagrangian approach with the plastic distortion specified that corresponds to simple static dislocations arrays. A linear elastic constitutive law for (3.106) is assumed with an elastic tensor being isotropic. Periodic boundary conditions are assumed throughout and no external loads are present. Details of the numerical solution scheme will appear in a future publication.

The first problem is one in which plastic distortion is introduced so as to correspond to a dislocation bundle in the form of a loop. A small plastic distortion is introduced first to enable comparison with the linearized (infinitesimal) eigenstrain problems, then a finite distortion is introduced to check the differences in the elastic fields between the two cases. The situation is illustrated in Fig. 3.2. The plastic distortion is smeared so as to correspond to a dislocation bundle that has a density of a Gaussian profile in both the radial and z directions. The stress field is plotted in Fig. 3.3 in the deformed configuration for the case of small strain along with the analytical solution reported in [112] for a loop embedded in an infinite domain. The comparison thus makes sense near the dislocation bundle and away from the domain boundary. The solution shows that the stress contours are equivalent. Good agreement of the solution near the dislocation loops, which is dominated by the singular field, is clear in Fig. 3.3.

Next, we consider a denser distribution of dislocations obtained by increasing the magnitude of the plastic distortion introduced into the domain of solution. In this case, the lattice rotation effects start to become significant. The plastic distortion is shown in

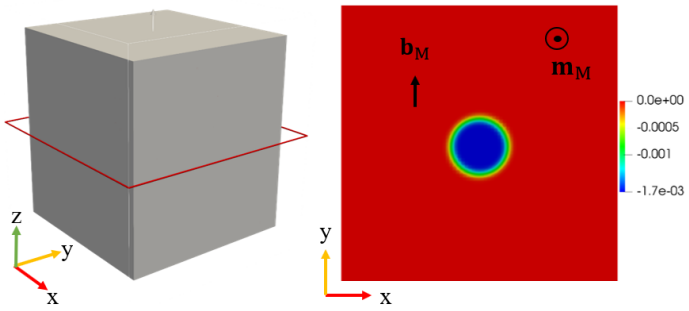

Figure 3.2. A 3D depiction of the simulation domain is shown to the left with a red plane intersecting it corresponding to the slip plan to the right, with the plastic slip field, γ, introduced parallel to the x-y plane and represented by colors. Burgers vector is oriented along the y direction and slip normal, $\mathbf{m}_M$, in the z direction.

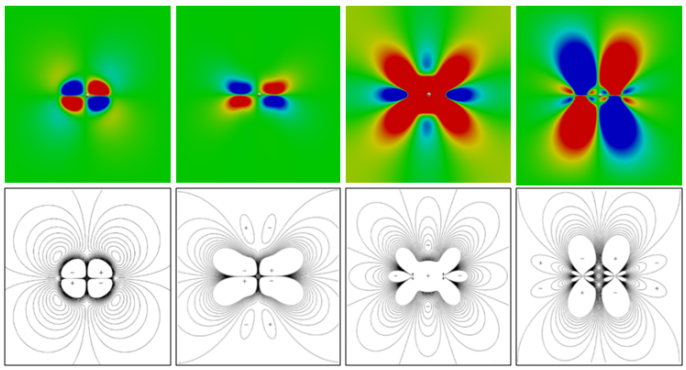

Figure 3.3. Cauchy stress in the y-z plane passing through the middle of the domain of solution. From the left to right the components are $\sigma_{11}, \sigma_{22}, \sigma_{23}$ and σ_{33}. The top panels are obtained by our solution method (with red and blue colors representing positive and negative stresses) and the lower panels represent the analytical solution of a dislocation loop in an infinite medium reported in [112].

Fig. 3.4. And the resulting Cauchy stress field is shown in Fig. 3.5 along with the solution produced in [112] for the linear elastic solution case. The figure shows that there is some rotation of the contours in the case of finite deformation (top panels). This rotation becomes more prominent when larger localized dislocation densities are introduced as the magnitude of the plastic distortion is increased.

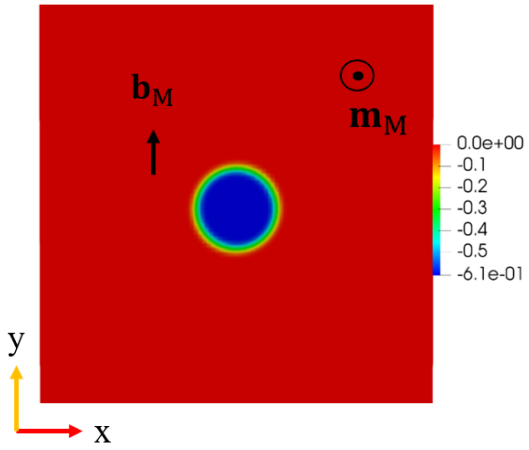

Figure 3.4. A finite plastic shear that is more than two orders of magnitude larger than that shown in Fig. 2. A finite-deformation solution of the eigenstrain problem is required in this case.

In this next test problem, we consider a plastic distortion giving rise to tilt boundaries. The tilt boundaries consist of vertical arrays of edge dislocations generated by uniform plastic slip of 4% in the channel between the boundaries. The termination of slip at the boundaries with sharp gradients creates the dislocation arrays. This situation is depicted in Fig. 3.6. The non-trivial component of the referential dislocation density tensor associated with the tilt boundaries is α^{R}_{12}. This component is shown in Fig. 3.7. The dislocation lines run along the x direction for positive dislocations and along the negative x direction for negative dislocations, with the crystallographic Burgers vector (the direction of slip) pointing in the y direction. The magnitude of the plastic distortion and its gradient at the channel ends fully fix the values of α^{R}_{12}.

We now illustrate the effect of lattice rotation on the dislocation density measure by investigating the density tensor in the deformed configuration for the tilt boundary case

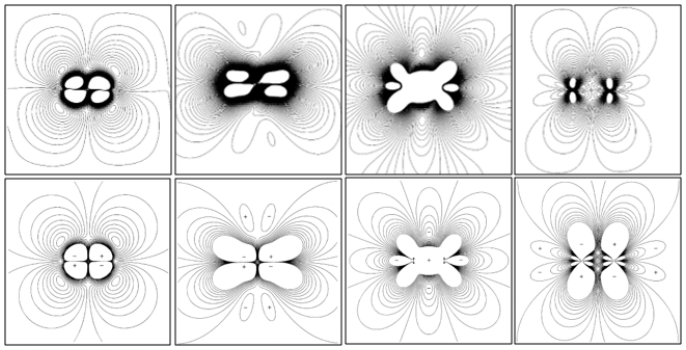

Figure 3.5. Cauchy stress corresponding to the finite plastic slip shown in Fig. 3.4, plotted in the deformed configuration on a y-z plane passing through the middle of the solution domain (Fig. 3.2). The top panels show our solution and the lower panels represent the analytical solution for a single dislocation loop in an infinite domain [112]. From the left to right the components are $\sigma_{11}, \sigma_{22}, \sigma_{23}$ and σ_{33}. The signs of our solution match the analytical result.

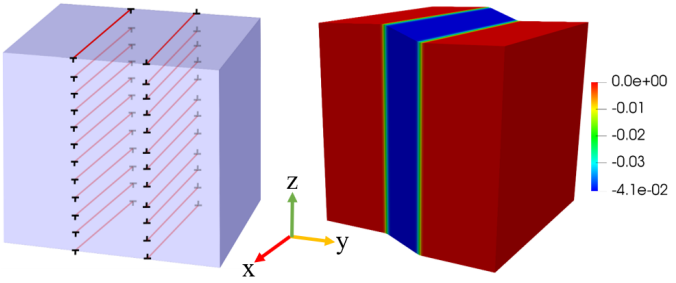

Figure 3.6. A discrete representation of the two tilt boundaries (left), with two vertical arrays of negative and positive edge dislocations forming the two boundaries. A uniform plastic slip of 4% was introduced in the channel between the boundaries, with sharp gradients giving rise to the dislocation arrays. The plastic slip is plotted to the right on the deformed configuration associated with the two tilt boundaries.

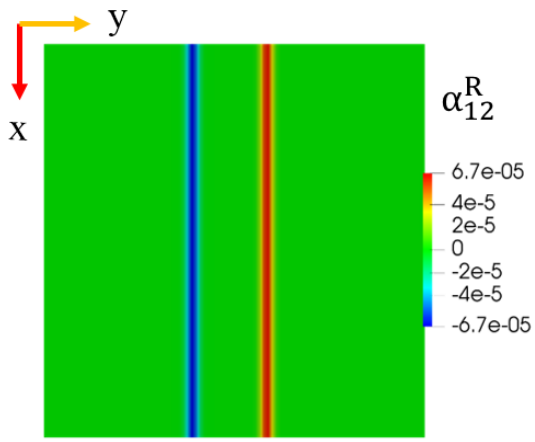

Figure 3.7. The non-zero component of the referential dislocation density tensor plotted in the reference configuration. The dislocation lines pointing in the x (vertical) direction with referential Burgers vector in the y (horizontal) direction, pulled back from the microstructure configuration.

discussed above. The non-zero components of the tensor are α^{D}_{12} and α^{D}_{13}, with the latter component arising due to the elastic lattice rotation of the microstructure Burgers vector. Both components are shown in Fig. 3.8. As clear from the figure, the rotation effects are non-negligible.

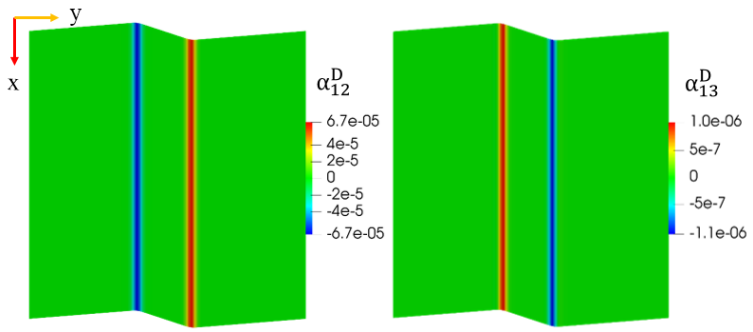

Figure 3.8. Plot of the non-zero components of the deformed dislocation density tensor in the deformed configuration. The microstructure Burgers vector points in the y (horizontal) direction which gets pushed forward to the deformed configuration where it has non-zero y and z component. The α^{D}_{13} component (right) results from the rotation about the x-axis of the microstructure Burgers vector as it is pushed forward to the deformed configuration.

To quantify the elastic lattice rotation further, we calculate that quantity in terms of a rotation vector $\boldsymbol{\theta} = \theta\mathbf{w}$, with θ being the magnitude of rotation about axis $\mathbf{w}$ [113]. The vector $\boldsymbol{\theta}$ is related to the pure rotation part $\mathbf{R}^{\mathrm{e}}$ of the elastic distortion $\mathbf{F}^{\mathrm{e}}$ via

$$\mathbf{R}^{\mathrm{e}}{=}\exp\left(\mathbf{W}\right) {=}\cos\left(\theta\right)\,\mathbf{I} = \sin\left(\theta\right)\;\left(\mathbf{w}\times\right) = \left(1 = \cos\left(\theta\right)\;\right)\mathbf{w}\otimes\mathbf{w}, \tag{3.119}$$

where $\mathbf{W} = \left(\,\boldsymbol{\theta}\times\right)$ is an anti-symmetric second order tensor with $\boldsymbol{\theta}$ as its axial vector, and the polar decomposition $\mathbf{F}^{\mathrm{e}} = \mathbf{R}^{\mathrm{e}}\mathbf{U}^{\mathrm{e}}$ holds with $\mathbf{U}^{\mathrm{e}}$ being the right stretch tensor. In the current case, $\mathbf{F}^{\mathrm{e}}$ is found from $\mathbf{F}^{\mathrm{e}} = \mathbf{F}\mathbf{F}^{\mathrm{p}-1}$, where $\mathbf{F}^{\mathrm{p}}$ is prescribed and $\mathbf{F}$ is found from the solution of the problem. Once the elastic distortion is known the rotation vector can be solved for using (3.119), which is trivial in 2D situations as in the tilt walls example discussed earlier. A line profile of the rotation angle θ is plotted along the y coordinate in Fig. 3.9. We see that the lattice is initially rotated slightly then at the first tilt boundary we get jump in the rotation angle due to the elastic strains from the dislocations and another

jump in the opposite direction at the next tilt boundary, resulting in a rotation angle which is periodic.

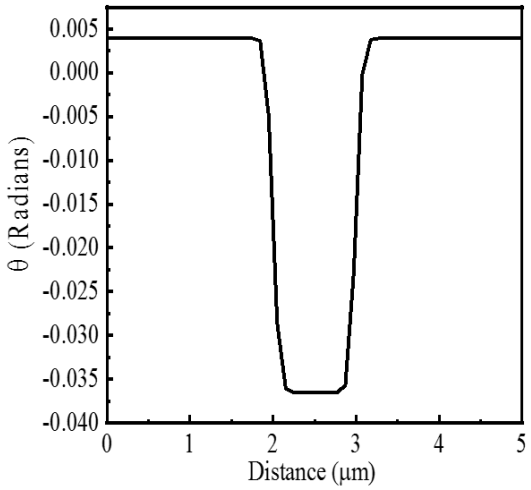

Figure 3.9. A line profile of the angle of rotation of lattice planes about the x-axis caused by the elastic distortion induced by the two tilt boundaries. The line profile is along the y-direction.

Finally, we compare Cauchy and Mandel stresses in Fig. 3.10 to show the similarities and differences in the forces that drive dislocation motion in the deformed and reference configurations. Cauchy stress to the left would be the stress driving dislocation motion in the deformed configuration, while the Mandel stress will do the same in the reference configuration. The magnitudes and distributions of the two stress measures are similar for this test case with the only minor difference being the 22 stress components at the tilt boundary. For larger elastic strains though these measures become increasingly different in the 32 and 22 components which is not shown here. An extra stress component is plotted for the Mandel stress to show that it is nearly symmetric for this magnitude of deformation used in this example.

The simulated configuration of two tilt boundaries with opposite signs was inspired by the general experimental observation of alternating signs of neighboring boundaries, which prevents the buildup of large orientation gradients in the center of most grains in deformed polycrystalline solids [124]. In [128] the angle across the tilt boundaries was on the order of 2

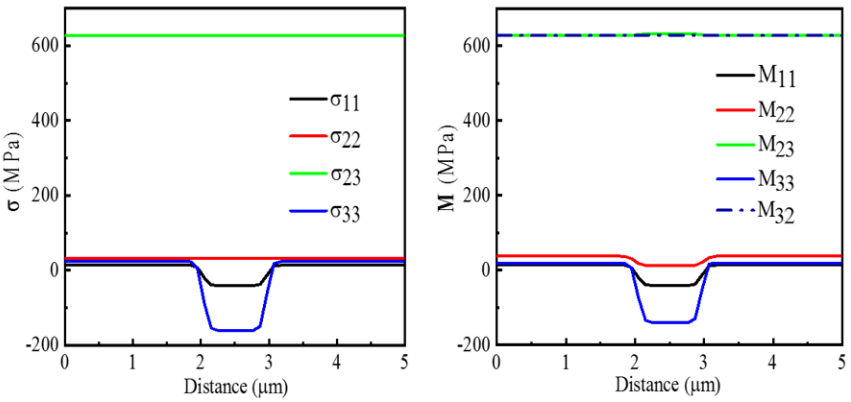

Figure 3.10. Line profile plots of the Cauchy (left) and Mandel (right) stress components through the tilt boundaries in the reference configuration.

to 3°, matching the misorientation level measured at the plastic strain of 4% simulated here. The boundary separation was on the low side compared with the experimental observations at that strain level.

The ability to compute stress fields within and close to dislocation boundaries in deformed crystals will enable direct and absolute comparison with X-ray measurements of lattice stress at mesoscale of the type reported in [120]. The specific stress profile shown in Fig. 3.10 between the two tilt boundaries is due to the piecewise constant distribution of the resulting elastic strain. We note that this solution is also consistent with the 2D solution obtained in [22] for the symmetric tilt boundaries similar to the case presented here. In passing, we further remark that the symmetric tilt boundary simulated above is different from the single tilt boundary found in, say, [9], which shows a strongly decaying stress field.

3.15 Summary and conclusions

A continuum dislocation dynamics formulation suitable for investigating mesoscale crystal plasticity and dislocation patterning at finite deformation has been developed. In this formulation, the key equations consist of slip system level transport equations for vector densities of dislocations, coupled with finite deformation crystal mechanics. The coupling is two-way in the sense that crystal mechanics yields the driving force for dislocation motion while the motion of dislocation provides the plastic distortion required for stress update. The transport equations for both the spatial and referential vector densities of dislocations were derived in the spatial frame and referential frame, respectively. These equations are frame invariant, i.e., having the same form, with the one difference that the transport velocity is the velocity of dislocations relative to the lattice in the referential case, Eq. (3.77), versus the absolute velocity consisting of the same plus the crystal velocity in the spatial form (3.85) of the transport equations. The referential dislocation dynamics problem is summarized in Eq. (3.118), consisting of the stress equilibrium equation, dislocation transport equation, and a mobility law. The latter connects the dislocation velocity with a generalized Peach-Koehler force fixed in the reference configuration terms of Mandel stress, Eq. (3.115).

Several dislocation density tensors were defined, some of which were already used by other authors [1, 34]. The two-point dislocation density tensors $\boldsymbol{\alpha}^{\mathrm{RM}}$ and $\boldsymbol{\alpha}^{\mathrm{DM}}$ were particularly useful in deriving the transport equations for the referential and spatial vector densities, respectively. Our derivation of all dislocation density and flux tensors relied on formulating the compatibility conditions in terms of an additive decomposition of the displacement and velocity gradients. The definitions of the resulting dislocation density tensors are consistent with those obtained from the multiplicative decomposition of the deformation gradient followed in the relevant literature. This makes our derivation similar to that used in the case of infinitesimal deformation, e.g., that by [108] , [41] and others, while fully accounting for the kinematics of finite deformation. In section (3.6), some aspects of the equivalence of the work reported in [70] were introduced at the level of transport equations for the tensor density fields, but differ in the results obtained for the transport of the vector densities.

Our development of the driving force for dislocations was based on thermodynamics. With a hypothesized free energy density that has both elastic and plastic (defect) contributions, Eq. (3.92), it was possible to reach the conventional hyperplastic stress-strain relationship for finite deformation, (3.107), and a generalized expression for the Peach-Koehler force, (3.115). The counterparts of such relationships for a dislocation tensor-based theory can be found in [4]. Two important observations are worth mentioning with regard to the generalized Peach-Koehler force expression obtained here. The first is that the elastic part of the Peach-Koehler force in the reference configuration is cast in terms of Mandel stress and the form is similar to that in the literature in terms of Cauchy stress, e.g., in [9]. The second is that any additional energy associated with the presence of dislocations in the crystal and which evolves with the evolution of dislocations, will exert resistive force to dislocation motion via the term $\boldsymbol{\omega}^{(l)}$ in Eq. (3.115) for the driving force for the dislocation motion. This term, which depends on the gradient of the plastic (defect) part of the free energy with respect to the vector density of dislocation, offers the possibility to include, say, core energy of dislocation lines into the driving force for dislocation motion and couple dislocation motion with other types of defects in a more expanded theory.

The referential form of the dislocation transport equations was developed with a total Lagrange numerical treatment in mind. Initial development of that scheme was already

carried out in solving the static test problems presented here, which were included to make a preliminary case of investigating the effects of lattice rotation in the context of finite deformation dislocation mechanics. The complete development, including a coupled solution of the continuum dislocation dynamics equations will be the subject of a more detailed future publication.

3.A Transport equations for the dislocation density tensors

3.A.1 Rederiving Gurtin's transport equations for the microstructure dislocation density tensor

In this appendix, we show that the transport equation (3.71) for the two-point tensor $\boldsymbol{\alpha}^{\mathrm{DM}}$ is consistent with the derivation of the transport equations for the microstructure dislocation density tensor given in [70], which, in our notation, reads

$$\dot{\boldsymbol{\alpha}}^{\mathrm{M}} - \mathbf{L}^{\mathrm{p}}\boldsymbol{\alpha}^{\mathrm{M}} - \boldsymbol{\alpha}^{\mathrm{M}}\mathbf{L}^{\mathrm{pT}} = \mathbf{F}^{\mathrm{p}}\,\mathrm{Curl}_{\mathrm{L^p}}\left(\mathbf{L}^{\mathrm{p}}\mathbf{F}^{\mathrm{p}}\right) \tag{3.120}$$

with $\mathrm{Curl}_{\mathrm{L^p}}\left(\mathbf{L}^{\mathrm{p}}\mathbf{F}^{\mathrm{p}}\right)$ being the Curl of $\mathbf{L}^{p}\mathbf{F}^{p}$ holding $\mathbf{F}^{p}$ fixed. We start by looking at the local transformation rule for $\boldsymbol{\alpha}^{\mathrm{M}}$ and the two-point tensor $\boldsymbol{\alpha}^{\mathrm{RM}}$, which is $\boldsymbol{\alpha}^{\mathrm{M}} = \frac{1}{\mathrm{J^p}}\mathbf{F}^{p}\boldsymbol{\alpha}^{\mathrm{RM}}$. Using relationship, we can then related the time derivatives of $\boldsymbol{\alpha}^{\mathrm{M}}$ and $\boldsymbol{\alpha}^{\mathrm{RM}}$ as follows:

$$\begin{aligned}
\dot{\boldsymbol{\alpha}}^{\mathrm{M}} &= \dot{\overline{\left(\frac{1}{\mathrm{J^p}}\mathbf{F}^{\mathrm{p}}\right)}}\boldsymbol{\alpha}^{\mathrm{RM}} + \frac{1}{\mathrm{J^p}}\mathbf{F}^{\mathrm{p}}\dot{\boldsymbol{\alpha}}^{\mathrm{RM}} \\
&= \left(\frac{\dot{1}}{\mathrm{J^p}}\mathbf{F}^{\mathrm{p}} + \frac{1}{\mathrm{J^p}}\mathbf{F}^{\mathrm{p}}\right)\boldsymbol{\alpha}^{\mathrm{RM}} + \frac{1}{\mathrm{J^p}}\mathbf{F}^{\mathrm{p}}\dot{\boldsymbol{\alpha}}^{\mathrm{RM}} \\
&= \left(-\frac{1}{\mathrm{J^{p2}}}\dot{J^p}\mathbf{F}^{\mathrm{p}} + \frac{1}{\mathrm{J^p}}\mathbf{F}^{\mathrm{p}}\right)\boldsymbol{\alpha}^{\mathrm{RM}} + \frac{1}{\mathrm{J^p}}\mathbf{F}^{\mathrm{p}}\dot{\boldsymbol{\alpha}}^{\mathrm{RM}}.
\end{aligned} \tag{3.121}$$

Using $\dot{\mathrm{J^p}} = \mathrm{J^p tr}(\boldsymbol{L}^{\mathrm{p}})$, the above simplifies to: $\dot{\boldsymbol{\alpha}}^{\mathrm{M}} = -\,\mathrm{tr}\left(\mathbf{L}^{\mathrm{p}}\right)\frac{1}{\mathrm{J^p}}\mathbf{F}^{\mathrm{p}}\boldsymbol{\alpha}^{\mathrm{RM}} + \mathbf{L}^{\mathrm{p}}\frac{1}{\mathrm{J^p}}\mathbf{F}^{\mathrm{p}}\boldsymbol{\alpha}^{\mathrm{RM}} + \frac{1}{\mathrm{Jp}}\mathrm{F^p}\dot{\boldsymbol{\alpha}}^{\mathrm{RM}}$. Using the transformation relation between $\boldsymbol{\alpha}^{\mathrm{RM}}$ and $\boldsymbol{\alpha}^{\mathrm{M}}$, we can rewrite the first two terms on the right-hand side of the last expression to get,

$$\dot{\boldsymbol{\alpha}}^{\mathrm{M}} = -\,\mathrm{tr}\left(\mathrm{L^p}\right)\boldsymbol{\alpha}^{\mathrm{M}} + \mathbf{L}^{\mathrm{p}}\boldsymbol{\alpha}^{\mathrm{M}} + \frac{1}{\mathrm{J^p}}\mathbf{F}^{\mathrm{p}}\dot{\boldsymbol{\alpha}}^{\mathrm{RM}}. \tag{3.122}$$

Or for glide only motion, $\mathrm{J}^{\mathrm{p}} = 1$ and $\mathrm{tr}(\boldsymbol{L}^{\mathrm{p}}) = 0$. Hence,

$$\dot{\boldsymbol{\alpha}}^{\mathrm{M}} - \mathbf{L}^{\mathrm{p}}\boldsymbol{\alpha}^{\mathrm{M}} = \mathbf{F}^{\mathrm{p}}\,\mathrm{Curl}(\boldsymbol{\phi}), \tag{3.123}$$

where we have used the compatibility condition (3.71) for $\boldsymbol{\alpha}^{\mathrm{RM}}$. Now, we can say that equation (3.123) ensures the compatibility of the total velocity field. We realize from (3.57) , (3.23) and (3.18) that

$$\boldsymbol{\phi} = \dot{\boldsymbol{\beta}}^{\mathrm{p}} = \dot{\mathbf{F}}^{\mathrm{p}} = \mathbf{L}^{\mathrm{p}}\mathbf{F}^{\mathrm{p}}, \tag{3.124}$$

and so we write (3.123) in the form,

$$\dot{\boldsymbol{\alpha}}^{\mathrm{M}} - \mathbf{L}^{\mathrm{p}}\boldsymbol{\alpha}^{\mathrm{M}} = \mathbf{F}^{\mathbf{P}}\,\mathrm{Curl}\,(\mathbf{L}^{\mathrm{p}}\mathbf{F}^{\mathrm{p}}) \tag{3.125}$$

Using the same notation to expand the product term in the Curl expression as used by Gurtin we get: $\dot{\boldsymbol{\alpha}}^{\mathrm{M}} - \mathbf{L}^{\mathrm{p}}\boldsymbol{\alpha}^{\mathrm{M}} = \mathbf{F}^{\mathrm{p}}\left(\mathrm{Curl}\,(\mathbf{F}^{\mathrm{p}})\,\mathbf{L}^{\mathrm{pT}} + \mathrm{Curl}_{\mathrm{L}^{\mathrm{p}}}\,(\mathbf{L}^{\mathrm{p}}\mathbf{F}^{\mathrm{p}})\right)$. Using the definition of the microstructure dislocation density tensor (3.35) for glide only motion we can write,

$$\dot{\boldsymbol{\alpha}}^{\mathrm{M}} - \mathbf{L}^{\mathrm{p}}\boldsymbol{\alpha}^{\mathrm{M}} - \boldsymbol{\alpha}^{\mathrm{M}}\mathbf{L}^{\mathrm{pT}} = \mathbf{F}^{\mathrm{p}}\,\mathrm{Curl}_{\mathrm{L}^{\mathrm{p}}}\,(\mathbf{L}^{\mathrm{p}}\mathbf{F}^{\mathrm{p}}) \tag{3.126}$$

which is (3.120) [70]. Starting with (3.73), a similar procedure will lead to this form of the transport equation for the microstructure dislocation density tensor.

3.A.2 Transport equations for the referential dislocation density tensor

In this appendix, we derive the transport relations for the referential dislocation density tensor, $\boldsymbol{\alpha}^{\mathrm{R}}$, starting from the transformation relations between $\boldsymbol{\alpha}^{\mathrm{RM}}$ and $\boldsymbol{\alpha}^{\mathrm{R}}$. This transformation has the form: $\boldsymbol{\alpha}^{\mathrm{RM}} = \boldsymbol{\alpha}^{\mathrm{R}}\mathbf{F}^{\mathrm{pT}}$, which by time differentiation yields: $\dot{\boldsymbol{\alpha}}^{\mathrm{RM}} = \dot{\boldsymbol{\alpha}}^{\mathrm{R}}\mathbf{F}^{\mathrm{pT}} + \boldsymbol{\alpha}^{\mathrm{R}}\dot{\mathbf{F}}^{\mathrm{pT}}$. By further using $\dot{\mathbf{F}}^{p} = \mathbf{L}^{p}\mathbf{F}^{p}, \dot{\mathbf{F}}^{pT} = \mathbf{F}^{pT}\mathbf{L}^{pT}$, the last expression can be rewritten in the form:$\dot{\boldsymbol{\alpha}}^{\mathrm{RM}} = \dot{\boldsymbol{\alpha}}^{\mathrm{R}}\mathbf{F}^{\mathrm{pT}} + \boldsymbol{\alpha}^{\mathrm{R}}\mathbf{F}^{\mathrm{pT}}\mathbf{L}^{\mathrm{pT}} = \dot{\boldsymbol{\alpha}}^{\mathrm{R}}\mathbf{F}^{\mathrm{pT}} + \boldsymbol{\alpha}^{\mathrm{RM}}\mathbf{L}^{\mathrm{pT}}$, which finally leads to

$$\dot{\boldsymbol{\alpha}}^{\mathrm{RM}} - \boldsymbol{\alpha}^{\mathrm{RM}}\mathbf{L}^{\mathrm{pT}} = \dot{\alpha}^{\mathrm{R}}\mathbf{F}^{\mathrm{pT}}. \tag{3.127}$$

Using the compatibility condition (3.71) and expanding the flux term like in (3.124) gives,

$$\dot{\boldsymbol{\alpha}}^{\mathrm{R}} = \mathrm{Curl}_{\mathrm{L^p}} \left(\mathbf{L}^{\mathrm{p}}\mathbf{F}^{\mathrm{p}}\right) \mathbf{F}^{\mathrm{p-T}}, \tag{3.128}$$

which is the transport equations for the referential dislocation density tensor.

3.A.3 Transport equations for the spatial dislocation density tensor

In this appendix, we derive the transport relations for the spatial dislocation density tensor, $\boldsymbol{\alpha}^{\mathrm{D}}$. The starting point is the transformation relation between the dislocation density tensor in the deformed configuration and the two-point tensor $\boldsymbol{\alpha}^{\mathrm{DM}}$, which has the form: $\boldsymbol{\alpha}^{\mathrm{DM}} = \boldsymbol{\alpha}^{\mathrm{D}}\mathbf{F}^{\mathrm{e-T}}$. By further taking the material time derivative, we obtain $\dot{\boldsymbol{\alpha}}^{\mathrm{DM}} = \dot{\boldsymbol{\alpha}}^{\mathrm{D}}\mathbf{F}^{\mathrm{e-T}} + \boldsymbol{\alpha}^{\mathrm{D}}\dot{\mathbf{F}}^{\mathrm{e-T}} = \dot{\boldsymbol{\alpha}}^{\mathrm{D}}\mathbf{F}^{\mathbf{e-T}} - \boldsymbol{\alpha}^{\mathrm{D}}\mathbf{L}^{\mathrm{eT}}\mathbf{F}^{\mathbf{e-T}}$, which simplifies to:

$$\dot{\boldsymbol{\alpha}}^{\mathrm{D}} - \boldsymbol{\alpha}^{\mathrm{D}}\mathbf{L}^{\mathrm{eT}} = \dot{\boldsymbol{\alpha}}^{\mathrm{DM}}\mathbf{F}^{\mathrm{eT}} \tag{3.129}$$

Inserting the compatibility condition (3.73) and solving for $\boldsymbol{\alpha}^{\mathrm{D}}$ gives,

$$\dot{\boldsymbol{\alpha}}^{\mathrm{D}} + \mathrm{tr}(\mathbf{L})\boldsymbol{\alpha}^{\mathrm{D}} - \mathbf{L}\boldsymbol{\alpha}^{\mathrm{D}} - \boldsymbol{\alpha}^{\mathrm{D}}\mathbf{L}^{\mathrm{eT}} = \mathrm{curl}\left(\boldsymbol{\phi}\mathbf{F}^{-1}\right)\mathbf{F}^{\mathrm{eT}} \tag{3.130}$$

Expanding the dislocation current term,

$$\begin{aligned}\mathrm{curl}\left(\boldsymbol{\phi}\mathbf{F}^{\mathbf{-1}}\right)\mathbf{F}^{\mathrm{eT}} &= \mathrm{curl}\left(\mathbf{L}^{\mathrm{p}}\mathbf{F}^{\mathrm{e-1}}\right)\mathbf{F}^{\mathrm{eT}} \\ &= \mathrm{curl}\left(\mathbf{F}^{\mathrm{e-1}}\right)\mathbf{L}^{\mathrm{pT}}\mathbf{F}^{\mathrm{eT}} + \mathrm{curl}_{\mathrm{L^p}}\left(\mathbf{L}^{\mathrm{p}}\mathbf{F}^{\mathrm{e-1}}\right)\mathbf{F}^{\mathrm{eT}}\end{aligned}$$

We can also write,

$$\begin{aligned}\mathrm{curl}\left(\mathbf{F}^{\mathrm{e-1}}\right)\mathbf{L}^{\mathrm{pT}}\mathbf{F}^{\mathrm{eT}} &= \mathrm{curl}\left(\mathbf{F}^{\mathrm{e-1}}\right)\mathbf{F}^{\mathrm{eT}}\mathbf{F}^{\mathrm{e-T}}\mathbf{L}^{\mathrm{pT}}\mathbf{F}^{\mathrm{eT}} \\ &= \boldsymbol{\alpha}^{\mathrm{D}}\mathbf{F}^{\mathrm{e-T}}\mathbf{L}^{\mathrm{pT}}\mathbf{F}^{\mathrm{eT}} = \boldsymbol{\alpha}^{\mathrm{D}}\left(\mathbf{L}^{\mathrm{T}} - \mathbf{L}^{\mathrm{eT}}\right)\end{aligned}$$

which leads to,

$$\mathrm{curl}\left(\boldsymbol{\phi}\mathbf{F}^{-1}\right)\mathbf{F}^{\mathrm{eT}} = \boldsymbol{\alpha}^{\mathrm{D}}\left(\mathbf{L}^{\mathrm{T}} - \mathbf{L}^{\mathrm{eT}}\right) + \mathrm{curl}_{\mathrm{L^p}}\left(\mathbf{L}^{\mathrm{p}}\mathbf{F}^{\mathrm{e-1}}\right)\mathbf{F}^{\mathrm{eT}} \tag{3.131}$$

Substituting this expansion into (3.130) and rearranging terms gives the transport equations for the dislocation density tensor in the deformed configuration,

$$\dot{\boldsymbol{\alpha}}^{\mathrm{D}} + \mathrm{tr}(\mathbf{L})\boldsymbol{\alpha}^{\mathrm{D}} - \mathbf{L}\boldsymbol{\alpha}^{\mathrm{D}} - \boldsymbol{\alpha}^{\mathrm{D}}\mathbf{L}^{\mathrm{T}} = \mathrm{curl}_{\mathrm{L}}\left(\mathbf{L}^{\mathrm{p}}\mathbf{F}^{\mathrm{e}-1}\right)\mathbf{F}^{\mathrm{eT}} \tag{3.132}$$

In this equation, the left-hand side is Oldroyd derivative [148]. The same expression can be derived by looking at the transformation relationship between the referential dislocation density tensor and the deformed tensor by taking its material time derivative and plugging in (3.128) for the $\boldsymbol{\alpha}^{\mathrm{R}}$. Using the relationships between the dislocation currents in (3.54) we obtain a relationship for the curl terms as: $\mathrm{Curl}_{\mathrm{L}^{\mathrm{p}}}\left(\mathbf{L}^{\mathrm{p}}\mathbf{F}^{\mathrm{p}}\right) = \mathrm{J}\mathrm{F}^{-1}\,\mathrm{curl}_{\mathrm{L}^{\mathrm{p}}}\left(\mathbf{L}^{\mathrm{p}}\mathbf{F}^{\mathrm{e}-1}\right)$, which is needed to show that (3.132) is consistent with (3.128).

3.B Simplifying power of deformation in reference configuration

In this appendix, we explain the details of reaching equation (3.90) starting from (3.89). Expanding the first material time derivative term and further using $\dot{\mathbf{F}}^{p} = \boldsymbol{\phi}$, we reach $\overline{\left(\mathbf{F}^{pT}\mathbf{E}^{\mathrm{e}}\mathbf{F}^{p}\right)} = \boldsymbol{\phi}^{\mathrm{T}}\mathbf{E}^{\mathrm{e}}\mathbf{F}^{p} + \mathbf{F}^{p\ \mathrm{T}}\mathbf{E}^{\mathrm{e}}\boldsymbol{\phi} + \mathbf{F}^{\mathrm{pT}}\dot{\mathbf{E}}^{\mathrm{e}}\mathbf{F}^{p}$. The first two terms in the last expression are both related to the motion of dislocations. They are segregated in the form:

$$\mathbf{Q}^{\mathrm{p}} \equiv \boldsymbol{\phi}^{\mathrm{T}}\mathbf{E}^{\mathrm{e}}\mathbf{F}^{\mathrm{p}} + \mathbf{F}^{\mathrm{pT}}\mathbf{E}^{\mathrm{e}}\boldsymbol{\phi} \tag{3.133}$$

The last term is related to the rate of elastic strain. Looking at the second term, $\mathbf{S} : \dot{\mathbf{E}}^{\mathrm{p}}$ in equation (3.89) and expanding $\dot{\mathbf{E}}^{p}$ we get: $\dot{\mathbf{E}}^{p} = \dot{\mathbf{C}}^{\mathrm{p}} = \mathbf{1}/2\left(\mathbf{F}^{\mathrm{pT}}\mathbf{L}^{\mathrm{p}}\mathbf{F}^{\mathrm{p}} + \mathbf{F}^{\mathrm{pT}}\mathbf{L}^{\mathrm{p}}\mathbf{F}^{\mathrm{p}}\right)$. Since this term will be contracted with a symmetric tensor we can write: $\mathbf{S} : \dot{\mathbf{E}}^{\mathrm{p}} = \mathbf{S} : \mathbf{1}/\mathbf{2}\left(\mathbf{F}^{\mathrm{pT}}\mathbf{L}^{\mathrm{p}}\mathbf{F}^{\mathrm{p}} + \mathbf{F}^{\mathrm{pT}}\mathbf{L}^{\mathrm{p}}\mathbf{F}^{\mathrm{p}}\right) = \mathbf{S} : \left(\mathbf{F}^{\mathrm{pT}}\mathbf{L}^{\mathrm{p}}\mathbf{F}^{\mathrm{p}}\right)$. We also notice that, since $\dot{\mathbf{F}}^{p} = \mathbf{L}^{p}\mathbf{F}^{p}$, we can replace the last term with $\mathbf{S} : \left(\mathbf{F}^{\mathrm{pT}}\dot{\mathbf{F}}^{p}\right)$, and by the definition of $\boldsymbol{\beta}^{p}$, we have $\dot{\mathbf{F}}^{p} = \dot{\boldsymbol{\beta}}^{p} = \boldsymbol{\phi}$. Then $\mathbf{S} : \dot{\mathbf{E}}^{\mathrm{p}} = \mathbf{S} : \left(\mathbf{F}^{\mathrm{pT}}\boldsymbol{\phi}\right) = \mathbf{S} : \left(\mathbf{F}^{\mathrm{pT}}\mathbf{F}^{\mathrm{p}}\mathbf{F}^{\mathrm{p}-1}\boldsymbol{\phi}\right) = \mathbf{S} : (\mathbf{C}^{\mathrm{p}}\mathbf{F}^{\mathrm{p}-1}\boldsymbol{\phi})$. Using properties of the double inner product we reach

$$\mathbf{S} : \dot{\mathbf{E}}^{\mathrm{p}} = \left(\mathbf{C}^{\mathrm{pT}}\mathbf{S}\right) : \left(\mathbf{F}^{\mathrm{p}-1}\boldsymbol{\phi}\right) = (\mathbf{C}^{\mathrm{p}}\mathbf{S}) : \left(\mathbf{F}^{\mathrm{p}-1}\boldsymbol{\phi}\right). \tag{3.134}$$

Now we will work on the $\boldsymbol{Q}^p$ term.

$$\mathbf{S} : \mathbf{Q}^{\mathrm{p}} = \mathbf{S} : \left(\boldsymbol{\phi}^{\mathrm{T}} \mathbf{E}^{\mathrm{e}} \mathbf{F}^{\mathrm{p}}\right) + \mathbf{S} : \left(\mathbf{F}^{\mathrm{p}\mathrm{T}} \mathbf{E}^{\mathrm{e}} \boldsymbol{\phi}\right). \tag{3.135}$$

For the first term we use the double inner product property (3.13), $\mathbf{A} : \mathbf{B} = \mathbf{A}^{\mathrm{T}} : \mathbf{B}^{\mathrm{T}}$, which yields: $\mathbf{S} : \left(\boldsymbol{\phi}^{\mathrm{T}} \mathbf{E}^{\mathrm{e}} \mathbf{F}^{\mathrm{p}}\right) = \mathbf{S}^{\mathrm{T}} : \left[\left(\mathbf{E}^{\mathrm{e}} \mathbf{F}^{\mathrm{p}}\right)^{\mathrm{T}} \boldsymbol{\phi}\right] = \mathbf{S} : \left[\left(\mathbf{E}^{\mathrm{e}} \mathbf{F}^{\mathrm{p}}\right)^{\mathrm{T}} \boldsymbol{\phi}\right]$. Then using (3.14) leads to $\mathbf{S} : \left(\boldsymbol{\phi}^{\mathrm{T}} \mathbf{E}^{\mathrm{e}} \mathbf{F}^{\mathrm{p}}\right) = \left[\mathbf{E}^{\mathrm{e}} \mathbf{F}^{\mathrm{p}} \mathbf{S}\right] : \boldsymbol{\phi}$. Applying the same inner product property (3.14) to the second term in (3.135) gives$\mathbf{S} : \left(\mathbf{F}^{\mathrm{p}\mathrm{T}} \mathbf{E}^{\mathrm{e}} \boldsymbol{\phi}\right) = \left[\mathbf{E}^{\mathrm{e}\mathrm{T}} \mathbf{F}^{\mathrm{p}} \mathbf{S}\right] : \boldsymbol{\phi} = \left[\mathbf{E}^{\mathrm{e}} \mathbf{F}^{\mathrm{p}} \mathbf{S}\right] : \boldsymbol{\phi}$, and so we reach

$$\mathbf{S} : \mathbf{Q}^{\mathrm{p}} = 2 \left[\mathbf{E}^{\mathrm{e}} \mathbf{F}^{\mathrm{p}} \mathbf{S}\right] : \boldsymbol{\phi}. \tag{3.136}$$

We choose to write (3.136) in the form:$2 \left[\mathbf{E}^{\mathrm{e}} \mathbf{F}^{\mathrm{p}} \mathbf{S}\right] : \boldsymbol{\phi} = 2 \left[\mathbf{E}^{\mathrm{e}} \mathbf{F}^{\mathrm{p}} \mathbf{S}\right] : \mathbf{F}^{\mathrm{p}} \left(\mathbf{F}^{\mathrm{p}-1} \boldsymbol{\phi}\right) = 2 \left[\mathbf{F}^{\mathrm{p}\mathrm{T}} \mathbf{E}^{\mathrm{e}} \mathbf{F}^{\mathrm{p}} \mathbf{S}\right] : \left(\mathbf{F}^{\mathrm{p}-1} \boldsymbol{\phi}\right) = 2 \left[\mathbf{E}_{\mathrm{R}}^{\mathrm{e}} \mathbf{S}\right] : \left(\mathbf{F}^{\mathrm{p}-1} \boldsymbol{\phi}\right)$, so that the power of deformation in the reference configuration becomes: $\mathbf{S} : \dot{\mathbf{E}} = \left\{\left(2\mathbf{E}_{\mathrm{R}}^{\mathrm{e}} + \mathbf{C}^{\mathrm{p}}\right) \mathbf{S}\right\} : \left(\mathbf{F}^{\mathrm{p}-1} \boldsymbol{\phi}\right) + \mathbf{S} : \left(\mathbf{F}^{\mathrm{p}\mathrm{T}} \mathbf{E}^{\mathrm{e}} \mathbf{F}^{\mathrm{p}}\right)$. We further simplify the first term as follows,

$$\begin{aligned} \left(2\mathbf{E}_{\mathrm{R}}^{\mathrm{e}} + \mathbf{C}^{\mathrm{p}}\right) \mathbf{S} &= 2 \left(\mathbf{E} - \mathbf{E}^{\mathrm{p}}\right) \mathbf{S} + \mathbf{C}^{\mathrm{p}} \mathbf{S} \\ &= 2\mathbf{E}\mathbf{S} - 2 \left(\frac{1}{2} \left[\mathbf{C}^{\mathrm{p}} - \mathbf{I}\right]\right) \mathbf{S} + \mathbf{C}^{\mathrm{p}} \mathbf{S} \\ &= 2\mathbf{E}\mathbf{S} + \mathbf{S} = (\mathbf{2E} + \mathbf{I})\mathbf{S} = \mathbf{C}\mathbf{S} = \mathbf{M}, \end{aligned} \tag{3.137}$$

with $\mathbf{M} = \mathbf{C}\mathbf{S}$ being the referential Mandel stress. This completes the rewriting of equation (3.89) into (3.90).

3.C Constitutive analysis in the deformed configuration

The statement of global free energy imbalance expressed in the deformed configuration, ignoring entropic effects, reads

$$\int \left(\rho_D \dot{\Psi}_D - \sigma : \mathbf{L}\right) \mathrm{dv}_{\mathrm{D}} \leq 0 \tag{3.138}$$

where Ψ_D is the specific free energy in the deformed configuration and ρ_D is the mass density. We use the fact that $\dot{\mathbf{F}}^p = \dot{\boldsymbol{\beta}}^p = \boldsymbol{\phi}$, (3.16), (3.18) and (3.62) to write the velocity gradient as $\mathbf{L} = \mathbf{L}^{\mathrm{e}} + \mathbf{F}^{\mathrm{e}} \sum_l \mathbf{b}_{\mathrm{M}}^{(l)} \otimes \left(\mathbf{v}_{\mathrm{D}}^{(l)} \times \boldsymbol{\rho}_{\mathrm{D}}^{(l)}\right)$. From, $\mathbf{F}^{\mathrm{e}}\mathbf{b}_{\mathbf{M}}^{(l)} = \mathbf{b}_{\mathrm{D}}^{(l)}$, and (3.17)

$$\mathbf{L} = \dot{\mathbf{F}}^{\mathrm{e}}\mathbf{F}^{\mathrm{e}-1} + \sum \mathbf{b}_{\mathrm{D}}^{(l)} \otimes \left(\mathbf{v}_{\mathrm{D}}^{(l)} \times \boldsymbol{\rho}_{\mathrm{D}}^{(l)}\right). \tag{3.139}$$

Then using (3.14), the free energy imbalance becomes,

$$\int \left(\rho_D \dot{\Psi}_D - \left(\boldsymbol{\sigma}\mathbf{F}^{\mathrm{e}-\mathrm{T}}\right) : \dot{\mathbf{F}}^{\mathrm{e}} - \boldsymbol{\sigma} : \left(\sum_l \mathbf{b}_{\mathrm{D}}^{(l)} \otimes \left(\mathbf{v}_{\mathrm{D}}^{(l)} \times \boldsymbol{\rho}_{\mathrm{D}}^{(l)}\right)\right)\right) \mathrm{dv}_{\mathrm{D}} \leq 0 \tag{3.140}$$

Let us rewrite the specific free energy in the form:

$$\Psi_{\mathrm{D}} = \widehat{\Psi}_{\mathrm{D}}^{\mathrm{e}}\left(\mathbf{F}^{\mathrm{e}}\right) + \widehat{\Psi}_{\mathrm{D}}^{\mathrm{p}}\left(\boldsymbol{\rho}_{\mathrm{R}}^{(l)}\right) \tag{3.141}$$

Taking the material time derivative of the elastic term gives: $\dot{\Psi}_D^{\mathrm{e}} = \frac{\partial \widehat{\psi}_D^{\mathrm{e}}}{\partial \mathbf{F}^{\mathrm{e}}} : \dot{\mathbf{F}}^{\mathrm{e}}$. Plugging this into the free energy imbalance yields,

$$\begin{aligned} \int \left(\left(\rho_D \frac{\partial \widehat{\psi}_{\mathrm{D}}^{\mathrm{e}}}{\partial \mathbf{F}^{\mathrm{e}}} - \boldsymbol{\sigma}\mathbf{F}^{\mathrm{e}-\mathrm{T}}\right) : \dot{\mathbf{F}}^{\mathrm{e}} + \rho_D \dot{\psi}_{\mathrm{D}}^{\mathrm{p}} - \boldsymbol{\sigma} : \left(\sum_l \mathbf{b}_{\mathrm{D}}^{(l)} \otimes \left(\mathbf{v}_{\mathrm{D}}^{(l)} \times \boldsymbol{\rho}_{\mathrm{D}}^{(l)}\right)\right)\right) \mathrm{dv}_{\mathrm{D}} \\ \leq 0 \end{aligned} \tag{3.142}$$

Using the transformation relation between the Cauchy stress and the PK1 stress in the microstructure configuration,$\boldsymbol{\sigma}\mathbf{F}^{\mathrm{e}-\mathrm{T}} = \mathrm{J}^{\mathrm{e}-1}\mathbf{P}^{\mathrm{e}}$, and the fact that there is no dissipation for the elastic terms we arrive at $\mathbf{P}^{\mathrm{e}} \equiv \rho_{\mathrm{M}} \frac{\partial \widehat{\Psi}_{\mathrm{D}}^{\mathrm{e}}}{\partial \mathbf{F}^{\mathrm{e}}}$ just like in (3.106). We now focus on the plastic terms. We start by noticing a relationship between the material time derivative and the Oldroyd derivative. From $\boldsymbol{\rho}_{\mathrm{R}} = \mathrm{J}\mathbf{F}^{-1}\boldsymbol{\rho}_{\mathrm{D}}$, and taking the material time derivative of both sides (3.42) we can write,

$$\dot{\boldsymbol{\rho}}_{\mathrm{R}} = \mathrm{J}\mathbf{F}^{-1}\left(\dot{\boldsymbol{\rho}}_{\mathrm{D}} + (\mathrm{tr}(\mathbf{L})\mathbf{I} - \mathbf{L})\boldsymbol{\rho}_{\mathrm{D}}\right). \tag{3.143}$$

We note that the term following $\mathrm{J}\mathbf{F}^{-1}$ in the above expression is the Oldroyd derivative of the spatial vector density, which is a frame indifferent time derivative. Recalling in (3.141)

that we have the constitutive form: $\Psi_{\mathrm{D}}^{\mathrm{p}} = \widehat{\Psi}_{\mathrm{D}}^{\mathrm{p}}\left(\boldsymbol{\rho}_{\mathrm{R}}^{(l)}\right)$, which is a frame indifferent constitutive function due to its dependence on the referential dislocation density. We now show that this is equivalent a form in which $\widehat{\Psi}_{\mathrm{D}}^{\mathrm{p}}$ depends on the spatial dislocation density, $\boldsymbol{\rho}_{\mathrm{D}}^{(l)}$. Taking the material time derivative of $\Psi_{\mathrm{D}}^{\mathrm{p}} = \widehat{\Psi}_{\mathrm{D}}^{\mathrm{p}}\left(\boldsymbol{\rho}_{\mathrm{R}}^{(l)}\right)$, and using (3.143) gives,

$$\begin{aligned}\dot{\Psi}_{\mathrm{D}}^{\mathrm{p}} &= \sum_{l} \frac{\partial \widehat{\Psi}_{\mathrm{D}}^{\mathrm{p}}}{\partial \boldsymbol{\rho}_{R}^{(l)}} \cdot \dot{\boldsymbol{\rho}}_{\mathrm{R}}^{(l)} \\ &= \sum_{l} \frac{\partial \widehat{\Psi}_{\mathrm{D}}^{\mathrm{p}}}{\partial \boldsymbol{\rho}_{R}^{(l)}} \cdot \left[\mathrm{J}\mathbf{F}^{-1}\left(\dot{\boldsymbol{\rho}}_{\mathrm{D}}^{(\mathrm{l})} + (\mathrm{tr}(\mathbf{L})\mathbf{I} - \mathbf{L})\boldsymbol{\rho}_{\mathrm{D}}^{(\mathrm{l})}\right)\right].\end{aligned} \tag{3.144}$$

From $\boldsymbol{\rho}_{\mathrm{R}}^{(l)} = \mathrm{J}\mathbf{F}^{-1}\boldsymbol{\rho}_{\mathrm{D}}^{(l)}$, we have that, $\frac{\partial \boldsymbol{\rho}_{R}^{(l)}}{\partial \boldsymbol{\rho}_{\mathrm{D}}^{(l)}} = \mathrm{J}\mathbf{F}^{-\mathbf{1}}$. Plugging this into the last expression gives,

$$\begin{aligned}\dot{\Psi}_{\mathrm{D}}^{\mathrm{p}} &= \sum_{l} \frac{\partial \widehat{\Psi}_{\mathrm{D}}^{\mathrm{p}}}{\partial \boldsymbol{\rho}_{R}^{(l)}} \frac{\partial \boldsymbol{\rho}_{R}^{(l)}}{\partial \boldsymbol{\rho}_{\mathrm{D}}^{(l)}} \left(\dot{\boldsymbol{\rho}}_{\mathrm{D}}^{(\mathrm{l})} + (\mathrm{tr}(\mathbf{L})\mathbf{I} - \mathbf{L})\boldsymbol{\rho}_{\mathrm{D}}^{(1)}\right) \\ &= \sum_{l} \frac{\partial \widehat{\Psi}_{\mathrm{D}}^{\mathrm{p}}}{\partial \boldsymbol{\rho}_{\mathrm{D}}^{(l)}} \left(\dot{\boldsymbol{\rho}}_{\mathrm{D}}^{(1)} + (\mathrm{tr}(\mathbf{L})\mathbf{I} - \mathbf{L})\boldsymbol{\rho}_{\mathrm{D}}^{(1)}\right)\end{aligned} \tag{3.145}$$

By using the transport relationship (3.106) without the network term into the last equation, we reach

$$\dot{\Psi}_{\mathrm{D}}^{\mathrm{p}} = \sum_{l} \frac{\partial \widehat{\Psi}_{\mathrm{D}}^{\mathrm{p}}}{\partial \boldsymbol{\rho}_{\mathrm{D}}^{(l)}} \mathrm{curl}\left(\mathbf{v}_{\mathrm{D}}^{(l)} \times \boldsymbol{\rho}_{\mathrm{D}}^{(l)}\right). \tag{3.146}$$

Both (3.145) and (3.146) suggest that the constitutive function $\widehat{\Psi}_{\mathrm{D}}^{\mathrm{p}}$ should depend on the spatial dislocation density, $\boldsymbol{\rho}_{\mathrm{D}}^{(l)}$. That is, $\Psi_{\mathrm{D}}^{\mathrm{p}} = \widehat{\Psi}_{\mathrm{D}}^{\mathrm{p}}\left(\boldsymbol{\rho}_{\mathrm{D}}^{(l)}\right)$. General treatments leading to frame indifference of the spatial constitutive laws in dissipative systems have also been explored in [141] and [185]. Multiplying both sides of (3.146) by the mass density ρ_D

$$\rho_{\mathrm{D}}\dot{\Psi}_{\mathrm{D}}^{\mathrm{p}} = \sum_{l} \frac{\partial\left(\rho_{\mathrm{D}}\widehat{\Psi}_{\mathrm{D}}^{\mathrm{p}}\right)}{\partial \boldsymbol{\rho}_{D}^{(l)}} \mathrm{curl}\left(\mathbf{v}_{\mathrm{D}}^{(l)} \times \boldsymbol{\rho}_{\mathrm{D}}^{(l)}\right), \tag{3.147}$$

and borrowing arguments from the text that lead to (3.113), namely, the equation before (3.111) and those leading up to (3.115), we may write,

$$\int \rho_D \dot{\Psi}_{\mathrm{D}}^{\mathrm{p}} dv_{\mathrm{D}} = -\int \sum_{l} \rho_{\mathrm{D}}^{(l)} \mathbf{v}_{\mathrm{D}}^{(l)} \cdot \left[\mathrm{curl}\left(\frac{\partial \hat{\widehat{\Psi}}_{\mathrm{D}}^{\mathrm{p}}}{\partial \rho_{\mathrm{D}}^{(l)}}\right) \times \boldsymbol{\xi}_{\mathrm{D}}^{(l)}\right] \mathrm{d}v_{\mathrm{D}}. \tag{3.148}$$

with $\widehat{\widehat{\Psi}}^{\mathrm{p}}_{\mathrm{D}} = \rho_{\mathrm{D}}\widehat{\Psi}^{\mathrm{p}}_{\mathrm{D}}$. With these simplification, the plastic free energy imbalance terms in (3.142) becomes

$$\int -\sum_{l} \rho^{(l)}_{\mathrm{D}} \mathbf{v}^{(l)}_{\mathrm{D}} \cdot \left[\left(\mathbf{b}^{(l)}_{\mathrm{D}} \cdot \boldsymbol{\sigma}^{\mathrm{T}} + \boldsymbol{\omega}^{(l)}_{\mathrm{D}}\right) \times \boldsymbol{\xi}^{(l)}_{\mathrm{D}}\right] \mathrm{dv}_{\mathrm{D}} \leq 0. \tag{3.149}$$

In the above, we have employed a simplification similar to the one used in (3.109) to factor out the dislocation velocity term and used $\boldsymbol{\omega}^{(l)}_{\mathrm{D}} \equiv \mathrm{curl}\left(\frac{\partial \widehat{\widehat{\psi}}^{\mathrm{p}}_{\mathrm{D}}}{\partial \rho^{(l)}_{\mathrm{D}}}\right)$. We may thus define the spatial Peach-Koehler force at finite deformation by,

$$\mathbf{f}^{(l)}_{\mathrm{D}} = \left(\mathbf{b}^{(l)}_{\mathrm{D}} \cdot \boldsymbol{\sigma}^{\mathrm{T}} + \boldsymbol{\omega}^{(l)}_{\mathrm{D}}\right) \times \boldsymbol{\xi}^{(l)}_{\mathrm{D}}, \tag{3.150}$$

which takes a form similar to the referential driving force in (3.115) . We could then use the Peach-Koehler force above into a mobility law, say: $\mathbf{v}^{(l)}_{\mathrm{D}} = \mathbf{M}\mathbf{f}^{(l)}_{\mathrm{D}}$, to show that the dissipation term always remains positive. In passing, we note that a form comparable to (3.150) was derived in [4] for a tensor representation of the dislocation density. In that form, a properly defined Cauchy stress appears in an expression for the dissipation in a quantity serving as the work conjugate for a velocity quantity defined on the basis of a density tensor representation of dislocations. That form reduces to the part $\left(\mathbf{b}^{(l)}_{\mathbf{D}} \cdot \boldsymbol{\sigma}^{\mathrm{T}}\right) \times \boldsymbol{\xi}^{(l)}_{\mathrm{D}}$ in (3.150)in the case of single slip system and the bundle representation of dislocations we adopt in our work, where the velocity in our case is definable and represents the local dislocation velocity. See also [3] for a related treatment of thermodynamics with a significantly different representation of the dislocation system in the constitutive hypothesis.

3.D Arbitrary reference configuration

In order to show what constraints are implied in the choice of reference configuration we set up a set of mappings as depicted in Fig. 3.11. In addition to the three usual configurations, the reference $\mathscr{B}$, microstructure, $\mathscr{M}$, and spatial, $\mathscr{D}$, we introduce a second arbitrary reference configuration, $\mathscr{B}'$, that is generated from $\mathscr{B}$ via an arbitrary map $\mathbf{G}$. We keep in mind here that the spatial (deformed) configuration $\mathscr{D}$ is the physical configuration of the material in its current state that is expressed in terms of the elastic and the defect states of

the material. This deformed configuration $\mathscr{D}$ is obtained by mapping from the microstructure configuration $\mathscr{M}$ via the elastic distortion, $\mathbf{F}^{\mathrm{e}}$, which is uniquely connected to the defect state. As such, in investigating the dependence of the theoretical development presented here on the reference configuration, we must maintain the uniqueness of the deformed state and its connection with the microstructure configurations as they, together, represent the physical state of the material.

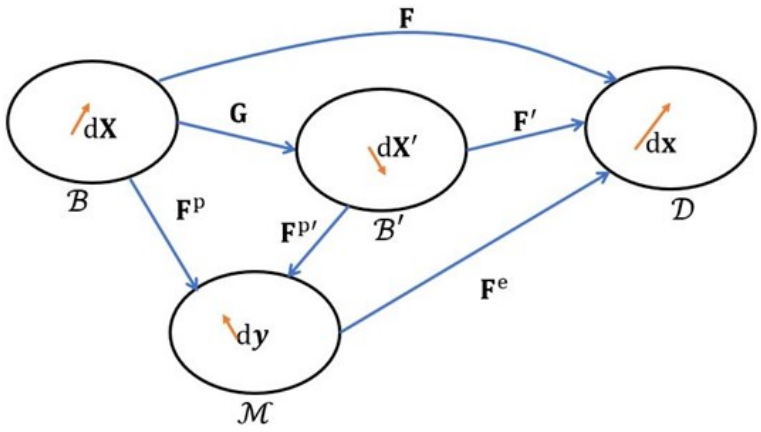

Figure 3.11. Depiction of the mapping relations showing two reference configurations denoted by their respective differential line elements $\mathrm{d}\mathbf{X}$ and $\mathrm{d}\mathbf{X}'$ related to each other by an arbitrary tangent map $\mathbf{G}$. Note that the addition of the primed reference configuration means that there are now two routes to the deformed configuration through the microstructure configuration.

Given the above argument, we then think of multiple reference configurations being mapped to the same microstructure configuration via different plastic distortions. Thus, two plastic distortions $\mathbf{F}^{\mathrm{p}}$ and $\mathbf{F}^{\mathrm{p}'}$ are to be used to reach the microstructure configuration $\mathscr{M}$ from the two reference configurations $\mathscr{B}$ and $\mathscr{B}'$. The corresponding (total) deformation gradients mapping these reference configurations to the deformed configuration are $\mathbf{F} = \mathbf{F}^{\mathrm{e}}\mathbf{F}^{p}$ and $\mathbf{F}' = \mathbf{F}^{\mathrm{e}}\mathbf{F}^{p'}$. From this we get the relations previously derived in the paper, namely (3.22) and (3.23) in addition to another set of relations,

$$\mathrm{d}\mathbf{u}' = \boldsymbol{\beta}'\mathrm{d}\mathbf{X} = \boldsymbol{\beta}^{\mathrm{p}'}\mathrm{d}\mathbf{X}' + \boldsymbol{\beta}^{\mathrm{e}}\mathrm{d}\mathbf{x} \tag{3.151}$$

where,

$$\boldsymbol{\beta}^{p'} \equiv \mathbf{F}^{p'} - \mathbf{I} \tag{3.152}$$

and $\boldsymbol{\beta}^{\mathrm{e}}$ is still defined by (3.23). Locally we also have that $\mathrm{d}\mathbf{X}' = \mathbf{G}\mathrm{d}\mathbf{X}$, for some arbitrary prescribed tangent map $\mathbf{G}$. In order to study the arbitrariness of the reference configuration we study the map $\mathbf{G}$ to see if any restrictions are placed on it. Implicit in our formulation are the assumption of the compactness of the reference and deformed configuration, which gave rise to the compatibility of the displacement, $\oint \mathrm{d}\mathbf{u} = \oint \boldsymbol{\beta}^{\mathrm{p}}\mathrm{d}\mathbf{X} + \oint \boldsymbol{\beta}^{\mathrm{e}}\mathrm{d}\mathbf{x} = 0$, for the displacement field that maps the reference configuration $\mathscr{B}$ onto the spatial, $\mathscr{D}$. Similarly, we have $\oint \mathrm{d}\mathbf{u}' = 0$ for the displacement field mapping the second reference configuration $\mathscr{B}'$ onto the spatial $\mathscr{D}$. Expanding this expression gives $\oint \mathrm{d}\mathbf{u} = \oint \boldsymbol{\beta}^{\mathrm{p}'}\mathrm{d}\mathbf{X}' + \oint \boldsymbol{\beta}^{\mathrm{e}}\mathrm{d}\mathbf{x}$. Since the deformation paths share the same microstructure space, $\oint \boldsymbol{\beta}^{\mathrm{e}}\mathrm{d}\mathbf{x}$ is common to both compatibility constraints, from which we conclude that the reference configurations must be related by,

$$\oint \boldsymbol{\beta}^{\mathrm{p}}\mathrm{d}\mathbf{X} = -\oint \boldsymbol{\beta}^{\mathrm{e}}\mathrm{d}\mathbf{x} = \oint \boldsymbol{\beta}^{\mathrm{p}'}\mathrm{d}\mathbf{X}' \tag{3.153}$$

Using the local relation, $\mathrm{d}\boldsymbol{X}' = \mathbf{G}\mathrm{d}\boldsymbol{X}$ and $\mathbf{F}^{p'} = \mathbf{F}^{p}\mathbf{G}^{-1}$ (from the diagram above), using (3.153) we can get a restriction on $\mathbf{G}$,

$$\begin{aligned}
\oint \boldsymbol{\beta}^{\mathrm{p}}\mathrm{d}\mathbf{X} &= \oint \left(\mathbf{F}^{\mathrm{p}'} - \mathbf{I}\right)\mathbf{G}\mathrm{d}\mathbf{X} \\
&= \oint \left(\mathbf{F}^{\mathrm{p}}\mathbf{G}^{-1} - \mathbf{I}\right)\mathbf{G}\mathrm{d}\mathbf{X} = \oint \mathbf{F}^{\mathrm{p}} - \mathbf{G}\mathrm{d}\mathbf{X} \\
&= \oint \left(\mathbf{F}^{\mathrm{p}} - \mathbf{I}\right)\mathrm{d}\mathbf{X} + \oint (\mathbf{I} - \mathbf{G})\mathrm{d}\mathbf{X} \\
&= \oint \boldsymbol{\beta}^{\mathrm{p}}\mathrm{d}\mathbf{X} + \oint (\mathbf{I} - \mathbf{G})\mathrm{d}\mathbf{X}
\end{aligned} \tag{3.154}$$

From (3.154) we see that the term $\oint(\mathbf{I} - \mathbf{G})\mathrm{d}\mathbf{X}$ should vanish. This means that $\mathbf{G}$ must be the derivative of some map, which means that the reference configuration is arbitrary up to compatible deformations. This result is very intuitive when considering topological defects, in that compatible maps should not change the nature of these defects, thus leaving (3.31) unchanged. Since the reference configuration is arbitrary up to compatible maps we can think of this map, $\mathbf{G}$, as just a relabeling of material points. An example of this is when

we take the reference configuration to be the deformed configuration, by setting $\mathbf{G} \to \mathbf{F}'^{-1}$ we get, $\mathbf{F} \to \mathbf{I}$ and thus $\mathbf{F}^{\mathrm{p}} = \mathbf{F}^{\mathrm{e}-1}$. The Mandel stress then becomes equivalent to the Cauchy stress and the form invariance of equations (3.151) with (3.115) and (3.85) with (3.77) become identical, where we would have to make use of the fact that, in this case, the material and spatial time derivatives coincide.

For computational purposes, however, we have taken the reference configuration to be the defect-free configuration. Such a choice is natural because the defects themselves are defined relative to the defect free state. In this case, the possible class of the tangent maps G may include the class of compatible elastic deformations because such deformation do not alter the defect state of the material.

4. NUMERICAL SOLUTION OF CONTINUUM DISLOCATION DYNAMICS AT FINITE DEFORMATION

A portion of this chapter was submitted to the International Journal of Plasticity by Kyle Starkey, Anter El-Azab as "Total Lagrange implementation of a finite-deformation continuum dislocation". In this chapter a numerical algorithm is developed to solve the CDD transport equations developed in the previous chapter and crystal mechanics equations.

4.1 Abstract

We present a computational algorithm for solving the recently developed finite-deformation continuum dislocation dynamics theory of mesoscale plastic deformation of single crystals [177]. This CDD theory is based on a vector density representation of dislocations governed by curl-type transport-reaction equations subjected to the divergence-free constraint of the appropriate dislocation density. These density evolution equations are to be solved simultaneously with the finite-deformation crystal mechanics. Specifically, our algorithm aims to solve the referential form of the governing equations for a representative volume element (RVE) subject to remote uniform loading. The mechanical fields at the mesoscale are thus split into RVE-averages plus fluctuating components and treated using a strain-driven homogenization scheme. A virtual work-based total Lagrange formulation was used to discretize the governing mechanics equations. A first-order system least squares finite element formulation was used to solve the transport equations. The two schemes are coupled in a staggered fashion. As a part of the crystal mechanics discretization, we derive a consistent tangent modulus and show that the stress update for this model is both linear and global. This linear stress update comes at the cost of solving the dislocation transport equations at every time step to update the plastic distortion caused by dislocation motion. Several test problems are given, demonstrating the ability of the discretization scheme to solve the problem, including the expansion of dislocation loop-like bundles under constant velocity and driven by a mean deformation gradient, dynamic recovery of two oppositely oriented tilt boundaries in a single crystal, and a uniaxial tension test of a single crystal with one slip

system activated. In most of these exmaples, the evolution behavior of the dislocations in the finite deformation regime is demonstrated.

4.2 Introduction

The current work is a first attempt at a numerical solution of the recently developed vector-density-based continuum dislocation dynamics formalism at finite crystal deformation [177]. This formalism is one of several that incorporate dislocation physics into formulations suitable for studying crystal deformation starting from the dislocation properties [125, 11, 153, 84]. These models differ from the conventional crystal plasticity models in which phenomenological constitutive laws are used to close the governing continuum mechanics equations [162, 127, 51, 118, 207, 121, 10]. While the latter models proved to be successful on the structural scales, they do not predict the dislocation patterning in the crystal, which play an important role in the hardening behavior of metals [94] and in recrystallization [60]. Continuum dislocation dynamics (CDD) models aim to fill this gap. As part of their structure, these models include some form of a transport equation of dislocations. For example, the formulation by Acharya and coworkers [11, 12] uses a density tensor to represent dislocations for which a curl-type transport equation governs its space and time evolution. Other models use scalar density [53, 52, 45, 171] or vector-density [198, 197] representations of dislocations. Yet, another class of models includes an extended representation of dislocations, including both scalar and vector density in addition to the so-called curvature density of dislocations, see [88, 86] and the simplified variants of this model in [167]. In some models, a combination of crystal plasticity and dislocation transport equations are used [195]. In all of these models, continuum dislocation transport equations are coupled to crystal mechanics using the plastic strain as eigenstrain to predict the internal stress contributing to the evolution of the dislocation system in the material.

The numerical treatment of the above models employ some space and time discretization schemes similar to those used in crystal plasticity. For example, [160] used the finite volume method to solve the dislocation transport model within a crystal plasticity framework solved by the finite element method (FEM). The latter method was also used by [153]

to solve a two dimensional indentation problem. A split solution scheme was used; first, the mechanics solution is obtained for a fixed plastic distortion followed by an update for the dislocation density and the plastic distortion. In [87], a finite volume method (FVM) was used to solve the dislocation transport equations and update the plastic distortion using a forward Euler time integration scheme. [170] used an implicit Runge-Kutta time integrator with a discontinuous Galerkin finite element method for the discretization of the dislocation transport equations. In [197], a least squares finite element method (LSFEM) was used to solve the dislocation transport equations. In the latter solution schemes, the mechanics and the dislocation transport parts of the problem were coupled in a staggered fashion, where the mechanical equilibrium problem was solved at each time-step for a fixed distribution of dislocations while the forces acting on the dislocations were computed from the stress solution and used to update the dislocation density and plastic distortion. In [11], a Galerkin FEM was used to update the mechanical equilibrium equations, LSFEM for the update of the incompatibility tensor, and a mixed Galerkin-Least-Squares FEM for the dislocation density tensor transport equations.

Of particular interest here is the vector density-based formalism of continuum dislocation dynamics developed recently by [177], which couples dislocation transport equations with crystal mechanics taking into consideration the finite deformation kinematics of the crystal. In the current work, we will present a numerical algorithm for the solution of that formalism, specifically for the case of a representative volume element (RVE) subject to uniform remote loading. This problem corresponds to a bulk-like behavior with a statistically homogeneous dislocation system. Spatial averaging will be applied to the mechanical fields such that the corresponding averages over the RVE match the remote fields. This approach is an important part of the homogenization theory in the mechanics of heterogeneous media. This theory provides a vast list of averaging relations that connect kinematic quantities across different scales [169]. The deformation gradient provides a natural way to express averaging relations in the finite deformation setting. [164] take advantage of these relations in the development of a strain-driven homogenization scheme. For stress-driven homogenization schemes variational methods can be used like in [186, 138].

The current research aims to apply the above homogenization concepts to the finite-deformation continuum dislocation dynamics framework by [177] for bulk plasticity simulations. We present a novel strain-driven homogenization scheme using the applied (mean) deformation gradient to drive dislocation evolution and plastic deformation at the mesoscale. A loose (staggered) coupling between the mechanical and continuum dislocation dynamics equations is used. This coupling scheme amounts to having a fixed plastic distortion during the iterative solution of the geometrically nonlinear mechanical equilibrium problem. It will be shown that the stress update is global and requires no iteration by itself once the displacement field is found during the solution of the nonlinear equilibrium problem. It is worth mentioning here that, in crystal plasticity, the stress requires an iterative local update from a non-linear stress-strain relationship [161]. After the mechanics problem is solved, the dislocation transport equations are then solved using a LSFEM method while the plastic distortion is updated from the dislocation motion. We obtain the compatible and incompatible parts of the plastic distortion using Galerkin FEM and LSFEM methods, respectively. This approach takes advantage of the field dislocation mechanics framework by [22] as has been recently explained in [126].

We start with fixing the notation in Section 2 and follow with a summary of the mechanics and dislocation dynamics boundary value problem (BVP) in Sections 3.1 and 3.2, respectively. In Section 3.3 we introduce a strain-homogenization scheme for the case of a remote (mean) deformation gradient, followed by the details of the numerical discretization of the mechanics problems in Section 4. In Section 5, we provide the details of the numerical discretization of the dislocation transport equations and the update of the plastic distortion. An overview of the numerical algorithm is then outlined. Finally, we present a set of test problems illustrating the utility of the developed algorithm.

4.3 Notation

Here we follow the notation used by [73]. In the following $\mathbf{T}$ represents a second order tensor field and $\mathbf{v}$ represents a vector field,

$$\operatorname{div}(\mathbf{v}) = \frac{\partial \mathrm{v_i}}{\partial \mathrm{x_i}} \tag{4.1}$$

$$\operatorname{curl}(\mathbf{v})_{\mathrm{i}} = \epsilon_{\mathrm{ijk}} \frac{\partial \mathrm{v_k}}{\partial \mathrm{x_j}} \tag{4.2}$$

$$\operatorname{div}(\mathbf{T})_{\mathrm{i}} = \frac{\partial \mathrm{T_{ij}}}{\partial \mathrm{x_j}} \tag{4.3}$$

$$\operatorname{curl}(\mathbf{T})_{\mathrm{ij}} = \epsilon_{\mathrm{ipq}} \frac{\partial \mathrm{T_{jq}}}{\partial \mathrm{x_p}}. \tag{4.4}$$

Stokes theorem applied to a second order tensor is expressed in the form:

$$\oint \mathbf{T} \mathrm{d}\mathbf{x} = \int \operatorname{curl}(\mathbf{T})^{\mathrm{T}} \mathbf{n} \mathrm{da} \ , \tag{4.5}$$

which follows from the well-known Stokes theorem for vector fields,

$$\oint \mathbf{v} \cdot \mathrm{d}\mathbf{x} = \int \mathbf{n} \cdot \operatorname{curl}(\mathbf{v}) \, \mathrm{da} \ , \tag{4.6}$$

with the substitution of $\mathbf{v} = \mathbf{T}\mathbf{c}$ where $\mathbf{c}$ is some arbitrary constant vector that can be factored out to give 4.5. We refer to the material time derivative operator with the usual superposed dot notation,

$$\dot{(\ \ )} = \frac{\partial}{\partial \mathrm{t}} (\ \ )_{\mathbf{x}}, \tag{4.7}$$

with $\mathbf{X}$ being the position vector in the reference configuration. We further denote the spatial derivative operators with respect to referential coordinate $\mathbf{X}$ with capital letters and while those with respect to spatial coordinate $\mathbf{x}$ with lower case letters. The definitions (4.2)-(4.6) already apply to the operators with respect to the coordinate $\mathbf{x}$. As for the referential derivative operators, for example, the divergence, we write

$$\operatorname{Div}(\mathbf{v}) = \frac{\partial \mathrm{v_i}}{\partial \mathrm{X_i}}. \tag{4.8}$$

We also use some tensor identities for the double inner product defined by:

$$\mathbf{A}{:}\mathbf{B} = \mathrm{A_{ij}B_{ij}}. \tag{4.9}$$

We further use the following identities:

$$\mathbf{A}{:}\mathbf{B} = \mathbf{A}^{\mathrm{T}}{:}\mathbf{B}^{\mathrm{T}} \tag{4.10}$$

$$\mathbf{A}{:}\,(\mathbf{BC}) = \left(\mathbf{B}^{\mathrm{T}}\mathbf{A}\right){:}\mathbf{C} = \left(\mathbf{AC}^{\mathrm{T}}\right){:}\mathbf{B} \tag{4.11}$$

The following section introduces the homogenization scheme which is used to relate the mesoscopic and macroscopic scales using spatial averaging. We also introduce the CDD equations for discretization in a later section.

4.4 Mathematical statement of the problem

4.4.1 Mechanical boundary value problem

We investigate the response of a macroscopic single-crystal subjected to an average deformation gradient. To fix ideas, we consider the case of a face-centered cubic (FCC) crystal. Within the continuum dislocation dynamics framework, our goal is to solve for all fields at the mesoscale, including the dislocation density. To this end we consider a time-parameterized deformation mapping $\mathbf{x} = \mathbf{\Psi}(\mathbf{X}, \mathrm{t})$ where $\mathbf{X}$ is the referential coordinate of all material points in the crystal and $\mathbf{x}$ refers to the current positions of those points. The deformation gradient at the mesoscale is then given by: $\mathbf{F} = \mathrm{Grad}(\mathbf{\Psi})$, with Grad being the gradient operator in the reference frame. We also consider the multiplicative decomposition of the deformation gradient in the form

$$\mathbf{F} = \mathbf{F}^{\mathrm{e}}\mathbf{F}^{\mathrm{p}}, \tag{4.12}$$

with $\mathbf{F}^{\mathrm{e}}$ and $\mathbf{F}^{\mathrm{p}}$ being the elastic and plastic distortions, respectively. These distortions are generally incompatible and not representing gradients of a deformation mapping as $\mathbf{F}$ itself does. $\mathbf{F}^{\mathrm{e}}$ holds the information about the rotation and stretch of the crystal lattice while

$\mathbf{F}^{\mathrm{p}}$ holds the information about the deformation due to the creation and motion of defects, dislocations in our case. The decomposition in (4.12) is understood in the sense that $\mathrm{d}\mathbf{x} = \mathbf{F}\mathrm{d}\mathbf{X}, \mathrm{d}\mathbf{y} = \mathbf{F}^{\mathrm{p}}\mathrm{d}\mathbf{X},$ and $\mathrm{d}\mathbf{x} = \mathbf{F}^{\mathrm{e}}\mathrm{d}\mathbf{y}$, with $\mathrm{d}\mathbf{X}$ and $\mathrm{d}\mathbf{x}$ being differential vector distances in the reference and deformed configurations of the crystal, respectively, and $\mathrm{d}\mathbf{y}$ is a corresponding distance in the microstructure (intermediate) space. The latter is considered to be isoclinic. Based upon the multiplicative decomposition shown above, the total Lagrangian strain can be decomposed into elastic and plastic parts [73], $\mathbf{E} = \mathbf{F}^{\mathrm{p}\mathrm{T}}\mathbf{E}^{\mathrm{e}}\mathbf{F}^{\mathrm{p}} + \mathbf{E}^{\mathrm{p}}$, where

$$\mathbf{E}^{\mathrm{p}} = \frac{\mathbf{1}}{2}\left(\mathbf{F}^{\mathrm{p}\mathrm{T}}\mathbf{F}^{\mathrm{p}} - \mathbf{I}\right), \tag{4.13}$$

$$\mathbf{E}^{\mathrm{e}} = \frac{1}{2}\left(\mathbf{F}^{\mathrm{e}\mathrm{T}}\mathbf{F}^{\mathrm{e}} - \mathbf{I}\right). \tag{4.14}$$

Anticipating the elastic strain to be small, a linear elastic constitutive law is used to connect the second Piola-Kirchhoff stress in the microstructure space, denoted by $\boldsymbol{\sigma}^{\mathrm{e}}$, to the elastic strain in the same space

$$\boldsymbol{\sigma}^{\mathrm{e}} = \mathbb{C}\mathbf{:}\mathbf{E}^{\mathrm{e}}, \tag{4.15}$$

where $\mathbb{C}$ is the fourth order elasticity tensor defined in the lattice or microstructure space.

In the absence of body forces, and considering a quasistatic situation, the stress equilibrium equation in the reference configuration takes on the form [73]

$$\mathrm{Div}\left(\mathbf{P}\right) = 0, \tag{4.16}$$

where $\mathbf{P}$ is the first Piola-Kirchoff (PK1) stress. The PK1 stress is related to the microstructure stress by

$$\begin{aligned}\mathbf{P} =& \mathrm{J}\boldsymbol{\sigma}\mathbf{F}^{-\mathrm{T}}, \\ =& \mathrm{J}^{\mathrm{p}}\mathbf{F}^{\mathrm{e}}\boldsymbol{\sigma}^{\mathrm{e}}\mathbf{F}^{\mathrm{p}-\mathrm{T}} = \mathrm{J}^{\mathrm{p}}\mathbf{F}\mathbf{F}^{\mathrm{p}-1}\boldsymbol{\sigma}^{\mathrm{e}}\mathbf{F}^{\mathrm{p}-\mathrm{T}}.\end{aligned} \tag{4.17}$$

In the above, the first equality is the usual connection between PK1 stress and Cauchy stress, $\boldsymbol{\sigma}$. The second connects the PK1 stress with the microstructure stress, $\boldsymbol{\sigma}^{\mathrm{e}}$ and the third is a slight modification of the second. The closure of this mechanical problem requires knowledge

of the plastic distortion coming from the history of the dislocation density transport in the crystal, which is summarized next.

4.4.2 Dislocation dynamics boundary value problem

We refer the reader to a recent publication of ours [177], where the connection between dislocation transport and plastic distortion is made for the case of the vector density-based CDD framework at finite deformation. The important results from that work are summarized here. Following Arora and Acharya [11], the plastic distortion is expressed using the Helmholtz decomposition

$$\begin{aligned} \mathbf{F}^{\mathrm{p}} =& \boldsymbol{\Phi}^{\mathrm{p}} + \boldsymbol{\chi}^{\mathrm{p}} \\ \boldsymbol{\Phi}^{\mathrm{p}} \equiv& \mathrm{Grad}\left(\mathbf{V}^{\mathrm{p}}\right), \quad \boldsymbol{\chi}^{\mathrm{p}} \equiv \mathrm{Curl}(\mathbf{A}^{\mathrm{p}})^{\mathrm{T}}. \end{aligned} \tag{4.18}$$

where $\mathbf{V}^{\mathrm{p}}$ is a vector potential and $\mathbf{A}^{\mathrm{p}}$ is a tensor potential. The above Helmholtz decomposition is introduced for purely numerical reasons for an accurate update of the plastic distortion; when the rate of plastic distortion is directly integrated numerical errors accumulate. Over the coarse of a simulation these errors can produce a plastic distortion that no longer satisfies $\boldsymbol{\alpha}^{\mathrm{RM}} \equiv \mathrm{Curl}(\mathbf{F}^{\mathrm{p}})$, leading to significant errors in the stress [126]. We are interested in representing each of these potentials in terms of the dislocation fields. We obtain the incompatible part of the plastic distortion directly from the distribution of dislocations from the definition of the two point dislocation density tensor $\boldsymbol{\alpha}^{\mathrm{RM}} \equiv \mathrm{Curl}(\mathbf{F}^{\mathrm{p}}) = \mathrm{Curl}(\boldsymbol{\chi}^{\mathrm{p}})$. The RM superscript refers to the fact that this density measure is integrated over a referential area (hence the R) and returns a Burgers vector resultant in the microstructure space (hence the M). We decompose $\boldsymbol{\alpha}^{\mathrm{RM}}$ in terms of its slip system components, which we represent as dislocation line bundles on each slip system,

$$\boldsymbol{\alpha}^{\mathrm{RM}} = \sum_{l} \boldsymbol{\rho}_{\mathrm{R}}^{(l)} \otimes \mathbf{b}_{\mathrm{M}}^{(l)}, \tag{4.19}$$

where $\boldsymbol{\rho}_{\mathrm{R}}^{(l)}$ is the vector density on slip system l and $\mathbf{b}_{\mathrm{M}}^{(l)}$ is the corresponding Burgers vector in the microstructure space. The vector density field $\boldsymbol{\rho}_{\mathrm{R}}^{(l)}$ is introduced here in accordance

with the line bundle representation of dislocation fields, see details in [8, 188, 176]. Using the above equation and the fact that $\boldsymbol{\alpha}^{\mathrm{RM}} = \mathrm{Curl}(\boldsymbol{\chi}^{\mathrm{p}})$, the relationship for the incompatible part of the plastic distortion can be written in terms of dislocations as

$$\mathrm{Curl}(\boldsymbol{\chi}^{\mathrm{p}}) = \sum_{l} \boldsymbol{\rho}_{\mathrm{R}}^{(l)} \otimes \mathbf{b}_{\mathrm{M}}^{(l)}. \tag{4.20}$$

For the compatible part we use

$$\dot{\mathbf{F}}^{\mathrm{p}} = \sum_{l} \mathbf{b}_{\mathrm{M}}^{(l)} \otimes \left(\mathbf{v}_{\mathrm{R}}^{(l)} \times \boldsymbol{\rho}_{\mathrm{R}}^{(l)} \right). \tag{4.21}$$

This relationship is a tensorial form of Orowan's law and it expresses the fact that the rate of plastic distortion is due to the movement of dislocations, where $\mathbf{v}_{\mathrm{R}}^{(l)}$ is the dislocation velocity relative to the material. Taking the divergence of this equation isolates the compatible part of $\dot{\mathbf{F}}^{\mathrm{p}}$ giving us

$$\mathrm{Div}\left(\dot{\mathbf{F}}^{\mathrm{p}}\right) = \mathrm{Div}\left(\mathrm{Grad}\left(\dot{\mathbf{V}}^{\mathrm{p}}\right) + \dot{\boldsymbol{\chi}}^{p}\right) = \mathrm{Div}\left(\mathrm{Grad}\left(\dot{\mathbf{V}}^{\mathrm{p}}\right)\right). \tag{4.22}$$

The above expression provides a way to update the compatible part of the plastic distortion,

$$\mathrm{Div}\left(\mathrm{Grad}\left(\dot{\mathbf{V}}^{\mathrm{p}}\right)\right) = \mathrm{Div}\left(\sum_{l} \mathbf{b}_{\mathrm{M}}^{(l)} \otimes \left(\mathbf{v}_{\mathrm{R}}^{(l)} \times \boldsymbol{\rho}_{\mathrm{R}}^{(l)} \right)\right). \tag{4.23}$$

Together (4.23) and (4.20) can be used to update the plastic distortion in terms of the dislocation density and velocity fields. The evolution of the dislocation density field itself is governed by a set of transport-reaction equations subject to the appropriate divergence constraints. In the absence of dislocation reactions, these equations have the form

$$\begin{aligned} \dot{\boldsymbol{\rho}}_{\mathrm{R}}^{(\mathrm{l})} &= \mathrm{Curl}\left(\mathbf{v}_{\mathrm{R}}^{(\mathrm{l})} \times \boldsymbol{\rho}_{\mathrm{R}}^{(\mathrm{l})} \right) \\ \mathrm{Div}\left(\boldsymbol{\rho}_{\mathrm{R}}^{(\mathrm{l})} \right) &= 0. \end{aligned} \tag{4.24}$$

A more elaborate form of the transport equation and the divergence constraint in the case of reactions can be found in [188]. The dislocation velocity can be specified using a linear constitutive law of the form

$$\mathbf{v}_{\mathrm{R}}^{(l)} = \frac{1}{\mathrm{B}}\left(\mathbf{f}_{\mathrm{R,g}}^{(l)} - \mathbf{f}_{\mathrm{L}}^{(l)}\right), \tag{4.25}$$

where B is the dislocation drag coefficient, $\mathbf{f}_{\mathrm{R,g}}^{(l)}$ is the glide component of the referential dislocation driving force on dislocations, and $\mathbf{f}_{\mathrm{L}}^{(l)}$ is the sum of all forces resisting the dislocation glide [126]. The referential driving force on dislocations is given by [177]

$$\mathbf{f}_{\mathrm{R}}^{(l)} = (\mathbf{b}_{\mathrm{R}}^{(l)} \cdot \mathbf{M}^{\mathrm{T}}) \times \frac{\boldsymbol{\rho}_{\mathrm{R}}^{(l)}}{|\boldsymbol{\rho}_{\mathrm{R}}^{(l)}|}, \tag{4.26}$$

where $\mathbf{M}$ is the referential Mandel stress, which defined by $\mathbf{M} = \mathbf{CS}$. This stress is the work conjugate to the plastic distortion rate. In the definition of $\mathbf{M}$, $\mathbf{S}$ is the second Piola-Kirchhoff stress and $\mathbf{C}$ is the right Cauchy-Green strain tensor. These relations give us a coupling between the dislocation motion and the stress equilibrium equations through the Mandel stress. The driving force in the deformed configuration is similar in form to (4.26) but the stress tensor is the Cauchy stress and the Burgers vector is pushed forward into the deformed configuration [177]. For glide motion, the dislocation velocity is given by

$$\begin{aligned} \mathbf{v}_{\mathrm{R}}^{(l)} &= |\mathrm{v}_{\mathrm{R}}^{(l)}|\boldsymbol{\xi} \times \mathbf{n}_{\mathrm{R}}^{(l)} \\ \mathrm{v}_{\mathrm{R}}^{(l)} &= \frac{b}{B}\left\langle |\tau|^{(l)} - \left(\tau_0 + \tau_{\mathrm{p}}^{(l)}\right)\right\rangle \operatorname{sgn}\left(\tau^{(l)}\right) \end{aligned} \tag{4.27}$$

where $\boldsymbol{\xi} = \boldsymbol{\rho}_{\mathrm{R}}^{(l)}/|\boldsymbol{\rho}_{\mathrm{R}}^{(l)}|$ is unit tangent of the dislocation density vector $\boldsymbol{\rho}_{\mathrm{R}}^{(l)}$, $\mathbf{n}_{\mathrm{R}}^{(l)}$ is the slip plane normal, b is the magnitude of the Burgers vector,$\langle\cdot\rangle$ corresponds to the Macauley bracket operation, $\tau^{(l)}$ is the contraction of the transpose of the Mandel stress with the referential Schmidt tensor, τ_0 is the Peierls stress, and $\tau_{\mathrm{p}}^{(l)}$ is the Taylor hardening stress which accounts for short range interactions. The Taylor stress is commonly given in the form [200, 125] :

$$\tau_{\mathrm{p}}^{(l)} = \mu b\sqrt{\sum_{\mathrm{j}} a_{(l,\mathrm{j})}|\boldsymbol{\rho}_{\mathrm{R}}^{(l)}|}, \tag{4.28}$$

with μ being the shear modulus and $a_{(l,\mathrm{j})}$ the average strength of the interaction between slip systems l and j. The Taylor stress form was employed in the 2D CDD models by [63], [203], [64]. In these models, the Taylor stress form was obtained from simplification of the dislocation correlation. [84] employed a similar form in his 3D CDD model.

4.4.3 Homogenization at finite deformation

The goal of the CDD framework is twofold, to predict the mesoscale details of the dislocation system and extract the macroscale deformation response of crystals from the mesoscale details via averaging. To accomplish this goal, it will be required to establish the connection between the two scales, which we do here using the homogenization theory. In the current work, we are particularly interested in using homogenization ideas pertaining to the use of the macroscale deformation and stress measures to derive the evolution of the dislocation system at the mesoscale. We will formulate the problem first using the macroscopic deformation gradient as the driving field.

In homogenization theory the macroscopic deformation gradient, denoted by $\bar{\mathbf{F}}$, is defined as the spatial average of the deformation gradient at the mesoscale, $\mathbf{F}$, over a representative volume element (RVE) of volume $\mathrm{V_{RVE}}$; see [164],

$$\bar{\mathbf{F}} = \frac{1}{\mathrm{V_{RVE}}} \int_{\mathrm{V_{RVE}}} \mathbf{F} \mathrm{dV}. \tag{4.29}$$

The volume $\mathrm{V_{RVE}}$ is selected to be large enough to contains sufficient details of the mesoscale fields to be statistically representative of the macroscale crystal. In this sense, the RVE itself is a portion of the crystal that is translation invariant. This property of the RVE is preserved here by constraining the dislocation fields to be periodic. The deformation mapping $\mathbf{x} = \boldsymbol{\Psi}(\mathbf{X}, \mathrm{t})$ and the displacement at the mesoscale can be decomposed into mean fields and fluctuations as follows [186],

$$\begin{aligned} \mathbf{x} =& \bar{\mathbf{F}}\mathbf{X} + \mathbf{w}, \\ \mathbf{u} =& \left(\bar{\mathbf{F}} - \mathbf{I}\right)\mathbf{X} + \mathbf{w}. \end{aligned} \tag{4.30}$$

In the above, $\mathbf{w}$ is the fluctuation in particle position at the mesoscale. Similarly, the mesoscale deformation gradient can be expressed in the form

$$\mathbf{F} = \mathrm{Grad}\,\mathbf{x} = \bar{\mathbf{F}} + \mathrm{Grad}\,\mathbf{w} = \bar{\mathbf{F}} + \widetilde{\mathbf{F}}, \tag{4.31}$$

where $\widetilde{\mathbf{F}}$ is the fluctuating part of the deformation gradient associated with the displacement $\mathbf{w}$. Substituting (4.31) into (4.29) yields

$$\begin{aligned}\bar{\mathbf{F}} =& \frac{1}{\mathrm{V_{RVE}}}\int_{\mathrm{V_{RVE}}} \mathbf{F}\mathrm{dV} \\ =& \bar{\mathbf{F}} + \frac{1}{\mathrm{V_{RVE}}}\int_{\mathrm{S_{RVE}}} \mathbf{w}\otimes\mathbf{N}\mathrm{dS},\end{aligned}$$

where $\mathrm{S_{RVE}}$ denotes the boundary of the RVE. From the above expression, the fluctuation displacement $\mathbf{w}$ must satisfy

$$\int_{\mathrm{S_{RVE}}} \mathbf{w}\otimes\mathbf{N}\mathrm{dS} = 0. \tag{4.32}$$

The contribution of the fluctuating displacement component to the macroscale deformation gradient is identically zero. It is easy to see that (4.32) holds when the displacement fluctuation is a periodic field.

In the sequel, we will develop the homogenization scheme with a prescribed macroscopic deformation gradient. With this given, it will be possible to write the mesoscale elastic distortion in the form:

$$\mathbf{F}^{\mathrm{e}} = \left(\bar{\mathbf{F}} + \widetilde{\mathbf{F}}\right)\mathbf{F}^{\mathrm{p}-1}, \tag{4.33}$$

which will become useful when calculating the mesoscopic stress using the elastic strain in (4.14) and Hooke's law (4.15). It is interesting to note that other forms of decomposition of the deformation gradient in terms of mean and fluctuating parts have been proposed [36].

4.5 Discretization of the crystal mechanics problem

In this section, we will discuss the discretization of the mechanical boundary valued problem, namely, the stress equilibrium equation (4.16). Due to the finite deformation kinematics, the discretization will be non-linear, thus requiring Newton's method to solve.

4.5.1 The total Lagrange formalism

We will consider the equilibrium equations in the reference configuration of the crystal and hence a total Lagrange formulation will be used [16]. In using the index notation below, we alert the reader that the upper and lower case roman indices refer to reference and spatial frames, respectively. Greek indices refer to the microstructure space. To derive a weak form of the equilibrium equation, we multiply (4.16) by a test function δu_{i} and integrate over the RVE,

$$\int_{\mathrm{V_{RVE}}} \frac{\partial \mathrm{P_{iJ}}}{\partial \mathrm{X_J}} \delta \mathrm{u_i} \mathrm{dV} = 0. \tag{4.34}$$

The PK1 stress in the above equation depends on the displacement field. We use integration by parts along with Gauss theorem to reduce the above equation to

$$\delta \mathrm{W} = \int_{\mathrm{V_{RVE}}} \mathrm{P_{iJ}} \delta \mathrm{F_{iJ}} \mathrm{dV} - \int_{\mathrm{S_{RVE}}} \mathrm{P_{iJ}} \mathrm{N_J} \delta \mathrm{u_i} \mathrm{dS} = 0, \tag{4.35}$$

where $\delta \mathrm{W}$ is the virtual work. In the above expression, we have also used the linearity of the variational derivative and regular derivative to write $(\delta \mathrm{u_i})_{,\mathrm{J}} = \delta(\mathrm{u_{i,J}}) = \delta \mathrm{F_{iJ}}$. Since we will be specifying the mean deformation gradient, the fluctuation is the only unknown part of the displacement field; see (4.30). Taking this into consideration, we implement a change of variable for this variational problem from $\mathrm{u_i}$ to $\mathrm{w_i}$,

$$\delta \frac{\partial (\mathrm{u_i})}{\partial \mathrm{X_J}} = \delta \left(\bar{\mathrm{F}}_{\mathrm{iJ}} + \frac{\partial (\mathrm{w_i})}{\partial \mathrm{X_J}} \right) = \delta \frac{\partial (\mathrm{w_i})}{\partial \mathrm{X_J}} = \frac{\partial (\delta \mathrm{w_i})}{\partial \mathrm{X_J}} = \delta \widetilde{\mathrm{F}}_{\mathrm{iJ}}.$$

With the above change of variable, the second integral in the weak form (4.35) vanishes due to the anti-periodicity of the traction and the periodicity of the test function fluctuations. The weak form of the mechanical homogenization problem then reduces to finding a periodic displacement fluctuation $\mathrm{w_i}$ for prescribed plastic distortion and mean deformation gradient such that

$$\delta \mathrm{W} = \int_{\mathrm{V_{RVE}}} \mathrm{P_{iJ}} \delta \widetilde{\mathrm{F}}_{\mathrm{iJ}} \mathrm{dV} = 0. \tag{4.36}$$

The solution of the stress equilibrium problem is evolutionary due to the time-dependence of the plastic distortion and the prescribed mean deformation gradient. This functional de-

pends on the displacement fluctuation $\mathbf{w}$ by virtue of the fact that its gradient is $\widetilde{\mathbf{F}}$, and on the elastic distortion, $\mathbf{F}^{\mathrm{e}}$, via Hooke's law. Through the use of the connection between the elastic distortion, plastic distortion, and the deformation gradient, this dependence can be turned into $\delta \mathrm{W}\left(\mathbf{w}, \mathbf{F}^{\mathrm{p}}, \bar{\mathbf{F}}\right)$. Because the virtual work functional corresponding to the solution of the problem is zero, we will consider it to be a residual $\mathrm{R}\left(\mathbf{w}, \mathbf{F}^{\mathrm{p}}, \bar{\mathbf{F}}\right)$ that must be set equal to zero at all steps.

As discussed later, the dependence on time comes from the fact that both the plastic distortion $\mathbf{F}^{\mathrm{e}}$ and the mean deformation gradient $\bar{\mathbf{F}}$ are time-dependent. Upon introducing time discretization, the residual will only depend on the unknown displacement fluctuation at the current time step. We thus rewrite the residual in the form: $\mathrm{R}\left(\mathbf{w}^{\mathrm{t}+\Delta \mathrm{t}}, \mathbf{F}^{\mathrm{p}(\mathrm{t}+\Delta \mathrm{t})}, \bar{\mathbf{F}}^{(\mathrm{t}+\Delta \mathrm{t})}\right) = 0$, with the superscript $\mathrm{t}+\Delta \mathrm{t}$ denoting the fact that it is being evaluated at the current time step. Here, we propose to use a staggered scheme to solve the coupled crystal mechanics/dislocation dynamics problem. Within this scheme, the plastic distortion in the residual is evaluated at the previous time step. With this in mind, we rewrite the residual explicitly in the form:

$$\mathrm{R}\left(\mathbf{w}^{\mathrm{t}+\Delta \mathrm{t}}\right) = \int_{\mathrm{V}_{\mathrm{RVE}}} \delta \widetilde{\mathbf{F}} \ : \mathbf{P}^{\mathrm{t}+\Delta \mathrm{t}}\left(\mathbf{w}^{\mathrm{t}+\Delta \mathrm{t}}, \mathbf{F}^{\mathrm{p}(\mathrm{t})}, \bar{\mathbf{F}}^{(\mathrm{t}+\Delta \mathrm{t})}\right) \mathrm{dV}. \tag{4.37}$$

A further justification for fixing the plastic distortion as the stress equilibrium problem is solved is given in a following section where we discuss the discretization of the dislocation density evolution problem. In (4.37) we have shown the explicit dependence of the PK1 stress on the mean deformation gradient as well as the plastic distortion to remind the reader that the stress is dependent on both of them. To solve (4.37) for $\mathbf{w}^{\mathrm{t}+\Delta \mathrm{t}}$ we linearize the equation. In this step we follow [20] and write the linearized equations in the form:

$$\begin{gathered} \mathrm{DR}\left(\mathbf{w}_{\mathrm{k}}^{\mathrm{t}+\Delta \mathrm{t}}\right)[\Delta \mathbf{w}] = -\mathrm{R}\left(\mathbf{w}_{\mathrm{k}}^{\mathrm{t}+\Delta \mathrm{t}}\right) \\ \Delta \mathbf{w} = \mathbf{w}_{\mathrm{k}+1}^{\mathrm{t}+\Delta \mathrm{t}} - \mathbf{w}_{\mathrm{k}}^{\mathrm{t}+\Delta \mathrm{t}} \end{gathered}, \tag{4.38}$$

where $\mathrm{DR}\left(\mathrm{w}_{\mathrm{k}}^{\mathrm{t}+\Delta\mathrm{t}}\right)[\Delta\mathbf{w}]$ is the directional derivative of the residual along an increment in the displacement fluctuations, $\Delta\mathbf{w}$. It is defined by [20]:

$$\mathrm{DR}(\mathbf{w})[\Delta\mathbf{w}] \equiv \left.\frac{\mathrm{d}}{\mathrm{d}\epsilon}\right|_{\epsilon=0} \mathrm{R}(\mathbf{w}+\epsilon\Delta\mathbf{w}).$$

In the rest of the paper we refer to the iterations in (4.38) as the geometric iteration. A finite element method which aims to solve the system (4.38) should include a stress update algorithm for updating the residual and should also include the evaluation of the tangent modulus, $\mathrm{DR}\left(\mathbf{w}_{\mathrm{k}}^{\mathrm{t}+\Delta\mathrm{t}}\right)$, in (4.38). These solution components are discussed in Sections 4.5.2 and 4.5.3, respectively.

4.5.2 Stress update algorithm

An iterative stress update is not required in the CDD-based plasticity solution. In the latter, the stress update simply consists of computing the fluctuation deformation gradient, $\widetilde{\mathbf{F}}$, using the known mean deformation gradient and the plastic distortion, followed by evaluating the elastic distortion using (4.33) and the elastic strain from (4.14). Using the linear elastic constitutive law (4.15) the microstructure stress can then be obtained. Furthermore, the transformation relation (4.17) can be used to obtain the PK1 stress. In addition, when considering dislocation glide only, we have that $\mathrm{J}^{\mathrm{p}} = 1$, so the stress update becomes

$$\mathbf{P} = \mathbf{F}^{\mathrm{e}}\boldsymbol{\sigma}^{\mathrm{e}}\mathbf{F}^{\mathrm{p}-\mathrm{T}}. \tag{4.39}$$

This will be used in the residual calculation at the previous iteration in (4.38).

4.5.3 Consistent tangent modulus

The goal of this section is to derive an explicit expression for the directional derivative $\mathrm{DR}\left(\mathbf{F}^{\mathrm{t}+\Delta\mathrm{t}}\right)[\Delta\mathbf{w}]$ of the residual R in (4.38). Since we evaluate the residual on the reference configuration, the domain of integration is fixed. Then, the directional derivative of the residual is just the directional derivative of the integrand of the residual. Computing this requires evaluating the directional derivative of the PK1 stress. To evaluate the latter we

start by rewriting the $\mathbf{P}\left(\mathbf{w}^{t+\Delta t}, \mathbf{F}^{p(t)}, \overline{\mathbf{F}}^{(t+\Delta t)}\right)$ in the form $\mathbf{P}(\mathbf{F}^{t+\Delta t}\ (\mathbf{w}^{\ t+\Delta t}))$, which is now a function of the updated displacement fluctuations. Taking the directional derivative then yields,

$$\begin{aligned} \mathrm{D}\mathbf{P}\left(\mathbf{F}^{t+\Delta t}\right)[\Delta \mathrm{w}] \equiv & \frac{\mathrm{d}}{\mathrm{d}\epsilon}\bigg|_{\epsilon=0} \mathbf{P}\left(\mathbf{F}^{t+\Delta t}\left(\mathbf{w}^{t+\Delta t}+\epsilon\Delta\mathbf{w}\right)\right) \\ = & \frac{\partial \mathbf{P}}{\partial \mathbf{F}^{t+\Delta t}} : \frac{\mathrm{d}}{\mathrm{d}\epsilon}\bigg|_{\epsilon=0} \mathbf{F}^{t+\Delta t}\ \left(\mathbf{w}^{t+\Delta t}+\epsilon\boldsymbol{\Delta}\mathbf{w}\right). \end{aligned} \tag{4.40}$$

From (4.30) we get

$$\begin{aligned} \mathbf{F}^{t+\Delta t}\left(\mathbf{w}^{t+\Delta t}+\epsilon\Delta\mathbf{w}\right) = & \nabla_0\left(\overline{\mathbf{F}}\mathbf{X}+\left(\mathbf{w}^{t+\Delta t}+\epsilon\Delta\mathbf{w}\right)\right) \\ = & \overline{\mathbf{F}}+\nabla_0\left(\mathbf{w}^{t+\Delta t}+\epsilon\Delta\mathbf{w}\right). \end{aligned}$$

Then (4.40) becomes

$$\begin{aligned} \mathrm{D}\mathbf{P}\left(\mathbf{F}^{t+\Delta t}\right)[\Delta \mathrm{w}] = & \frac{\partial \mathbf{P}}{\partial \mathbf{F}^{t+\Delta t}} : \frac{\mathrm{d}}{\mathrm{d}\epsilon}\bigg|_{\epsilon=0} \left(\overline{\mathbf{F}}+\nabla_0\left(\mathbf{w}^{t+\Delta t}+\epsilon\Delta\mathbf{w}\right)\right) \\ = & \frac{\partial \mathbf{P}}{\partial \mathbf{F}^{t+\Delta t}} : \nabla_0\Delta\mathbf{w}, \end{aligned}$$

and the linearized form (4.38) becomes

$$\int_{\mathrm{V}} \delta\widetilde{\mathbf{F}}^{\mathrm{T}} : \Delta\mathbf{P}\mathrm{dV} = -\int_{\mathrm{V}} \delta\widetilde{\mathbf{F}}^{\mathrm{T}} : \mathbf{P}_{\mathrm{k}}^{t+\Delta t}\mathrm{dV}, \tag{4.41}$$

with

$$\Delta\mathbf{P} \equiv \frac{\partial \mathbf{P}}{\partial \mathbf{F}^{t+\Delta t}} : \nabla_0\Delta\mathbf{w} \tag{4.42}$$

and $\partial\mathbf{P}/\partial\mathbf{F}^{\mathbf{t+\Delta t}}$ is a fourth order tensor called the stress tangent. We refer the reader to the 4.A where the explicit form of the stress tangent is computed and only state the result here,

$$\frac{\partial \mathrm{P}_{\mathrm{iJ}}}{\partial \mathrm{F}_{\mathrm{kL}}^{t+\Delta t}} = \delta_{\mathrm{ik}}\mathrm{F}_{\mathrm{L}\alpha}^{\mathrm{p}-1}\sigma_{\alpha\beta}^{\mathrm{e}}\mathrm{F}_{\beta\mathrm{J}}^{\mathrm{p}-\mathrm{T}} + \mathrm{F}_{\mathrm{i}\alpha}^{\mathrm{e}(t+\Delta t)}\mathbb{C}_{\alpha\beta\theta\delta}\mathrm{F}_{\mathrm{k}\delta}^{\mathrm{e}}\mathrm{F}_{\mathrm{L}\theta}^{\mathrm{p}-1}\mathrm{F}_{\mathrm{J}\beta}^{\mathrm{p}-1}. \tag{4.43}$$

This expression will be used to form the stiffness matrix while solving the linearized system of equations (4.38). It is written here in component form to show the connection of various

quantities and configurations. The last discretization step would be to approximate the test and trial displacement fluctuations using finite element shape functions upon discretizing the space into finite elements. We omit this step here and refer the reader to various standard texts for details [16, 20]. We do, however, perform this step in the next section for the dislocation discretization to illuminate a difference between conventional finite element formulations and First-Order Systems Least Squares (FOSLS) finite element methods.

4.6 Discretization of the continuum dislocation dynamics problem

In this section, we discretize the dislocation transport relations in (4.24) and discuss the plastic distortion update. The discussion is limited here to the case where no dislocation reactions take place. The reader is referred to [188] and [125] for details related to the case where dislocation reactions are considered.

4.6.1 Discretization of the dislocation transport equations

We start by rewriting the individual transport equations (4.24) in a matrix form

$$[\mathbf{A}_{\mathrm{t}}]\begin{bmatrix}\dot{\rho}^{(l)}_{\mathrm{R1}}\\ \dot{\rho}^{(l)}_{\mathrm{R2}}\\ \dot{\rho}^{(l)}_{\mathrm{R3}}\end{bmatrix} = \left\{[\mathbf{A}_0] + [\mathbf{A}_{\mathrm{X}_1}]\frac{\partial}{\partial \mathrm{X}_1} + [\mathbf{A}_{\mathrm{X}_2}]\frac{\partial}{\partial \mathrm{X}_2} + [\mathbf{A}_{\mathrm{X}_3}]\frac{\partial}{\partial \mathrm{X}_3}\right\}\begin{bmatrix}\rho^{(l)}_{\mathrm{R1}}\\ \rho^{(l)}_{\mathrm{R2}}\\ \rho^{(l)}_{\mathrm{R3}}\end{bmatrix}, \tag{4.44}$$

where the matrices $[\mathbf{A}_{\mathrm{t}}], [\mathbf{A}_0], [\mathbf{A}_{\mathrm{X}_1}], [\mathbf{A}_{\mathrm{X}_2}]$, and $[\mathbf{A}_{\mathrm{X}_3}]$ in the above equation are given in 4.B and are functions of the dislocation velocity and its derivatives. As can be seen in the appendix, these matrices are rectangular due to the assembly of the divergence constraint together with transport equations in (4.24) in writing the above matrix form. The backward Euler method is used to discretize the above system in time [137]. In doing this, we note that when the velocity is evaluated at the updated time step we produce a nonlinearity from its dependence on the stress; see the mobility law (4.25) and the driving force in (4.26). We can eliminate this nonlinearity by evaluating the velocity at the previous time step, which

renders the time integration scheme semi-implicit. This results in the operator matrices in the above equation being evaluated at the previous time step,

$$\frac{[\mathbf{A}_{\mathrm{t}}]\left(\boldsymbol{\rho}_{\mathrm{R}}^{(l)(\mathrm{t}+\Delta\mathrm{t})}-\boldsymbol{\rho}_{\mathrm{R}}^{(l)(\mathrm{t})}\right)}{\boldsymbol{\Delta}\mathrm{t}}=\left\{[\mathbf{A}_0]+[\mathbf{A}_{\mathrm{X}_1}]\frac{\partial}{\partial \mathrm{X}_1}+[\mathbf{A}_{\mathrm{X}_2}]\frac{\partial}{\partial \mathrm{X}_2}+[\mathbf{A}_{\mathrm{X}_3}]\frac{\partial}{\partial \mathrm{X}_3}\right\}^{(\mathrm{t})}\boldsymbol{\rho}_{\mathrm{R}}^{(l)(\mathrm{t}+\Delta\mathrm{t})}, \tag{4.45}$$

which is consistent with the staggered scheme used to solve the coupled mechanics/dislocation dynamics problem [126]. Rearranging the above equations yields:

$$\left[[\mathbf{A}_{\mathrm{t}}]-\Delta\mathrm{t}\left([\mathbf{A}_0]+[\mathbf{A}_{\mathrm{X}_1}]\frac{\partial}{\partial \mathrm{X}_1}+[\mathbf{A}_{\mathrm{X}_2}]\frac{\partial}{\partial \mathrm{X}_2}+[\mathbf{A}_{\mathrm{X}_3}]\frac{\partial}{\partial \mathrm{X}_3}\right)\right]^{(\mathrm{t})}\begin{bmatrix}\rho_{\mathrm{R}1}^{(l)(\mathrm{t}+\Delta\mathrm{t})}\\ \rho_{\mathrm{R}2}^{(l)(\mathrm{t}+\Delta\mathrm{t})}\\ \rho_{\mathrm{R}3}^{(l)(\mathrm{t}+\Delta\mathrm{t})}\end{bmatrix}=[\mathbf{A}_{\mathrm{t}}]\begin{bmatrix}\rho_{\mathrm{R}1}^{(l)(\mathrm{t})}\\ \rho_{\mathrm{R}2}^{(l)(\mathrm{t})}\\ \rho_{\mathrm{R}3}^{(l)(\mathrm{t})}\end{bmatrix}. \tag{4.46}$$

In previous related works, e.g., [198, 197, 125, 188], an implicit time integrator with a First Order Systems Least Squares (FOSLS) finite element spatial discretization have been successfully used to solve the dislocation transport equations. FOSLS was specifically used for its ability to enforce the divergence free constraint in (4.24) without the need to use a Lagrange multiplier or penalty type method. FOSLS was also applied in conjunction with an explicit time integration to solve dislocation transport equations by [187], where the least squares method was coupled with a Galkerin finite element method. Performing a Von Neuman stability analysis, the latter authors showed various aspects of the stability and behavior of their explicit scheme. In the current work we use the implicit method used by [198, 197], [125] and [188]. The basics of this method can be found in [67]. Following [126], the least-squares residual (functional) $\mathrm{R}_{\boldsymbol{\rho}}$ corresponding to equation (4.46) can be expressed in the form

$$\mathrm{R}_{\boldsymbol{\rho}}=\int_{V_{\mathrm{RVE}}}\left[\mathbf{L}_{\rho}\left(\left\{\boldsymbol{\rho}_{\mathrm{R}}^{(l)}\right\}^{(\mathrm{t}+\Delta\mathrm{t})}\right)-\mathbf{P}_{\rho}\left(\left\{\boldsymbol{\rho}_{\mathrm{R}}^{(l)}\right\}^{(\mathrm{t})}\right)\right]^2\mathrm{d}\Omega, \tag{4.47}$$

where

$$\mathbf{L}_{\rho}\equiv\left[[\mathbf{A}_{\mathrm{t}}]-\Delta\mathrm{t}\left([\mathbf{A}_0]+[\mathbf{A}_{\mathrm{X}_1}]\frac{\partial}{\partial \mathrm{X}_1}+[\mathbf{A}_{\mathrm{X}_2}]\frac{\partial}{\partial \mathrm{X}_2}+[\mathbf{A}_{\mathrm{X}_3}]\frac{\partial}{\partial \mathrm{X}_3}\right)\right]\quad\text{and}\quad\mathbf{P}_{\rho}\equiv\mathbf{A}_{\mathrm{t}}. \tag{4.48}$$

We seek to minimize the functional $\mathrm{R}_{\boldsymbol{\rho}}$ to obtain the solution of the transport equations for the updated densities. Taking the variational derivative of (4.47) and setting it equal to zero gives

$$\delta \mathrm{R}_{\boldsymbol{\rho}} = 2 \int_{V_{\mathrm{RVE}}} \left[\mathbf{L}_{\rho} \left(\left\{ \boldsymbol{\rho}_{\mathrm{R}}^{(l)} \right\}^{(\mathrm{t}+\Delta \mathrm{t})} \right) - \mathbf{P}_{\rho} \left(\left\{ \boldsymbol{\rho}_{\mathrm{R}}^{(l)} \right\}^{(\mathrm{t})} \right) \right] \mathbf{L}_{\rho} \left(\{ \delta \boldsymbol{\rho} \} \right) \mathrm{d}\Omega = 0. \tag{4.49}$$

Solving this variational expression for the updated dislocation density requires a spatial discretization of the domain and expressing the unknown or trial density in terms of the corresponding shape functions. Doing so leaves us with a discrete version of the least squares operator (4.48), which now operates on the nodal values of the discrete dislocation density. This operator is given by

$$[\mathbf{L}_{\rho}] = \{ [\mathbf{A}_{\mathrm{t}}] - \Delta \mathrm{t} \, [\mathbf{A}_0] \} \, [\mathbf{N}] - \Delta \mathrm{t} \left([\mathbf{A}_{\mathrm{X}_1}][\mathbf{B}_{\mathrm{X}_1}] + [\mathbf{A}_{\mathrm{X}_2}][\mathbf{B}_{\mathrm{X}_2}] + [\mathbf{A}_{\mathrm{X}_3}][\mathbf{B}_{\mathrm{X}_3}] \right). \tag{4.50}$$

In the above, the matrices $[\mathbf{B}_{\mathrm{X}_1}], [\mathbf{B}_{\mathrm{X}_2}]$ and $[\mathbf{B}_{\mathrm{X}_3}]$ contain the derivative of the shape functions, and $[\mathbf{N}]$ is a matrix containing the shape functions. These matrices are all given in 4.B. The the discretized form of the variational statement (4.49) is then given by

$$[\mathbf{K}_{\rho}] \left\{ \rho_{\mathrm{R}}^{(l)(\mathrm{t}+\Delta \mathrm{t})} \right\} = [\mathbf{P}_{\rho}] \left\{ \rho_{\mathrm{R}}^{(l)(\mathrm{t})} \right\}, \tag{4.51}$$

with $[\mathbf{K}_{\rho}]$ and $[\mathbf{P}_{\rho}]$ given by

$$[\mathbf{K}_{\rho}] = \int_{\mathrm{V}_{\mathrm{RVE}}} [\mathbf{L}_{\rho}]^{\mathrm{T}} \, [\mathbf{L}_{\rho}] \, \mathrm{dV} \quad \text{and} \quad [\mathbf{P}_{\rho}] = \int_{\mathrm{V}_{\mathrm{RVE}}} [\mathbf{L}_{\rho}]^{\mathrm{T}} \, [\mathbf{A}_{\mathrm{t}}] \, [\mathbf{N}] \mathrm{dV}. \tag{4.52}$$

Equation (4.51) gives the linear algebraic system the solution of which updates the dislocation density field. Because the the least squares operator depends on the previous time step the resulting discretized system is linear in the updated dislocation density. It is important to mention here that, due to the lack of a direct coupling between the dislocation transport equations corresponding to various slip systems, the evolution of the individual slip system densities can be updated individually. Further details on how to separate the transport equations when reactions are present can be found in [188].

4.6.2 Field dislocation mechanics update of plastic distortion

Updating the dislocation density over a time step incrementally changes the dislocation configuration. This update then contains the information required to compute the increment in the plastic distortion over the same time step. Since it is hard to compute the differential change in the plastic distortion from the differential change in the dislocation configuration, Orowan's equation is often used to give the plastic distortion rate, which can then be integrated in time to update the plastic distortion. This update algorithm proved to result in inconsistencies between the dislocation field and the stress field. In the recent work by [126], it was shown that the field dislocation mechanics approach [12] is more effective as it computes the incompatible part of the plastic distortion from the dislocation content. The latter approach is based on the use of the relationship between the vector density of dislocations and the incompatible and compatible parts of the plastic distortion, see equations (4.20) and (4.23). Within the field dislocation mechanics framework, the incompatible part of the plastic distortion satisfies the boundary value problem:

$$\begin{aligned} \mathrm{Curl}\Big(\boldsymbol{\chi}^{\mathrm{p}(\mathrm{t}+\Delta\mathrm{t})}\Big) = \boldsymbol{\alpha}^{\mathrm{RM}} &= \sum_{l} \boldsymbol{\rho}_{\mathrm{R}}^{(l)(\mathrm{t}+\Delta\mathrm{t})} \otimes \mathbf{b}_{\mathrm{M}}^{(l)} \text{ in } V_{\mathrm{RVE}} \\ \mathrm{Div}(\boldsymbol{\chi}^{\mathrm{p}(\mathrm{t}+\Delta\mathrm{t})}) &= 0, \text{ in } V_{\mathrm{RVE}} \\ \mathbf{n} \cdot \chi &= 0 \text{ on } \partial V_{\mathrm{RVE}}. \end{aligned} \tag{4.53}$$

In the above, the time-dependence is implied via the dislocation density $\boldsymbol{\rho}_{\mathrm{R}}^{(l)(\mathrm{t}+\Delta\mathrm{t})}$. We obtain a discretized form of these equations using the FOSLS approach. We start by first writing these equations in a matrix form,

$$\begin{bmatrix} 0 & -\partial_{\mathrm{X}_3} & \partial_{\mathrm{X}_2} \\ \partial_{\mathrm{X}_3} & 0 & -\partial_{\mathrm{X}_1} \\ -\partial_{\mathrm{X}_2} & \partial_{\mathrm{X}_1} & 0 \\ \partial_{\mathrm{X}_1} & \partial_{\mathrm{X}_2} & \partial_{\mathrm{X}_3} \end{bmatrix} \begin{bmatrix} \chi^{\mathrm{p}}_{11} & \chi^{\mathrm{p}}_{21} & \chi^{\mathrm{p}}_{31} \\ \chi^{\mathrm{p}}_{12} & \chi^{\mathrm{p}}_{22} & \chi^{\mathrm{p}}_{32} \\ \chi^{\mathrm{p}}_{13} & \chi^{\mathrm{p}}_{23} & \chi^{\mathrm{p}}_{33} \end{bmatrix} = \begin{bmatrix} \alpha^{\mathrm{RM}}_{11} & \alpha^{\mathrm{RM}}_{12} & \alpha^{\mathrm{RM}}_{13} \\ \alpha^{\mathrm{RM}}_{21} & \alpha^{\mathrm{RM}}_{22} & \alpha^{\mathrm{RM}}_{23} \\ \alpha^{\mathrm{RM}}_{31} & \alpha^{\mathrm{RM}}_{32} & \alpha^{\mathrm{RM}}_{33} \\ 0 & 0 & 0 \end{bmatrix}. \tag{4.54}$$

The above system of equations can be thought of as solving three partial differential equations for the columns of the tensor $\boldsymbol{\chi}^{p(t+\Delta t)}$,

$$\mathbf{L}_{\chi^p}\begin{bmatrix}\chi^p_{i1}\\ \chi^p_{i2}\\ \chi^p_{i3}\end{bmatrix}=\begin{bmatrix}\alpha^{RM}_{1i}\\ \alpha^{RM}_{2i}\\ \alpha^{RM}_{3i}\\ 0\end{bmatrix},\quad i=[1,2,3] \tag{4.55}$$

where $\mathbf{L}_{\chi^p}$ is given by

$$\mathbf{L}_{\chi^p}=[\mathbf{C}_{X_1}]\frac{\partial}{\partial X_1}+[\mathbf{C}_{X_2}]\frac{\partial}{\partial X_2}+[\mathbf{C}_{X_3}]\frac{\partial}{\partial X_3} \tag{4.56}$$

and the matrices $[\mathbf{C}_{X_1}],[\mathbf{C}_{X_2}]$ and $[\mathbf{C}_{X_3}]$ by

$$[\mathbf{C}_{X_1}]=\begin{bmatrix}0&0&0\\0&0&-1\\0&1&0\\1&0&0\end{bmatrix},\quad [\mathbf{C}_{X_2}]=\begin{bmatrix}0&0&1\\0&0&0\\-1&0&0\\0&1&0\end{bmatrix},\quad [\mathbf{C}_{X_3}]=\begin{bmatrix}0&-1&0\\1&0&0\\0&0&0\\0&0&1\end{bmatrix}. \tag{4.57}$$

The least squares residual corresponding to (4.55) can then be developed by moving all terms to the left-hand side, squaring that side and integrating over the domain of the solution. Upon discretization of the domain, taking the first variation of that residual and setting that equal to zero, we obtain the algebraic system in the form

$$[\mathbf{K}_{\chi^p}]\left\{\chi^{p(t+\Delta t)}\right\}=[\mathbf{P}_{\chi^p}]\left\{\alpha^{MR(t+\Delta t)}\right\}, \tag{4.58}$$

where

$$\begin{aligned}[\mathbf{K}_{\chi^p}]&=\int_{V_{RVE}}\left[\mathbf{L}_{\chi^p}\right]^T\left[\mathbf{L}_{\chi^p}\right]dV\\ [\mathbf{P}_{\chi^p}]&=\int_{V_{RVE}}\left[\mathbf{L}_{\chi^p}\right]^T[\mathbf{C}_0][\mathbf{N}]dV\\ \left[\mathbf{L}_{\chi^p}\right]&=[\mathbf{C}_{X_1}][\mathbf{B}_{X_1}]+[\mathbf{C}_{X_2}][\mathbf{B}_{X_2}]+[\mathbf{C}_{X_3}][\mathbf{B}_{X_3}].\end{aligned} \tag{4.59}$$

In the above, the matrices $\mathbf{B}_{\mathrm{X}_1}, \mathbf{B}_{\mathrm{X}_2}$ and $\mathbf{B}_{\mathrm{X}_3}$ are the same as the ones in (4.50) and $[\mathbf{C}_0]$ is defined by

$$[\mathbf{C}_0] = \begin{bmatrix} 1 & 0 & 0 \\ 0 & 1 & 0 \\ 0 & 0 & 1 \\ 0 & 0 & 0 \end{bmatrix}. \tag{4.60}$$

Next, we turn attention to updating the compatible part of the plastic distortion. Starting with (4.23), the governing field equations are:

$$\begin{aligned} \mathrm{Div}\left(\mathrm{Grad}\left(\dot{\mathbf{V}}^{\mathrm{p}}\right)\right) =& \mathrm{Div}\left(\sum_l \mathbf{b}_{\mathrm{M}}^{(l)} \otimes \left(\mathbf{v}_{\mathrm{R}}^{(l)} \times \boldsymbol{\rho}_{\mathrm{R}}^{(l)}\right)\right) \text{ in } V_{\mathrm{RVE}} \\ \mathbf{n} \cdot \mathrm{Grad}\dot{\mathbf{V}}^{\mathrm{p}} =& \mathbf{n} \cdot \left(\sum_l \mathbf{b}_{\mathrm{M}}^{(l)} \otimes \left(\mathbf{v}_{\mathrm{R}}^{(l)} \times \boldsymbol{\rho}_{\mathrm{R}}^{(l)}\right)\right) \text{ on } \partial \mathrm{V}_{\mathrm{RVE}} \\ \mathbf{V}^{\mathrm{p}} =& \mathbf{V}_0^{\mathrm{p}} \text{ (arbitrary value) at one point in } V_{\mathrm{RVE}}. \end{aligned} \tag{4.61}$$

Equations (4.61) and (4.53) are valid in general and produce a unique decomposition of the plastic distortion. The reader is referred to [12] where these equations are discussed in more detail. Following [126], a time discretization may be introduced as follows:

$$\mathrm{Div}\left(\mathrm{Grad}\left(\mathbf{V}^{\mathrm{p(t+\Delta t)}}\right)\right) = \mathrm{Div}\left(\mathrm{Grad}\left(\mathbf{V}_0^{\mathrm{p(t)}}\right)\right) + \Delta \mathrm{t} \mathrm{Div}\left(\sum_l \mathbf{b}_{\mathrm{M}}^{(l)} \otimes \left(\mathbf{v}_{\mathrm{R}}^{(l)(\mathrm{t})} \times \boldsymbol{\rho}_{\mathrm{R}}^{(l)(\mathrm{t+\Delta t})}\right)\right). \tag{4.62}$$

Furthermore, a standard Galerkin finite element method can be used to develop the corresponding weak form,

$$\begin{aligned} \{\delta \mathbf{V}\}^{\mathrm{T}} \int_{V_{\mathrm{RVE}}} [\mathbf{B}]^{\mathrm{T}} [\mathbf{B}] \mathrm{d}\Omega \left\{\mathbf{V}^{\mathrm{p(t+\Delta t)}}\right\} =& \{\delta \mathbf{V}\}^{\mathrm{T}} \int_{V_{\mathrm{RVE}}} [\mathbf{B}]^{\mathrm{T}} [\mathbf{B}] \mathrm{d}\Omega \left\{\mathbf{V}^{\mathrm{p(t)}}\right\} \\ &+ \{\delta \mathbf{V}\}^{\mathrm{T}} \int_{V_{\mathrm{RVE}}} [\mathbf{B}]^{\mathrm{T}} \mathrm{d}\Omega \left\{\mathbf{p}^{\mathrm{t+\Delta t}}\right\}, \end{aligned} \tag{4.63}$$

where $\{\delta \mathbf{V}\}$ denotes the nodal values of the test functions, $[\mathbf{B}]$ is a matrix containing the derivative of the shape functions, $\left\{\mathbf{V}^{\mathrm{p(t+\Delta t)}}\right\}$ denotes the nodal values of the updated compatible plastic distortion and $\mathbf{p}^{\mathrm{t+\Delta t}}$ equals the quantity $\Delta t \sum_l \mathbf{b}_{\mathrm{M}}^{(l)} \otimes \left(\mathbf{v}_{\mathrm{R}}^{(l)(\mathrm{t})} \times \boldsymbol{\rho}_{\mathrm{R}}^{(l)(\mathrm{t+\Delta t})}\right)$ in-

terpolated to the the Gauss points. For an arbitrary $\{\delta\mathbf{V}\}$ the above weak form reduces to

$$[\mathbf{K}_{\mathbf{V}^{\mathrm{P}}}]\left\{\boldsymbol{V}^{\mathrm{p(t+\Delta t)}}\right\}+[\mathbf{M}]\left\{\mathbf{p}^{\mathrm{t+\Delta t}}\right\}=[\mathbf{K}_{\mathrm{V}\boldsymbol{p}}]\left\{\mathbf{V}^{\mathrm{p(t)}}\right\}. \tag{4.64}$$

where

$$\begin{aligned}[\mathbf{K}_{\mathbf{V}^{\mathrm{P}}}]&=\int_{V_{\mathrm{RVE}}}[\mathbf{B}]^{\mathrm{T}}[\mathbf{B}]\mathrm{d}\Omega \\ [\mathbf{M}]&=\int_{V_{\mathrm{RVE}}}[\mathbf{B}]^{\mathrm{T}}\mathrm{d}\Omega.\end{aligned} \tag{4.65}$$

The discretized forms (4.51), (4.58) and (4.64) for the dislocation density, the incompatible and the compatible parts of the plastic distortion, respectively, are solved concurrently to yield the dislocation density field and the plastic distortion field. The latter is constructed from its compatible and incompatible parts according to (4.18). As mentioned in Section 4, the updated plastic distortion is used in the calculation of the tangent modulus (4.43) and in the stress update (4.39).

4.7 Overview of computational algorithm

This section summarizes the overall algorithm used to update both the crystal mechanics and dislocation fields. We adopt a staggered scheme for solving the mechanics and dislocation field problems. In a future extension of this work, a fully coupled scheme can be implemented in which the transport solution can be incorporated within the iterative process used to handle the geometric non-linearity of the mechanics problem. The staggered scheme adopted here solves the mechanics problem first, then exports the stress solution via a mobility law to the dislocation transport problem. The update of the plastic distortion is then sent back to the mechanics problem in the next time step, and the solution proceeds as such until a stop criterion is satisfied. The plastic distortion update is completed using the field dislocation mechanics equations (4.53) and (4.61), and it can be fully coupled with the transport solution as done here or separate from the transport equations as was done in [188, 126].

The initialization of the overall algorithm starts by introducing an initial dislocation density field and the associated plastic distortion field. The algorithm then begins by solving the crystal mechanics problem at the first time step upon applying a load increment and using the initial plastic distortion field. The obtained stress is used to solve the transport problem for the first update of the dislocation field and update the plastic distortion field. The initial dislocation density can be prescribed in any fashion, so long as it satisfies the line continuity properly. In our case, we use ensembles of 'diffuse' loops distributed randomly in the simulation volume, with periodicity enforced so that a given loop can be full or segmented depending on the location of its center in the domain and its size. All initial fields are thus periodic and, by enforcing periodicity on the solution, they remain so throughout the evolution process. The driving Peach-Koehler force on dislocations is computed from (4.26) in terms of Mandel stress. The dislocation velocity is then found using the mobility law (4.25), which is used as an input field in the dislocation transport problem. The overall computational solution algorithm is illustrated in 4.1.

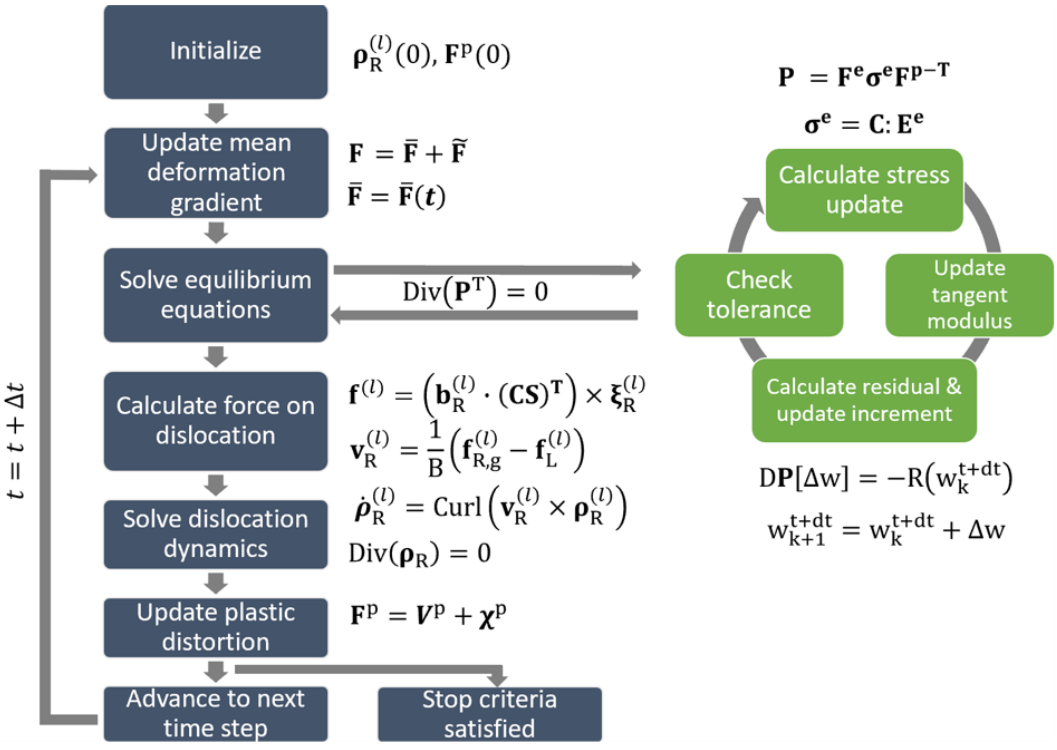

Figure 4.1. Algorithm for solving the strain controlled continuum dislocation dynamics problem at finite deformation.

The time step is controlled by the accuracy of the solution of the transport problem. Of course, time step considerations also arise in updating the plastic distortion field, particularly in solving the field problem of the incompatible part, see (4.61), but this problem is coupled to the solution of the transport problem in our case. Here, the time step is determined such that the dislocation cannot traverse the smallest element in the mesh in one time step. This is quantified by introducing the Courant–Friedrichs–Lewy (CFL) number. The CFL number, which is defined by,

$$\text{CFL} = \frac{|\boldsymbol{v}_{\max}|\Delta t}{l_{\min}} \tag{4.66}$$

where $l_{\min}$ is the minimal element dimension size over the whole mesh, Δt is the timestep size, and $|\boldsymbol{v}_{\max}|$ is the magnitude of the max velocity over all slip systems and nodes in the simulation domain. In a typical simulation the CFL number is specified and the timestep Δt is determined using (4.66).

The computational algorithm outlined above is implemented in the open-source, massively parallel finite element software called MOOSE [7, 61]. This implementation is accomplished by creating a CDD application within the MOOSE framework. In this application kernels for the set of transport equations (4.51), (4.58), and (4.64) are created. Another application for the total Lagrangian implementation of the crystal mechanics equations is created and includes kernels for the equilibrium equations (4.38) along with a material model for computing the PK1 stress (4.39) and the tangent modulus (4.43). The staggered scheme is implemented using the MultiApp feature in MOOSE and data transfers between both applications to transfer the plastic distortion tensor to the total Lagrange application and dislocation forces to the CDD application. Time stepping is implemented so that the time step size depends on the dislocation velocity and the smallest element size.

4.8 Test problems

This section presents several test problems with increasing complexity to illustrate the effectiveness of the numerical algorithm. The mesh used in these tests consists of a mixture of tetrahedron and pyramid elements such that each slip plane is reproduced so as to capture the planar motion of dislocations accurately. On each slip plane, the mesh contains

equilateral triangles with the exception of elements near the boundary where different size elements are used to create a flat face on the boundary of the solution domain. The reader is referred to [197] for more details on the creation of the mesh. A sample mesh is shown in Figure 4.2. In these tests the slip system $(111)[0\bar{1}1]$ will be used and denoted by SS1. The computation domain is oriented such that the x, y and z axes correspond to the [110], $[\bar{1}10]$ and [001] crystal directions, respectively. The calculations are performed on copper with a shear modulus of 44 GPa, Poisson's ratio of 0.34 and Burgers vector magnitude of 0.254 nm. These values are adopted from [172]. We also use a dislocation drag coefficient of 5.5×10^{-5} MPa s.

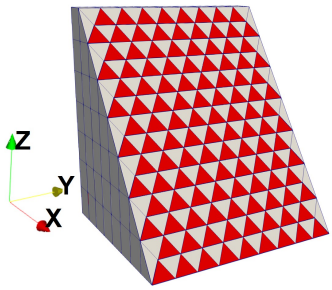

Figure 4.2. The mesh used in the test problems consists of tetrahedron and pyramid elements. This special mesh is able to capture the slip planes in FCC crystals, which accurately reproduces the planar motion of dislocations.

4.8.1 A loop-like dislocation configuration under constant velocity

In this test we consider a loop-like dislocation configuration on slip system SS1, which we will refer to as a loop for simplicity. The loop is located at the center of the simulation domain with a density distribution that is created using a Gaussian profile for the dislocation density field over its azimuthal cross sections. The loop is subjected to a prescribed glide velocity of magnitude $|\mathbf{v}_{\mathrm{R}}^{(l)}|$ to test the discretized transport relations in (4.51) without coupling to crystal mechanics. Time snapshots of the simulation are shown in Fig. 4.3, where we see the initial loop expanding and annihilating as it comes in contact with the periodic neighboring loops at the boundary of the simulation domain.

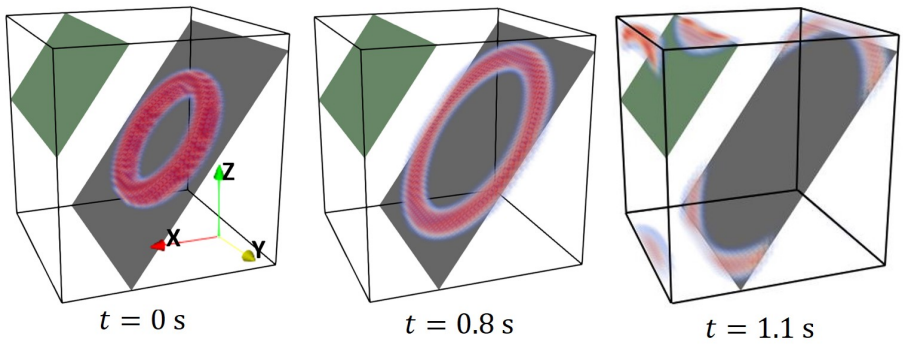

Figure 4.3. Snapshots showing the evolution of an expanding dislocation loop. In the middle snapshot the loop starts to annihilate with its periodic images on both sides in the y-direction. The last snapshot shows the periodic images expanding into the simulation domain.

Under a prescribed dislocation velocity the following analytical form holds as the solution of the transport equation (4.24) in cylindrical coordinates for a circular dislocation loop (bundle) in an infinite domain:

$$\boldsymbol{\rho}_{\mathrm{R}}^{(\mathrm{l})}(\mathrm{r},\theta,\mathrm{h},\mathrm{t}) = \frac{1}{2\pi \mathrm{L}^2}\exp\left(\frac{-[\mathrm{r}-(\mathrm{R}_0+|\mathbf{v}_{\mathrm{R}}^{(l)}|\mathrm{t})]^2-\mathrm{h}^2}{2\mathrm{L}^2}\right)\mathbf{e}_\theta. \tag{4.67}$$

In the above, R_0 is the major radius of the loop, h is the coordinate normal to the slip plane, r is the radial coordinate on the cross section of the loop, L is a parameter that controls the width of the loop, and $\mathbf{e}_\theta$ is the unit vector that points the azimuthal direction of the loop. This analytical solution can be used to assess the accuracy of the numerical solution. However, we remove the periodic boundary conditions to make this comparison, allowing dislocations to flow out of the domain and mimic the infinite domain solution. In this test we use a loop with a radius of $\mathrm{R}_0 = 0.25\,\mu\mathrm{m}$ and $|\mathbf{v}_{\mathrm{R}}^{(l)}| = 0.3\,\mu\mathrm{m/s}$ in a simulation domain of size $1\mu\mathrm{m} \times 1\mu\mathrm{m} \times 1\mu\mathrm{m}$. Fig. 4.4 shows a line plot of the dislocation density along the radial direction AA′ of the loop on a central plane. The figure compares the analytical solution with the numerical solution at different mesh densities. The density is plotted at the time at which the density peak crosses the domain boundary. It can be noted that the numerical solution results in some level of diffusion, which is characteristic of the backward Euler time integration. We also see that the solution does not change appreciably when

the mesh density is changed for the range of mesh resolution considered here. We further notice that the dislocation distribution travels at the same speed as the analytic solution and therefore does not develop any dispersion errors.

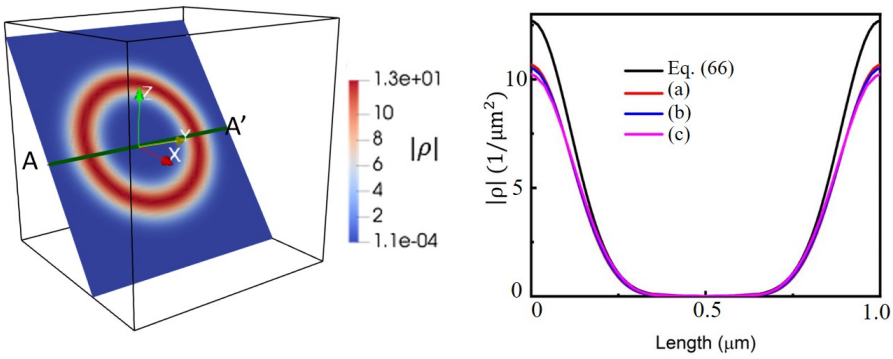

Figure 4.4. A snapshot of the solution corresponding to the moment at which the peak density crosses the boundary of the domain, corresponding to different mesh density, plotted together with the analytical solution (4.67). (a), (b) and (c) correspond to 80, 60 and 40 mesh points along the line AA′ in the left part of the figure, respectively.

4.8.2 A loop-like dislocation configuration coupled with crystal mechanics

In this subsection, we present a test problem similar to the one described above but with the dislocation velocity given in terms of the stress using the mobility law (4.27), with the Taylor term dropped. The dislocation density is placed on slip system SS1 and the evolution is driven by an imposed domain-average constant deformation gradient

$$\bar{\mathbf{F}} = \begin{bmatrix} 1 & 0 & 0 \\ 0 & 1 & 0 \\ 0 & 0 & 1.0001 \end{bmatrix}, \tag{4.68}$$

where the 33 component is chosen to be larger than unity so that the dislocation loop expands under its own induced self stress. A simulation domain of size $5\mu\text{m} \times 5\mu\text{m} \times 5.3\mu\text{m}$ is considered in this and all subsequent tests. Fig. 4.5 (a) shows the evolution of the dislocation density. The behavior of the dislocation density evolution is similar to the constant velocity

test case in the previous subsection, see Fig. 4.3, where we observe mutual annihilation with the periodic images on the sides and the emergence of the periodic images at the top and bottom of the solution domain.

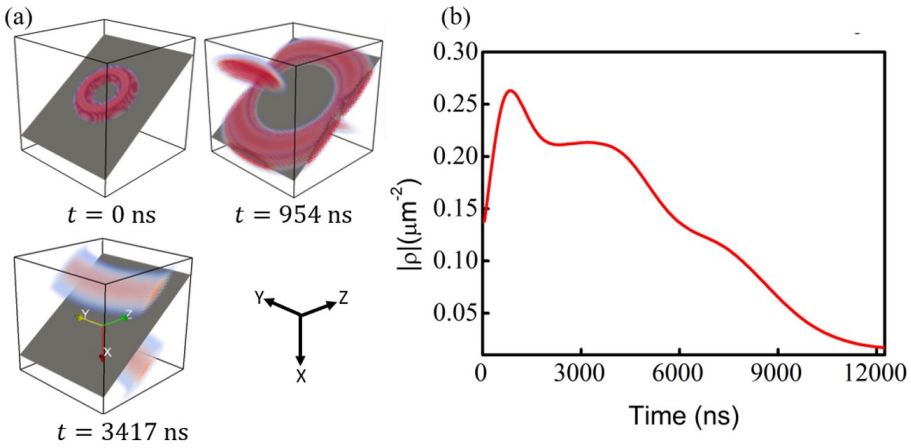

Figure 4.5. A loop configuration on a single slip system under an imposed constant deformation gradient. (a) Snapshots of the evolution of the dislocation configuration. The glide planes are parallel to grey plane in the figure. Annihilation of the loop with its periodic images is shown in the second snapshot in part (a) while the periodic images are shooting into the domain in the third snapshot. (b) The average dislocation density in the domain plotted as a function of time.

In Fig. 4.5 (b) the average dislocation density evolution is shown which is obtained by integrating the local norm $||\boldsymbol{\rho}|| = \sqrt{\rho_1^2 + \rho_2^2 + \rho_3^2}$ over the volume of the domain in the reference configuration,

$$\frac{1}{\mathrm{V}} \int_{\mathrm{V}} ||\boldsymbol{\rho}_{\mathrm{R}}|| \mathrm{dV}. \tag{4.69}$$

We see that the density initially increases due to the expansion of the loop, then decreases due to the loop annihilating with its periodic neighbor. After around 2000 nanoseconds, the average density briefly flattens marking the end of the annihilation of a portion of the loop on the sides. Now the loop consists of approximately straight segments at the top and bottom sides that span the width of the box; see the last snapshot in Fig. 4.5 (a). These straight segments pass through the periodic domain until they are close to one another leading to subsequent partial annihilation. As they continue to annihilate, the total density decreases, as seen in Fig. 4.5 (b).

In Fig. 4.6, we compare the evolution of the average dislocation density over time for various CFL numbers. The CFL numbers are prescribed, and the timestep is determined from (4.66). When the CFL number is 2, the average dislocation density vastly differs from the other cases. This is due to the large diffusion that the implicit Euler time integrator introduces at larger timesteps. To a lesser extent, this can also be seen in the CFL = 1 curve, where the density starts to dip after 2000 nanoseconds again deviating from the more accurate behavior at CFL values below 1. For value of CFL = 0.25 and CFL = 0.5 the curves are closer together idicating that a CFL value of 0.5 or less is adequate.

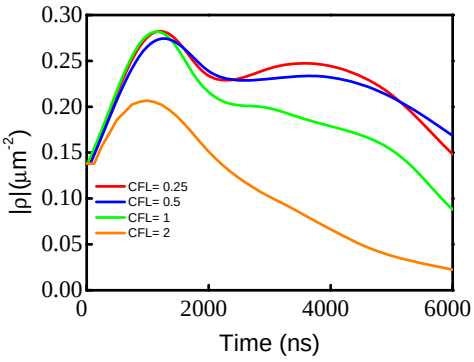

Figure 4.6. Evolution of the dislocation density for the single loop test. Each colored plot corresponds to a different CFL number used in calculating the timestep size.

In a previous publication [177] we have shown the stress field of the loop-like configuration. Here we show the corresponding distortion of the crystal. Fig. 4.7 shows a snapshot of the displacement fluctuation field, $\mathbf{w}$, as a distribution of vectors whose length is proportional to its magnitude. In this case, $\mathbf{w}$ corresponds to the displacement caused by the loop itself. We note that the displacement on either side of the glide plane passing trough the center of the loop is opposite, which is consistent with the fact that we have a jump in the displacement field due the slip caused by the dislocation creation and motion.

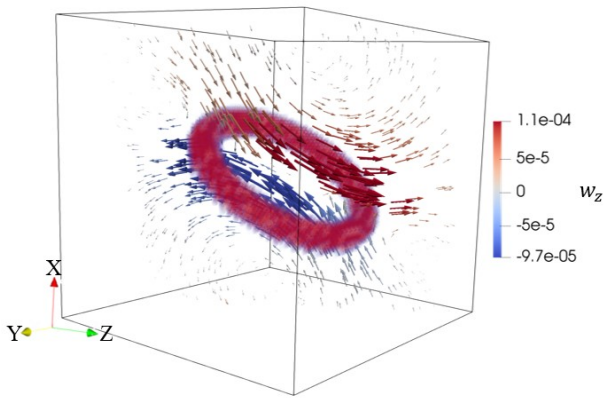

Figure 4.7. Displacement fluctuation field associated with the dislocation loop shown on a slice perpendicular to the glide plane. The vectors are colored according to the z component of the displacement fluctuations.

4.8.3 A loop-like dislocation configuration of a high density

For this dislocation configuration we are interested in viewing the elastic fields that a large localized plastic distortion causes in the crystal. We initialize a dense dislocation loop (100 times as dense as in previous test case) in the center of the cube on SS1, with a radius of 1.5 μm. First we apply an identity tensor for the mean deformation gradient that drives the loop to shrink and disappear. The initial density distribution and time snapshots of the dislocation configuration are shown in Fig. 4.8. In part (a) of this figure we see that the interior of the loop shrinks faster than the exterior part due to the attractive forces caused by the oppositely oriented periodic neighboring loops. A plot of the dislocation density calculated from (4.69) versus time is shown in part (b). In the latter plot, we see that as the loop shrinks the total density decreases. At a certain point in time the dislocation density starts decreasing at a slower rate due to the exterior part of the line bundle being attracted to the oppositely oriented neighboring loop. This has the effect of smearing out the dislocation bundle as can be seen in the last snapshot in Fig. 4.8 (a).

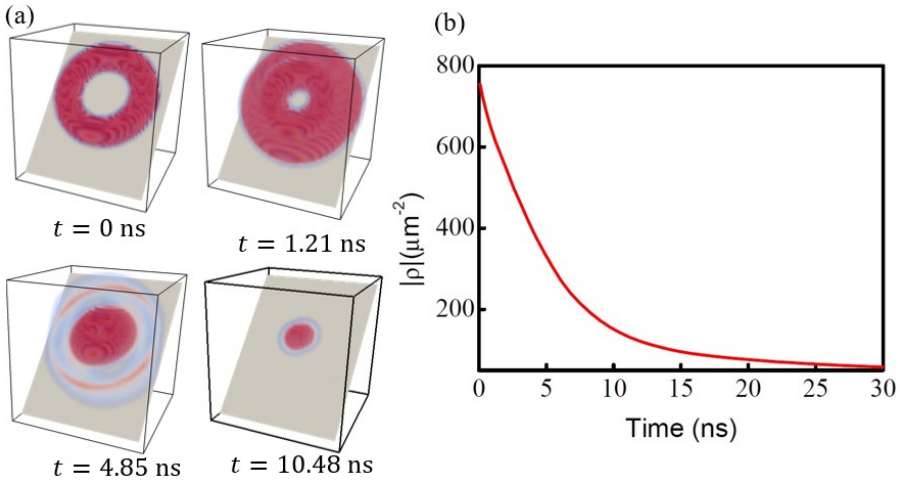

Figure 4.8. Dense dislocation loop with an applied mean deformation gradient equal to the identity. (a) Evolution of the loop configuration with time. (b) The dislocation density versus time. We see in part (a) that the interior of the loop shrinks faster than then its exterior due to the periodicity of the domain.

Next, we apply a deformation gradient that forces the loop to expand. This gradient is given by

$$\overline{\mathbf{F}} = \begin{bmatrix} 1 & 0 & 0 \\ 0 & 1 & 0 \\ 0 & 0 & 1.015 \end{bmatrix}.$$

We note that, in this case, a larger deformation compared to (4.68) was required to overcome the self stresses that would cause the dislocation loop to shrink. Fig. 4.9 (a) shows the plot four snapshots of the expanding dislocation loop along with the time evolution of the density in the domain. We note that the behavior of the dislocation density is similar to the less dense loop case given in Fig. 4.5 (a). However, the step-like shape of the dislocation density plot in Fig. 4.5 (b) have now been smoothed out in the current test, see Fig. 4.9 (b), due to the spreading of the loop caused by the intense repulsion within. We also notice that the time scales for the evolution of the less dense and the dense dislocation loops are vastly different. This difference is due to the larger stresses introduced by the 33 component of the mean deformation gradient in the latter case, which was needed to overcome the self stress

that the dense loop suffers. This lead to a larger elastic response of the crystal and thus larger driving forces for the expansion of the loop.

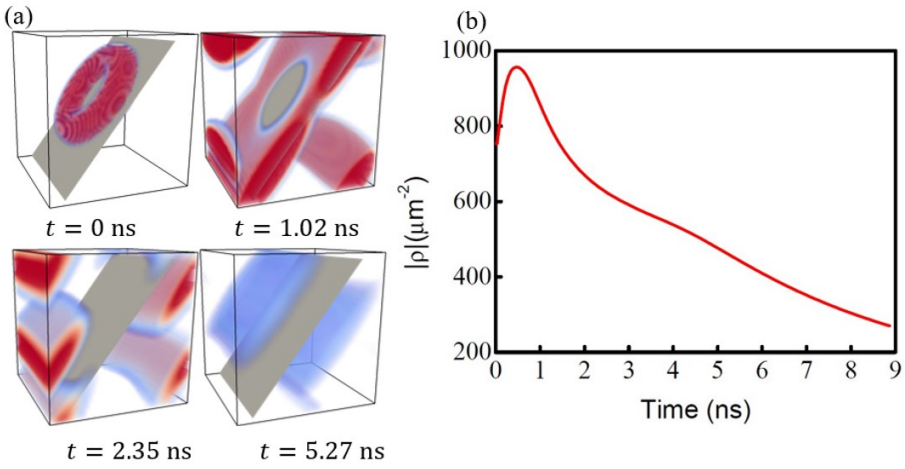

Figure 4.9. Dense dislocation bundle test loaded along the z-axis with a 1.5% strain for the 33 component of the mean deformation gradient. (a) Time snapshots of a dense dislocation loop expanding under the applied mean deformation gradient. (b) The dislocation density plotted versus time.

To quantify the elastic lattice rotation in the case of the dense dislocation loop, the polar decomposition $\mathbf{F}^{\mathrm{e}} = \mathbf{R}^{\mathrm{e}}\mathbf{U}^{\mathrm{e}}$ is used with $\mathbf{U}^{\mathrm{e}}$ being the right stretch tensor and $\mathbf{R}^{\mathrm{e}}$ being the elastic rotation. We calculate the rotation in terms of a rotation vector $\boldsymbol{\theta} = \theta\boldsymbol{\omega}$, with θ being the magnitude of rotation about axis $\boldsymbol{\omega}$ [113]. The vector $\boldsymbol{\omega}$ is related to the pure rotation part $\mathbf{R}^{\mathrm{e}}$ of the elastic distortion $\mathbf{F}^{\mathrm{e}}$ via,

$$\mathbf{R}^{\mathrm{e}} = \exp(\boldsymbol{\Omega}) = \cos(\theta)\mathbf{I} + \sin(\theta)\,(\boldsymbol{\omega}\times) + (1 - \cos(\theta))\,\boldsymbol{\omega}\otimes\boldsymbol{\omega} \tag{4.70}$$

where $\boldsymbol{\Omega} = (\boldsymbol{\theta}\times)$ is an anti-symmetric second order tensor with $\boldsymbol{\theta}$ as its axial vector. In the current case, $\mathbf{F}^{\mathrm{e}}$ is found from $\mathbf{F}^{\mathrm{e}} = \mathbf{F}\mathbf{F}^{\mathrm{p}-1}$. Once the elastic distortion is known the rotation vector can be solved for using (4.70), following the procedure laid out in [123]. In the following figure we plot the axial vector for the dense dislocation loop. We notice in this figure that the rotation is localized near the dislocation loop, as expected, due to the jump in the displacement field across the slipped surface and the induced elastic strains. We also notice that the Burgers vector is perpendicular to the rotation vector on the slipped surface.

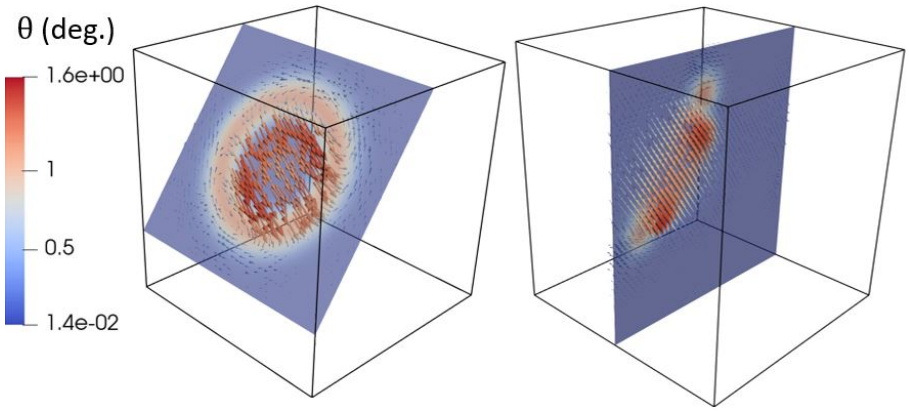

Figure 4.10. Rotation vector displayed on two sections in the domain of the solution. The dislocation density field is plotted as the background on each section to show where the dislocation are relative to the rotation vectors. We see that the majority of the rotation is localized near the dense dislocation loop, specifically near the slipped area where the displacement field takes a jump by the Burgers vector.

4.8.4 Tilt boundary test

This test demonstrates the dynamic recovery process associated with the annihilation of two oppositely oriented tilt boundaries. In a previous publication we analyzed the stress distribution across the two tilt boundaries [177]. In this test, we use the same configuration but analyze the dynamics of boundary annihilation. The tilt boundaries consist of a vertical arrays of edge dislocations generated by uniform plastic strain of 4% in the channel between the boundaries. The plastic strain is large enough to fall within the realm of finite deformation. The termination of slip at the boundaries with sharp gradients creates the dislocation arrays. The non-trivial component of the plastic distortion is F^p_{13} along with the only nonzero corresponding referential dislocation density tensor α^R_{21}. The dislocation lines run along the y-direction for positive dislocations and along the negative y-direction for negative dislocations, with the crystallographic Burgers vector (the direction of slip) pointing in the x-direction, see Fig. 4.11.

The recovery process occurs by applying a deformation gradient equal to the identity, which, in effect, reverses the plastic distortion introduced initially and annihilates all dislocations. Fig. 4.12 shows the evolution of the dislocation density and lattice rotation during

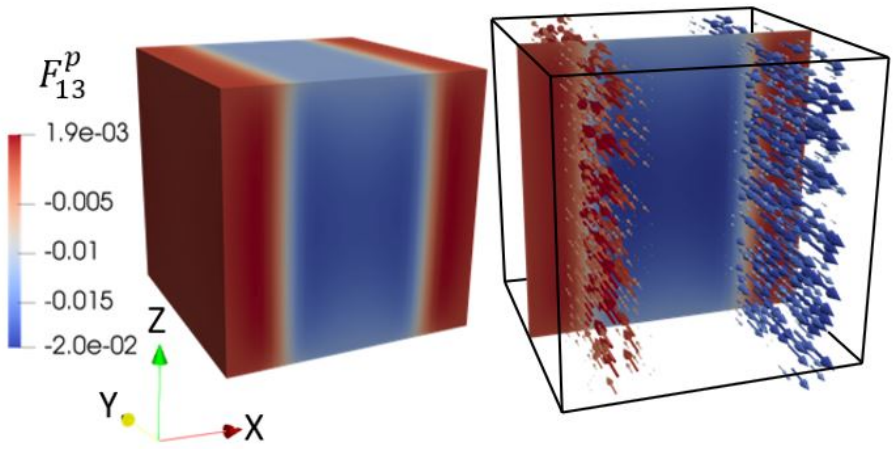

Figure 4.11. Initial configuration of the two tilt boundaries. The left cube shows the only component of the plastic distortion differing from the identity. On the right, a section on the x-z plane indicates the uniform distribution of the plastic distortion through the thickness of the domain. The arrows on that section represent the vector dislocation density, which point in opposite directions in the two tilt walls.

the recovery process. The figure shows that, as the tilt boundaries approach each other and annihilate, the rotation of the crystal is reduced in the deformed configuration. In the last time frame we see that the deformation has completely vanished due to the annihilation of the the tilt boundaries. The average dislocation density is plotted in Fig. 4.13, which shows that the density decays slowly first as the dislocations spread out of the walls, but then faster as more opposite dislocations encounter each other. The decay of the density in time slows down again when the density is mostly consumed by annihilation.

4.8.5 One slip system with an ensemble of Frank-Read sources

A single slip, uniaxial tension simulation test is presented in this subsection. An initial dislocation configuration consisting of an ensemble of loops distributed randomly throughout the domain over SS1 is considered. To avoid the effect of self-annihilation due to periodic boundary conditions, we introduce Frank-Read sources to aid the multiplication process, which would occur due to cross slip under multi-slip conditions. The sources are placed at random locations in the simulation domain and added as half loops with an initial radius of

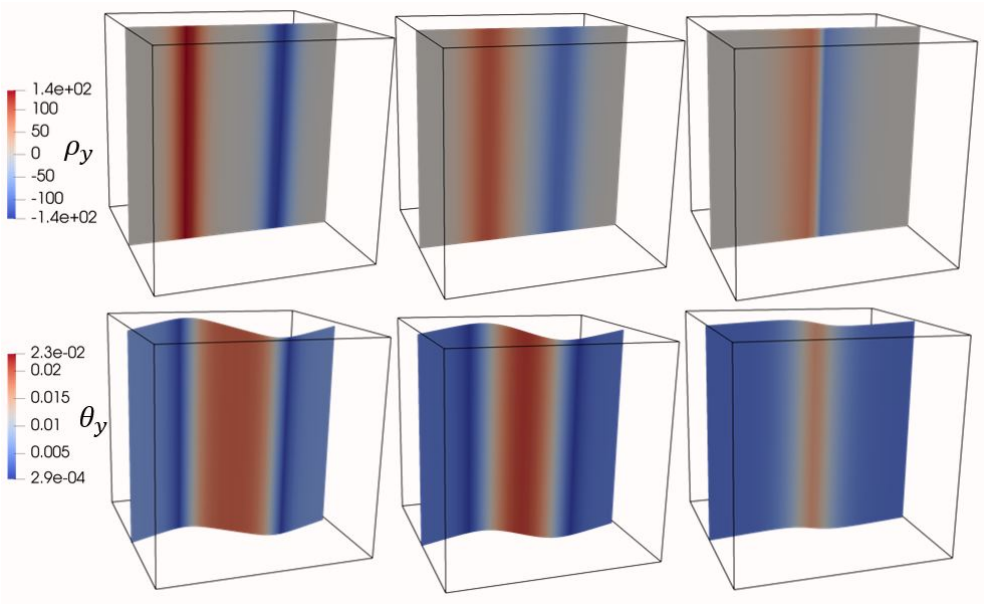

Figure 4.12. Depiction of the time evolution of a recovery process for two tilt boundaries. Time increases from left to right. The top shows a slice through the domain of the dislocation density and the bottom shows the corresponding deformed configuration (with the deformation magnified for clarity). We see that as the dislocation bundles start to annihilate the deformed configuration relaxes to a state with no deformation.

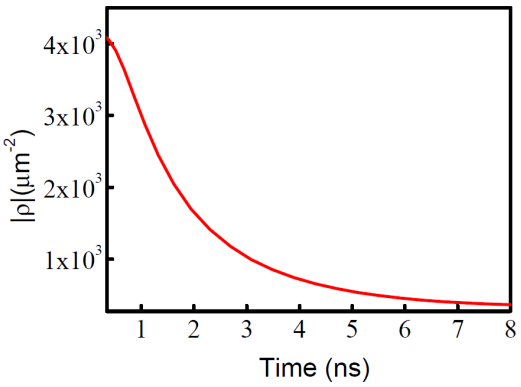

Figure 4.13. The dislocation density versus time for the case of annihilation of two opposite tilt boundaries

1.5μm. The uniaxial tension test loading conditions are realized through a mixture of stress and strain loading conditions. For this test, we load the $5\mu\text{m} \times 5\mu\text{m} \times 5.3\mu\text{m}$ simulation box under uniaxial tension by prescribing the 33 component of the mean deformation gradient at a prescribed rate and force all the components of the mean stress field to zero except the

33 component. To accomplish this with minimal effort we introduce the small deformation approximate of the mean stress field

$$\overline{\boldsymbol{\sigma}} = \mathbb{C}\left(\overline{\boldsymbol{\beta}} - \overline{\boldsymbol{\beta}}^{p}\right) \tag{4.71}$$

where $\mathbb{C}$ is the fourth order elasticity tensor, $\overline{\boldsymbol{\beta}} = \overline{\mathbf{F}} - \mathbf{I}$ is the mean displacement gradient, and $\overline{\boldsymbol{\beta}}^{p} = \overline{\mathbf{F}^{\mathrm{p}}} - \mathbf{I}$ is the mean plastic distortion. At every timestep we fix the 33 component of the mean deformation gradient and then solve for the remaining components so that (4.71) is zero for each stress component that is not in the loading direction. We specify the rate of the mean displacement gradient in the 33 direction to be 20/s and thus the 33 component of the mean deformation gradient is specified as one plus this rate term. We also include the Taylor friction stress term in the velocity expression with a hardening coefficient of 0.6 [188].

Fig. 4.14 (a) shows the predicted 33 component of the PK1 stress against the the strain imposed by the deformation gradient. The figure also shows the evolution of the dislocation density as a function of strain in part (b). We notice that, initially, the stress-strain curve is nearly purely elastic due to the resolved shear stress being less than the lattice friction stress. This results in little or no dislocation activity and no changes in the plastic distortion. As the applied strain increases so does the stress, which increases the resolved shear stress and the dislocations gradually start to glide, increasing the plastic slip at an increasing rate. This can be seen in the increase of the dislocation density in part (b) of Fig. 4.14. In this region in the stress-strain curve the plastic distortion rate is larger than the mean applied strain rate of $20/s$ and thus the mean stress reaches a peak and then begins to decrease. After this, the plastic distortion rate approaches a constant value that is just below the mean applied strain rate leading to a positive elastic strain rate and and subsequently an increase in the mean stress over time. We note that the shape of the stress-strain curve (peak of mean stress, followed by a decrease, then a gradual increase) obtained above is similar in form to the one obtained in [166] which also depicts the stress-strain curve for the single slip system case.

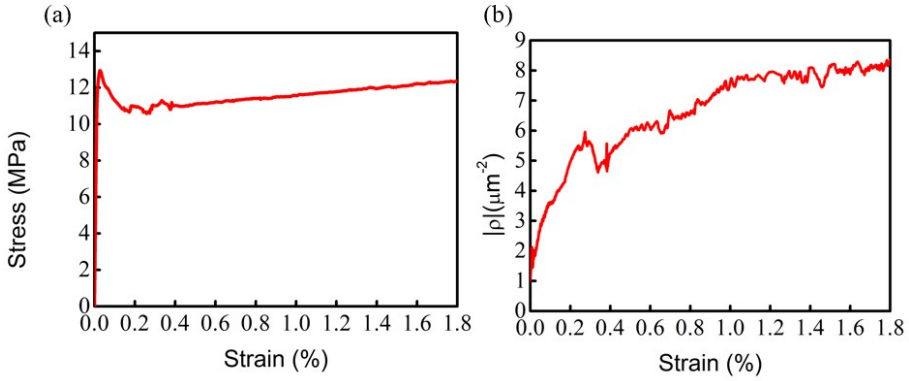

Figure 4.14. Uniaxial tension test with single slip. (a) Stress-strain curve. (b) Dislocation density evolution against strain.

Some important features of the numerical algorithm developed here have been examined in the test problems presented in this section. The first test problem illustrated the solution of the transport equations without coupling with crystal mechanics by prescribing a velocity field for the dislocations. Crystal mechanics was then added to the solution scheme in the test given in Section 7.2, which tests the full solution of the dislocation density evolution at small strain. Following this test, the effect of finite deformation on the solution was tested by introducing a dense dislocation field in the form of a loop within the line bundle representation of dislocations. The latter test was meant to show the effect of finite lattice rotation on the dislocation evolution. In Section 7.4 a test simulating two opposing tilt boundaries is introduced which also shows the effects of large lattice rotation. This test also illustrates the evolution of the lattice rotation field as the tilt boundary evolve. Finally, in Section 7.5, a uniaxial tension test is performed on a single slip system with multiple Frank-Read sources to analyze the evolution of the average dislocation density and stress-strain curve.

The first test illustrates the stability of the numerical algorithm in solving the CDD transport equations with the FOSLS algorithm, although there is some numerical diffusion. The next test showed the numerical stability of the algorithm when the crystal mechanics were coupled. A comparison of different CFL numbers was also made where it was shown that a CFL values of 0.5 was adequate for these simulations. The large density loop tests

and tilt boundary test introduce large lattice rotation effects which did not seem to affect the stability of the numerical algorithm. The last test displayed the long-term stability of the fully coupled numerical scheme. The majority of tests above were performed on a mesh consisting of a mixture of tetrahedral and pyramid elements summing to 458,489 elements. The typical element side length is on the order of 0.1μm. With a CFL value of 0.5 the typical timestep size ranged from $6 - 15$ ns in the last test, which is comparable to a small deformation simulation of the same test. Therefore, a similar number of timesteps are taken for the large deformation simulation. However, slightly more computational work is required for each step in the finite deformation code due to sub-iterations necessary for the geometric nonlinearities. We note that the diffusive nature of the numerical algorithm does not seem to affect the models ability to capture material hardening as can be seen in the single slip system test.

4.9 Concluding remarks

A numerical algorithm for solving the coupled mesoscale dislocation transport and mechanical equilibrium equations at finite deformation was developed using a total Lagrangian approach. The algorithm developed here is based upon a homogenization scheme, which makes it suitable for solving mesoscale plasticity problems driven by average deformation gradient or strain. The key components on the mechanics side of this algorithm include the calculation of the consistent tangent modulus for each element in (4.40) and the stress update in (4.39). The latter involves an updated value of the plastic distortion obtained from the continuum dislocation dynamics model. Due to the dependence of the dislocation velocity on the previous time-step solution, we were able to decouple the nonlinear iterations of the mechanics problem from the update of the dislocation transport equations in (4.51). After discretizing both the mechanics and CDD boundary value problems, we introduce a number of test problems to demonstrate the performance of our algorithm, including loop-like configurations of dislocations driven by constant velocity and applied deformation gradient (Strain), annihilation of two opposite tilt boundaries, and a single slip stress-strain behavior test.

In the kinematic test of a loop-like configuration driven by a constant velocity, it was shown that the numerical solution exhibited some diffusive behavior, an issue that is well documented for the backward Euler time integration scheme. We also noticed that the dislocation bundle traveled at the same speed as the analytic solution, which we attribute to low dispersion errors. In the subsequent cases where the dislocation velocity was computed using the referential Mandel stress through the mobility law of the dislocations, the solution behaved as expected, namely, the loop-like dislocation configurations shrank or expanded depending on the imposed deformation gradients. In the tilt boundary problem, dynamic recovery process was demonstrated, where dislocations on the opposite walls collided and annihilated each other giving an undeformed final configuration. Finally, the predicted stress-strain curve and dislocation density evolution in the uniaxial tensile test problem showed an identical behavior to a similar case in the literature [166], where a uniaxial single slip test was carried out using a different dislocation dynamics model.

An alternative to the staggered solution scheme presented in this work would be to strongly couple the crystal mechanics and dislocation transport equations. However, this strong coupling would introduce a nonlinearity in the transport equations due to the dependence of the dislocation velocity on the updated stress field. Furthermore, more computational work would be required to calculate the Jacobian of the residuals at each iteration within each time step. For this reason, we chose at this stage to use the staggered approach presented here, but a comparison of the staggered approach and the strongly coupled case would be an important topic of future work.

Due to the staggered solution scheme used here, we treated the plastic distortion as fixed over each time step, and only the geometric nonlinearity of crystal mechanics part is handled iteratively. A fixed value of the plastic distortion over a time step allowed us to have a linear stress update, differing from conventional crystal plasticity theories. However, this linear stress update was at the cost of solving an additional transport equations of the dislocation density update.

4.A Tangent modulus

This section provides the details of the derivation of the tangent modulus,$\partial\mathbf{P}/\partial\mathbf{F}^{\mathbf{t+\Delta t}}$, which is given in the main document. To evaluate this expression we introduce the transformation relation between the PK1 stress and the PK2 stress in the microstructure space, $\mathbf{P}{=}\mathbf{F}\mathbf{F}^{\mathrm{p}-1}\boldsymbol{\sigma}^{\mathrm{e}}\mathbf{F}^{\mathrm{p}-\mathrm{T}}$ where $\mathrm{J}^{\mathrm{p}}=1$ has been used because we are considering dislocation glide motion only. We write the PK2 stress in the microstructure space as a function of the updated deformation gradient and get

$$\mathbf{P}{=}\mathbf{F}^{\mathrm{t}+\Delta\mathrm{t}}\mathbf{F}^{\mathrm{p}-1}\boldsymbol{\sigma}^{\mathrm{e}}\left(\mathbf{F}^{\mathrm{t}+\Delta\mathrm{t}}\right)\mathbf{F}^{\mathrm{p}-\mathrm{T}}.$$

For the remaining derivation we will switch to index notation to make the derivation more explicit. Taking the derivative of the above expression and by using the product rule, we write,

$$\begin{aligned}\frac{\partial \mathrm{P}_{\mathrm{iJ}}}{\partial \mathrm{F}^{\mathrm{t}+\Delta\mathrm{t}}_{\mathrm{kL}}}&=\frac{\partial \mathrm{F}^{\mathrm{t}+\Delta\mathrm{t}}_{\mathrm{im}}}{\partial \mathrm{F}^{\mathrm{t}+\Delta\mathrm{t}}_{\mathrm{kL}}}\mathrm{F}^{\mathrm{p}-1}_{\mathrm{m}\alpha}\sigma^{\mathrm{e}}_{\alpha\beta}\mathrm{F}^{\mathrm{p}-\mathrm{T}}_{\beta\mathrm{J}}+\mathrm{F}^{\mathrm{t}+\Delta\mathrm{t}}_{\mathrm{iM}}\mathrm{F}^{\mathrm{p}-1}_{\mathrm{M}\alpha}\frac{\partial \sigma^{\mathrm{e}}_{\alpha\beta}}{\partial \mathrm{F}^{\mathrm{t}+\Delta\mathrm{t}}_{\mathrm{kL}}}\mathrm{F}^{\mathrm{p}-\mathrm{T}}_{\beta\mathrm{J}} \qquad (4.72)\\ &=\frac{\partial \mathrm{F}^{\mathrm{t}+\Delta\mathrm{t}}_{\mathrm{im}}}{\partial \mathrm{F}^{\mathrm{t}+\Delta\mathrm{t}}_{\mathrm{kL}}}\mathrm{F}^{\mathrm{p}-1}_{\mathrm{m}\alpha}\sigma^{\mathrm{e}}_{\alpha\beta}\mathrm{F}^{\mathrm{p}-\mathrm{T}}_{\beta\mathrm{J}}+\mathrm{F}^{\mathrm{e}(\mathrm{t}+\Delta\mathrm{t})}_{\mathrm{i}\alpha}\frac{\partial \sigma^{\mathrm{e}}_{\alpha\beta}}{\partial \mathrm{F}^{\mathrm{t}+\Delta\mathrm{t}}_{\mathrm{kL}}}\mathrm{F}^{\mathrm{p}-\mathrm{T}}_{\beta\mathrm{J}}, \qquad (4.73)\end{aligned}$$

To compute the tangent modulus we have to compute the $\frac{\partial \sigma^{\mathrm{e}}_{\mathrm{no}}}{\partial \mathrm{F}^{\mathrm{t}+\Delta\mathrm{t}}_{\mathrm{kl}}}$ term. Using the chain rule we get,

$$\frac{\partial \sigma^{\mathrm{e}}_{\alpha\beta}}{\partial \mathrm{F}^{\mathrm{t}+\Delta\mathrm{t}}_{\mathrm{kL}}}=\frac{\partial \sigma^{\mathrm{e}}_{\alpha\beta}}{\partial \mathrm{E}^{\mathrm{e}}_{\gamma\delta}}\frac{\partial \mathrm{E}^{\mathrm{e}}_{\gamma\delta}}{\partial \mathrm{F}^{\mathrm{e}}_{\mathrm{c}\theta}}\frac{\partial \mathrm{F}^{\mathrm{e}}_{\mathrm{c}\theta}}{\partial \mathrm{F}^{\mathrm{t}+\Delta\mathrm{t}}_{\mathrm{kL}}}. \qquad (4.74)$$

From the multiplicative decomposition,$\mathrm{F}^{\mathrm{e}}_{\mathrm{c}\gamma}{=}\mathrm{F}_{\mathrm{cM}}\mathrm{F}^{\mathrm{p}-1}_{\mathrm{M}\gamma}$, the last term $\frac{\partial \mathrm{F}^{\mathrm{e}(\mathrm{t}+\Delta\mathrm{t})}_{\mathrm{c}\theta}}{\partial \mathrm{F}^{\mathrm{t}+\Delta\mathrm{t}}_{\mathrm{kL}}}$ can be written as,$\frac{\partial \mathrm{F}^{\mathrm{e}(\mathrm{t}+\Delta\mathrm{t})}_{\mathrm{c}\theta}}{\partial \mathrm{F}^{\mathrm{t}+\Delta\mathrm{t}}_{\mathrm{kL}}}{=}\delta_{\mathrm{ck}}\delta_{\mathrm{ML}}\ \mathrm{F}^{\mathrm{p}-1}_{\mathrm{M}\theta}{=}\delta_{\mathrm{ck}}\mathrm{F}^{\mathrm{p}-1}_{\mathrm{L}\theta}$. From the constitutive relation, $\sigma^{\mathrm{e}}_{\alpha\beta}{=}\mathbb{C}_{\alpha\beta\gamma\delta}\mathrm{E}^{\mathrm{e}}_{\gamma\delta}$, we get $\frac{\partial \sigma^{\mathrm{e}}_{\alpha\beta}}{\partial \mathrm{E}^{\mathrm{e}}_{\gamma\delta}}{=}\mathbb{C}_{\alpha\beta\gamma\delta}$. Also, from (4.14) we have,

$$\frac{\partial \mathrm{E}^{\mathrm{e}}_{\gamma\delta}}{\partial \mathrm{F}^{\mathrm{e}}_{\mathrm{c}\theta}}=\frac{1}{2}\left(\delta_{\gamma\theta}\mathrm{F}^{\mathrm{e}}_{\mathrm{c}\delta}+\mathrm{F}^{\mathrm{e}}_{\mathrm{c}\gamma}\delta_{\delta\theta}\right).$$

Due to the symmetry properties of the elasticity tensor we can write

$$\begin{aligned}\frac{\partial \sigma^{e}_{\alpha\beta}}{\partial F^{e}_{c\theta}} =& \frac{\partial \sigma^{e}_{\alpha\beta}}{\partial E^{e}_{\gamma\delta}} \frac{\partial E^{e}_{\gamma\delta}}{\partial F^{e}_{c\theta}} \\ =& \mathbb{C}_{\alpha\beta\theta\delta} F^{e}_{c\delta}.\end{aligned}$$

Then (4.74) becomes

$$\frac{\partial \sigma^{e}_{\alpha\beta}}{\partial F^{t+\Delta t}_{kL}} = \frac{\partial \sigma^{e}_{\alpha\beta}}{\partial F^{e}_{c\theta}} \frac{\partial F^{e}_{c\theta}}{\partial F^{t+\Delta t}_{kL}} = \mathbb{C}_{\alpha\beta\theta\delta} F^{e}_{k\delta} F^{p-1}_{L\theta}. \tag{4.75}$$

From (4.75), (4.73) becomes

$$\frac{\partial P_{iJ}}{\partial F^{t+\Delta t}_{kL}} = \delta_{ik} F^{p-1}_{L\alpha} \sigma^{e}_{\alpha\beta} F^{p-T}_{\beta J} + F^{e(t+\Delta t)}_{i\alpha} \mathbb{C}_{\alpha\beta\theta\delta} F^{e}_{k\delta} F^{p-1}_{L\theta} F^{p-1}_{J\beta} \tag{4.76}$$

which is the expression used in the main document.

4.B CDD discretization

The following matrices are used in the discretization of the dislocation transport equations section and have been put here for readability of the main document.

$$[\mathbf{A}_t] \equiv \begin{bmatrix} 1 & 0 & 0 \\ 0 & 1 & 0 \\ 0 & 0 & 1 \\ 0 & 0 & 0 \end{bmatrix}, [\mathbf{A}_0] \equiv \begin{bmatrix} -\partial_{X_2} v_2 - \partial_{X_3} v_3 & \partial_{X_2} v_1 & \partial_{X_3} v_1 \\ \partial_{X_1} v_2 & -\partial_{X_1} v_1 - \partial_{X_3} v_3 & \partial_3 v_2 \\ \partial_{X_1} v_3 & \partial_{X_2} v_3 & -\partial_{X_1} v_1 - \partial_{X_2} v_2 \\ 0 & 0 & 0 \end{bmatrix}. \tag{4.77}$$

$$[\mathbf{A}_{X_1}] \equiv \begin{bmatrix} 0 & 0 & 0 \\ v_2 & -v_1 & 0 \\ v_3 & 0 & -v_1 \\ 1 & 0 & 0 \end{bmatrix}, [\mathbf{A}_{X_2}] \equiv \begin{bmatrix} -v_2 & v_1 & 0 \\ 0 & 0 & 0 \\ 0 & v_3 & -v_2 \\ 0 & 1 & 0 \end{bmatrix}, [\mathbf{A}_{X_3}] \equiv \begin{bmatrix} -v_3 & 0 & v_1 \\ 0 & -v_3 & v_2 \\ 0 & 0 & 0 \\ 0 & 0 & 1 \end{bmatrix} \tag{4.78}$$

We also derive the discretized least squares operator given in the transport section which is integrated in the weak form expression in (4.49). We approximate the integral by the Gauss quadrature method [16] which is typically done in finite element methods [16] By using finite element shape functions, we can represent the unknown density vector at each quadrature point by its interpolation from nodal values on each base element.

$$\{\boldsymbol{\rho}\} = [\mathbf{N}] \begin{bmatrix} \rho_1^{\mathrm{n1}} \\ \rho_2^{\mathrm{n1}} \\ \rho_3^{\mathrm{n1}} \\ \dots \\ \rho_1^{\mathrm{nN}} \\ \rho_2^{\mathrm{nN}} \\ \rho_3^{\mathrm{nN}} \end{bmatrix}, \{\delta\boldsymbol{\rho}\} = [\mathbf{N}] \begin{bmatrix} \delta\rho_1^{\mathrm{n1}} \\ \delta\rho_2^{\mathrm{n1}} \\ \delta\rho_3^{\mathrm{n1}} \\ \dots \\ \delta\rho_1^{\mathrm{nN}} \\ \delta\rho_2^{\mathrm{nN}} \\ \delta\rho_3^{\mathrm{nN}} \end{bmatrix},$$

where $[\mathbf{N}]$ is the vector shape function operator defined by,

$$[\mathbf{N}] = \begin{bmatrix} \mathrm{N}_1 & 0 & 0 & \dots & \mathrm{N}_\mathrm{N} & 0 & 0 \\ 0 & \mathrm{N}_1 & 0 & \dots & 0 & \mathrm{N}_\mathrm{N} & 0 \\ 0 & 0 & \mathrm{N}_1 & \dots & 0 & 0 & \mathrm{N}_\mathrm{N} \end{bmatrix},$$

and each of the $\mathrm{N_i}$ are the shape functions evaluated at each node in the element. Typical analytic expressions for these (isoparametric) shape functions evaluated on their base ele-

ments can be found in [16]. We can also interpolate derivatives to the quadrature points using the derivatives of these shape functions,

$$\frac{\partial}{\partial \mathrm{X_i}}\left\{\boldsymbol{\rho}\right\} = \left[\mathbf{B}_{\mathrm{X_i}}\right]\begin{bmatrix} \rho_1^{\mathrm{n1}} \\ \rho_2^{\mathrm{n1}} \\ \rho_3^{\mathrm{n1}} \\ \dots \\ \rho_1^{\mathrm{nN}} \\ \rho_2^{\mathrm{nN}} \\ \rho_3^{\mathrm{nN}} \end{bmatrix}, \frac{\partial}{\partial \mathrm{X_i}}\left\{\delta\boldsymbol{\rho}\right\} = \left[\mathbf{B}_{\mathrm{X_i}}\right]\begin{bmatrix} \delta\rho_1^{\mathrm{n1}} \\ \delta\rho_2^{\mathrm{n1}} \\ \delta\rho_3^{\mathrm{n1}} \\ \dots \\ \delta\rho_1^{\mathrm{nN}} \\ \delta\rho_2^{\mathrm{nN}} \\ \delta\rho_3^{\mathrm{nN}} \end{bmatrix},$$

where ρ_1^{n1} denotes the first density component value at node 1 in the element and $\mathrm{B_{x_i}}$ is defined by,

$$\left[\mathbf{B}_{\mathrm{X_i}}\right] = \begin{bmatrix} \frac{\partial \mathrm{N_1}}{\partial \mathrm{X_i}} & 0 & 0 & \dots & \frac{\partial \mathrm{N_N}}{\partial \mathrm{X_i}} & 0 & 0 \\ 0 & \frac{\partial \mathrm{N_1}}{\partial \mathrm{X_i}} & 0 & \dots & 0 & \frac{\partial \mathrm{N_N}}{\partial \mathrm{X_i}} & 0 \\ 0 & 0 & \frac{\partial \mathrm{N_1}}{\partial \mathrm{X_i}} & \dots & 0 & 0 & \frac{\partial \mathrm{N_N}}{\partial \mathrm{X_i}} \end{bmatrix}.$$

Using these definitions, we can form the discretized least squares operator,

$$\left[\mathbf{L}_\rho\right] = \left\{\left[\mathbf{A}_\mathrm{t}\right] - \Delta \mathrm{t}\left[\mathbf{A}_0\right]\right\}\left[\mathbf{N}\right] - \Delta \mathrm{t}\left(\left[\mathbf{A}_{\mathrm{X_1}}\right]\left[\mathbf{B}_{\mathrm{X_1}}\right] + \left[\mathbf{A}_{\mathrm{X_2}}\right]\left[\mathbf{B}_{\mathrm{X_2}}\right] + \left[\mathbf{A}_{\mathrm{X_3}}\right]\left[\mathbf{B}_{\mathrm{X_3}}\right]\right). \tag{4.79}$$

5. THEORY OF DISLOCATION REACTIONS

A portion of this chapter is previously published in the Journal of the Mechanics and Physics of Solids by Kyle Starkey, Thomas Hochrainer, Anter El-Azab as "Development of mean-field continuum dislocation kinematics with junction reactions using de Rham currents and graph theory", 158, 104685. https://doi.org/10.1016/j.jmps.2021.104685

5.1 Abstract

An accurate description of the evolution of dislocation networks is an essential part of discrete and continuum dislocation dynamics models. These networks evolve by motion of the dislocation lines and by forming junctions between these lines via cross slip, annihilation and junction reactions. In this work, we introduce these dislocation reactions into continuum dislocation models using the theory of de Rham currents. We introduce dislocations on each slip system as potentially open lines whose boundaries are associated with junction points and, therefore, still create a network of collectively closed lines that satisfy the classical relations $\boldsymbol{\alpha} = \mathrm{curl}\boldsymbol{\beta}^{\mathrm{p}}$ and $\mathrm{div}\boldsymbol{\alpha} = 0$ for the dislocation density tensor $\boldsymbol{\alpha}$ and the plastic distortion $\boldsymbol{\beta}^{p}$. To ensure this, we leverage Frank's second rule at the junction nodes and the concept of virtual dislocation segments. We introduce the junction point density as a new state variable that represents the distribution of junction points within the crystal containing the dislocation network. Adding this information requires knowledge of the global structure of the dislocation network, which we obtain from its representation as a graph. We derive transport relations for the dislocation line density on each slip system in the crystal, which now includes a term that corresponds to the motion of junction points. We also derive the transport relations for junction points, which include source terms that reflect the topology changes of the dislocation network due to junction formation.

5.2 Introduction

The present work introduces a new paradigm for incorporating dislocation junction reactions in continuum dislocation dynamics modeling of mesocale plasticity. The development

of plasticity theories using continuum descriptions of dislocations has received much attention in the mathematics, mechanics, and materials science communities for many decades [109, 43, 88, 62]. It is known that the treatment of dislocations within a continuum or density-based framework presents a major challenge, not least because they react to form complex three-dimensional networks [175]. Dislocation reactions include cross slip, a process by which a moving dislocation line changes its glide plane, annihilation reactions, and junction formation. Such processes are responsible for the dislocation multiplication, immobilization of a significant part of the dislocation population, and the subsequent emergence of self-organized dislocation density patterns [24]. A junction reaction is one in which two dislocation segments with different Burgers vectors react to form a segment of a third Burgers vector, which may be mobile in the crystal (glissile junction), immobile (sessile junction), or null (annihilation).

Junction formation has received a great deal of attention in discrete dislocation dynamics models [131, 174]. Many authors have also investigated the strength of these junctions using atomic scale models [159, 133, 205, 173]. In discrete dislocation dynamics, it has been shown that among the various types of junctions reactions, glissile junctions are one of the main contributors to hardening because they lead to dislocation multiplication [175]. Sessile junctions, on the other hand, are believed to anchor the dislocation pattern and lead to its refinement. Currently, the literature on discrete dislocation dynamics has abundant information describing the topology of dislocation networks including junctions. This information comes in the form of the connectivity information between the lines and nodes in the dislocation network [154], which is updated as the network evolves under applied stress. While the discrete dislocation dynamics models easily track dislocation networks in 3D by introducing rules for cross slip and junction formation, continuum dislocation dynamics formulations are still lacking such a representation as they mostly rely on the average line length information, see, for example, [180], [177], [11], and [84].

Continuum dislocation dynamics (CDD) theories which incorporate long range interactions in microscopic driving forces (resolved shear stresses) have been derived from pair correlations for strongly simplified systems of straight parallel edge dislocation [62, 63, 96]. Continuum variables suited to characterize systems of curved dislocation lines have been

introduced, which may be combined with standard methods of irreversible thermodynamics to obtain natural generalizations of the quasi-2D theory of straight edge dislocations [84]. However, the continuum theory of curved dislocations currently lacks the consideration of dislocation junctions and other dislocation reactions, which are known to cause the emergence of a yield stress and its evolution in strain hardening, a process that is attributed to the multiplication of dislocations. Various dislocation reactions and dislocation multiplication have been recently incorporated in continuum theories of dislocations, both in the so-called line-bundle approximation [125] and in the higher length scale CDD theory [140, 179, 182]. The available models for dislocation reactions and junctions are usually adopted from empirical rules and are based on statistical dislocation variables, which do not reflect the complex interconnected network formed by dislocations. Ideally, if the dislocation density variables would reflect the salient features of the dislocation networks, their evolution should 'naturally' account for reactions and multiplication. However, so far, no continuum variables have been suggested which would reflect at least in a rudimentary way the complexity of an interconnected network of dislocations.

As of now, the most detailed way of describing the dislocation content of a volume element in CDD is a series of dislocation alignment and curvature tensors [83, 189] which approximate a higher dimensional vectorial description of closed dislocation lines [81]. Differential forms have been an important tool for the development of the higher dimensional theory, which are obtained from averaging dislocations viewed as (vector valued and higher dimensional) de Rham currents [81]. Also the named tensor series may be obtained from averaging tensor valued de Rham currents. In an n-dimensional space, smooth differential $(n-1)$ forms may represent densities of curves and thus in principle also curves which make up a complex network. However, while the notion of closeness of differential forms comprises some topological information, most of the topology of the network is not reflected in such differential forms; the topology of networks falls in the realm of graph theory but the graph theory itself does not describe the geometry of the dislocation network.

In the current work, we take first steps to integrate dislocation network information, including dislocation junctions and their connections to adjacent lines, into a continuum description of dislocations. In doing so, we use a vector representation of the dislocation

density within the line bundle approximation, where the density on a given slip system has a single line direction at every 'continuum' point in space. Within this framework, the resolution is selected such that the geometric cancellation due to the use of a vector representation of the density coincides with the physical annihilation of dislocations [188, 8]. An important tool to be used regard to developing a continuum description of dislocations is de Rham integral currents [38], where we consider dislocation networks to consist of junction points and line like interconnects. The connectivity information of the dislocation network is established by using the graph theory. In doing so, we exploit the partitioning characteristics of dislocation networks which result from the nature of the junction formation process, specifically the induced subgraphs corresponding to each type of junction. Focusing mainly on glissile junction representation in continuum dislocation dynamics, we introduce a junction point density to model the evolving dislocation network. The introduction of this density amounts to building connectivity information into the continuum dislocation dynamics framework.

In the next section, we introduce some of the mathematical preliminaries, including de Rham integral currents. The following section introduces the dislocation density tensor on each slip system for the case in which dislocations may be open or closed lines due to reactions. We show that, due to Frank's second rule the total dislocation density tensor and plastic distortion still satisfy $\int_F \boldsymbol{\alpha} = \int_{\partial F} \boldsymbol{\beta}^p$. In the next section, we introduce a new object, $\mathbf{\Pi}^{(l)}$, which is a measure of the endpoints of dislocation lines of each slip system l. We show that this new measure is related to the dislocation density tensor on the lth slip system, through $\mathbf{\Pi}^{(l)} = \mathrm{d}\boldsymbol{\alpha}^{(l)}$. We then represent the dislocation network in a graph-theoretic setting in order to establish a connection between the endpoint density and the junction point density for one junction type. While establishing this connection, we found that, for the case of dislocation networks established via glissile junction formation among different slip systems, the graph representing the dislocation network is r-partite, which allows us to consistently orient the graph and relate its orientation to the sign of the junction point density. This ultimately helps in developing the transport equations for open dislocation lines and the junction points for a mean-field description. In these transport equations, the mean-field velocity is assumed to be a prescribed field that is to be determined from the

kinetics of the dislocation system. We end with a section on deriving source terms for the junction point density transport equation.

5.3 A brief overview of currents

The concept of de Rham currents generalizes Dirac delta distributions, which are localized at a point, to singular objects localized on extended objects, like, e.g., curves or surfaces. Relatively recently, currents have been used in the mathematical modeling of dislocations. [33] showed that, due to their additive group structure, de Rham currents can be used to represent crystal dislocations. In [88], this additive structure has been employed in ensemble averaging to derive continuum measures of dislocations. In [56], a continuum mechanics framework of defects was proposed through the use of currents in which dislocations represent a special case. [147] used spatial averaging to show that the smooth continuum measure of dislocations is a limit of singular de Rham currents. An important relation regarding dislocation reactions is Frank's second rule at each junction node. [55] used currents to show Frank's second rule can be viewed as a consequence of a topological property, $\partial\partial = \emptyset$, where ∂ denotes the boundary operator on manifolds. They also introduce the idea of a signed point current defined by the boundary of a dislocation line. In the present work we employ currents for averaging and make use of the innate geometrical calculus defined on them, including their connection to conservation laws in terms of Lie derivatives.

Some mathematical preliminaries regarding de Rham currents are introduced first to motivate further developments. A broader introduction to the relevant concepts can be found in [38] and [57]. Since we will only be using integral currents, the algebra and calculus of differential forms will be useful and we refer the reader to many texts introducing differential forms [132, 21, 149]. In the following, all manifolds and submanifolds are always implicitly understood as *oriented* manifolds. We assume an underlying n-dimensional manifold $\mathcal{M}$. Currents on $\mathcal{M}$ are continuous linear functionals on the space of smooth differential forms with compact support in $\mathcal{M}$. Differential forms of degree k may be integrated over k-

dimensional sub-manifolds. Given a k-submanifold, $\mathcal{N}$, it defines a k-current, denoted by $T_{\mathcal{N}}$, acting on k-forms θ through

$$T_{\mathcal{N}}[\theta] = \int_{\mathcal{N}} \theta. \tag{5.1}$$

For obvious reasons, a k-current is said to have dimension k. We will use currents defined this way to represent the singular defects. As discussed in Section 5.4, averages over such singular objects are expected to yield smooth differential $(n-k)$-forms. The latter constitute the other basic example of k-currents, defined by an $(n-k)$-form ω through,

$$T_{\omega}[\theta] = \int_{\mathcal{M}} \omega \wedge \theta. \tag{5.2}$$

Dual to the dimension k we call $(n-k)$ the degree of a current. As currents are dual to differential forms, key operations on differential forms induce corresponding operations on currents. We start with the definition of the wedge product of a current T with a differential form ω, denoted by $T \wedge \omega[\theta]$, and defined by

$$T \wedge \omega[\theta] = T[\omega \wedge \theta]. \tag{5.3}$$

The reverse order is defined by the antisymmetry property of the wedge product on differential forms, i.e., $\omega \wedge T = (-1)^{pq} T \wedge \omega$ if ω and T are of degree p and q, respectively. The wedge product of two currents is in general not defined. However, for two currents $T_{\mathcal{N}_1}$ and $T_{\mathcal{N}_2}$ originating from two submanifolds $\mathcal{N}_1$ and $\mathcal{N}_2$ of complementary dimension in $\mathcal{M}$, i.e., $\dim(\mathcal{N}_1) + \dim(\mathcal{N}_1) = n$, which only intersect transversally and neither meets the boundary of the other, the wedge product is a 0-dimensional current, which when applied to the constant function 1 yields the oriented intersection number $I(\mathcal{N}_1, \mathcal{N}_2)$ of the (oriented) submanifolds [65],

$$T_{\mathcal{N}_1} \wedge T_{\mathcal{N}_2}[1] = I(\mathcal{N}_1, \mathcal{N}_2). \tag{5.4}$$

The interior product of a p-current T with vector field $\boldsymbol{X}$ is a $p+1$-current defined by

$$\mathrm{i}_{\boldsymbol{X}} T[\theta] = (-1)^{p+1} T\left[\mathrm{i}_{\boldsymbol{X}} \theta\right]. \tag{5.5}$$

In the case where the current is defined from a submanifold, the interior product yields a current which can be thought of representing the infinitesimal increment of the submanifold being swept along with the vector field $\boldsymbol{X}$ [88].

Stokes theorem for differential forms,

$$\int_{\partial\mathcal{N}} \theta = \int_{\mathcal{N}} d\theta, \tag{5.6}$$

is used to define both the boundary operator and the exterior differential of currents. The boundary operator on currents is defined as

$$\partial T[\theta] = T[\mathrm{d}\theta], \tag{5.7}$$

while the exterior derivative on currents is defined as,

$$\mathrm{d}T[\theta] = (-1)^{p+1} T[\mathrm{d}\theta], \tag{5.8}$$

where the sign may be rationalized from the product rule of the exterior differential. For two currents T_1 and T_2, the dimensions of which add up to $n+1$, one of which has compact support, and if either $\partial T_1 \wedge T_2[1]$ or $T_1 \wedge \mathrm{d}T_2[1]$ is defined, then so is the other and they are equivalent [38],

$$\partial T_1 \wedge T_2[1] = T_1 \wedge \mathrm{d}T_2[1]. \tag{5.9}$$

If one of the currents is derived from a differential form and the other from a submanifold this recovers Stokes' theorem; if both currents derive from submanifolds, this yields a generalization of the linking number of curves.

The Lie derivative of a current T is defined through Cartan's formula

$$\mathcal{L}_{\boldsymbol{X}} T = (\mathrm{d}\,\mathrm{i}_{\boldsymbol{X}} + \mathrm{i}_{\boldsymbol{X}}\mathrm{d})\, T. \tag{5.10}$$

The Lie-derivative occurs in the time evolution of a current induced by a time-dependent (moving) submanifold $\mathcal{N}_t$, whose point-wise motion at $t = 0$ is given by a vector field $\boldsymbol{X}$ defined on $\mathcal{N}_t$. In this case [81, 56],

$$\left.\frac{d}{dt}\right|_{t=0} T_{\mathcal{N}_t} = -\mathcal{L}_{\boldsymbol{X}} T_{\mathcal{N}}, \tag{5.11}$$

where the negative sign comes from the product rule of the Lie derivative which yields $\mathcal{L}_{\boldsymbol{X}} T[\theta] = -T[\mathcal{L}_{\boldsymbol{X}}\theta]$.

5.4 Dislocation systems with reactions

We define junction nodes as points where two or more planar dislocation lines meet. To make clear the relevant definitions, the reader is reminded that dislocation lines are piecewise planar curves on a discrete set of slip planes. A planar closed dislocation line, denoted here by c_{c}, falls completely on a single plane and is not involved in junctions. A planar open dislocation line, denoted here by c_{o}, is one that is not closed on its glide plane and as such meets at common junction nodes with other open lines of the same Burgers vector, as in cross slip, or different Burgers vector, as in junction reactions. Both closed and open dislocation lines are boundaries of planar slipped areas that themselves demarcate the surfaces over which both sides of the crystal have slipped relative to one another by a vector amount equal to Burgers vector. We distinguish the surfaces whose boundaries contain open dislocation lines by calling them open surfaces, denoted by S_{o}, and those whose boundaries a closed dislocation lines by S_{c}. The open surface boundary contains open dislocation lines along with virtual dislocation segments, denoted by c_{v}. The virtual segments denote the lines of intersection of the open slipped surfaces on different slip systems involved in the reaction. We note that we have a virtual dislocation segment for each one of the open surfaces, which covers as a limiting case also when one of the involved open surfaces collapses to the junction line, such that the location of the according open and virtual segment coincide but they have opposite orientation.When the junction segment expands it leaves behind the virtual junction segment which has the opposite orientation to the original junction segment, such that the net Burgers vector of all involved virtual segments along the intersecting line of the

involved slip systems always vanishes. These concepts are sketched in Fig. 5.1. The virtual dislocations naturally appear as part of the boundary of the swept surfaces within the slip planes, but because the net Burgers vector always sums to zero they are in-fact physically non-existent.

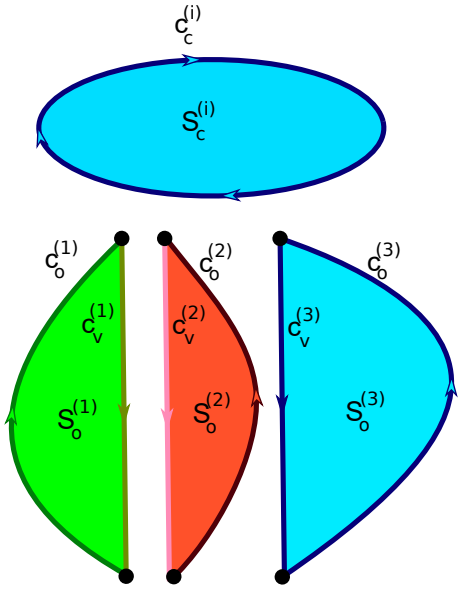

Figure 5.1. Graphical depiction of the terminology used to distinguish the open and closed line segments, the virtual segments, and the open and closed slipped surfaces.

The distinctions between closed, open and virtual segments is also reflected in the definition of the dislocation density tensor, $\boldsymbol{\alpha}$. Also this is considered to be made up of slip system contents, $\boldsymbol{\alpha} = \sum_l \boldsymbol{\alpha}_{\text{tot}}^{(l)}$, where the total slip system contribution $\boldsymbol{\alpha}_{\text{tot}}^{(l)}$ contains open, closed, and virtual dislocation line segments. The total dislocation density on a slip system thus corresponds to the boundaries of the slipped areas, as depicted in Figure 5.1. We further split the slip system dislocation line content into physical and virtual dislocation contributions, $\boldsymbol{\alpha}_{\text{tot}}^{(l)} = \boldsymbol{\alpha}^{(l)} + \boldsymbol{\alpha}_{\text{v}}^{(l)}$, with the physical dislocations including the open and closed lines introduced above. Because the virtual lines cancel upon summation over all slip systems, the total dislocation density is likewise obtained as the sum of only the physical contributions, i.e. $\boldsymbol{\alpha} = \sum_l \boldsymbol{\alpha}^{(l)}$.

The physical slip system's dislocation density tensor is defined as a vector valued current through

$$\boldsymbol{\alpha}^{(l)} = \boldsymbol{b}^{(l)} \otimes \left\langle \sum_k T_{c^{(l)}_{\mathrm{c}(k)}} + \sum_n T_{c^{(l)}_{\mathrm{o}(n)}} \right\rangle \tag{5.12}$$

where the sum over k is over the closed disjoint dislocation lines embedded in the crystal manifold M (in the sense of [117]) and the sum over n is over open dislocation lines embedded in M. A similar current denoted by $\boldsymbol{\alpha}^{(l)}_{\mathrm{v}}$ can be constructed for the virtual dislocations, except, in this case, there is only a sum over open line segments. We note again that no dislocation actually ends inside the crystal and that any endpoint of an open segment on a given slip system must be matched by the endpoint of another open segment on a different slip system. Furthermore, we remark that there is an ambiguity in defining the dislocation density current in (5.12), because reversing the line sense and the Burgers vector simultaneously yields the same vector valued current. This non-uniqueness is eliminated by fixing Burgers vectors *a priori*. In (5.12), the notation $\langle \cdot \rangle$ refers to the ensemble average. An ensemble is a set of statistically independent and identically distributed random variables and the ensemble averaging yields expectation values of functions of these random variables. Ensemble averaging of currents was first applied to dislocations by [88]; see also [32]. The average current on the right hand side of (5.12), defined as

$$\boldsymbol{\rho}^{(l)} = \left\langle \sum_k T_{c^{(l)}_{\mathrm{c}(k)}} + \sum_n T_{c^{(l)}_{\mathrm{o}(n)}} \right\rangle, \tag{5.13}$$

is assumed to be generated by a smooth differential 2-form $\boldsymbol{\rho}^{(l)}_{\mathrm{s}}$ such that

$$T_{\boldsymbol{\rho}^{(l)}_{\mathrm{s}}}[\theta] = \boldsymbol{\rho}^{(l)}[\theta]. \tag{5.14}$$

We remark here that the subscript s refers to the smooth differential form representation of the dislocations. This convention will be repeated for all other averaged quantities. In a similar fashion a 2-form representing the virtual segments can be constructed and will be denoted by $\boldsymbol{\rho}^{(l)}_{\mathrm{s,v}}$. The dislocation density tensor of the lth slip system now has the form

$$\boldsymbol{\alpha}^{(l)}_{\mathrm{s}} = \boldsymbol{b}^{(l)} \otimes \boldsymbol{\rho}^{(l)}_{\mathrm{s}}. \tag{5.15}$$

Moreover, as usual in standard coordinates with standard volume element dV, we shall also identify the differential 2-form $\boldsymbol{\rho}_{\mathrm{s}}^{(l)}$ with its generating vector field for which $\boldsymbol{\rho}_{\mathrm{s}}^{(l)} = \mathrm{i}_{\boldsymbol{\rho}_{\mathrm{s}}^{(l)}} dV$ (we make no notational distinction between the 2-form $\boldsymbol{\rho}_{\mathrm{s}}^{(l)}$ and the vector field $\boldsymbol{\rho}_{\mathrm{s}}^{(l)}$). Note that the coefficients of this vector field may be obtained from averaging as

$$\boldsymbol{\rho}_{\mathrm{s}}^{(l)}(\boldsymbol{x}) = \lim_{r\to 0} \frac{1}{\mathrm{Vol}\left(B(\boldsymbol{x},r)\right)} \left\langle \sum_k \boldsymbol{\Delta c}_{\mathrm{c}(k)}^{(l)}\left(B(\boldsymbol{x},r)\right) + \sum_n \boldsymbol{\Delta c}_{\mathrm{o}(n)}^{(l)}\left(B(\boldsymbol{x},r)\right) \right\rangle, \tag{5.16}$$

where $\boldsymbol{\Delta c}_{\mathrm{c}(k)}^{(l)}\left(B(\boldsymbol{x},r)\right)$ denotes the connecting vector from the point of entry of a dislocation into the ball $B(\boldsymbol{x},r)$ centered at $\boldsymbol{x}$ with radius r to where it leaves the ball. Such a vector is identically zero if the segment does not intersect the ball. In the sum over open dislocation lines, $\boldsymbol{\Delta c}_{\mathrm{o}(n)}^{(l)}\left(B(\boldsymbol{x},r)\right)$ connects the points of entry and leaving or, if the segment starts or ends in the ball, it connects the intersection point with the surface of the ball and the boundary point inside the ball, directed in accordance with the line-sense of the curve. We refer the reader to [88] for more details on the definition of smooth objects from averages over currents. See also **(author?)** [189] for practical applications of these concepts to discrete dislocation data.

We now define the plastic distortion current by its slip system constituents $\boldsymbol{\beta}^{p} = \sum_l \boldsymbol{\beta}^{p(l)}$. Each slip system current contribution is defined by

$$\boldsymbol{\beta}^{p(l)} \equiv \boldsymbol{b}^{(l)} \otimes \left\langle \sum_k T_{S_{\mathrm{c}(k)}^{(l)}} + \sum_n T_{S_{\mathrm{o}(n)}^{(l)}} \right\rangle, \tag{5.17}$$

where the sum over k and n, respectively, signify the sum over all closed and open slipped surfaces embedded in M. The current on the right hand side of (5.17), which given by

$$\boldsymbol{\gamma}^{(l)} = \left\langle \sum_k T_{S_{\mathrm{c}(k)}^{(l)}} + \sum_n T_{S_{\mathrm{o}(n)}^{(l)}} \right\rangle, \tag{5.18}$$

is assumed to yield a smooth differential 1-form defined such that

$$T_{\boldsymbol{\gamma}_{\mathrm{s}}^{(l)}}[\theta] \equiv \boldsymbol{\gamma}^{(l)}[\theta]. \tag{5.19}$$

In the last expression, $T_{\boldsymbol{\gamma}_{\mathrm{s}}^{(l)}}$ is the current defined by the differential 1-form, $\boldsymbol{\gamma}_{\mathrm{s}}^{(l)}$. This 1-form can be identified with a vector field via the standard metric. Using virtual dislocation segments and the definitions of the dislocation density tensor and the plastic distortion, which now contain open and closed segments, we can reach the classic integral relationship $\int_F \boldsymbol{\alpha} = \int_{\partial F} \boldsymbol{\beta}^p$. To show this, we first observe the following geometric relations for a given open surface S_{o}, see Fig. 5.1:

$$\begin{aligned} c_{\mathrm{o}} &= \partial S_{\mathrm{o}} - c_{\mathrm{v}} \\ \partial c_{\mathrm{o}} &= -\partial c_{\mathrm{v}}. \end{aligned} \tag{5.20}$$

This allows us to rewrite (5.12) as

$$\begin{aligned} \boldsymbol{\alpha}^{(l)} &= \boldsymbol{b}^{(l)} \otimes \left\langle \sum_k T_{\partial S^{(l)}_{\mathrm{c}(k)}} + \sum_n T_{\partial S^{(l)}_{\mathrm{o}(n)}} - \sum_n T_{c^{(l)}_{\mathrm{v}(n)}} \right\rangle \\ &= \boldsymbol{b}^{(l)} \otimes \partial \left\langle \sum_k T_{S^{(l)}_{\mathrm{c}(k)}} + \sum_n T_{S^{(l)}_{\mathrm{o}(n)}} \right\rangle - \boldsymbol{b}^{(l)} \otimes \left\langle \sum_n T_{c^{(l)}_{\mathrm{v}(n)}} \right\rangle =: \boldsymbol{\alpha}^{(l)}_{\mathrm{tot}} - \boldsymbol{\alpha}^{(l)}_{\mathrm{v}}, \end{aligned} \tag{5.21}$$

where we have used (5.20) and the fact that the boundary operator is a continuous linear map of currents, see [38], which commutes with the ensemble averaging operation. Since the virtual segments collectively vanish upon summation over the slip systems, the total dislocation density tensor takes on the form

$$\boldsymbol{\alpha} = \sum_l \boldsymbol{\alpha}^{(l)} = \sum_l \left[\boldsymbol{b}^{(l)} \otimes \partial \left\langle \sum_k T_{S^{(l)}_{\mathrm{c}(k)}} + \sum_n T_{S^{(l)}_{\mathrm{o}(n)}} \right\rangle \right]. \tag{5.22}$$

We can have the vector current $\boldsymbol{\alpha}$ act on a current T_F which represents the area element that bounds the Burgers circuit, denoted by $\boldsymbol{\alpha} \wedge T_F[1]$. Using property (5.9) and $\mathrm{d}T_F = (-1)^2 \partial T_F = T_{\partial F}$, we may write

$$\begin{aligned} \boldsymbol{\alpha} \wedge T_F[1] &= \sum_l \left[\boldsymbol{b}^{(l)} \otimes \partial \left\langle \sum_k T_{S^{(l)}_{\mathrm{c}(k)}} + \sum_n T_{S^{(l)}_{\mathrm{o}(n)}} \right\rangle \wedge T_F[1] \right] \\ &= \sum_l \left[\boldsymbol{b}^{(l)} \otimes \left\langle \sum_k T_{S^{(l)}_{\mathrm{c}(k)}} + \sum_n T_{S^{(l)}_{\mathrm{o}(n)}} \right\rangle \wedge T_{\partial F}[1] \right] \\ &= \sum_l \left[\boldsymbol{\beta}^{p(l)} \right] \wedge T_{\partial F}[1] \\ &= \boldsymbol{\beta}^p \wedge T_{\partial F}[1], \end{aligned} \tag{5.23}$$

which is equivalent to $\int_F \boldsymbol{\alpha}_\mathrm{s} = \int_{\partial F} \boldsymbol{\beta}_\mathrm{s}^p$. We may interpret this expression in terms of currents as the equality of the signed intersections of dislocations with the Burgers surface to the signed intersections of the circuit with the slipped surface. This is illustrated in Fig. 5.2. We note that this method of measuring signed intersections via the integral relation $\int_F \boldsymbol{\alpha}_\mathrm{s} = \int_{\partial F} \boldsymbol{\beta}_\mathrm{s}^p$ can equally be used as a definition of the dislocation density tensor. This is, in fact, how the dislocation density tensor is defined in the classical literature, which reads in differential form notation

$$\boldsymbol{\alpha}_\mathrm{s} = \mathrm{d}\boldsymbol{\beta}_\mathrm{s}^p \,. \tag{5.24}$$

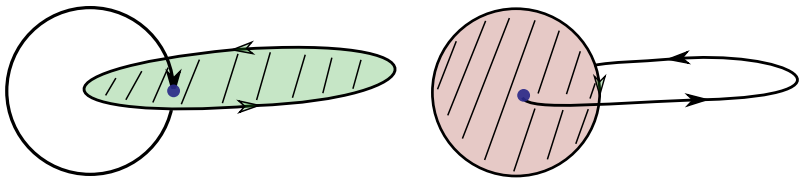

Figure 5.2. Depiction of the signed intersection of a dislocation line with the Burgers surface (in green) and the signed intersection of the Burgers circuit with the slipped area (in red).

Note that when considering junctions, this relation holds for the total dislocation density, while on the slip system level, the exterior derivative of the accumulated plastic slip contains the virtual segments, i.e. we have

$$\boldsymbol{\alpha}_\mathrm{s}^{(l)} + \boldsymbol{\alpha}_\mathrm{s,v}^{(l)} = \mathrm{d}\boldsymbol{\beta}_\mathrm{s}^{p(l)} \tag{5.25}$$

because each slip system may contain dislocations that are open. Taking the exterior derivative of the last expression and noting that the Burgers vector is constant we arrive at a constraint on each slip system of the form

$$\mathrm{d}\boldsymbol{\rho}_\mathrm{s}^{(l)} + \mathrm{d}\boldsymbol{\rho}_\mathrm{s,v}^{(l)} = 0. \tag{5.26}$$

This constraint reflects that the 2-form $\boldsymbol{\rho}_\mathrm{s}^{(l)}$ represents open and closed lines. In the case where there are only closed dislocation lines, this expression reduces to $\mathrm{d}\boldsymbol{\rho}_\mathrm{s}^{(l)} = 0$. The constraint (5.26) will become important when numerically solving the transport equations

for $\boldsymbol{\rho}_{\mathrm{s}}^{(l)}$. While the virtual density naturally occurs when connecting to the plastic slip per slip system, we will see in the next section that the virtual dislocations and their density may be replaced by the proper state variables of endpoints and endpoint densities when modeling the evolution of the dislocation system.

5.5 Measure of dislocation reactions

When dislocations react and form complex networks, the set consisting of the dislocation lines is in general not a one-dimensional manifold. This fact can be seen by analyzing the location of the triple junction point in Fig 5.3. It has three arms extending from it, and thus an open neighborhood around this point is not one dimensional, and therefore not homeomorphic to R^1 at the junction point. It does, however, decompose into zero and one dimensional manifold parts (dislocation lines being one dimensional if we split each line at the junction point). Likewise, the slipped areas can be decomposed by splitting along the virtual dislocation segments. All the theorems involving manifolds and submanifolds, like (5.11), can be applied to the manifold parts of the dislocation system but there should be a relationship tying together the manifold parts, e.g. junction arms to junction points.

The kinematic evolution of junctions involves the reaction of two dislocations over a finite segment with two junction nodes as well as the motion of these nodes. Fig. 5.3 illustrates this process, which is elaborated mathematically later.

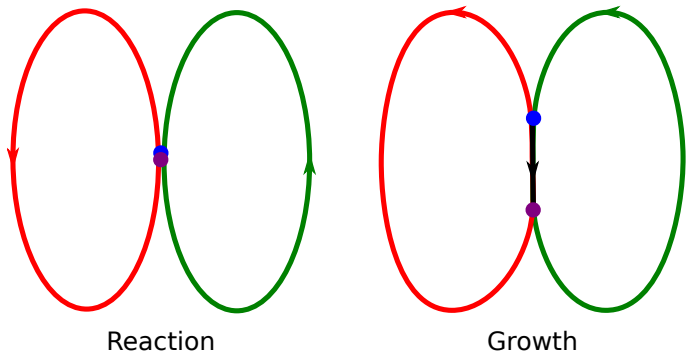

Figure 5.3. Depiction of the junction formation process, which starts with the creation of two overlapping junction nodes and then the progressive growth of the junction segment by the separation of the junction nodes.

An important relation between junction arms and junction points is Frank's second rule [80], which states that the sum of Burgers vectors entering into a junction node must be equal to the sum of Burgers vectors exiting the node. Frank's second rule is important in describing junctions and other network-forming processes in general. At a single junction node P, this rule is written in terms of currents as a sum over the connecting (open) dislocation arms $c_{\mathrm{o}}^{(\mathrm{i})}$, i.e. with positive or negative end-point at P, as

$$\sum_{\mathrm{i}:\,\pm P\in\partial c_{\mathrm{o}}^{(\mathrm{i})}} T_{\partial c_{\mathrm{o}}^{(\mathrm{i})}}(P)\boldsymbol{b}^{(\mathrm{i})} := \sum_{\mathrm{i}:\,\pm P\in\partial c_{\mathrm{o}}^{(\mathrm{i})}} \mathrm{sgn}_P(\partial c_{\mathrm{o}}^{(\mathrm{i})})\boldsymbol{b}^{(\mathrm{i})} = 0\,, \tag{5.27}$$

where, by abuse of notation, we use the point P as argument of the currents on the left hand side. This notation is interpreted as determining the signs of the oriented boundary points located at the junction point P, as denoted by the function $\mathrm{sgn}_P(\partial c_{\mathrm{o}}^{(\mathrm{i})})$ on the right hand side.

This section describes how the endpoint densities of dislocations on all slip systems are described. The current representation of the endpoints is the vector valued 0-current, which is defined by

$$\boldsymbol{\Pi}^{(l)} \equiv -\boldsymbol{b}^{(l)} \otimes \left\langle \sum_n T_{\partial c_{\mathrm{o}(n)}^{(l)}} \right\rangle. \tag{5.28}$$

Since $\partial c_{\mathrm{c}} = \emptyset$, the latter can be written as

$$\boldsymbol{\Pi}^{(l)} = -\boldsymbol{b}^{(l)} \otimes \partial \left\langle \sum_k T_{c_{\mathrm{c}(k)}^{(l)}} + \sum_n T_{c_{\mathrm{o}(n)}^{(l)}} \right\rangle. \tag{5.29}$$

Ensemble averaging then yields a smooth differential form $\pi_{\mathrm{s}}^{(l)}$ of degree 3 such that

$$\pi^{(l)} = -\partial \left\langle \sum_k T_{c_{\mathrm{c}(k)}^{(l)}} + \sum_n T_{c_{\mathrm{o}(n)}^{(l)}} \right\rangle, \tag{5.30}$$

and

$$\pi^{(l)}[\theta] \equiv T_{\pi_{\mathrm{s}}^{(l)}}[\theta] = \int_M \pi_{\mathrm{s}}^{(l)} \wedge \theta. \tag{5.31}$$

Following [88], the smooth form, $\pi_{\mathrm{s}}^{(l)}$, can be obtained from averages over currents which allows us to interpret the smooth form as the signed sum of endpoints of dislocation lines on

slip system l at a given point in space. This interpretation may also be inferred from (5.28). Comparing (5.12) and (5.29), it is easy to see that $T_{\mathbf{\Pi}_{\mathrm{s}}^{(l)}} = \partial T_{\boldsymbol{\alpha}_{\mathrm{s}}^{(l)}} = T_{\mathrm{d}\boldsymbol{\alpha}_{\mathrm{s}}^{(l)}}$. We note here that

$$\mathbf{\Pi}_{\mathrm{s}}^{(l)} = \mathrm{d}\boldsymbol{\alpha}_{\mathrm{s}}^{(l)} \tag{5.32}$$

because we have defined the endpoints in (5.28) to be oriented opposite of the orientation given by the boundary operator.

The relationship (5.32) can also be shown using the product property (5.9) to produce $\int_{\partial V} \boldsymbol{\alpha}_{\mathrm{s}}^{(l)} = \int_V \mathbf{\Pi}_{\mathrm{s}}^{(l)}$. This can be shown by writing the intersection product as $\boldsymbol{\alpha}^{(l)} \wedge T_{\partial V}[1] = \mathbf{\Pi}^{(l)} \wedge T_V[1]$. The above relationship is thus interpreted as the differential form equivalent to the equality of the signed intersections of open lines with the closed surface ∂V to the signed intersection of endpoints within the volume V. This is shown in Fig. 5.4. Given the intersection relationship we can alternatively define the endpoint densities based upon (5.32). This definition will aid our understanding when we look at these measures at different lengths scales in Section 5.6. As we can write $\Pi_{\mathrm{s}}^{(l)}$ in the form

$$\mathbf{\Pi}_{\mathrm{s}}^{(l)} = \boldsymbol{b}^{(l)} \otimes \pi_{\mathrm{s}}^{(l)}, \tag{5.33}$$

it follows from (5.31) that

$$\pi_{\mathrm{s}}^{(l)} = \mathrm{d}\boldsymbol{\rho}_{\mathrm{s}}^{(l)}. \tag{5.34}$$

The constraint (5.26) can then be written as $\pi_{\mathrm{s}}^{(l)} = \mathrm{d}\boldsymbol{\rho}_{\mathrm{s}}^{(l)} = -\mathrm{d}\boldsymbol{\rho}_{\mathrm{s,v}}^{(l)}$ and thus introducing the endpoint removes the need to model the virtual dislocation segments. In a vector field notation, (5.34) may be written as $\pi_{\mathrm{s}}^{(l)} = \mathrm{div}\boldsymbol{\rho}_{\mathrm{s}}^{(l)}$. From the closedness of the total dislocation density tensor we have

$$\mathrm{d}\boldsymbol{\alpha}_{\mathrm{s}} = \sum_l \mathbf{\Pi}_{\mathrm{s}}^{(l)} = 0, \tag{5.35}$$

which we rewrite as

$$\sum_l \mathrm{d}\boldsymbol{\rho}_{\mathrm{s}}^{(l)} \boldsymbol{b}^{(l)} = \sum_l \pi_{\mathrm{s}}^{(l)} \boldsymbol{b}^l = 0. \tag{5.36}$$

We interpret this as the continuum counterpart to Frank's second rule, saying that sums of Burgers vectors at all junctions cancel.

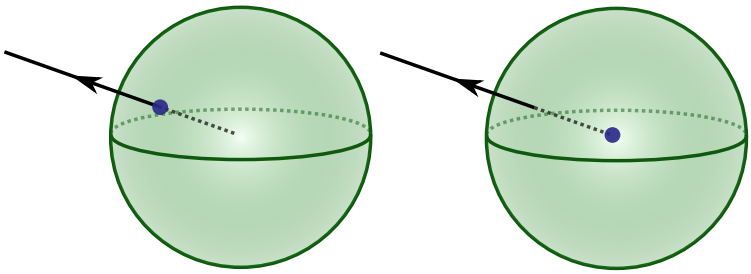

Figure 5.4. Depiction of the signed intersection of the open dislocation line with the closed surface (boundary of the sphere) and the signed intersection of the endpoint with the volume of the sphere.

So far, we have introduced density measures to describe endpoints of open dislocation lines on various slip systems of a crystal. We note here that the endpoints of open lines on different slip systems are coupled since they relate to the junction points, which is reflected in (5.36). We also note that every endpoint may be assigned to a junction point and that we may accordingly introduce currents and differential forms for the junction points. It is further important to realize that the endpoints inherit an orientation or sign (used interchangeably in the sequel) from the orientation of the dislocation line and that the junction points are signed objects, where the sign needs to be determined from the signs of the contributing endpoints. For this reason, we need to develop a way to orient the junction nodes and to ensure consistency of such an orientation. We delay discussing the issue of a consistent orientation until the next section where we introduce graphs to represent the dislocation networks.

Let us denote junction points locations as $P^{(pqr)}_{(\mathrm{j})}$, where j is an index labeling the points. We exclusively work with three-armed junctions and label the Burgers vectors of the involved arms by p, q, and r. As will be discussed in Section 5.7, a meaningful definition of the junction point sign is given by the product of the signs of the connecting arms, i.e.,

$$\mathrm{sgn}(P^{(pqr)}_{(\mathrm{j})}) \coloneqq \mathrm{sgn}_P(\partial c^{(p)}_{\mathrm{o}(\mathrm{j})})\mathrm{sgn}_P(\partial c^{(q)}_{\mathrm{o}(\mathrm{j})})\mathrm{sgn}_P(\partial c^{(r)}_{\mathrm{o}(\mathrm{j})}), \tag{5.37}$$

where $\mathrm{sgn}_P(\partial c^{(p)}_{\mathrm{o}(\mathrm{j})})$ denotes the sign of the endpoint of the dislocation line $c^{(p)}_{\mathrm{o}(\mathrm{j})}$ involved in the jth junction point. Given the sign $\mathrm{sgn}(P^{(pqr)}_{(\mathrm{j})})$ of the junction point j, the junction point current is defined as

$$\pi^{pqr}_{\mathrm{J}} = \left\langle \sum_{\mathrm{j}} \mathrm{sgn}(P^{(pqr)}_{(\mathrm{j})}) T_{P^{(pqr)}_{(\mathrm{j})}} \right\rangle . \tag{5.38}$$

We note that in the above expression, $T_{P^{(pqr)}_{(\mathrm{j})}}$ is an unsigned, i.e., positive current. We can make use of the ensemble average again to obtain a smooth 3-form representing this current. This form contains the signed sum of junction points at a given point in space. An example for the junction point orientation is shown in the Fig. 5.5. We note the importance of the sign being dependent on whether the lines point into or out of the junction point. Consequently, when the network evolves in time, the sign of the junction point does not change. We will

see that the definition of the junction point sign given by (5.37) is consistent with a coloring property of the graphs created by dislocations when we are only considering one junction group involving a triplet of Burgers vectors as is the case in face-centered cubic (FCC) crystals. We will thus be able to form a correspondence between the endpoints and signed junction points. When multiple types of junctions are considered more care is needed to establish a relationship between the endpoints and junction points. This is touched upon in Section 5.8.

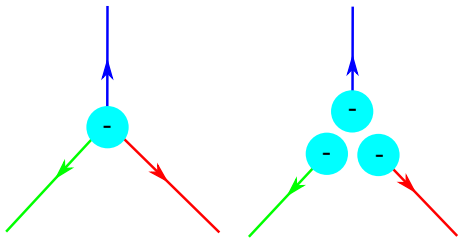

Figure 5.5. Depiction of the particular case where the orientation of the junction node (on the left) is the same as the orientations of the endpoint densities (on the right). The orientation is denoted by the blue color of the dot which represents the location of the junction node (on the left) and 3 endpoint nodes (on the right).

5.6 Length scale considerations

The signed nature of endpoints and junction point densities stems from the fact that they are defined from oriented intersections, see (5.24) and (5.31). The corresponding densities are thus geometric quantities that depend on the length scale over which they are defined. In a dense dislocation systems, these densities measure the net number of end points and junction points. The sign issue arises also in the representation of the endpoint and junction point currents, as in (5.13), (5.18), and (5.38) where the averaged currents are defined by summing over oriented submanifolds. Following the terminology in dislocation theory we refer to the net densities as geometrically necessary.

Due to the signed nature, defining these net densities is always tied to length scale resolution much like in defining the dislocation density tensor, $\boldsymbol{\alpha}$. Hence, a problem that might arise when considering a model that contains the endpoint and junction point densities,

along with the dislocation densities, is the difference in the length scale at which each of these density measures can accurately represent the dislocation network. When referring to a length scale, it is convenient to view the intersection product definitions of the density measures like in (5.32) and (5.24). When using intersections to define the density measures, the length scale of the model is a characteristic length associated with the submanifold used to measure intersections. For instance, in the intersection definition of the endpoint densities (5.32), the characteristic length would be the radius of the solid sphere used to intersect with the endpoints. Another example is the radius of the Burgers circuit used in the definition of the dislocation density tensor in (5.24). The question now is whether or not a length scale used to define the geometrically necessary dislocation densities (GND) overlaps with those associated with the geometrically necessary endpoint or geometrically necessary junction point densities. For simplicity, we will call the latter the endpoint and junction point densities.

We begin the consideration of the length scale issue posed above with motivating the use of the junction point densities rather than the endpoint densities, using a specific example. The signed nature of endpoints make their geometric density dependent upon the length scale resolution of the model. This is depicted in Fig. 5.6, where we describe two scenarios which have in common one dislocation type (the red line) which enters both junction points with opposite orientations. In both parts of the figure, this would look like a closed line on larger length scale for the slip system that shares the common arm; thus after integrating over the surface of the solid sphere, V, we have $\int_{\partial V} \boldsymbol{\rho}_{\mathrm{s}}^{(3)} = 1 - 1 = 0$ where we have used the intersection of the open dislocation lines with ∂V to evaluate this integral. If we were using the endpoints to model the dislocation system then the information about the multiple types of junctions would be lost from the perspective of this slip system due to the fact that $\int_V \mathrm{d}\boldsymbol{\rho}_{\mathrm{s}}^{(3)} = 0$. Now consider the right part of Fig. 5.6. If we represent the system using junction point densities we obtain $\int_V \mathrm{d}\boldsymbol{\rho}_{\mathrm{s}}^{(3)} = \int_V \pi_{\mathrm{sJ}}^{(123)} + \pi_{\mathrm{sJ}}^{(345)} = 1 - 1 = 0$ where we have used intersections to evaluate both integrals. That is, we still have $\int_V \mathrm{d}\boldsymbol{\rho}_{\mathrm{s}}^{(3)} = 0$ but we retain the information about the junction points. This problem arises because $\boldsymbol{\rho}_{\mathrm{s}}^{(3)}$ is involved in more than one junction type. Therefore, the specification of the endpoint density does not lead to a unique specification of junction point densities. This issue can

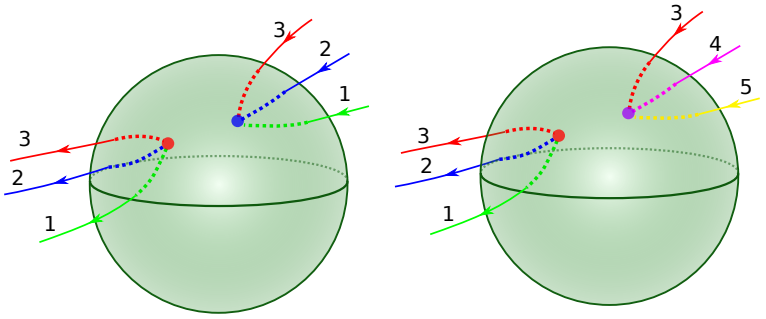

Figure 5.6. Illustration of the loss of information that end point density causes when multiple junction types are present. In the left figure, the red, blue and green lines appear continuous due to cancellation of endpoints for each color. In the right part, the red line appears continuous for the same reason but the other colors have net endpoints.

be solved by modeling the state of the system with the junction point densities instead of the endpoint densities and this is the approach taken in this paper. In the specific example given in the right part of Fig. 5.6 we noted that $\int_V \mathrm{d}\boldsymbol{\rho}_{\mathrm{s}}^{(3)} = \int_V \pi_{\mathrm{sJ}}^{(123)} + \pi_{\mathrm{sJ}}^{(345)}$ which implies that $\pi_{\mathrm{s}}^{(3)} = \pi_{\mathrm{sJ}}^{(123)} + \pi_{\mathrm{sJ}}^{(345)}$. In subsequent sections we will show why we expect such a relation to exist and give a more general expression between the endpoints and junction points.

The definition of the junction point density may also suffer from cancellations when defined on the same length scale as the dislocation density vector. To illustrate this we refer to low energy dislocation structures observed in rolled aluminum [89, 194], where we can observe a potential discrepancy in the length scales over which the dislocation, endpoint and junction point densities are representative of the system at the same time. To illustrate such a discrepancy, we modify a figure from [194] to produce Fig. 5.7. In doing so, the inclusion of the junction points as a signed measure is made clear by assigning them the red and blue colors. This will serve our purpose of introducing graphs representing the dislocation networks later. For now, we observe in Fig. 5.7 that the line orientation of all dislocation segments of every color is along one direction and thus the corresponding dislocation density vectors are representative of this system at the depicted scale (roughly 200nm). However, the junction point densities corresponding to the red and blue colors vary at a shorter length scale and thus the geometric junction point density would not accurately represent the system. From this discussion it can be seen that the net number of junction points in the volume

depicted in the figure, which is suited for the vector density description, is not representative of the total number of junction points in the same volume. Due to the signed nature of these junction points, there is a geometric cancellation and statistical storage.

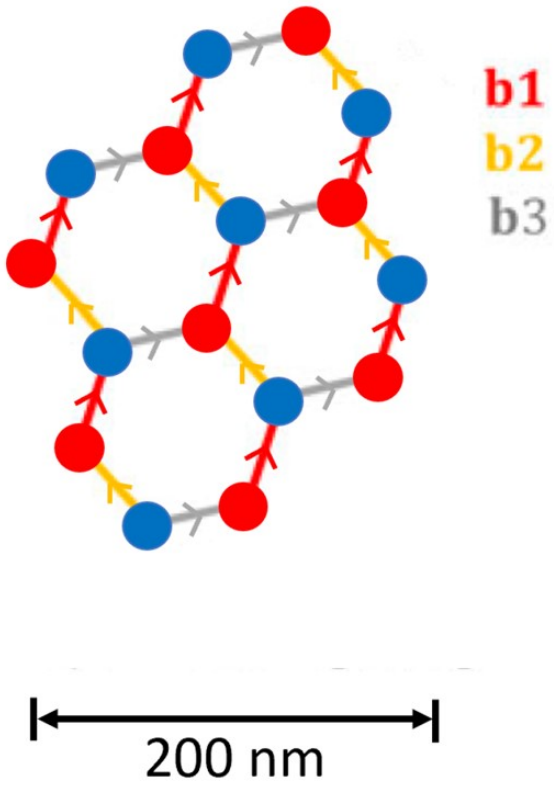

Figure 5.7. A figure adopted from [194] depicting a low energy dislocation structure involving dislocations of three Burgers vectors represented by three different colors. The dots are junction points. The scale of the part of the network shown is on the order of 200nm.

In order to have a dislocation network model consistent with the line bundle picture of continuum dislocation dynamics [8], we shall, therefore, represent the endpoints in terms of positive and negative densities whose difference is the geometric density. This is possible because each of the $T_{\partial c^{(l)}_{o(n)}}$ currents in (5.28) represent both the positive and negative endpoints of each open dislocation line respectively. Since the endpoints of an open dislocation line are in different locations we can represent using separate points and thus define two

new signed currents corresponding to each of these points. We proceed analogously for the junction point density. We thus write

$$\pi_{\mathrm{s}}^{(l)} = \pi_{\mathrm{s}}^{(l)+} - \pi_{\mathrm{s}}^{(l)-}, \quad \pi_{\mathrm{sJ}}^{(pqr)} = \pi_{\mathrm{sJ}}^{(pqr)+} - \pi_{\mathrm{sJ}}^{(pqr)-}. \tag{5.39}$$

In this representation we retain the information of positive and negative endpoints and junction points, which makes their density representation consistent with the dislocation density from a length scale perspective.

In the next section we establish a unique connection between the signed endpoint densities and the signed junction point densities.

5.7 Graph theoretic approach to dislocation networks

This section has two objectives, to introduce the dislocation network in terms of graph theory and use the tools of the latter theory to interpret and derive relations for the continuum representation of dislocations. This is important for establishing a relationship between the sign of the junction point density and the sign of the corresponding endpoint densities.

A graph G is a pair $G = (V, E)$ of lists. V is a list of vertices (nodes) and $E \subseteq V \times V$ a list of pairs of vertices called edges. A graph is called r-partite if its vertex set can be split into r disjoint sets $V_1, V_2, .., V_r$ such that every edge connects a pair of vertices from two different sets. This means that vertices in a given set are not adjacent [48]. A graph that can be split into two sets of vertices in this manner is called a bipartite graph. In this case the sets of vertices may be identified by a sign, which is why this property relates to the signed junction points in the current case. The property of a graph being bipartite or not may be checked by counting edges along closed paths in the graph – so called cycles. A path is a sequence of edges joining disjoint sets of vertices, typically denoted by a list of vertices. A cycle is a path which starts and ends at the same vertex and contains any edge at most one time. When considering whether a graph is bipartite we can equivalently show that there are no odd length cycles [48], where the length of the cycle is the number of edges in the cycle.

Dislocation networks in crystals can be easily represented by graphs. For analysing the properties of graphs which represent dislocation networks we focus here on junction formation in FCC crystals. In such crystals, there are four distinct slip planes, commonly denoted by A,B,C, and D. In each plane there are 3 slip directions identified with Burgers vectors. Due to symmetry considerations, there are only six unique Burgers vector, denoted $b_1, b_2, \ldots, b_6$. We follow [6] in using the Schmid and Boas (SB) notation for slip systems. In this notation, the slip normal and Burgers vector are paired. For example A3 denotes a slip system with slip plane A and Burgers vector b_3. A summary of FCC slip systems (and their glissile reactions, see below) in this notation is given in Table 5.1. According to [168], junctions are classified into sessile and glissile types. If the resulting dislocation junction is in one of the twelve slip systems given in Table 5.1 then the junction is glissile. Otherwise, the junction is sessile. The latter junctions are either of Lomar type or of Hirth type [80]. A coplanar junction is one in which the Burgers vectors of the dislocation lines ending at the junction point fall in the same plane. When two dislocations on different slip planes have the same Burgers vector they may react to annihilate each other. This reaction is called collinear annihilation.

Table 5.1. Slip systems in FCC crystals in Schmid-Boas (SB) notion. The last column denotes the SB index for the reacting systems that produce a glissile junction segment on this row's slip system. The table is modified from [6].

Index	Slip plane	b	SB index	Glissile reaction
1	$(\bar{1}11)$	$\frac{1}{2}[0\bar{1}1]$	A2	A3+D6,A6+C3
2	$(\bar{1}11)$	$\frac{1}{2}[101]$	A3	A2+D6, A6+B2
3	$(\bar{1}11)$	$\frac{1}{2}[110]$	A6	A2+C3, A3+B2
4	(111)	$\frac{1}{2}[0\bar{1}1]$	B2	B4+C5, B5+D4
5	(111)	$\frac{1}{2}[\bar{1}01]$	B4	A2+B5, B2+C5
6	(111)	$\frac{1}{2}[\bar{1}10]$	B5	A2+B4, B2+D4
7	$(\bar{1}\ \bar{1}1)$	$\frac{1}{2}[011]$	C1	A3+C5, B5+C3
8	$(\bar{1}\ \bar{1}1)$	$\frac{1}{2}[101]$	C3	B5+C1, C5+D1
9	$(\bar{1}\ \bar{1}1)$	$\frac{1}{2}[\bar{1}10]$	C5	A3+C1, C3+D1
10	$(1\bar{1}1)$	$\frac{1}{2}[011]$	D1	A6+D4, B4+D6
11	$(1\bar{1}1)$	$\frac{1}{2}[\bar{1}01]$	D4	A6+D1, C1+D6
12	$(1\bar{1}1)$	$\frac{1}{2}[110]$	D6	B4+D1, C1+D4

To fix ideas, we only consider glissile junctions with three-armed junction nodes in this communication. However, as discussed later, the final results are general and apply when all other networking mechanisms are present. We start by requiring a vertex or a node in the graph representing the dislocation network to correspond to the junction point. The open dislocation lines connecting the junction points are taken to be the edges of the graph. As explained below, the graph created in this fashion is r-partite. Fig. 5.8 shows some glissile junction reaction among multiple dislocation loops that form a network, which is represented by a graph. Regardless of the Burgers vector types involved, the junction starts at the intersection point of two reacting dislocations then splits into two vertices connected by a new edge. The junction segments are differentiated by their color, which signifies the different Burgers vectors of the lines corresponding to the edges. We note that the list of edges in the graph contain non-unique entries. For example, edges 1 and 2 both share the same vertices, as well as edges 5 and 6. Graphs with this property are called multigraphs [48].

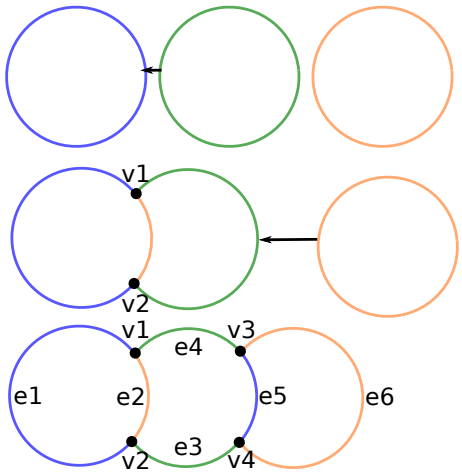

Figure 5.8. An illustration of coplanar junction formation in FCC crystals using graphs. Three loops (top) are about to react. The green and blue loops react to form the orange dislocation segment connecting the junction nodes (middle). Next, the open green line and the orange loop react to form a blue junction segment (bottom).

Before moving on, we define some terminology that will become important when talking about the graphs representing dislocation networks. We define a dislocation junction group

to be a triplet of different Burgers vectors that correspond to a glissile junction reaction. We also define a junction type to be a triplet of different slip systems. With this terminology each junction group contains multiple junction types. For instance, the glissile reactions A2+A3+D6 and A2+C3+A6 both form different junction types but since the Burgers vectors involved in these reactions are the same, they are also in the same junction group. When only considering one junction group, we cannot allow one loop to react with two edges connected to the same junction node. The reasoning for this is given in 5.A.

The graph created by a given junction group is bipartite. We can prove this by showing that all cycles in the graph are even. To do so we consider two cases, one where the dislocations involved in the reaction are in two different connected components in the graph, like in Fig. 5.8, and another where they are in the same connected component. Two vertices are considered to be in the same connected component if there is a path connecting them. We start with the case where the edges are in different connected components. We create a cycle by first starting with an arbitrary edge, say e_6, of the final graph in Fig. 5.8, now isolated in Fig.5.9. For the cycle to be of even length, the dotted path length from node v_3 to v_4 must be odd because odd + odd = even. For this example, we can evaluate all the remaining paths and show that they are of odd length. For an arbitrary graph, though, we rely on the fact that each additional junction reaction added to the graph gives 2 additional odd-length paths. In Fig. 5.8 the path from vertex v1 to v2, in the middle part has odd length equal to one (every path from v1 to v2 has to be odd because they are adjacent and thus in different vertex sets). In the lower part of the figure, a junction segment is added between vertices v1 and v2. In doing so, an alternative odd-length paths from v1 to v2 is added. Since the junction reaction preserves the oddness property of paths lengths between the points involved in the reaction, any subsequent junction reaction does not alter the bipartite property of the graph. Since the junction group consists of multiple junction types, the bipartite vertex sets can be further decomposed into different junction types. In the following we focus primarily on the bipartite vertex sets because they will be important for establishing orientation relations between junction points and endpoints.

In the case where the reacting edges are in the same connected component we refer to Fig 5.10, where the vertex sets are assigned positive and negative signs. Looking at the

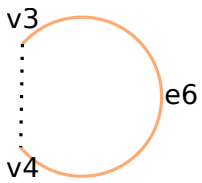

Figure 5.9. An arbitrary chosen edge of the dislocation network shown in Fig. 5.8. The dotted lines denote the possible paths that create a cycle with the inclusion of edge e_6.

graph we see that the vertex sets containing v1, v2, v3, and v4 are left unchanged after the reaction because the additional paths from v1 to v2 have odd lengths and the additional paths from v4 to v1 also have odd lengths. We also have additional vertices, v5 and v6, that have been added to the graph which are consistent with the bipartite property of the graph.

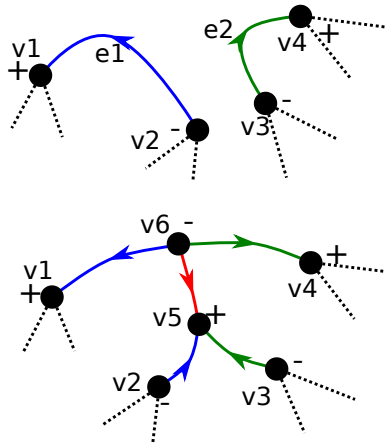

Figure 5.10. A depiction of junction formation when reacting segments come from the same connected component of the graph. The dotted lines represent connectivity with the rest of the graph not shown in the figure.

An important property of bipartite graphs is that they are 2-colorable [48]. By 2-colorable it is meant that a color can be assigned to each vertex so that pairs of adjacent vertices do not share the same color. The bipartite property also provides us with an easy way to recover the directed graph of the dislocation network by specifying rules for line directions into or out of the vertices. Consider, for example, the 2-colorable graph in Fig.5.11 where we show an undirected graph in the left part. By specifying that all edges should point towards the green-colored vertices and away from every adjacent red-colored vertices, we recover the directed graph to the right of the figure. For this reason, we use color and orientation interchangeably.

We are more interested in less arbitrary ways of providing rules for the orientations of edges connecting the vertices in the dislocation network graph. We can provide rules for

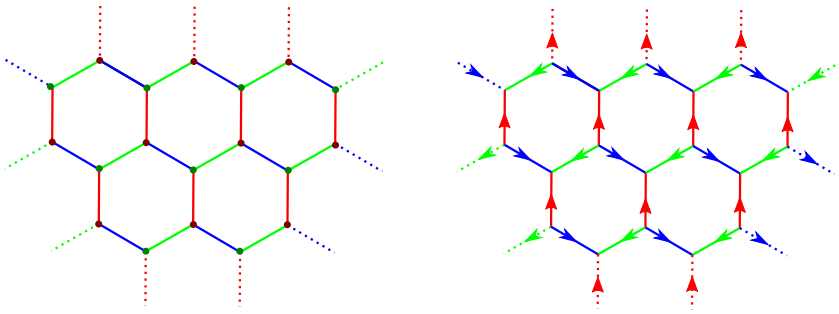

Figure 5.11. Depiction of the recovery of a directed graph from an undirected graph given a set of rules for how the lines should be directed base on the coloring of the edges. The dashed lines denote connections to the other junction points not shown in the figure.

these orientations using Frank's second rule, given by (5.27), at each vertex. For instance, the graph in Fig. 5.11 would also be created when we fix the Burgers vectors such that

$$\boldsymbol{b}^{(1)} + \boldsymbol{b}^{(2)} + \boldsymbol{b}^{(3)} = 0. \tag{5.40}$$

In Fig.5.11, we color the edges with Burgers vector $\boldsymbol{b}^{(1)}$ green, those with Burgers vector $\boldsymbol{b}^{(2)}$ blue, and the edges with Burgers vector $\boldsymbol{b}^{(3)}$ red. With the Burgers vectors fixed in this way, there would only be two types of junction nodes (vertices), those with all the segments pointing into the vertices and those with all the segments pointing out. If we now fix the Burgers vectors such that

$$\boldsymbol{b}^{(1)} + \boldsymbol{b}^{(2)} - \boldsymbol{b}^{(3)} = 0, \tag{5.41}$$

then one set of vertices would have edges with $\boldsymbol{b}^{(1)}$ and $\boldsymbol{b}^{(2)}$ pointing into while $\boldsymbol{b}^{(3)}$ is pointing out of the vertices, and another set having $\boldsymbol{b}^{(1)}$ and $\boldsymbol{b}^{(2)}$ directed out while $\boldsymbol{b}^{(3)}$ directed into the vertices.

We now recall the definition of the sign of the junction point current in (5.37). Here we show that such a definition corresponds to the bipartite property of the graph. This can be shown for both of the examples mentioned above. In the first, $\boldsymbol{b}^{(1)} + \boldsymbol{b}^{(2)} + \boldsymbol{b}^{(3)} = 0$ and the sign of the junction point determined from (5.37) is the same as the sign of each endpoint. In this case, we trivially recover the bipartite property because every adjacent node has a different orientation. In the second example, $\boldsymbol{b}^{(1)} + \boldsymbol{b}^{(2)} - \boldsymbol{b}^{(3)} = 0$. From the 3-term product in (5.37), we know that 2 of the terms have the same sign. Therefore, the sign of their product does not contribute to the junction point sign; the third term, however, determines that sign. We can then view the set of edges with Burgers vectors given by $\boldsymbol{b}^{(3)}$ as providing the sign of the junction nodes. Since we are considering only one junction group (every node contains a $\boldsymbol{b}^{(3)}$ edge), every adjacent node has to have a differing sign because the orientation of the endpoints of each $\boldsymbol{b}^{(3)}$ edge is different. Thus, junction sign definition given by (5.37) is consistent with the bipartite property as well.

In the next section we consider multiple junctions groups. It will be shown that the ideas developed in this section carry over to that situation and that the presence of different

junction groups introduces another level of complexity that can still be simplified by looking at the graph structure of the dislocation network.

5.8 Graphs of dislocation networks involving all junction groups

When dislocations on all slip systems are involved in junctions all junction groups contribute to the dislocation network. In this case, the bipartite graph concept of a single junction group, which was developed in the previous section can be generalized to a r-partite graph to represent the dislocation network. Here, the number of vertex sets r of such a graph is equal to $2n$, where n is the number of junction types and the factor of 2 represents the different orientations for each group. At the end of Appendix 5.A we show why junction formation in this case retains the r-partite property of the graph. To orient these junction groups we continue to use (5.37) and refer to this definition as the r-partite coloring. With this definition, when we are only considering one group of junctions, we recover the results obtained in the previous section.

As discussed in the previous section, neighboring nodes in the graph within the same junction group have different orientations (signs). However, this does not guarantee differing signs of nodes on parts of the graph where adjacent nodes have different junction groups. This will have implications for how we convert between the endpoint orientations and each junction group orientation.

Let us now look at the definition of endpoints from the prospective of the graph theoretic ideas, with the goal of illustrating the relationship between the signs of the junction points and endpoints in the case of multiple junction groups. Let us consider the dislocation density tensor on a given slip system as given by (5.12). Applying the exterior derivative gives

$$\mathrm{d}\boldsymbol{\alpha}^{(l)} = \mathrm{d}\rho^{(l)}\boldsymbol{b}^{(l)}.$$

We note that $\mathrm{d}\rho^{(l)}$ can be written as a sum containing all the endpoint densities inside the volume which is integrated over. From (5.8) and (5.7) , it follows that

$$\mathrm{d}\boldsymbol{\rho}^{(l)} = -\left\langle \sum_{k}^{N^l} T_{\partial c^{(l)}_{\mathrm{o}(k)}} \right\rangle,$$

where $N^{(l)}$ is the number of open lines for a given slip system and $T_{\partial c_{\mathrm{o}}(k)}$ represents the (signed) point Dirac delta function representing an endpoint. Our aim is to model the system using the junction point densities, and since every term in this sum can be identified with one of these junction points (up to a sign), we split this sum into a sum over junction types and a nested sum over the number of points in each type:

$$\begin{aligned}
\mathrm{d}\boldsymbol{\rho}^{(l)} &= -\left\langle \sum_{p,q:\,(lpq)\in S^l} \sum_{\mathrm{i}(lpq)} \mathrm{sgn}(\partial c^{(l)}_{\mathrm{o(i)}}) T_{P^{(lpq)}_{(\mathrm{i})}} \right\rangle \\
&= -\left\langle \sum_{p,q:\,(lpq)\in S^l} \sum_{\mathrm{i}(lpq)} \mathrm{sgn}^{(lpq,l)} \mathrm{sgn}(P^{(lpq)}_{(\mathrm{i})}) T_{P^{(lpq)}_{(\mathrm{i})}} \right\rangle \\
&= -\sum_{p,q:\,(lpq)\in S^l} \mathrm{sgn}^{(lpq,l)} \left\langle \sum_{\mathrm{i}(lpq)} \mathrm{sgn}(P^{(lpq)}_{(\mathrm{i})}) T_{P^{(lpq)}_{(\mathrm{i})}} \right\rangle.
\end{aligned} \tag{5.42}$$

In this expression S^l is an index set containing all the junction types that slip system l is part of and $\mathrm{i}(lpq)$ denotes an index for the sum over all junction nodes which are of type lpq. In the second line the innermost sum is replaced by the junction point currents. This step relies on the fact that every endpoint, $\partial c^{(l)}_{\mathrm{o(i)}}$, can be associated with two other endpoint densities (on other slip systems) to make up the (signed) ith junction point $\mathrm{p(i)}$. We have also added $\mathrm{sgn}^{(lpq,l)}$ to convert the junction point orientation (sign) into the endpoint orientation (sign). From (5.37) we can obtain $\mathrm{sgn}^{(lpq,l)}$ as

$$\mathrm{sgn}^{(lpq,l)} = \frac{1}{\mathrm{sgn}_P(\partial c^{(p)}_{o(\mathrm{i})})\mathrm{sgn}_P(\partial c^{(q)}_{o(\mathrm{i})})} = \mathrm{sgn}_P(\partial c^{(p)}_{o(\mathrm{i})})\mathrm{sgn}_P(\partial c^{(q)}_{o(\mathrm{i})}) \tag{5.43}$$

We note the dependence on the junction type and slip system (s, l) because the endpoints can be oriented differently relative to adjacent junction groups. We note that $\mathrm{sgn}^{(lpq,l)}$ does not depend on the specific junction point P because, for a given junction group, the relative

orientations of the connecting arms are the same. We note here that junction types within the same junction group have the same sign $\mathrm{sgn}^{(lpq,l)}$ because this sign is determined from the Burgers vectors.

With this we can express the endpoint currents in terms of the junction currents as

$$\mathrm{d}\boldsymbol{\rho}^{(l)} = \pi^{(l)} = \sum_{p,q:\,(lpq)\in S^l} \mathrm{sgn}^{(lpq,l)} \pi_{\mathrm{J}}^{(lpq)}, \tag{5.44}$$

where the junction current is still defined by (5.38) for each group. When this is represented by smooth forms we obtain

$$\mathrm{d}\boldsymbol{\rho}_{\mathrm{s}}^{(l)} = \pi_s^{(l)} = \sum_{p,q:\,(lpq)\in S^l} \mathrm{sgn}^{(lpq,l)} \pi_{\mathrm{sJ}}^{(lpq)}. \tag{5.45}$$

The last relationship is viewed as gluing the arms together since in order to arrive at this relationship we had to associate the signs of the endpoint currents to the junction currents. In the above, the signs $\mathrm{sgn}^{(s,l)}$ are determined by the fixing the Burgers vectors of the dislocations. For example, if only two type of junctions are present, which are in different junction groups, and we fixed the Burgers vectors such that

$$\begin{aligned}
\boldsymbol{b}^{(1)} + \boldsymbol{b}^{(2)} + \boldsymbol{b}^{(3)} &= 0 \\
\boldsymbol{b}^{(1)} - \boldsymbol{b}^{(4)} + \boldsymbol{b}^{(5)} &= 0,
\end{aligned}$$

and if the vector density $\boldsymbol{\rho}_s^{(1)}$ has Burgers vector $\boldsymbol{b}^{(1)}$, $\boldsymbol{\rho}_s^{(2)}$ has $\boldsymbol{b}^{(2)}$, and so on, then the index set is $S^1 = \{\{1,2,3\},\{1,4,5\}\}$ and the endpoint density relationships would be:

$$\begin{aligned}
\mathrm{div}\boldsymbol{\rho}_{\mathrm{s}}^{(1)} &= \pi_{\mathrm{sJ}}^{123} - \pi_{\mathrm{sJ}}^{145} \\
\mathrm{div}\boldsymbol{\rho}_{\mathrm{s}}^{(2)} &= \pi_{\mathrm{sJ}}^{123} \\
\mathrm{div}\boldsymbol{\rho}_{\mathrm{s}}^{(3)} &= \pi_{\mathrm{sJ}}^{123} \\
\mathrm{div}\boldsymbol{\rho}_{\mathrm{s}}^{(4)} &= \pi_{\mathrm{sJ}}^{145} \\
\mathrm{div}\boldsymbol{\rho}_{\mathrm{s}}^{(5)} &= -\pi_{\mathrm{sJ}}^{145}.
\end{aligned}$$

Corresponding to this example is the graph shown in Fig.5.12. In this graph we denote 1 with the color blue, 2 with red, 3 with green, 4 with gold, and 5 with cyan. In that figure, it can be seen that adjacent junction nodes are either of opposite sign or opposite junction group. This property is consistent with r-partite graphs, more specifically a 4-partite graph because the nodes can be split into 4 groups which consist of 2 junction groups each with a positive and negative orientation.

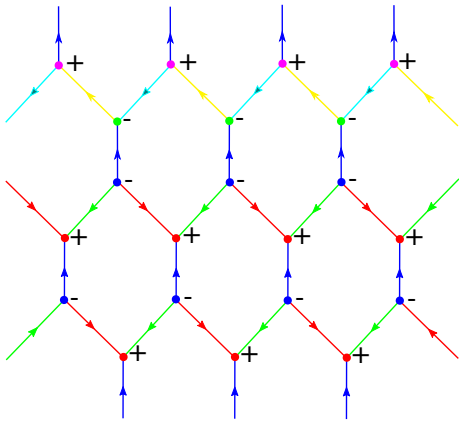

Figure 5.12. Illustration of the relationship between the signs of the end-points and junction points for the example in the text. The different color nodes denote the r-partite coloring of the nodes. The corresponding sign is given next to the node.

We end this section by providing a proof that the collinear annihilation preserves the r-partite property of the dislocation network. This reaction is illustrated in Fig. 5.13, where the reacting dislocations segments e1 and e2 annihilate each other to produce new edges in the graph denoted by e1' and e2'. Looking at the incident vertices v1, v2, v3 and v4, it is possible to identify cases when the nodes (v1,v2) and (v3,v4) are in the same junction group and when they are not. To prove that the annihilation reaction preserves the r-partite property of the graph, let us first consider the case when (v1,v2) and (v3,v4) belong to the same junction group. In this case, it is sufficient to show that the resulting graph is bipartite. Since collinear annihilation amounts to swapping one of the nodes from each edge to another node in the same vertex set, the bipartite property of the graph is preserved. We know that the vertex sets are the same because this is required for the reaction to take place. We note that this process can result in the merging of two previously disconnected components of the

graph. When the junction groups are different the r-partite property is trivially preserved because after the reaction v2 and v3 are adjacent and have different junction groups. The same holds for v1 and v4.

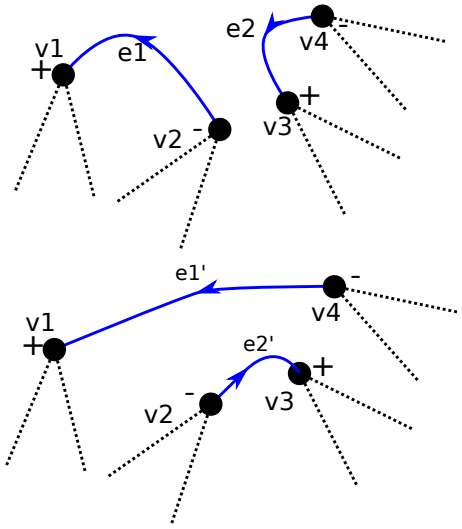

Figure 5.13. Illustration of collinear annihilation of two dislocation segments in blue before (top) and after the reaction (bottom). The dotted edges signify that these nodes are connected to other nodes that are not shown in the graph.

5.9 Transport relations for the dislocation network

In this section, the transport equations for the dislocation network are derived. In doing so, we make use of (5.45), the relationship between the endpoints and the junction points. We state again that the dislocation junction reaction starts out as a crossed state in which two junction points are overlapping then proceeds to form a junction segment via the separation of the two junction points. Here, we will analyze the continuum kinematics associated with open dislocation line segments coupled to the motion of junction points.

5.9.1 Transport of dislocation lines

Taking the time derivative of (5.13) gives the transport equation for the vector density of dislocations,

$$\frac{d}{dt}\boldsymbol{\rho}^{(l)} = \left\langle \sum_{k}^{N_{\mathrm{c}}^{(l)}} \frac{d}{dt} T_{c_{\mathrm{c}(k)}^{(l)}} + \sum_{n}^{N_{\mathrm{o}}^{(l)}} \frac{d}{dt} T_{c_{\mathrm{o}(n)}^{(l)}} \right\rangle . \tag{5.46}$$

As the equation indicates, the dislocation population is assumed to have both closed and open lines. The summand in the first summation above is given by

$$\frac{d}{dt} T_{c_{\mathrm{c}(k)}^{(l)}} = -\mathrm{d}\, \mathrm{i}_{\boldsymbol{v}|_{c_{\mathrm{c}(k)}^{(l)}}} T_{c_{\mathrm{c}(k)}^{(l)}} , \tag{5.47}$$

where use has been made of Lie derivative relation (5.11) and the fact that $\partial c_{\mathrm{c}(k)}^{(l)} = \emptyset$ for closed lines. In this result, the current $\mathrm{i}_{\boldsymbol{v}|_{c_{\mathrm{c}(k)}^{(l)}}} T_{c_{\mathrm{c}(k)}^{(l)}}$ represents the rate of increment in slipped area due to the movement of closed lines. In the time evolution of the current induced by open line segments, an extra term emerges which represents the line created by dragging the endpoint of the lines. Accounting for the fact that $\mathrm{d}T_{c_{\mathrm{c}(k)}} = (-1)^{p+1} T_{\partial c_{\mathrm{c}(k)}}$, we may then write

$$\frac{d}{dt} T_{c_{\mathrm{o}(n)}^{(l)}} = -\mathrm{d}\, \mathrm{i}_{\boldsymbol{v}^{(l)}|_{c_{\mathrm{o}(n)}^{(l)}}} \mathrm{T}_{c_{\mathrm{o}(n)}^{(l)}} + \mathrm{i}_{\boldsymbol{v}^{(l)}|_{\partial c_{\mathrm{o}(n)}^{(l)}}} \mathrm{T}_{\partial c_{\mathrm{o}(n)}^{(l)}} . \tag{5.48}$$

Again, use has been made of Lie derivative relation (5.11). In the last expression the velocity evaluated at the endpoint of the open line is denoted by $\boldsymbol{v}^{(l)}|_{\partial c_{\mathrm{o}(n)}^{(l)}}$ while the velocity along the bulk part of the line is denoted by $\boldsymbol{v}^{(l)}|_{c_{\mathrm{o}(n)}^{(l)}}$. Substituting (5.47) and (5.48) into (5.46) and using the fact that the exterior derivative commutes with ensemble averaging yields

$$\frac{d}{dt}\boldsymbol{\rho}^{(l)} = -\mathrm{d} \left\langle \sum_{k}^{N_{\mathrm{c}}^{(l)}} \mathrm{i}_{\boldsymbol{v}^{(l)}|_{c_{\mathrm{c}(k)}^{(l)}}} T_{c_{\mathrm{c}(k)}^{(l)}} + \sum_{n}^{N_{\mathrm{o}}^{(l)}} \mathrm{i}_{\boldsymbol{v}^{(l)}|_{c_{\mathrm{o}(n)}^{(l)}}} T_{c_{\mathrm{o}(n)}^{(l)}} \right\rangle + \left\langle \sum_{n}^{N_{\mathrm{o}}^{(l)}} \mathrm{i}_{\boldsymbol{v}^{(l)}|_{\partial c_{\mathrm{o}(n)}^{(l)}}} T_{\partial c_{\mathrm{o}(n)}^{(l)}} \right\rangle \tag{5.49}$$

for the evolution of the slip system dislocation current $\boldsymbol{\rho}^{(l)}$.

We note that the interior multiplication with respect to the dislocation velocity $\boldsymbol{v}_k$ of the kth dislocation does not commute with the ensemble average unless all dislocations contributing to the local density share (almost) the same direction [81], as in the line bundle approximation. In this case also the velocity vectors share the same direction and an average

velocity vector $\bar{\boldsymbol{v}}$ may be defined, which enters the interior multiplication within the ensemble average.

Since we are representing the dislocation network in terms of the junction point densities, we convert the endpoint currents to junction point currents via:

$$-T_{\partial c^l_{o(\mathrm{j})}} = \mathrm{sgn}^{(lpq,l)}\mathrm{sgn}(P^{(lpq)}_{(\mathrm{j})})T_{P^{(lpq)}_{(\mathrm{j})}}. \tag{5.50}$$

We further introduce a junction constraint on the endpoint velocities in (5.49) so that each of the connecting arms at the junction point move together at the speed of the junction point itself, $\boldsymbol{v}^{(lpq)}_{\mathrm{J}(n)}$. Moreover, we assume that an ensemble average velocity field can be defined for the junction points. Note that the junction point velocities are in general not perpendicular to the line direction. The junction points are, however, usually restricted to move along intersection lines of slip systems. The average junction point velocity shall be denoted with $\bar{\boldsymbol{v}}^{(lpq)}_{\mathrm{J}}$. With currents being represented by smooth forms, these steps lead to the following evolution law for the dislocation density:

$$\frac{d}{dt}\boldsymbol{\rho}_{\mathbf{s}}{}^{(l)} = -\mathrm{d}\,\mathrm{i}_{\bar{\boldsymbol{v}}^{(l)}}\boldsymbol{\rho}^{(l)}_{\mathrm{s}} - \sum_{p,q:\,(lpq)\in S^l} \mathrm{sgn}^{(lpq,l)}\mathrm{i}_{\bar{\boldsymbol{v}}^{(lpq)}_{\mathrm{J}}}\pi^{(lpq)}_{\mathrm{sJ}}, \tag{5.51}$$

where the convention that the smooth endpoint densities are positive at the start of the line has been used. When written using vector calculus notion for vectors fields in R^3 (given a Euclidean metric) [117, p. 368] the last equations reads

$$\frac{d}{dt}\boldsymbol{\rho}^{(l)}_{\mathrm{s}} = \mathrm{curl}\left(\overline{\boldsymbol{v}}^{(l)} \times \boldsymbol{\rho}^{(l)}_{\mathrm{s}}\right) - \sum_{p,q:\,(lpq)\in S^l} \mathrm{sgn}^{(lpq,l)}\overline{\boldsymbol{v}}^{(lpq)}_{\mathrm{J}}\pi^{(lpq)}_{\mathrm{sJ}}. \tag{5.52}$$

The first term in (5.52) accounts for the transport of the dislocation lines while the second term reflects the movement of the junction points. Note that setting the junction point velocity to zero produces Frank-Read type multiplication [190], while the motion of the junction points would leave the kinematics of the dislocation 'unaffected' if the junction point velocity equals the dislocation velocity. Finding suitable constitutive assumptions for the junction point velocity is yet an open topic.

It is now possible to cast the evolution model of the dislocations on a given slip system in terms of a single dislocation density and two junction density measures for each junction group, one for the positive junction points and one for the negative junction points. In this case, arguments similar to which allowed us to arrive at (5.52) can be used to write

$$\frac{d}{dt}\boldsymbol{\rho}_{\mathrm{s}}^{(l)} = \operatorname{curl}\left(\overline{\boldsymbol{v}}^{(l)} \times \boldsymbol{\rho}_{\mathrm{s}}^{(l)}\right) - \sum_{p,q:\,(lpq)\in S^l} \operatorname{sgn}^{(lpq,l)}\left(\overline{\boldsymbol{v}}_{\mathrm{J}}^{(lpq)+}\pi_{\mathrm{sJ}}^{(lpq)+} - \overline{\boldsymbol{v}}_{\mathrm{J}}^{(lpq)-}\pi_{\mathrm{sJ}}^{(lpq)-}\right). \tag{5.53}$$

In the above, we have grouped junction densities according to their sign and the sign of the negative junction point density has been explicitly taken into account by the minus sign. The reaction term in (5.53) is fundamentally different from similar terms added in previous CDD models [125, 181] where such terms were cast as products of the reacting densities.

5.9.2 Transport of junction point densities

Next, we provide transport relations for the junction point density and the associated positive and negative junction point densities. From their definitions in (5.38), these densities represent signed zero currents and will be treated as such in the following derivations. Taking the time derivative of (5.38) combined with the Lie derivative relation (5.11), considering that zero dimensional currents have no boundary, and that the exterior derivative commutes with averaging we obtain

$$\frac{d}{dt}\pi_{\mathrm{J}}^{(pqr)} = -\mathrm{d}\left\langle \sum_n \mathrm{i}_{\boldsymbol{v}_{J(n)}^{(pqr)}} \operatorname{sgn}(P_{(n)}^{(pqr)}) T_{P_{(n)}^{(pqr)}} \right\rangle. \tag{5.54}$$

When the currents are represented by smooth forms the closed form of the equation becomes

$$\frac{d}{dt}\pi_{\mathrm{sJ}}^{(pqr)} = -\mathrm{d}\,\mathrm{i}_{\overline{\boldsymbol{v}}_{\mathrm{J}}^{(pqr)}}\pi_{\mathrm{sJ}}^{(pqr)}, \tag{5.55}$$

with $\overline{\boldsymbol{v}}_{\mathrm{J}}^{(pqr)}$ denoting the average velocity of junction points. In terms of vector calculus operations acting on the corresponding vector fields in R^3 (given an Euclidean metric) [117, p. 368] we can write the last equation in the form

$$\frac{d}{dt}\pi_{\mathrm{sJ}}^{(pqr)} = -\mathrm{div}\left(\bar{\boldsymbol{v}}_{\mathrm{J}}^{(pqr)}\pi_{\mathrm{sJ}}^{(pqr)}\right). \tag{5.56}$$

For the reasons described in section 5.6 we decide to describe the dislocation network using positive and negative junction densities. When dislocations react and form glissile junctions, two junction points are created with opposite orientations. To model this, source terms are added to the transport equations for the positive and negative junction densities. Using arguments similar to those that led to (5.56) we arrive at

$$\begin{aligned}\frac{d}{dt}\pi_{\mathrm{sJ}}^{(pqr)+} &= -\mathrm{div}\left(\bar{\boldsymbol{v}}_{\mathrm{J}}^{(pqr)+}\pi_{\mathrm{s}}^{(pqr)+}\right) + S^{+} \\ \frac{d}{dt}\pi_{\mathrm{sJ}}^{(pqr)-} &= -\mathrm{div}\left(\bar{\boldsymbol{v}}_{\mathrm{J}}^{(pqr)-}\pi_{\mathrm{s}}^{(pqr)-}\right) + S^{-}.\end{aligned} \tag{5.57}$$

We note that $\pi_{\mathrm{sJ}}^{pqr} = \pi_{\mathrm{sJ}}^{(pqr)+} - \pi_{\mathrm{sJ}}^{(pqr)-}$, with $\pi^{(pqr)+}$ and $\pi^{(pqr)-}$ being positive scalars, and thus $\dot{\pi}_{sJ}^{pqr} = \dot{\pi}_{\mathrm{sJ}}^{(pqr)+} - \dot{\pi}_{\mathrm{sJ}}^{(pqr)-}$. From this we find that we must require, $\bar{\boldsymbol{v}}_{\mathrm{J}}^{(pqr)}\pi_{s}^{(pqr)} = \bar{\boldsymbol{v}}_{J}^{(pqr)+}\pi_{\mathrm{s}}^{(pqr)+} - \bar{\boldsymbol{v}}_{\mathrm{J}}^{(pqr)-}\pi_{\mathrm{s}}^{(pqr)-}$, which we could interpret as a definition of the mean signed point density velocity $\bar{\boldsymbol{v}}_{J}^{(pqr)}$, and $S^{+} = S^{-} = S$. To summarize, the dislocation network evolution can be described in terms of the evolution laws (5.53) and (5.57):

$$\begin{aligned}\frac{d}{dt}\boldsymbol{\rho}_{\mathrm{s}}^{(l)} &= \mathrm{curl}\left(\overline{\boldsymbol{v}}^{(l)} \times \boldsymbol{\rho}_{\mathrm{s}}^{(l)}\right) - \sum_{p,q:\,(lpq)\in S^{l}} \mathrm{sgn}^{(lpq,l)}\left(\overline{\boldsymbol{v}}_{\mathrm{J}}^{(lpq)+}\pi_{\mathrm{sJ}}^{(lpq)+} - \overline{\boldsymbol{v}}_{\mathrm{J}}^{(lpq)-}\pi_{\mathrm{sJ}}^{(lpq)-}\right) \\ \frac{d}{dt}\pi_{\mathrm{sJ}}^{(pqr)+} &= -\mathrm{div}\left(\bar{\boldsymbol{v}}_{\mathrm{J}}^{(pqr)+}\pi_{\mathrm{sJ}}^{(pqr)+}\right) + S \\ \frac{d}{dt}\pi_{\mathrm{sJ}}^{(pqr)-} &= -\mathrm{div}\left(\bar{\boldsymbol{v}}_{\mathrm{J}}^{(pqr)-}\pi_{\mathrm{sJ}}^{(pqr)-}\right) + S.\end{aligned} \tag{5.58}$$

For completeness, we also introduce the transport relations for the virtual segments which are given in the form

$$\frac{d}{dt}\boldsymbol{\rho}_{\mathrm{v,s}}^{(l)} = \sum_{p,q:\,(lpq)\in S^{l}} \mathrm{sgn}^{(lpq,l)}\left(\overline{\boldsymbol{v}}_{\mathrm{J}}^{(lpq)+}\pi_{\mathrm{sJ}}^{(lpq)+} - \overline{\boldsymbol{v}}_{\mathrm{J}}^{(lpq)-}\pi_{\mathrm{sJ}}^{(lpq)-}\right) \tag{5.59}$$

These equations represent the fact that the virtual segments only grow due to movement of junction points which they are attached to. We note that modeling the evolution of the density of virtual segments is not necessary to describe the transport of the system given by (5.58), because this evolution is equivalent to the transport of the endpoint densities.

5.10 Dislocation reactions as source terms

The evolution laws (5.58) do not describe the reaction process itself, i.e, the change in the topology of the dislocation network associated with the creation of new junction points. This a task requires the specification of the source term S introduced in the transport equations for the positive and negative junction point densities in (5.57) and (5.58). In the discrete dislocation dynamics (DDD) literature, these processes are referred to as node merging and node splitting. The goal of this section is to incorporate this type of information into the transport equations (5.58). In doing so, we use the notion of transversal intersections to get a measure of when dislocations intersect.

Geometrically, the formation of junctions starts with the intersection of two lines and the creation of two overlapping junction nodes, as detailed in [27]. An important issue here is to quantify the intersection of two lines in R^3. The machinery of transversal intersections can help in this regard but we are faced with the fact that the transversal intersection depends on the ambient space [66], which makes it difficult to define the intersection between two lines in R^3. It is, however, easier to define the transversal intersection of the surfaces swept by two dislocations due to their motion in four-dimensional space-time. This intersection corresponds to the cutting of dislocations and thus gives a measure of how many dislocation-dislocation reactions occur.

To determine the rate of dislocation cutting we introduce a zero-dimensional space-time current $\mathcal{T}_{\pitchfork}$, which yields a 4-form, i.e., a rate of volume density, upon averaging. This current is defined from the space-time surfaces (world sheets) drawn by the dislocations. Let the dislocation c_t for every time $t \in [0, T)$ be parametrized by some parameter $s \in [0, S)$,

such that $c_t = \{c_t(s), s \in [0, S)\}$. Then the space-time surface of the moving dislocation is a two-dimensional submanifold Σ of 4D space-time, which is parametrized by

$$\Sigma(s,t) = (t, c_t(s)). \tag{5.60}$$

Let $\Sigma_{\mathrm{j}}^{(k)}$ be the space-time surface of dislocation $c_{\mathrm{j}}^{(k)}$, then to get a measure of dislocation-dislocation cutting we define the space-time current

$$\mathcal{T}_{\pitchfork}^{(l,k)}[\theta] \equiv \left\langle \sum_{\mathrm{i}\in N^{(l)},\mathrm{j}\in N^{(k)}} \mathcal{T}_{\Sigma_{\mathrm{i}}^{(l)}\pitchfork\Sigma_{\mathrm{j}}^{(k)}}[\theta] \right\rangle,$$

where $\Sigma_{\mathrm{i}}^{(l)} \pitchfork \Sigma_{\mathrm{j}}^{(k)}$ denotes the transversal intersection of the two space-time surfaces. The restriction to transversal intersections excludes intersections of dislocations which move on the same glide plane, because the intersection of their world-sheets would be a curve in space-time. For the transversal case we depict the intersection of two world sheets by projecting the 4D space-time manifolds onto 3D space in Fig. 5.14. Note that while the spatial surfaces swept by the two dislocations intersect along a line, the curves only actually met each other at a given point in time, indicated by the blue dot in the figure. Transversal intersection in space-time yields this point in space-time, which combines the spatial position and the time of encounter. The transversal intersection of the submanifolds which induce the current $\mathcal{T}_{\pitchfork}^{(l,k)}$ corresponds to the exterior product of the currents induced by the involved submanifolds, i.e.,

$$\mathcal{T}_{\pitchfork}^{(l,k)} = \left\langle \sum_{\mathrm{i}\in N^{(l)},\mathrm{j}\in N^{(k)}} \mathcal{T}_{\Sigma_{\mathrm{i}}^{(l)}} \wedge \mathcal{T}_{\Sigma_{\mathrm{j}}^{(k)}} \right\rangle. \tag{5.61}$$

Ensemble averaging then yields a smooth differential 4-form, $\Gamma_{\mathrm{s}}^{(l,k)}$, such that $\mathcal{T}_{\pitchfork}^{(l,k)}[\theta] = \mathcal{T}_{\Gamma_{\mathrm{s}}^{(l,k)}}[\theta]$.

In general, the dislocation positions and their velocities on the involved slip systems will be correlated and the average of the product currents in (5.61) will not be the product of the average currents but contain additional correlation information. Such correlation information may in principle be obtained from DDD simulations. However, no such information

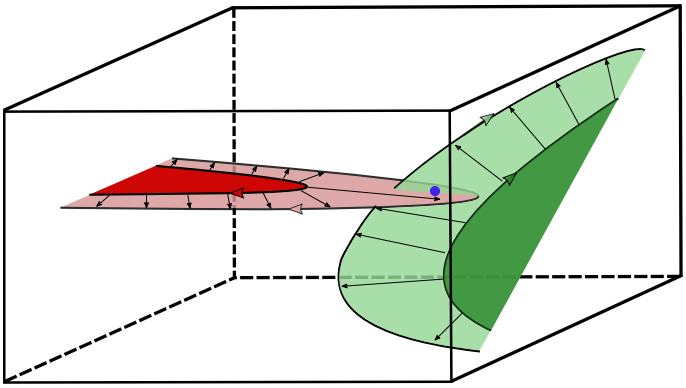

Figure 5.14. Intersection of dislocation worldsheets projected onto three dimensional space. The intersection point of the corresponding worldsheets in 4D space is projected onto the blue point in the figure.

is currently available and therefore we shall assume the space-time sheets to be uncorrelated, such that

$$\mathcal{T}_{\pitchfork}^{(l,k)} = \left\langle \sum_{\mathrm{i}\in N^{(l)}} \mathcal{T}_{\Sigma_{\mathrm{i}}^{(l)}} \right\rangle \wedge \left\langle \sum_{\mathrm{j}\in N^{(k)}} \mathcal{T}_{\Sigma_{\mathrm{j}}^{(k)}} \right\rangle. \tag{5.62}$$

The space-time currents on the right hand side are due to the line-density assumption and by definition of the average velocity given by

$$\left\langle \sum_{\mathrm{i}\in N^{(l)}} \mathcal{T}_{\Sigma_{\mathrm{i}}^{(l)}} \right\rangle = \mathrm{i}_{(1,\,\bar{\boldsymbol{v}}^{(l)})}\mathrm{i}_{(0,\,\boldsymbol{\rho}_{\mathrm{s}}{}^{(l)})}\mathrm{d}V_t = \mathrm{i}_{\boldsymbol{\rho}_{\mathrm{s}}{}^{(l)}}\mathrm{d}V + \left(\mathrm{i}_{\bar{\boldsymbol{v}}^{(l)}}\mathrm{i}_{\boldsymbol{\rho}_{\mathrm{s}}{}^{(l)}}\mathrm{d}V\right) \wedge \mathrm{d}t, \tag{5.63}$$

where $\mathrm{d}V_t = \mathrm{d}V \wedge \mathrm{d}t$ is the space-time volume form and the space time velocity $\mathcal{V} = (1, \boldsymbol{v}^{(l)})$ has unit speed in time direction, while the time-component of the space-time dislocation density vanishes. The smooth 4-form $\Gamma_{\mathrm{s}}^{(l,k)}$ corresponding to the average current (5.62) is accordingly given by

$$\begin{aligned}
\Gamma_{\mathrm{s}}^{(l,k)} &= \left[\mathrm{i}_{\boldsymbol{\rho}_{\mathrm{s}}^{(l)}}\mathrm{d}V + \left(\mathrm{i}_{\bar{\boldsymbol{v}}^{(l)}}\mathrm{i}_{\boldsymbol{\rho}_{\mathrm{s}}^{(l)}}\mathrm{d}V\right) \wedge \mathrm{d}t\right] \wedge \left[\mathrm{i}_{\boldsymbol{\rho}_{\mathrm{s}}^{(k)}}\mathrm{d}V + \left(\mathrm{i}_{\bar{\boldsymbol{v}}^{(k)}}\mathrm{i}_{\boldsymbol{\rho}_{\mathrm{s}}^{(k)}}\mathrm{d}V\right) \wedge \mathrm{d}t\right] \\
&= \left[\boldsymbol{\rho}_{\mathrm{s}}^{(l)} \cdot \left(\boldsymbol{\rho}_{\mathrm{s}}^{(k)} \times \bar{\boldsymbol{v}}^{(k)}\right) + \boldsymbol{\rho}_{\mathrm{s}}^{(k)} \cdot \left(\boldsymbol{\rho}_{\mathrm{s}}^{(l)} \times \bar{\boldsymbol{v}}^{(l)}\right)\right] \mathrm{d}V_t \\
&= \left(\boldsymbol{\rho}_{\mathrm{s}}^{(l)} \times \boldsymbol{\rho}_{\mathrm{s}}^{(k)}\right) \cdot \left(\bar{\boldsymbol{v}}^{(k)} - \bar{\boldsymbol{v}}^{(l)}\right) \mathrm{d}V_t.
\end{aligned} \tag{5.64}$$

The 4-form $\Gamma_{\mathrm{s}}^{(l,k)}$ defines the rate of signed intersections between two slip systems, when dislocations on the slip systems move independently of each other and remain unaffected by the intersections. A very preliminary investigation on non-linearities which would emerge from considering the mutual intersections in the dislocation velocities has been provided in [85]. In the current work we consider the interactions of the slip systems by assuming that a certain fraction of the encounters yield junction points. This fraction may be determined from reaction maps available from discrete dislocation studies [110, 192]. The propensity of two intersecting dislocations to form a junction strongly depends on the relative orientation of dislocations. However, we shall suppress this dependency in the following notation and

assume reaction coefficients $R^{(l,k)}$ given. The creation rate of junction points between slip systems is then given by

$$\bar{S}^{(l,k)} = R^{(l,k)} \left(\boldsymbol{\rho}_{\mathrm{s}}^{(l)} \times \boldsymbol{\rho}_{\mathrm{s}}^{(k)} \right) \cdot \left(\bar{\boldsymbol{v}}^{(k)} - \bar{\boldsymbol{v}}^{(l)} \right). \tag{5.65}$$

We note that since the intersection rate was defined using the notion of a transversal intersection it does not give a measure of reactions when dislocations (and their velocities) are coplanar or when the line directions are parallel, i.e. if $\boldsymbol{\rho}_{\mathrm{s}}^{(k)} \times \boldsymbol{\rho}_{\mathrm{s}}^{(l)} = 0$. Due to the signed nature of this measure, we also encounter cancellations when using it at increasing scales.

We now introduce the source term for the positive and negative junction points into the transport relations (5.58), which now read

$$\begin{aligned}
\frac{d}{dt}\boldsymbol{\rho}_{\mathrm{s}}^{(l)} &= \operatorname{curl}\left(\overline{\boldsymbol{v}}^{(l)} \times \boldsymbol{\rho}_{\mathrm{s}}^{(l)} \right) - \sum_{p,q:\,(lpq)\in S^l} \operatorname{sgn}^{(lpq,l)} \left(\overline{\boldsymbol{v}}_{\mathrm{J}}^{(lpq)+} \pi_{\mathrm{sJ}}^{(lpq)+} - \overline{\boldsymbol{v}}_{\mathrm{J}}^{(lpq)-} \pi_{\mathrm{sJ}}^{(lpq)-} \right) \\
\frac{d}{dt}\pi_{\mathrm{sJ}}^{(p)+} &= -\operatorname{div}\left(\bar{\boldsymbol{v}}_{\mathrm{J}}^{(p)+} \pi_{\mathrm{sJ}}^{(p)+} \right) + \sum_{\mathrm{j}\in I^p} \bar{S}^{(p,\mathrm{j})} \\
\frac{d}{dt}\pi_{\mathrm{sJ}}^{(p)-} &= -\operatorname{div}\left(\bar{\boldsymbol{v}}_{\mathrm{J}}^{(p)-} \pi_{\mathrm{sJ}}^{-(p)} \right) + \sum_{\mathrm{j}\in I^p} \bar{S}^{(p,\mathrm{j})}.
\end{aligned} \tag{5.66}$$

In the above, $\bar{S}^{(s,\mathrm{j})}$ is obtained from (5.65) and I^p is an index set containing the number of unique pairs of slip systems that react to form the junction type associated to $\pi^{(p)}$.

We now give an explicit example for the case of 3 slip systems and only 1 junction type with Burgers vector fixed such that $\boldsymbol{b}^{(1)} + \boldsymbol{b}^{(2)} - \boldsymbol{b}^{(3)} = 0$. In this case, the evolution equations for the dislocation densities read:

$$\begin{aligned}
\frac{d}{dt}\boldsymbol{\rho}_{\mathrm{s}}^{(1)} &= \operatorname{curl}\left(\overline{\boldsymbol{v}}^{(1)} \times \boldsymbol{\rho}_{\mathrm{s}}^{(1)} \right) - \left(\overline{\boldsymbol{v}}_{\mathrm{J}}^{+(123)} \pi_{\mathrm{sJ}}^{(123)+} - \overline{\boldsymbol{v}}_{\mathrm{J}}^{(123)-} \pi_{\mathrm{sJ}}^{(123)-} \right) \\
\frac{d}{dt}\boldsymbol{\rho}_{\mathrm{s}}^{(2)} &= \operatorname{curl}\left(\overline{\boldsymbol{v}}^{(2)} \times \boldsymbol{\rho}_{\mathrm{s}}^{(2)} \right) - \left(\overline{\boldsymbol{v}}_{\mathrm{J}}^{(123)+} \pi_{\mathrm{sJ}}^{(123)+} - \overline{\boldsymbol{v}}_{\mathrm{J}}^{-(123)} \pi_{\mathrm{sJ}}^{(123)-} \right) \\
\frac{d}{dt}\boldsymbol{\rho}_{\mathrm{s}}^{(3)} &= \operatorname{curl}\left(\overline{\boldsymbol{v}}^{(3)} \times \boldsymbol{\rho}_{\mathrm{s}}^{(3)} \right) + \left(\overline{\boldsymbol{v}}_{\mathrm{J}}^{(123)+} \pi_{\mathrm{sJ}}^{(123)+} - \overline{\boldsymbol{v}}_{\mathrm{J}}^{-(123)} \pi_{\mathrm{sJ}}^{(123)-} \right),
\end{aligned} \tag{5.67}$$

and those for the junction point densities read:

$$\begin{aligned}
\frac{d}{dt}\pi_{\mathrm{sJ}}^{(123)+} &= -\mathrm{div}\left(\bar{\boldsymbol{v}}_{\mathrm{J}}^{(123)+}\pi_{\mathrm{sJ}}^{(123)+}\right) \\
&\quad + R^{(1,2)}\left(\boldsymbol{\rho}_s^{(2)} \times \boldsymbol{\rho}_s^{(1)}\right)\cdot \boldsymbol{v}_{\mathrm{rel}}^{(1,2)} + R^{(3,1)}\left(\boldsymbol{\rho}_{\mathrm{s}}^{(3)} \times \boldsymbol{\rho}_{\mathrm{s}}^{(1)}\right)\cdot \boldsymbol{v}_{\mathrm{rel}}^{(1,3)} + R^{(3,2)}\left(\boldsymbol{\rho}_{\mathrm{s}}^{(3)} \times \boldsymbol{\rho}_{\mathrm{s}}^{(2)}\right)\cdot \boldsymbol{v}_{\mathrm{rel}}^{(2,3)} \\
\frac{d}{dt}\pi_{\mathrm{sJ}}^{(123)-} &= -\mathrm{div}\left(\bar{\boldsymbol{v}}_{\mathrm{J}}{}^{(123)-}\pi_{\mathrm{sJ}}^{(123)-}\right) \\
&\quad + R^{(1,2)}\left(\boldsymbol{\rho}_{\mathrm{s}}^{(2)} \times \boldsymbol{\rho}_{\mathrm{s}}^{(1)}\right)\cdot \boldsymbol{v}_{\mathrm{rel}}^{(1,2)} + R^{(3,1)}\left(\boldsymbol{\rho}_{\mathrm{s}}^{(3)} \times \boldsymbol{\rho}_{\mathrm{s}}^{(1)}\right)\cdot \boldsymbol{v}_{\mathrm{rel}}^{(1,3)} + R^{(3,2)}\left(\boldsymbol{\rho}_{\mathrm{s}}^{(3)} \times \boldsymbol{\rho}_{\mathrm{s}}^{(2)}\right)\cdot \boldsymbol{v}_{\mathrm{rel}}^{(2,3)}.
\end{aligned} \tag{5.68}$$

We end this section with a test simulation illustrating the role of the source terms in the dislocation density evolution equation (5.58), which is tied to the transport of the junction point densities. In the 3-slip system case shown in equation (5.67) and (5.68), we simulate the evolution of the dislocation density of one slip system by suppressing the transport part and activating the junction point transport part. Since we only simulate one vector density, the reaction terms are eliminated from the positive and negative junction transport equations, which then simplify to:

$$\begin{aligned}
\frac{d}{dt}\boldsymbol{\rho}_{\mathrm{s}}^{(1)} &= -\left(\overline{\boldsymbol{v}}_{\mathrm{J}}^{+(123)}\pi_{\mathrm{sJ}}^{(123)+} - \overline{\boldsymbol{v}}_{\mathrm{J}}^{(123)-}\pi_{\mathrm{sJ}}^{(123)-}\right) \\
\frac{d}{dt}\pi_{\mathrm{sJ}}^{(123)+} &= -\mathrm{div}\left(\bar{\boldsymbol{v}}_{\mathrm{J}}^{(123)+}\pi_{\mathrm{sJ}}^{(123)+}\right) \\
\frac{d}{dt}\pi_{\mathrm{sJ}}^{(123)-} &= -\mathrm{div}\left(\bar{\boldsymbol{v}}_{\mathrm{J}}^{(123)-}\pi_{\mathrm{sJ}}^{(123)-}\right).
\end{aligned}$$

We start by initializing overlapping positive and negative junction point densities in the center of the simulation domain and a zero initial value of the simulated dislocation density. We specify a junction point velocity field that separates positive and negative junction point densities apart along the y-axis such that a dislocation junction segment is created between them. The positive and negative junction point velocities are then reversed and the junction segment between the two densities is gradually erased as the junction densities approach each other. A first-order system least-squares (FOSLS) finite element method with an implicit Euler time integrator was used to discretize the system in space and time. Fig. 5.15 shows a line profile of the evolution of the dislocation density and the junction point densities along the y-axis. In this figure, we notice some numerical diffusion of the junction point

densities, which is expected with the use of implicit Euler time integrator with no diffusion correction. Even with this numerical diffusion, the junction densities are still conserved during the evolution and can still completely remove the junction segment after the junction point velocities are fully reversed.

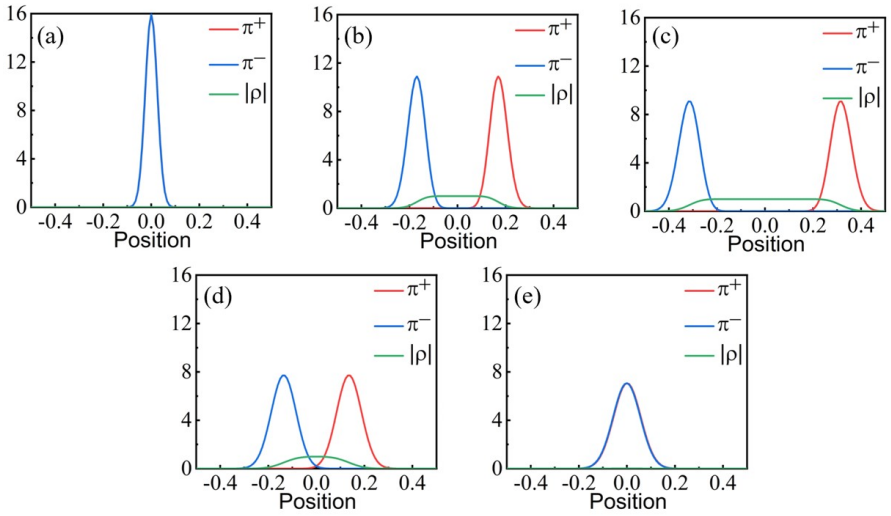

Figure 5.15. Evolution of the dislocation density and the positive and negative junction point densities along the y-axis of the simulation domain. As the system evolves from its initial conditions (a) to subsequent configurations (b) through (e), the junction points initially move away from each other in (a)-(c), drawing out a junction segment. Then the junction velocities are reversed starting at (c) and the junction segment is gradually erased as the junction point densities move closer until the process is completed in (e).

5.11 Concluding remarks

A novel representation of complex dislocation configurations in FCC crystals has been established by viewing dislocation configurations as networks consisting of dislocation lines ending at junction points. In addition to the dislocation density, the junction point densities were introduced as kinematic variables of the dislocation network. Graph theory was used to investigate the connectivity of the dislocation network and establish a connection between endpoints and junction points for open dislocation lines. The concept of de Rham currents along with ensemble averaging were used to derive the evolution laws for the dislocation and junction point densities. These laws comprise the transport-reaction equations for the

dislocation density and junction point densities which are coupled via source terms arising from the transport of junction points and intersections of dislocations.

It was shown that the integral relation $\int_F \boldsymbol{\alpha} = \int_{\partial F} \boldsymbol{\beta}^p$ can be recovered with the help of Frank's second rule along with the use of virtual dislocation segments. It was also found that the graph representing the dislocation network under the condition of glissile junction formation is a r-partite multigraph and that the collinear annihilation reaction of dislocations does not destroy this property. These findings were used to establish a relationship between the line endpoint and junction points, which was crucial in writing the final form for the transport relations of the relevant densities. In addition, the use of the concept of transversal intersections made it possible to define a measure of dislocation reactions leading to junction formation. This measure was essential in defining the source terms in the evolution laws for the junction point densities.

From a geometric standpoint, the introduction of end and junction point densities and open line densities is intuitive and naturally represents topological information of the dislocation network. This opens the way to modify current continuum dislocation dynamics frameworks, which are mostly based upon dislocation line information. The introduction of the junction points can also enable the use of graph theory ideas to analyze complex dislocations networks where information about lines and nodes is important in the constitutive behavior of the dislocation systems.

In developing the current framework for handling the kinematics of complex dislocation configurations, glissile junction reactions were considered in illustrating the basic ideas. However, the final form of the evolution laws of the dislocation and junction point densities are valid when other reactions such cross slip, annihilation reactions, and sessile junction formation are allowed. The properties of the associated graphs in these cases require further investigation.

The introduction of junction point densities enables us to define an edge number density of the open dislocation lines. We have shown this in 5.B. This information could then be used to construct an average link length density (at no additional cost) which is shown to be a useful quantity [174] in characterizing the network.

The current work on modeling dislocation network kinematics is preliminary and is still at the conceptual stage. However, the principal step to move from line information to combined line and point information, i.e., from planar closed dislocation curves to planar segments, holds the promise to incorporate salient topological information into the largely geometric dislocation density descriptions used in continuum dislocation theories. For developing an actual continuum theory of evolving dislocation networks there are still major open questions to be answered. Still on the kinematic level, for example, the connectivity between dislocations and junction points was in the current work established in the line density approximation by introducing the junction point densities. But when the averaging volume additionally contains statistically stored dislocations on each slip system, this connection will only be given in a statistical sense. One avenue for dealing with this may be to again resort to the higher dimensional description in orientation space [81], where the endpoints still carry the line orientation information. The higher dimensional end- or junction point density could then likewise be projected to alignment tensors in physical space. Directional differences between the segments involved in junctions would be expected to yield a generalization of curvature variables. The latter have been recently connected to orientation changes in evaluating straight segment based upon DDD simulations [189]. The curvature variables [81] carry some topological information in the case without junctions. If and in case how this information is connected to the topological information of graph theory will be one of the key questions for developing a general continuum description of dislocation networks. However, in order to describe evolving networks, reaction kinetics, as well as junction and junction point mobilities will be needed. Specifically, the driving forces for junction node motion must be developed and connected with the junction node velocity. Statistical information on reactions has already been successfully incorporated in continuum dislocation descriptions [179, 125, 188], but for obvious reasons they have not yet been connected to the newly introduced junction point densities, their creation, destruction, or motion. This will require novel approaches to evaluating dynamic information from DDD simulations.

5.A Graph formation argument

In Section 5.7, it was mentioned that the graph representing a single junction group is bipartite under the rule that a dislocation can only react with a single arm of a junction. This is a topological requirement dictated by the physics of junction formation. Fig. 5.8 shows a typical graph for this case. In this appendix, we clarify how this topological requirement arises. In Section 5.8, the case of multiple junction groups was also considered. In this case, the graph representing the dislocation network was said to be r-partite. It will be shown in this appendix that, in this case, a dislocation can react with more than one arm of the junction node without altering the r-partite characteristic of the graph.

We start with the case of a single junction group. With Burgers vectors fixed as given in Table 5.1 the corresponding junction reactions at each node in the corresponding graph must be given in the form (modulo a sign)

$$\begin{aligned} \boldsymbol{b}_2 + \boldsymbol{b}_6 - \boldsymbol{b}_3 &= 0 \\ \boldsymbol{b}_3 + \boldsymbol{b}_5 - \boldsymbol{b}_1 &= 0 \\ \boldsymbol{b}_2 + \boldsymbol{b}_5 - \boldsymbol{b}_4 &= 0 \\ \boldsymbol{b}_4 + \boldsymbol{b}_6 - \boldsymbol{b}_1 &= 0. \end{aligned} \tag{5.69}$$

The set of Burgers vectors in Table 5.1 can be represented geometrically as edges of a tetrahedron, see Fig. 5.16. The equations above thus correspond to the reactions formed by considering Burgers vector on the individual faces of the tetrahedron. Junctions resulting from such reactions are called coplanar and they are glissile in nature. It is convenient in this case to associate each face of the tetrahedron with a certain junction group. Let us assume that it is possible for an incoming dislocation to react with two arms connected to the same junction node. Fig. 5.17 (a) and (b) depicts this situation, where the black dislocation is about to react with two segments (arms), the orange and the green. If these reaction were possible, then the resulting graph would look like those in parts (c) and (d) in the figure, respectively. We have marked this reacting loop with the color black to signify that, at

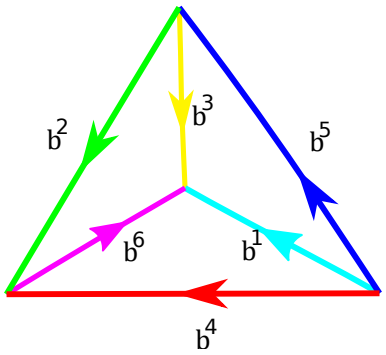

Figure 5.16. Depiction of how the Burgers vectors in Table 5.1 are fixed on a tetrahedron, which is similar to the Thompson tetrahedron for FCC crystals.

this moment, its Burgers vector can be any of the three Burgers vector group (blue, orange, green) shown in the figure. We now show that no matter what the Burgers vector chosen for the black loop is, a glissile junction cannot form when considering only one junction group (a triplet of Burgers vector). We note that the junction type (and thus group) of node v4 is the same as v3 (but opposite in orientation). The same can be said for nodes v5 and v6. In choosing a Burgers vector for the black segments, there are two options to choose from. The first is that both nodes v3 and v5 belong to the same junction group, and the second is that they do not. For the first option, if the black segment is to react with both

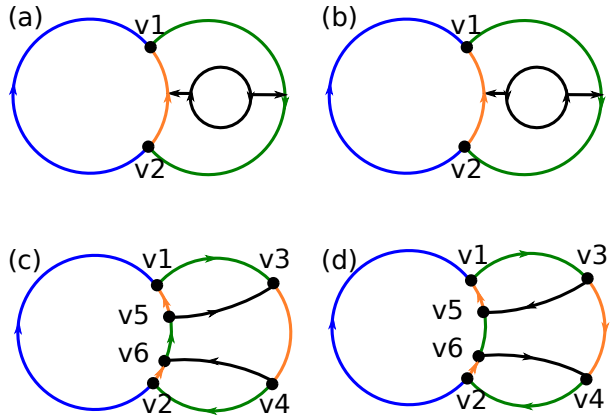

Figure 5.17. A dislocation loop (black) is about to react with two arms (orange and green) connected to junction point v1. Two different reactions (a) and (b) are taking place to show how the orientation of the black segment affects the resulting graphs shown on the bottom.

the green and orange segments (imagine picking two edges on the tetrahedron), then there is only one Burgers vector to chose from depending on what the Burgers vectors of the green and orange segments are (the last edge on the face which contains the previous two edges). With the coloring scheme provided in Fig. 5.17 the black segment must be blue to have a chance to react with both segments. From the equation set in (5.69) we know that in each reaction two of the segments must be oriented similarly, and the third must be opposite. We note that the colors on the graph in Fig 5.17 could correspond to any set of three Burgers vectors given in (5.69). With this in mind, if we look at nodes v1,v3 and v5, we see that the set of segments that are oriented similarly change as we traverse from node to node in the graph, which is inconsistent with (5.69). We also note that this inconsistency is independent

of how we fix the orientations of the Burgers vectors in Table 5.1. We can consider another scenario where we fix the burgers vectors such that $\boldsymbol{b}_1 + \boldsymbol{b}_2 + \boldsymbol{b}_3 = 0$, but there would still be inconsistency in this case due to the triangle that formed in the graph. We conclude that this first option, where nodes v3 and v5 have the same junction group, cannot produce junctions of one group.

Next, we address the second option where we allow the junction groups of nodes v3 and v5 to differ. In this case, it *is* possible for an incoming dislocation to react with two arms of the same junction node, but the bipartite property of the graph is destroyed. As mentioned in the main text, when multiple junction groups are considered, the graph is now r-partite, where r is 2n, and n is the number of junction groups. To remain a r-partite, the newly created junction nodes v3 and v5 must either all have different junction groups or be a mixture of different junction groups and orientations. It will be sufficient to show that whenever we have a triangle in the graph, like the one created by vertices v1,v3 and v5, we must have different junction groups for each of these vertices. This is because we are guaranteed differing orientations between v3 and v4 and also v5 and v6. To show that each node has a different junction group, we can use the closedness property of the total dislocation density tensor. If we draw a surface that encloses the triangle v1,v3, and v5, we can use the intersection property and the closedness property of the dislocation density tensor,

$$\int_{\partial V} \sum_{l=1}^{3} \boldsymbol{\alpha}_{\mathrm{s}}^{(l)} = 0. \tag{5.70}$$

This surface, ∂V, is depicted by the red line in the plane in Fig. 5.18.

From Fig. 5.18 we learn that the segments e1, e5, and e6 must have Burgers vectors such that they could react with one another. We could for instance imagine that the Burgers vector of e1 was $\boldsymbol{b}_2$ then the edges e5 and e6 could either be $\boldsymbol{b}_6$ and $\boldsymbol{b}_3$ or $\boldsymbol{b}_5$ and $\boldsymbol{b}_4$. Whichever set is chosen for these edges ($\boldsymbol{b}_6$ and $\boldsymbol{b}_3$ or $\boldsymbol{b}_5$ and $\boldsymbol{b}_4$), it is important to note that the junction groups of the interior nodes v1, v2, and v3 cannot be part of the junction group which consist of the Burgers vectors for e1, e5, and e6. To show the latter, let e1, e2, and e3 be in this junction group by giving them the Burgers vector $\boldsymbol{b}_2$, $\boldsymbol{b}_6$, and $\boldsymbol{b}_3$ respectively. In this case, e3 and e6 have the same Burgers vector and is not a valid junction type. If we now set e1,

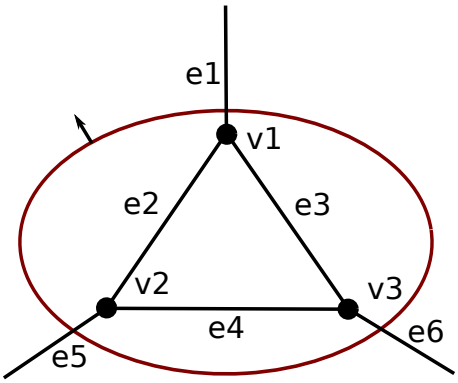

Figure 5.18. A graphical representation of a dislocation network containing a triangle. This triangle is enclosed by a closed surface denoted by the red line.

e2, and e3 to be $\boldsymbol{b}_2$, $\boldsymbol{b}_3$, and $\boldsymbol{b}_6$, respectively, then node v3 would also have to be in this group because the only reaction with both $\boldsymbol{b}_3$ and $\boldsymbol{b}_6$ is the junction group with $\boldsymbol{b}_2$,$\boldsymbol{b}_6$, and $\boldsymbol{b}_3$. Similar arguments hold for v2, and thus they have to all fall in the same group. We have shown earlier in this appendix that this is not allowed.

We refer to the choice of Burgers vectors for edges e1, e5, and e6 in Fig. 5.18 as the 'face constraint', meaning that the remaining edges (e2,e3 and e4) in the same figure cannot form reactions with edges e1, e5, and e6 to give junction points (vertices) in the same junction group as that would result from the e1, e5, and e6 reaction. According to Fig. 5.16 each Burgers vector may be involved in two junction groups corresponding to the faces that it is coincident with. This statement is valid for e1 which must form a reaction with e2 and e3 that is different from the reaction corresponding to the face constraint. Similarly edge e5 must form a reaction with e2 and e4 that is different than the reaction corresponding to the face constraint. Also e6 must form a reaction with e3 and e4 that is different than the reaction corresponding to the face constraint. Due to the geometry of the tetrahedron, the faces opposite of the constraint face are not the same, and thus the junction groups of the nodes v1,v2, and v3 are different. Interestingly, this results in the specification of a different Burgers vector for each of the six edges connected to the triangle.

5.B Open line number density

In this appendix, we define a density variable associated with open dislocation lines, which represents the number density of dislocations ending or starting in a unit volume at a given point in space. Although this density is not used in our model equations, it is derived here for completeness. To obtain this density, we use a famous relation in graph theory called the degree sum formula (sometimes called the handshaking lemma), which takes on the form

$$|E| = \frac{1}{2}\sum_{v\in V}\deg(v), \tag{5.71}$$

where $|E|$ denotes the number of edges, deg is the number of edges connected to a vertex $v \in V$ with V denoting the vertex set of the graph. In this work, we argue for the use of positive and negative junction point densities, denoted by $\pi_{\mathrm{sJ}}^{+(p)}$ and $\pi_{\mathrm{sJ}}^{-(p)}$, respectively, to

represent the junction nodes in the network. Since we are only considering junctions with 3 arms, the degree of each vertex is 3. From this information and (5.71), we define the open line number density E to be,

$$E = \frac{1}{2}\left[3\sum_{p\in S}(\pi_{\mathrm{sJ}}^{+(p)} + \pi_{\mathrm{sJ}}^{-(p)})\right] \tag{5.72}$$

where S is an index set containing all the junction types. We note that when we have information about the junction point densities we can obtain this measure at no additional cost. It is easy to see that this definition can be specialized to counting the number density of open lines belonging to a given slip system, ending or starting in a unit volume at a given point in space by considering only $\pi_{\mathrm{sJ}}^{+(p)}$ and $\pi_{\mathrm{sJ}}^{-(p)}$ for that slip system in the above expression. Such a density can be further defined for open dislocation lines involved in a particular junction group or junction type.

6. JUNCTION POINT KINETICS

This chapter picks up where the previous chapter on the kinematics of the dislocation network left off. It develops the kinetics of dislocation junction points and, after postulating a junction point mobility law for the junction points, it obtains a mean velocity field for the junction points. This mean velocity field closes the set of transport equations posed in the previous chapter.

6.1 Abstract

In this work, a closed form set of transport equations that model the evolution of the dislocation network, including terms that account for the introduction of junction points is derived. A previous model that considers junction points has been derived in [176]; however, the model lacks a definition for the mean velocity field of junction nodes which must be obtained from driving forces on the nodes. In this work, the mean velocity field is obtained by averaging the velocity fields of each junction node. Each node's velocity is obtained by deriving a driving force realized by evaluating variational derivatives of the elastic energy with respect to the motion of that node. The driving force is related to the velocity field by introducing a linear velocity mobility law for the junction nodes. The elastic energy is decomposed into self, and interaction energy terms, and only the self-energy terms are considered in deriving the driving forces on each junction node. These forces depend on the line length and orientation relative to the Burgers vector of each dislocation segment attached to the junction node. Since the driving forces are dependent on the line length, an average line length per dislocation segment is needed and introduced to obtain the mean velocity field.

6.2 Introduction

In a recent work, [176] developed a mean-field continuum dislocation dynamics (CDD) model that considers dislocation lines on each slip system as open lines connected to junction points. Considering such an intuitive geometric description of the dislocation network, the

model introduces a set of junction point densities as state variables in describing the dislocation network. The model primarily focused on the kinematics of the evolution of dislocation networks and introduced a set of transport equations for dislocation and junction point densities. In this framework, the junction point velocity was left unspecified. Obtaining a mean velocity field for the junction points therefore required for properly closing the model equations in [176]. Working out the physics leading to such a velocity field thus gives insight into the dynamics of the overall dislocation network and, will thus impact how continuum dislocation dynamics models are developed. This, in turn, has its benefits in better predictions of the patterning of the dislocations in deforming crystals and in understanding how metal harden during deformation. It is the objective of the current work to present preliminary ideas to specify the velocity field of junction points much in the same fashion as done for the dislocation lines [151, 80]. Some continuum dislocation dynamics models have considered the dislocation population in deforming crystals to comprise ensembles of closed loops, see, for example, [177, 1, 81]. This assumption naturally guarantees the divergence-free dislocation density tensor or vector in the respective theories, complying with the physical requirement that no lines ends inside the crystal. A notable deviation from this concept was pursued by [190], where they considered Frank-Read sources from finite segments pinned at their ends. An improvement over these models was introduced by [188] and by [125], who modeled cross slip and reactions with virtual dislocation densities ensuring the divergence-free of the density of the dislocation network, taking into consideration the virtual density itself. The evolution of the virtual density was then fully described in terms of local cross slip and junction reactions. While the work by [176] is similar in spirit to the latter works, it introduces the junction point density instead as a more natural description of the network. To our knowledge, most of the current continuum dislocation models have not considered the altered kinematics of open dislocation lines on each slip system and its connection to the motion of junction points.

Numerous authors analyzed open discrete dislocation line configurations and forces on junctions and pinning points. The relevant works typically use the line tension approximation [79, 80, 50, 23] to study the equilibrium configurations of junctions [50] or to compute the self-energies of the dislocation lines and compare the total elastic energies of various dislocation

configurations [80]. There also exist line tension approximations in anisotropic media [19]. [130] and [193] use the line tension approximation to analyze crossed states (a state where a junction reaction has occurred, but the product junction segment has zero length). [130] used an orientation-dependent line tension model to determine whether two reacting dislocations would produce an energetically favorable junction reaction. This energy criterion considers the relative orientation of the reacting segments rather than the cruder and commonly used Frank criteria [80]. In these models, though, the line configurations are considered static, and thus there is no net motion of the junction point.

Considering junction points to be part of the dislocation network configuration, it is possible to determine their evolution through forces acting upon them. In a generic sense, they do not differ from other defects in crystals, which suffer configuration forces [68, 136] if the changes in their positions alter the energy of the crystal. In this regard, and taking dislocation lines themselves as an example, there seem to be at least two approaches to derive the corresponding configurational forces upon them. The first approach is to develop an energy functional that depends on the dislocation configuration as was done by [202] and [8]. In this case, the driving forces are computed as variational derivatives of this energy functional with respect to average state variables representing the dislocation configuration, for instance, the dislocation density. The second approach considers averaging the discrete driving forces [62]. In the cited work, a system of parallel edge dislocations is analyzed in 2D, where dislocations are viewed as particles so that classical statistical methods can be applied to derive the mean-field expressions for the evolution of the dislocation density. In subsequent models, [63, 64] pair correlation functions are used to introduce short-range interactions to the evolution equations. This second approach is the one taken in this work where we average the discrete forces on the junction points.

The approach to line dislocation dynamics developed in [24] might be of relevance here, where the generalized forces acting on the dislocation configuration is made to depend on nodes between dislocation segments, via a discretization of the lines. Then the force acting on all nodes was found as a variational derivative of the energy of the system with respect to the positions of the nodes. This is not different from the works mentioned above but it

sheds light as to how the development in the current work was carried out for the forces acting on junction points.

In 3D dislocations models, dislocations are treated as space curves, adding a layer of complexity related to defining an ensemble average of a collection of curves. De Rham integral currents [38] help in this regard as they turn out to be a useful mathematical tool to approach the problem of averaging a collection of manifolds [32]. The application of currents to dislocation systems was first done in [81]. In the latter work, random currents were used to represent the dislocations to derive the mean field equations describing the dislocation density evolution through ensemble averaging. A wide range of applications of random currents to physical systems can be found in [32]. Preliminary work for studying pair correlations for 3D models of dislocations also exists [8, 37]. The junction points in this work are represented using integral currents with the goal of providing a closed-form expression for the transport of junction points which will indeed require obtaining a mean velocity field.

The current paper is organized as follows. We derive the discrete forces on a dislocation junction node in Section 6.3 assuming that the dislocation lines are not closed loops. In Section 6.4, we perform numerical validation of the forces, followed by the derivation of mean forces for the junction densities in Section 6.5 and introduce a velocity mobility law relating the mean force to the velocity of the junction nodes. In Section 6.6 an average length per dislocation segment is defined to complete the definition of the average force driving the junction densities. The assumptions used to derive this mean force is discussed in Section 6.7. Lastly, a section on concluding remarks and a discussion of future work is presented.

6.3 Line tension and endpoint force derivation

In this section, an expression for the force on an individual junction point is derived as the variational derivative of the elastic energy functional with respect to the position of the junction point. It is to be noted that our interest is limited to studying the behavior of junction points and thus will not analyze the forces on the dislocation lines themselves since this is already a classical topic. Having said so, we draw the reader's attention to the fact

that the forces on the entire configuration combining both junction points and dislocation lines can be derived in a unified fashion from the appropriate variational derivatives of the system energy with respect to the degrees of freedom of the dislocation system.

To this end, we consider our dislocation configuration to consist of lines, c_i, and junction points. The lines themselves may be closed or open, and only the latter are incident with junction points. Regardless of the slip systems containing these lines, each line has its own Burgers vector. The lines are contained in glide planes, which, along with their Burgers vectors, define the slip systems they belong to. The dislocation lines are collectively denoted by $\mathcal{L} = \cup_\mathrm{i} c_\mathrm{i}$. The elastic energy of a system of dislocations, $\mathrm{E_e}$ can be expressed as a functional of the line configuration, c, as given by [80, 29]:

$$\mathrm{E_e}[\mathcal{L}] = \sum_{\mathrm{i,j}} \int_{c_\mathrm{i}} \int_{c_\mathrm{j}} (\mathbf{t}_\mathrm{i} \cdot \boldsymbol{\mathcal{E}}_{\mathrm{int(i,j)}} \cdot \mathbf{t}_\mathrm{j}) \mathrm{d}\ell_\mathrm{i} \mathrm{d}\ell_\mathrm{j}, \tag{6.1}$$

where the tensor $\boldsymbol{\mathcal{E}}_{\mathrm{int(i,j)}}$ is an interaction kernel between lines c_i and c_j, $\mathbf{t}_\mathrm{i}$ is the unit tangent vector to the curve c_i and $\mathrm{d}\ell_\mathrm{i}$ is its differential arclength. The kernel of the double integral above can be expressed in the form [202]

$$\boldsymbol{\mathcal{E}}_{\mathrm{int(i,j)}} = \frac{\mu}{4\pi} \left\{ \left[2\boldsymbol{b}_\mathrm{j} \otimes \boldsymbol{b}_\mathrm{i} - \boldsymbol{b}_\mathrm{i} \otimes \boldsymbol{b}_\mathrm{j} \right] \frac{1}{|\Delta \boldsymbol{r}|} + \frac{1}{1-\nu} \left[(\boldsymbol{b}_\mathrm{i} \times \nabla) \otimes (\boldsymbol{b}_\mathrm{j} \times \nabla) \right] |\Delta \boldsymbol{r}| \right\}, \tag{6.2}$$

with μ being the shear modulus, ν Poisson's ratio, $\mathbf{b}_\mathrm{i}$ the Burgers vector on dislocation line c_i, $\Delta \boldsymbol{r}$ the difference between the position vectors of the differential elements $\mathrm{d}\ell_\mathrm{i}$ and $\mathrm{d}\ell_\mathrm{j}$, and ∇ the del operator. It is customary to decompose (6.1) into self and pairwise interaction terms,

$$\mathrm{E_e}[\mathcal{L}] = \sum_{\mathrm{i}} \int_{c_\mathrm{i}} \mathcal{E}_{\mathrm{self(i)}} \mathrm{d}\ell_\mathrm{i} + \sum_{\mathrm{i,j\ i>j}} \int_{c_\mathrm{i}} \int_{c_\mathrm{j}} (\mathbf{t}_\mathrm{i} \cdot \boldsymbol{\mathcal{E}}_{\mathrm{int(i,j)}} \cdot \mathbf{t}_\mathrm{j}) \mathrm{d}\ell_\mathrm{i} \mathrm{d}\ell_\mathrm{j}. \tag{6.3}$$

In the above, $\mathcal{E}_{\mathrm{self(i)}} = \int_{c_\mathrm{i}} (\mathbf{t}_\mathrm{i} \cdot \boldsymbol{\mathcal{E}}_{\mathrm{int(i,i)}} \cdot \mathbf{t}_\mathrm{i}) \mathrm{d}\ell_\mathrm{i}$ is the self-energy of a dislocation line c_i per unit length, which is a scalar quantity. The indices $\mathrm{i}, \mathrm{j} \in [1, N_\mathrm{o} + N_\mathrm{c}]$ where N_o and N_c are the

number of open and closed dislocation lines, respectively. The first term in (6.3) is a sum over self-energies of the individual lines defined by

$$\mathrm{E}_{\mathrm{self(i)}} = \int_{c_\mathrm{i}} \mathcal{E}_{\mathrm{self(i)}} \mathrm{d}\ell_\mathrm{i}, \tag{6.4}$$

and will be referred to as the total self-energy of the system of lines, $\mathrm{E}_{\mathrm{self}}$. The second term in (6.3) will be referred to as the interaction energy and denoted by $\mathrm{E}_{\mathrm{int}}$. The latter is the sum of interaction energy of unique pairs of lines, $\mathrm{E}_{\mathrm{int(i,j)}}$, written in the form

$$\mathrm{E}_{\mathrm{int(i,j)}} = \int_{c_\mathrm{i}} \int_{c_\mathrm{j}} (\mathbf{t}_\mathrm{i} \cdot \boldsymbol{\mathcal{E}}_{\mathrm{int(i,j)}} \cdot \mathbf{t}_\mathrm{j}) \mathrm{d}\ell_\mathrm{i} \mathrm{d}\ell_\mathrm{j}. \tag{6.5}$$

When considering the self terms in (6.3), the line tension approximation is typically used [59]. In this approximation, the energy density of a dislocation line is approximated by a local expression giving a line energy per length, denote by $\mathrm{E}(\theta)$, of the dislocation line. The self-energy of all the dislocation lines can then be written in the form

$$\mathrm{E}_{\mathrm{self}} := \sum_{\mathrm{i}}^{N_\mathrm{o}+N_\mathrm{c}} \int_{c_\mathrm{i}} \mathrm{E}_\mathrm{i}(\theta) \mathrm{d}\ell_\mathrm{i}. \tag{6.6}$$

For instance, in [80], the expression

$$\mathrm{E}_\mathrm{i}(\theta) = \frac{\mu b^2}{4\pi(1-\nu)} (1 - \nu \mathrm{cos}(\theta)^2) \mathrm{ln}\left(\frac{L_\mathrm{i}}{\mathrm{e}\rho}\right) \tag{6.7}$$

is used where L_i is the length of the dislocation segment and ρ is a cut-off parameter which lies in the range $\frac{b}{10} < \rho < \frac{b}{4}$ [79], b is the magnitude of the Burgers vector and θ is the angle between the Burgers vector and line direction. To obtain the driving force on a junction point p_k, a variational derivative of the energy expression (6.3) with respect to changes in all the endpoints attached to the junction point p_k is applied. Let $\boldsymbol{r}_{c_\mathrm{i}}(\ell)$ be an arclength parameterization of the curve c_i, and $\boldsymbol{u}_{c_\mathrm{i}}$ be an arbitrary perturbation of the line restricted to

its glide plane including arbitrary perturbations at the endpoints denoted by $\boldsymbol{u}_{\partial c_\mathrm{i}} = \boldsymbol{u}_{c_\mathrm{i}}(\partial c_\mathrm{i})$. The perturbed curve $c_\mathrm{i} + \delta c_\mathrm{i}$ is defined by

$$\boldsymbol{r}_{c_\mathrm{i}+\delta c_\mathrm{i}}(\ell, t) = \boldsymbol{r}_{c_\mathrm{i}}(\ell) + t\boldsymbol{u}_{c_\mathrm{i}}(\ell). \tag{6.8}$$

Taking the variational derivative of the elastic energy expression (6.3) with respect to perturbations of a junction node amounts to computing $\delta \mathrm{E}_{\mathrm{self}} + \delta(\sum_{\mathrm{i,j\ i>j}} \mathrm{E}_{\mathrm{int(i,j)}})$, where the variation of the self-energy is given as

$$\begin{aligned}\delta \mathrm{E}_{\mathrm{self}} = \frac{\mathrm{d}}{\mathrm{d}t} \sum_{\mathrm{i}}^{N_\mathrm{o}(p_k)} \int_{c_\mathrm{i}+\delta c_\mathrm{i}} \mathrm{E}_\mathrm{i}|_{t=0} \mathrm{d}\ell_\mathrm{i} = \sum_{\mathrm{i}}^{N_\mathrm{o}(p_k)} \int_{c_\mathrm{i}} -\kappa \left(\mathrm{E}_\mathrm{i}(\theta) + \frac{\mathrm{d}^2 \mathrm{E}_\mathrm{i}(\theta)}{\mathrm{d}\theta^2} \right) \mathbf{n}_\mathrm{i} \cdot \mathbf{u}_{c_\mathrm{i}} \mathrm{d}\ell_\mathrm{i} \\ + \sum_{\mathrm{i}}^{N_\mathrm{o}} \int_{\partial c_\mathrm{i}} \mathrm{E}_\mathrm{i}(\theta) \mathbf{t}_\mathrm{i} \cdot \mathbf{u}_{\partial c_\mathrm{i}} + \frac{\mathrm{dE}_\mathrm{i}(\theta)}{\mathrm{d}\theta} \mathbf{n}_\mathrm{i} \cdot \mathbf{u}_{\partial c_\mathrm{i}}.\end{aligned} \tag{6.9}$$

In the above, $N_\mathrm{o}(p_k)$ denotes the number of open line segments connected to the junction point p_k, κ is the curvature of the line, and $\mathbf{n}$ is the normal of the dislocation line in its glide plane. The above expression can be found using standard identities found in [69]. The reader is directed to 6.A where the derivation is performed. The evolution of the dislocation configuration results in energy dissipation due to drag. Considering a perturbation $\mathbf{u}_{c_\mathrm{i}}$ of the dislocation lines, a variation of the dissipated energy $\mathrm{E}_{\mathrm{d_{Bulk}}}$ can be written in the form

$$\delta \mathrm{E}_{\mathrm{d_{Bulk}}}(c_\mathrm{i}) = \int_{c_\mathrm{i}} \mathbf{F}_{c_\mathrm{i}} \cdot \mathbf{u}_{c_\mathrm{i}} \mathrm{d}\ell_\mathrm{i}, \tag{6.10}$$

where the drag force is denoted by $\mathbf{F}_{c_\mathrm{i}}$ and applied to the dislocation line. A similar drag force, $\mathbf{F}_\mathrm{J}$, can be defined for junctions. This force is introduced to account for the variation of the dissipated energy due to the motion $\mathbf{u}_{\mathrm{J_k}}$ of the junction point p_k,

$$\delta \mathrm{E}_{\mathrm{d_{Junction}}}(p_k) = \int_{p_k} \mathbf{F}_{\mathrm{J_k}} \cdot \mathbf{u}_{\mathrm{J_k}}. \tag{6.11}$$

From the principle of virtual work, $\delta \mathrm{E_e} + \sum_{\mathrm{i}} \delta \mathrm{E_{d_{Bulk}}}(c_{\mathrm{i}}) + \delta \mathrm{E_{d_{Junction}}}(p_k) = 0$. This can be expanded to

$$\begin{aligned}
&\sum_{\mathrm{i}}^{N_{\mathrm{o}}(p_k)} \left(\int_{c_{\mathrm{i}}} \left[-\kappa \left(\mathrm{E_i}(\theta) + \frac{\mathrm{d}^2 \mathrm{E_i}(\theta)}{\mathrm{d}\theta^2} \right) \mathbf{n}_{\mathrm{i}} + \mathbf{F}_{c_{\mathrm{i}}} \right] \cdot \mathbf{u}_{c_{\mathrm{i}}} \right) \mathrm{d}\ell_{\mathrm{i}} \\
&+ \sum_{\mathrm{i}}^{N_{\mathrm{o}}(p_k)} \left(\int_{\partial c_{\mathrm{i}}} \mathrm{E_i}(\theta) \mathbf{t}_{\mathrm{i}} \cdot \mathbf{u}_{\partial c_{\mathrm{i}}} + \frac{\mathrm{dE_i}(\theta)}{\mathrm{d}\theta} \mathbf{n}_{\mathrm{i}} \cdot \mathbf{u}_{\partial c_{\mathrm{i}}} \right) + \int_{p_k} \mathbf{F}_{\mathrm{J_k}} \cdot \mathbf{u}_{\mathrm{J_k}} \\
&+ \delta \sum_{\mathrm{i,j\ i \neq j}} \int_{c_{\mathrm{i}}} \int_{c_{\mathrm{j}}} (\mathbf{t}_{\mathrm{i}} \cdot \boldsymbol{\mathcal{E}}_{\mathrm{int(i,j)}} \cdot \mathbf{t}_{\mathrm{j}}) \mathrm{d}\ell_{\mathrm{i}} \mathrm{d}\ell_{\mathrm{j}} = 0.
\end{aligned} \tag{6.12}$$

The second and third terms can be simplified by invoking a constraint which says that the variation of each of the endpoints connected to a junction node p_k is equal to the variation of that junction node $\boldsymbol{u}_{\partial c_{\mathrm{i}}(p_k)} = \boldsymbol{u}_{\mathrm{J_k}}, \mathrm{i} = 1, 2, ..., N_{\mathrm{o}}(p_k)$. Enforcing the latter constraint leads to

$$\begin{aligned}
&\sum_{\mathrm{i}}^{N_{\mathrm{o}}(p_k)} \left(\int_{\partial c_{\mathrm{i}}} \mathrm{E_i}(\theta) \mathbf{t}_{\mathrm{i}} \cdot \mathbf{u}_{\partial c_{\mathrm{i}}} + \frac{\mathrm{dE_i}(\theta)}{\mathrm{d}\theta} \mathbf{n}_{\mathrm{i}} \cdot \mathbf{u}_{\partial c_{\mathrm{i}}} \right) + \int_{p_k} \mathbf{F}_J \cdot \mathbf{u}_{J_k} \\
&= \int_{p_k} \left[\sum_{\mathrm{i}}^{N_{\mathrm{o}}(p_k)} \mathrm{sgn}_{p_k}(\partial c_{\mathrm{i}}) \left(\mathrm{E_i}(\theta) \mathbf{t}_{\mathrm{i}} + \frac{\mathrm{dE_i}(\theta)}{\mathrm{d}\theta} \mathbf{n}_{\mathrm{i}} \right) + \mathbf{F}_{\mathrm{J_k}} \right] \cdot \mathbf{u}_{\mathrm{J_k}}
\end{aligned} \tag{6.13}$$

where $\mathrm{sgn}_{p_k}(\partial c_{\mathrm{j}})$ denotes the sign of the endpoint ∂c_{j} of the curve c_{j} at the junction point p_k. In [193], it was observed that the self-energy terms alone were enough to predict whether or not it was energetically favorable for two reacting dislocations to form a junction, crossed state, or no junction at all. For this reason, only the self-energy terms of the dislocation lines are used in deriving the forces on the junction nodes. For a first pass at developing a model, the interaction terms in (6.12) are neglected. In doing this, the following set of forces on the dislocation line and junction node are obtained:

$$\begin{aligned}
\mathbf{F}_{c_{\mathrm{i}}} &= \kappa \left(\mathrm{E_i}(\theta) + \frac{\mathrm{d}^2 \mathrm{E_i}(\theta)}{\mathrm{d}\theta^2} \right) \mathbf{n}_{\mathrm{i}} \\
\mathbf{F}_{\mathrm{J_k}} &= - \sum_{\mathrm{j}}^{N_{\mathrm{o}}(p_k)} \mathrm{sgn}_{p_k}(\partial c_{\mathrm{j}}) \left(\mathrm{E_j}(\theta) \mathbf{t}_{\mathrm{j}} + \frac{\mathrm{dE_j}(\theta)}{\mathrm{d}\theta} \mathbf{n}_{\mathrm{j}} \right).
\end{aligned} \tag{6.14}$$

In the first set of equations in (6.14), the usual line tension force $\kappa \mathrm{F_T}\mathbf{n}$ is identified where $\mathrm{F_T} = \mathrm{E}(\theta) + \frac{\mathrm{d}^2\mathrm{E}(\theta)}{\mathrm{d}\theta}$. This force acts on the bulk of the dislocation lines to reduce the total line length. The second set of equations acts at the endpoints of the dislocation lines. Each of the terms in the summand is oriented along the tangent and directed into each dislocation line. When the forces are unbalanced, this results in the motion of the junction node. The net force on the junction point has contributions from a line tension term, given by the $\mathrm{E_j}(\theta)\mathbf{t_j}$ terms in the summand, and a moment term given by the $\mathrm{dE_j}(\theta)/\mathrm{d}\theta\mathbf{n_j}$ terms which are due to the orientation dependence elastic energy density. The latter terms tends to rotate each dislocation arm towards their respective screw segments. Notice that the forces on the bulk part of the dislocation lines are drastically different than those on the junction points. This difference further motivates the need to model both the dislocation lines and the junction points to capture this difference.

The driving forces (6.14) may be related to a junction velocity field by using a linear velocity mobility law $\mathbf{F} = B\mathbf{v}$ and $\mathbf{F}_\mathrm{J} = B_\mathrm{J}\mathbf{v}_\mathrm{J}$, where B and B_J are dislocation and junction drag coefficients. This is done with uncertainty for the junction drag coefficients because there should be additional studies to establish this relationship. A lattice resistance term may also be considered in the mobility law. Some preliminary work in [26] suggests that the junction points may have a different Peierls barrier than the Peierls barrier of the dislocation lines.

6.4 Numerical tests and validation

In this section, the force expressions in the previous section are numerically validated providing a validation of the line tension approximation of the self-energy. An example of one dislocation segment pinned at its endpoints is simulated and the forces obtained in the previous section are compared to those numerically obtained here. To calculate the force numerically, the variational derivative of the energy is taken with respect to changes in the position of the endpoints. This requires computing the elastic energy by integrating the expression (6.1). The integration of (6.1) over the dislocation line can be numerically approximated by breaking the line into smaller linear segments and using Gaussian integration

to perform the integration on each of the smaller segments. The code obtained from [28] was used to perform the integration. This code implements the non-singular energy expressions derived in [29]. In this paper, a regularization parameter, a, is introduced to eliminate the singularities in the elastic energy expression. As a tends to 0, these expressions match the singular expressions used in this work.

To approximate the variational derivative, the forward difference approximation is used

$$\mathrm{F}^{\mathrm{i}}{}_{\mathrm{J}_k} = \frac{\mathrm{E}(p_k + \mathrm{e}^{\mathrm{i}}\delta u) - \mathrm{E}(p_k)}{\delta u} \tag{6.15}$$

where e^{i} denotes the vector with all components zero except the i^{th} component which is one, δu is some small parameter which denotes the perturbation of the junction node and is set to 10^{-6}, p_k is the position of the k^{th} junction point, and E is the elastic energy given by (6.1). The initial line configuration is prescribed as a circular arc with radius R in the xy plane with a Burgers vector pointing in the y direction with a magnitude of $|b| = 2.554()$. This is shown in Fig. 6.1. A shear modulus of $\mu = 45(\mathrm{GPa})$ and a Poissons ratio of $\nu = 0.34$ is used.

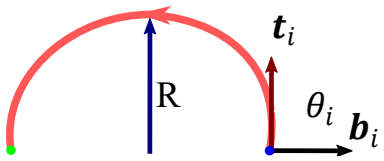

Fig.6.1. Circular arc dislocation configuration with the dislocation pinned at its endpoints.

Both the radius and the fraction of the arc are varied, resulting in a variation of the length of the pinned dislocation line and angle the line tangent makes with respect to the Burgers vector at the endpoints. This is done because the energy per unit line length contained in the force expression (6.14) depends on both the line length and orientation of the line. For this test, the numerical force computed from (6.15) is compared against the force that is obtained from the self-energy (6.14), where the pinning point is viewed as a junction point with one arm. To make this comparison both the magnitude and directions of the two forces should be compared. The cosine of the angle between the two forces is

used to compare their directions and the ratio of their magnitudes is used to compare their magnitudes. In Fig. 6.2 (a) the colorbar on the plot can be used to obtain the cosine of the angle between the two forces where the x-axis is the length of the dislocation segment and the y-axis is the angle the segment makes relative to the Burgers vector. A similar plot is shown in Fig. 6.2 (b) but the color represents the ratio of the magnitudes.

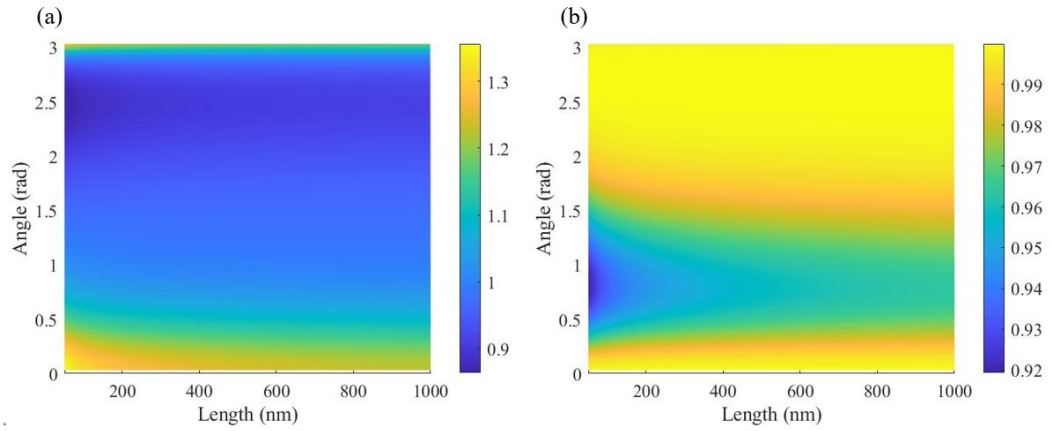

Fig.6.2. (a) Ratio of the magnitudes of the self-force at the pinned node and the numerically obtained force. (b) Cosine angle similarity between self-force at the pinned node and the numerically obtained force.

In Fig. 6.2 (a), the orientations of both forces are shown to be, for the most part, aligned. In the regions corresponding to an angle of $\pi/4$, the orientations differ the most. Interestingly, this corresponds to a mixed character dislocation segment which is evenly split between an edge and screw segment. The orientation of the two forces differs most at small segment lengths (less than 100 nm). The ratio of force's magnitude is only minimally affected by a change in the length of the dislocation segment, as can be seen in Fig. 6.2 (b). It does, however, have a slight dependence on the orientation of the dislocation segment.

6.5 Continuum force derivation

The discrete forces given in (6.14) along with a velocity mobility law are used to obtain an expression for average velocity of the junction densities in this section. This velocity field is obtained by looking at the ensemble average of the flux of junction nodes. In a closed system of transport equations the ensemble average of the junction flux can be written as

the product of the mean junction point density and a mean velocity field. To write the mean junction flux, the definition of the dislocation endpoint current is stated here to facilitate the introduction of the junction point currents and flux

$$\begin{aligned} \Pi^{(l)} &= -b^{(l)} \otimes \pi^{(l)} \\ \pi^{(l)} &= \left\langle \sum_n T_{\partial c_n^{(l)}} \right\rangle . \end{aligned} \tag{6.16}$$

In the last expression, $\pi^{(l)}$ is the current containing the endpoints of the dislocation lines on the l^{th} slip system and $\partial c_n^{(l)}$ denotes the n^{th} endpoint pair in the domain. A slight notation change has been made in the above definition where we now explicitly keep track of the slip system of the dislocation line c_n with the superscript (l). In this expression, the angle brackets denote an ensemble average. From the ensemble average, the current (6.16) can equivalently be expressed using smooth differential 3-form $\pi_s^{(l)}$ [81]. The current defined using this 3-form is denoted as $T_{\pi_s^{(l)}}$. Using $\pi_s^{(l)} = p^{(l)} dV$ the 3-form can be expressed in terms of endpoints with the following limit process:

$$p^{(l)}(x) = \lim_{r \to 0} \frac{\pi^{(l)}[1_B]}{\text{Vol}(B(x,r))} \tag{6.17}$$

where $B(x,r)$ is a ball centered at x with radius r. This limit process is explained in more detail in [81, 32] Using the equivalence of the two currents $\pi^{(l)}$ and $T_{\pi_s^{(l)}}$ i.e. $\pi^{(l)}[1_B] = T_{\pi_s^{(l)}}[1_B]$. It can be shown that

$$p^{(l)}(x) = \lim_{r \to 0} \frac{1}{\text{Vol}(B(x,r))} \left\langle \sum_n \partial c_n^{(l)} \cap B(x,r) \right\rangle , \tag{6.18}$$

so that the function $p^{(l)}(x)$ represents the volume average of the signed sum of endpoints contained in a ball B. This expression allows us to interpret the endpoint 3-form $\pi_s^{(l)}$ as the signed sum of endpoints at a point x. It has been demonstrated by [176] that the endpoint currents can be related to the dislocation junction currents due to the r-partite property of the graphs created by the dislocation network. To introduce the junction point current let

$P_{\mathrm{j}}^{(pqr)}$ denote the j-th junction point which is assumed to have only three arms which are on the p, q and r slip system, respectively. The sign of the junction point is defined as

$$\mathrm{sgn}(P_{\mathrm{j}}^{(pqr)}) \coloneqq \mathrm{sgn}_{p_{\mathrm{j}}}(\partial c_{\mathrm{j}}^{(p)})\mathrm{sgn}_{p_{\mathrm{j}}}(\partial c_{\mathrm{j}}^{(q)})\mathrm{sgn}_{p_{\mathrm{j}}}(\partial c_{\mathrm{j}}^{(r)}) \tag{6.19}$$

where $\mathrm{sgn}_{p_{\mathrm{j}}}(\partial c_{\mathrm{j}}^{(p)})$ denotes the sign of the endpoint of the dislocation line $c_{\mathrm{j}}^{(p)}$ attached to the jth junction point. Then, the junction point current can be defined as

$$\pi_{\mathrm{J}}^{(pqr)} = \left\langle \sum_{\mathrm{j}} \mathrm{sgn}(P_{\mathrm{j}}^{(pqr)}) T_{P_{\mathrm{j}}^{(pqr)}} \right\rangle. \tag{6.20}$$

In this expression, $T_{P_{\mathrm{j}}^{(pqr)}}$ is the (unsigned) current representing the location of the junction point and the current $\mathrm{sgn}(P_{\mathrm{j}}^{(pqr)}) T_{P_{\mathrm{j}}^{(pqr)}}$ is the signed current representing the junction node. [176] alluded that the dislocation network could be more accurately represented using both the positive and negative junction point currents. To split the junction current into positive and negative parts, functions $\mathrm{sgn}(P_n^{(pqr)})^+$ and $\mathrm{sgn}(P_n^{(pqr)})^-$ are introduced to filter out all positive and negative junction points, respectively. These functions are given by

$$\begin{aligned} \mathrm{sgn}(P_n^{(pqr)})^+ &= \frac{\left(\mathrm{sgn}(P_n^{(pqr)} + |\mathrm{sgn}(P_n^{(pqr)}|\right)}{2} \\ \mathrm{sgn}(P_n^{(pqr)})^- &= \frac{\left(\mathrm{sgn}(P_n^{(pqr)} - |\mathrm{sgn}(P_n^{(pqr)}|\right)}{2}. \end{aligned} \tag{6.21}$$

The function $\mathrm{sgn}(P_n^{(pqr)})^+$ returns a 1 is $\mathrm{sgn}(P_n^{(pqr)})$ is positive and a 0 otherwise, whereas the function $\mathrm{sgn}(P_n^{(pqr)})^-$ returns a -1 if $\mathrm{sgn}(P_n^{(pqr)})$ is negative and 0 otherwise. With the above functions, the junction point current can be decomposed as

$$\pi_{\mathrm{J}}^{(pqr)} = \pi_{\mathrm{J}}^{(pqr)+} + \pi_{\mathrm{J}}^{(pqr)-}, \tag{6.22}$$

where

$$\pi_{\mathrm{J}}^{(pqr)+} = \left\langle \sum_{\mathrm{j}} \operatorname{sgn}(P_{\mathrm{j}}^{(pqr)})^{+} T_{P_{\mathrm{j}}^{(pqr)}} \right\rangle \tag{6.23}$$

$$\pi_{\mathrm{J}}^{(pqr)-} = \left\langle \sum_{\mathrm{j}} \operatorname{sgn}(P_{\mathrm{j}}^{(pqr)})^{-} T_{P_{\mathrm{j}}^{(pqr)}} \right\rangle . \tag{6.24}$$

In [176], it was shown that the transport equations for the junction current was,

$$\frac{\mathrm{d}}{\mathrm{dt}} \pi_{\mathrm{J}}^{(pqr)} = -\mathrm{d} \left\langle \sum_{n} \mathrm{i}_{\mathbf{v}_{\mathrm{J}_n}^{(pqr)}} \operatorname{sgn}(P_n^{(pqr)}) T_{P_n^{(pqr)}} \right\rangle . \tag{6.25}$$

In a similar fashion, the transport relations for the positive and negative junction point currents read:

$$\begin{aligned} \frac{\mathrm{d}}{\mathrm{dt}} \pi_{\mathrm{J}}^{(pqr)+} &= -\mathrm{d} \left\langle \sum_{n} \mathrm{i}_{\mathbf{v}_{\mathrm{J}_n}^{(pqr)}} \operatorname{sgn}(P_n^{(pqr)})^{+} T_{P_n^{(pqr)}} \right\rangle \\ \frac{\mathrm{d}}{\mathrm{dt}} \pi_{\mathrm{J}}^{(pqr)-} &= -\mathrm{d} \left\langle \sum_{n} \mathrm{i}_{\mathbf{v}_{\mathrm{J}_n}^{(pqr)}} \operatorname{sgn}(P_n^{(pqr)})^{-} T_{P_n^{(pqr)}} \right\rangle \end{aligned} \tag{6.26}$$

Source terms were also introduced in the transport equations (6.26) in [176]. However in this work, the focus is primarily on the mean junction point velocity, so these terms are omitted.

Looking at (6.25), the net junction flux current is defined to be,

$$J^{(pqr)} = \left\langle \sum_{n} \mathrm{i}_{\mathbf{v}_{\mathrm{J}_n}^{(pqr)}} \operatorname{sgn}(P_n^{(pqr)}) T_{P_n^{(pqr)}} \right\rangle . \tag{6.27}$$

Using the sign filtering functions in (6.21), the net junction flux current can be decomposed into positive and negative contributions as $J^{(pqr)} = J^{(pqr)+} + J^{(pqr)-}$where

$$\begin{aligned} J^{(pqr)+} &= \left\langle \sum_{n} \mathrm{i}_{\mathbf{v}_{\mathrm{J}_n}^{(pqr)}} \operatorname{sgn}(P_n^{(pqr)})^{+} T_{P_n^{(pqr)}} \right\rangle \\ J^{(pqr)-} &= \left\langle \sum_{n} \mathrm{i}_{\mathbf{v}_{\mathrm{J}_n}^{(pqr)}} \operatorname{sgn}(P_n^{(pqr)})^{-} T_{P_n^{(pqr)}} \right\rangle . \end{aligned} \tag{6.28}$$

These currents can be represented using smooth differential forms from the ensemble average, ie $J^{(pqr)+}[\boldsymbol{\theta}] = T_{\mathbf{j}_{\mathrm{s}}^{(pqr)+}}[\boldsymbol{\theta}]$ and $J^{(pqr)-}[\boldsymbol{\theta}] = T_{\mathbf{j}_{\mathrm{s}}^{(pqr)-}}[\boldsymbol{\theta}]$, where

$$\begin{aligned} T_{\mathbf{j}_{\mathrm{s}}^{(pqr)+}}[\boldsymbol{\theta}] &= \int_M \mathbf{j}_{\mathrm{s}}^{(pqr)+} \wedge \boldsymbol{\theta}, \\ T_{\mathbf{j}_{\mathrm{s}}^{(pqr)-}}[\boldsymbol{\theta}] &= \int_M \mathbf{j}_{\mathrm{s}}^{(pqr)-} \wedge \boldsymbol{\theta}. \end{aligned} \tag{6.29}$$

In the last expression, $\mathbf{j}_s^{(pqr)+}$ and $\mathbf{j}_s^{(pqr)-}$ are smooth differential 2-forms. To get a closed form expression for the transport equations (6.26), the junction point fluxes $\mathbf{j}_s^{(pqr)+}$ and $\mathbf{j}_s^{(pqr)-}$ should be written as $\mathbf{j}_{\mathrm{s}}^{(pqr)+} = \mathrm{i}_{\overline{\mathbf{v}}_{\mathrm{J}}^{(pqr)+}} \pi_{\mathrm{s,J}}^{(pqr)+}$ and $\mathbf{j}_{\mathrm{s}}^{(pqr)-} = \mathrm{i}_{\overline{\mathbf{v}}_{\mathrm{J}}^{(pqr)-}} \pi_{\mathrm{s,J}}^{(pqr)-}$ respectively where $\overline{\mathbf{v}}_{\mathrm{J}}^{(pqr)+}$ and $\overline{\mathbf{v}}_{\mathrm{J}}^{(pqr)-}$ are the average positive and negative junction point velocities. The junction flux 2-form can be written in terms of a vector field, which we also denote as $\mathbf{j}_s^{(pqr)+}$, through the relation $\mathrm{i}_{\mathbf{j}_s^{(pqr)+}} dV = \mathbf{j}_s^{(pqr)+}$. The i-th component of this vector field $\mathbf{j}_s^{(pqr)+}$ can be obtained by integrating over a ball of radius r and evaluating [81]

$$\begin{aligned} \mathrm{j}_s^{\mathrm{i}(pqr)+} &= \lim_{r\to 0} \frac{1}{\mathrm{Vol}(B(x,r))} J_{\pi^{(pqr)+}}[1_B dx^{\mathrm{i}}] \\ &= \lim_{r\to 0} \frac{1}{\mathrm{Vol}(B(x,r))} \left\langle \sum_n \mathrm{sgn}(P_n^{(pqr)})^+ T_{P_n^{(pqr)}}[1_B \mathrm{v}_{\mathrm{J}_n}^{\mathrm{i}+}] \right\rangle. \end{aligned} \tag{6.30}$$

In the above expression, $T_{\mathbf{j}_{\mathrm{s}}^{(pqr)+}}[1_B dx^{\mathrm{i}}] = J_{\pi^{(pqr)+}}[1_B dx^{\mathrm{i}}]$ is used to obtain the second equality in (6.30). In this work, junctions with only three arms are considered to be consistent with our previous work [176]. The driving force with these assumptions will be denoted as $\mathbf{F}_{\mathrm{J_n}}^{(pqr)}$ to signify that it is obtained by only considering the forces at junction node n from the three connecting dislocation arms, which are on slip system p, q and r, respectively. We write the driving force with these assumptions and notation change as

$$\mathbf{F}_{\mathrm{J_n}}^{(pqr)} = -\sum_{\mathrm{j}}^{3} \mathrm{sgn}_P(\partial c_{\mathrm{j}}) \left(\mathrm{E_j}(\theta) \mathbf{t}_{\mathrm{j}} + \frac{d\mathrm{E_j}(\theta)}{\mathrm{d}\theta} \mathbf{n}_{\mathrm{j}} \right) \tag{6.31}$$

The following velocity mobility law is introduced for the junction points

$$\mathbf{v}_{\mathrm{J}_n}^{(pqr)} = \mathrm{M} \mathbf{F}_{\mathrm{J_n}}^{(pqr)}. \tag{6.32}$$

Using (6.32) and (6.31), the positive junction flux (6.30) becomes,

$$\mathrm{j}_s^{\mathrm{i}(pqr)+} = \lim_{r\to 0} \frac{1}{\mathrm{Vol}(B(x,r))} \left\langle \sum_n \mathrm{sgn}(P_n^{(pqr)})^+ T_{P_n^{(pqr)}}[1_B \mathrm{M}\ \mathrm{F}_{\mathrm{J_n}}^{\mathrm{i}(pqr)+}] \right\rangle \tag{6.33}$$

where the force is given by (6.31). To further simplify this expression it is assumed that all the junction arms on the same slip system contained in the ball B are oriented similarly and approximately equal to the average line bundle tangent. Also, that all of the junction segments within the ball B have similar length and equal to the average length denoted by $\overline{\mathrm{L}}_{\mathrm{o}}$. A discussion of the latter orientation assumptions is had in a later section and an expression for the average line length is given in the next section. With the previously stated assumptions, the sum of $T_p[1_B M \mathrm{F}_{\mathrm{J}}^{\mathrm{i}(pqr)+}]$ over n ends up being a signed sum of the same expression evaluated at different junction points which we subsequently denote by $\overline{\mathbf{F}}_{\mathrm{J}}^{(pqr)+}$. This gives

$$\mathrm{j}_s^{\mathrm{i}(pqr)+} = \lim_{r\to 0} \frac{1}{\mathrm{Vol}(B(x,r))} \left\langle \left(\sum_n p^+ \in B \right) \left(M \overline{\mathrm{F}}_{\mathrm{J}}^{\mathrm{i}(pqr)+} \right) \right\rangle \tag{6.34}$$

where

$$\overline{\mathbf{F}}_{\mathrm{J}}^{(pqr)+} = -\sum_{\mathrm{j}=(p,q,r)} \mathrm{sgn}_P(\partial c_{\mathrm{j}}) \left(\overline{\mathrm{E}}_{\mathrm{j}}(\theta) \overline{\mathbf{t}}^{(\mathrm{j})} + \frac{d\overline{\mathrm{E}}_{\mathrm{j}}(\theta)}{\mathrm{d}\theta} \overline{\mathbf{n}}^{(\mathrm{j})} \right) \tag{6.35}$$

In the previous expression, $\overline{\mathbf{t}}^{(\mathrm{j})}$ is the average line tangent on slip system j, $\overline{\mathbf{n}}^{(\mathrm{j})}$ is the average normal vector of the bundle on slip system j in the glide plane, $\overline{\mathrm{E}}_{\mathrm{j}}(\theta) = \frac{\mu b^2}{4\pi(1-\nu)}(1 - \nu\cos(\theta)^2)\ln\left(\frac{\overline{\mathrm{L}}_{\mathrm{o}}^{(\mathrm{j})}}{\mathrm{e}\rho}\right)$ is the average energy per length of the dislocation, and $\overline{\mathrm{L}}_{\mathrm{o}}^{(\mathrm{j})}$ is the average open dislocation line length on slip system j. Since $\overline{\mathbf{F}}_{\mathrm{J}}^{(pqr)+}$ is the average force, it can be pulled out of the ensemble average operation in (6.34) allowing us to write (6.34) in the form

$$\mathrm{j}_s^{\mathrm{i}(pqr)+} = \left\langle \left(\sum_n p^+ \in B \right) \right\rangle M \overline{\mathrm{F}}_{\mathrm{J}}^{\mathrm{i}(pqr)+} = p_s^{(pqr)+} M \overline{\mathrm{F}}_{\mathrm{J}}^{\mathrm{i}(pqr)+}. \tag{6.36}$$

With (6.36), the junction density flux 2-form can be written in a closed form expression as

$$\mathbf{j}_{\mathrm{s}}^{(pqr)+} = \mathrm{i}_{\mathbf{j}_s^{(pqr)+}} \mathrm{dV} = \mathrm{i}_{M\overline{\mathbf{F}}_{\mathrm{J}}^{(pqr)+}} (p_s^{(pqr)+} \mathrm{dV}) = \mathrm{i}_{\overline{\mathbf{v}}_{\mathrm{J}}^{(pqr)+}} \pi_{\mathrm{sJ}}^{(pqr)+} \tag{6.37}$$

where $\overline{\mathbf{v}}_{\mathrm{J}}^{(pqr)+} = \mathrm{M}\overline{\mathbf{F}}_{\mathrm{J}}^{(pqr)+}$. A similar analysis for the negative junction density flux can be performed resulting in a pair of closed form expressions for the transport equations of the junction densities

$$\begin{aligned} \frac{\mathrm{d}}{\mathrm{dt}}\pi_{\mathrm{sJ}}^{(pqr)+} &= -\,\mathrm{d}(\mathrm{i}_{\overline{\mathbf{v}}_{\mathrm{J}}^{(pqr)+}}\pi_{\mathrm{sJ}}^{(pqr)+}) \\ \frac{\mathrm{d}}{\mathrm{dt}}\pi_{\mathrm{sJ}}^{(pqr)-} &= -\,\mathrm{d}(\mathrm{i}_{\overline{\mathbf{v}}_{\mathrm{J}}^{(pqr)-}}\pi_{\mathrm{sJ}}^{(pqr)-}) \end{aligned} \tag{6.38}$$

where $\overline{\mathbf{v}}_{\mathrm{J}}^{(pqr)-} = \mathrm{M}\overline{\mathbf{F}}_{\mathrm{J}}^{(pqr)-}$ and the mean force is given by a similar expression to (6.35). However, the signs of the endpoints in this case are opposite of the positive mean junction force case. Therefore, $\overline{\mathbf{F}}^{(pqr)-} = -\overline{\mathbf{F}}^{(pqr)+}$. The last equality is only true because the same average line orientation (equal to the line bundle orientation) was used at each of the endpoints connected to the junction nodes. Rewriting (6.38) in terms of vector calculus operations acting on vector fields in R^3 (given a Euclidean metric) [117, pp. 368], gives

$$\frac{\mathrm{d}}{\mathrm{dt}}\pi_{J}^{(pqr)+} = -\,\mathrm{div}(\overline{\mathbf{v}}_{\mathrm{J}}^{(pqr)+}\pi_{J}^{(pqr)+}) \tag{6.39}$$

$$\frac{\mathrm{d}}{\mathrm{dt}}\pi_{J}^{(pqr)-} = -\,\mathrm{div}(\overline{\mathbf{v}}_{\mathrm{J}}^{(pqr)-}\pi_{J}^{(pqr)-}). \tag{6.40}$$

When using the vector density model derived in [176], the junction velocity can be expressed as

$$\overline{\mathbf{v}}_{\mathrm{J}}^{(pqr)+} = -\mathrm{M}\sum_{\mathrm{j}\in(p,q,r)}^{3}\mathrm{sgn}^{(pqr,\mathrm{j})}\left(\overline{\mathrm{E}}_{\mathrm{j}}(\theta)\frac{\boldsymbol{\rho}_{\mathrm{s}}^{(\mathrm{j})}}{|\boldsymbol{\rho}_{\mathrm{s}}^{(\mathrm{j})}|} + \frac{d\overline{\mathrm{E}}_{\mathrm{j}}(\theta)}{\mathrm{d}\theta}\mathbf{n}^{(\mathrm{j})}\times\frac{\boldsymbol{\rho}_{\mathrm{s}}^{(\mathrm{j})}}{|\boldsymbol{\rho}_{\mathrm{s}}^{(\mathrm{j})}|}\right) \tag{6.41}$$

where $\mathrm{sgn}_P(\partial c_{\mathrm{j}}) = \mathrm{sgn}^{(pqr,\mathrm{j})}\mathrm{sgn}(\pi_J)$ is the conversion of the endpoint sign to the junction point sign for each arm and $\mathbf{n}^{(\mathrm{j})}$ is the unit normal of the glide plane on slip system j. A similar analysis which lead to (6.41) can be used to find the mean negative junction point velocity

$$\overline{\mathbf{v}}_{\mathrm{J}}^{(pqr)-} = \mathrm{M}\sum_{\mathrm{j}\in(p,q,r)}^{3}\mathrm{sgn}^{(pqr,\mathrm{j})}\left(\overline{\mathrm{E}}_{\mathrm{j}}(\theta)\frac{\boldsymbol{\rho}_{\mathrm{s}}^{(\mathrm{j})}}{|\boldsymbol{\rho}_{\mathrm{s}}^{(\mathrm{j})}|} + \frac{d\overline{\mathrm{E}}_{\mathrm{j}}(\theta)}{\mathrm{d}\theta}\mathbf{n}^{(\mathrm{j})}\times\frac{\boldsymbol{\rho}_{\mathrm{s}}^{(\mathrm{j})}}{|\boldsymbol{\rho}_{\mathrm{s}}^{(\mathrm{j})}|}\right). \tag{6.42}$$

Interestingly, the average velocity of the junction density has terms in the summand, $\overline{\mathrm{E}}_{\mathrm{j}}(\theta)\frac{\boldsymbol{\rho}_{\mathrm{s}}^{(\mathrm{j})}}{|\boldsymbol{\rho}_{\mathrm{s}}^{(\mathrm{j})}|}$, that are tangent to each of the dislocation line bundles and terms, $\frac{d\overline{\mathrm{E}}_{\mathrm{j}}(\theta)}{\mathrm{d}\theta}\mathbf{n}^{(\mathrm{j})}\times\frac{\boldsymbol{\rho}_{\mathrm{s}}^{(\mathrm{j})}}{|\boldsymbol{\rho}_{\mathrm{s}}^{(\mathrm{j})}|}$, that tend

to rotate each dislocation bundle arms towards the lower energy screw segment. The average velocity field of both the positive and negative junction point densities are a competition of these effects.

6.6 Computation of the average open dislocation segment length

The goal of this section is to obtain an expression for the average line length per open dislocation line segment. To accomplish this goal, the graph representing the dislocation network is introduced to form a relationship between the number of line segments contained in a region of the crystal to the number of junction points in that region. This relationship is used to define an edge number density. This density is used in conjunction with the dislocation line length to determine the average line length of the open dislocation segments. We start by introducing the dislocation network graph.

A graph G is a pair $G = (V, E)$ of lists. V is a list of vertices (nodes), and $E \subseteq V \times V$ is a list of pairs of vertices called edges. A graph is called r-partite if its vertex set can be split into r disjoint sets $V_1, V_2, .., V_r$ such that every edge connects a pair of vertices from two different sets. This means that vertices in a given set are not adjacent [48]. A node in the graph representing the dislocation network corresponds to a junction point. The open dislocation lines connecting the junction points are the graph's edges. As explained in [176], the graph representing the dislocation network created in this fashion is r-partite.

We now introduce the edge number density that we create using graph theory ideas. This density was first introduced in an appendix in [176], but is introduced here for a further description. To obtain this density, a famous relation in graph theory called the degree sum formula (also known as the handshaking lemma) is introduced which relates the number of edges in a graph to information on the nodes

$$|E| = \frac{1}{2} \sum_{v \in V} \deg(v). \tag{6.43}$$

In the previous equations $|E|$ denotes the number of edges, deg is the number of edges connected to a vertex $v \in V$ with V denoting the vertex set of the graph. The degree of

each vertex is three in the case where junction nodes only have three arms. Using (6.43) as a guide and assuming that the degree of each node is 3, the edge number current is defined by

$$\lambda = \frac{1}{2}\left[3\sum_{p\in S}(\pi_{\mathrm{J}}^{+(p)} + \pi_{\mathrm{J}}^{-(p)})\right]. \tag{6.44}$$

From the ensemble average the above current can also be expressed by a smooth differential 3-form, λ_s, which we denote by T_{λ_s}. The 3-form can be written as $\lambda_s = l\mathrm{dV}$. The function l can be obtained from the same limiting process which lead to (6.18) and the fact that $T_{\lambda_s}[1_B] = \lambda[1_B]$. This process leads to l being defined in terms of the sum of the number of junction points ,weighted by their degree, in some averaging volume. Then, the edge number density can be written in terms of the junction point densities as

$$\lambda_s = \frac{1}{2}\left[3\sum_{p\in S}(\pi_{\mathrm{sJ}}^{+(p)} + \pi_{\mathrm{sJ}}^{-(p)})\right] \tag{6.45}$$

where S is an index set containing all the junction types. An edge number density on each slip system can also be defined by using the same formula (6.43) applied to a subgraph that is obtained by only including edges that correspond to a specific slip system. The degree of the nodes, in this case, is now one rather than three because each junction node has arms on three unique slip systems. We can then write the edge number density for slip system (l) as

$$\lambda_s^{(l)} = \frac{1}{2}\left[\sum_{p\in S^{(l)}}(\pi_{\mathrm{sJ}}^{+(p)} + \pi_{\mathrm{sJ}}^{-(p)})\right] \tag{6.46}$$

where $S^{(l)}$ is an index set over junction types that contain slip system (l). The definitions (6.45) and (6.46) provide the relation $\lambda_s = \sum_l \lambda_s^{(l)}$.

There is one issue with the above definition (6.43) when viewed as a density measure in (6.45). In the density measure representation, the spatial arrangement of the network matters. However, this is not the case in the definition (6.43). The degree sum formula in (6.43) is only valid when analyzing whole parts of a graph (or subgraph). This range of validity is problematic when converting (6.43) to a density measure in (6.45), where, when we average over some volume, we only measure the parts of the network contained in the

volume. In this averaging process, some dislocation segments intersect with the averaging volume's surface, and thus the volume contains only a subset of the total junction points in the system. In this case, the degree sum formula only halfway counts the dislocation lines that intersect the averaging volume's surface. This is a problem that exists in both (6.45) and (6.46). However, this is not a problem when a whole dislocation segment is contained in the averaging volume because each junction point gets weighted by half its degree. After summing over all nodes in the volume, the segment fully contained in the volume is fully counted. An example of this scenario is given in Fig. 6.3. In this case, the dislocation lines that have only one of their endpoints in the volume are only half counted using the formula (6.45).

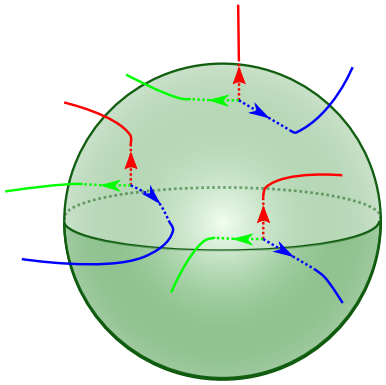

Fig.6.3. Dislocation configuration where the number of edges given by (6.46) only halfway counts the edges that intersect the surface of the ball.

Unfortunately, this issue is only be partially solved in this work. The solution requires knowledge of the total number of edges that intersect with the surface, but the only information available is the net information of this type. This information is contained in the endpoint density. The net information refers to the fact that the endpoint density represents the difference between the positive and negative endpoints. Since the endpoint density variable cancels for segments that have both endpoints in the volume, it is only nonzero when there is a net number of dislocations intersecting the surface of the volume. This interpretation was also recognized in [176]. Since the endpoint density is a signed measure, the

absolute value of this expression is added (to remove the sign) to the edge number density (6.46)

$$\lambda_s^{(l)} = \frac{1}{2}\left[\sum_{p\in S^{(l)}} (\pi_{\mathrm{sJ}}^{+(p)} + \pi_{\mathrm{sJ}}^{-(p)}) + |\pi_s^{(l)}|\right]. \tag{6.47}$$

The addition of the absolute value of the endpoint density corrects for some of the surface contributions to the edge number density. The endpoint density can also be written as a signed sum of junction points [176] given by

$$\pi_s^{(l)} = \sum_{p,q:\,(lpq)\in S^l} \mathrm{sgn}^{(lpq,l)}(\pi_{\mathrm{sJ}}^{+(lpq)} - \pi_{\mathrm{sJ}}^{-(lpq)}). \tag{6.48}$$

The density measure (6.47) can underestimate the number of edges contained in some regions in certain cases. A discussion of the assumptions made in this section to arrive at the final form of the edge number density in (6.47) is delayed until the next section.

In [176], it was noted that the dislocation density vector field may be obtained from averaging and written as

$$\boldsymbol{\rho}_{\mathrm{s}}^{(l)}(\boldsymbol{x}) = \lim_{r\to 0} \frac{1}{\mathrm{Vol}\,(B(\boldsymbol{x},r))} \left\langle \sum_k \boldsymbol{\Delta c}_{\mathrm{c}(k)}^{(l)}\,(B(\boldsymbol{x},r)) + \sum_n \boldsymbol{\Delta c}_{\mathrm{o}(n)}^{(l)}\,(B(\boldsymbol{x},r)) \right\rangle \tag{6.49}$$

where the summation over the index k and n is for the closed and open dislocation segments, respectively. In the last expression, $\boldsymbol{\Delta c}_{\mathrm{c}(k)}^{(l)}\,(B(\boldsymbol{x},r))$ denotes the connecting vector from the point of entry of a closed dislocation line into the ball $B(\boldsymbol{x},r)$ centered at $\boldsymbol{x}$ with radius r to where it leaves the ball. Such a vector is identically zero if the segment does not intersect the ball. In the sum over open dislocation lines, $\boldsymbol{\Delta c}_{\mathrm{o}(n)}^{(l)}\,(B(\boldsymbol{x},r))$ connects the points of entry and leaving or, if the segment starts or ends in the ball, it connects the intersection point with the surface of the ball and the boundary point inside the ball, directed in accordance with the line-sense of the curve. This can be written in an equivalent form

$$\boldsymbol{\rho}_{\mathrm{s}}^{(l)}(\boldsymbol{x}) = \lim_{r\to 0} \frac{1}{\mathrm{Vol}\,(B(\boldsymbol{x},r))} \left\langle \sum_k \mathrm{L}_{\mathrm{c}}^{\mathrm{k}} \mathbf{t}_{\mathrm{c}(k)}^{(l)} + \sum_n \mathrm{L}_{\mathrm{o}}^{\mathrm{n}} \mathbf{t}_{\mathrm{o}(n)}^{(l)} \right\rangle \tag{6.50}$$

where $\mathrm{L}_{\mathrm{c}}^{\mathrm{k}} = |\boldsymbol{\Delta c}_{\mathrm{c}(k)}^{(l)}(B(\boldsymbol{x},r))|$ and $\mathrm{L}_{\mathrm{o}}^{\mathrm{n}} = |\boldsymbol{\Delta c}_{\mathrm{o}(n)}^{(l)}(B(\boldsymbol{x},r))|$ are the lengths of the *geometrically necessary* parts of the closed and open curves that passes through the ball B, respectfully, and $\mathbf{t}_{\mathrm{c}(k)}^{(l)}$ and $\mathbf{t}_{\mathrm{o}(n)}^{(l)}$ are the unit tangents to the curves. Taking the normal of this vector field yields

$$|\boldsymbol{\rho}|_{\mathrm{s}}^{(l)}(\boldsymbol{x}) = \lim_{r\to 0} \frac{1}{\mathrm{Vol}\left(B(\boldsymbol{x},r)\right)} \left\langle \sum_k \mathrm{L}_{\mathrm{c}}^{\mathrm{k}} + \sum_n \mathrm{L}_{\mathrm{o}}^{\mathrm{n}} \right\rangle. \tag{6.51}$$

The norm is taken to facilitate the introduction of an expression relating the total geometrically necessary line length and the product of an average line length per segment with the number of segments. The average geometrically necessary line lengths are defined as

$$\begin{aligned} \overline{\mathrm{L}}_{\mathrm{c}} &= \frac{1}{\mathrm{N}_{\mathrm{c}}} \sum_k \mathrm{L}_{\mathrm{c}}^{\mathrm{k}} \\ \overline{\mathrm{L}}_{\mathrm{o}} &= \frac{1}{\mathrm{N}_{\mathrm{o}}} \sum_n \mathrm{L}_{\mathrm{o}}^{\mathrm{n}} \end{aligned} \tag{6.52}$$

where N_{c} and N_{o} are the number of closed and open line segments, so that,

$$|\boldsymbol{\rho}|_{\mathrm{s}}^{(l)}(\boldsymbol{x}) = \lim_{r\to 0} \frac{1}{\mathrm{Vol}\left(B(\boldsymbol{x},r)\right)} \left\langle \mathrm{N}_{\mathrm{c}}\overline{\mathrm{L}}_{\mathrm{c}} + \mathrm{N}_{\mathrm{o}}\overline{\mathrm{L}}_{\mathrm{o}} \right\rangle. \tag{6.53}$$

The situations of interest are when dislocation reactions occur. Depending on the length scale of interest, it seems reasonable to assume that the total line length is predominantly made of open line segments. With this assumption, we write (6.53) as

$$|\boldsymbol{\rho}|_{\mathrm{s}}^{(l)} = \lambda_s^{(l)} \overline{\mathrm{L}}_{\mathrm{o}}. \tag{6.54}$$

Rearranging the last expression for the the average open segment length gives

$$\overline{\mathrm{L}}_{\mathrm{o}}^{(l)} = \frac{2|\boldsymbol{\rho}|_{\mathrm{s}}^{(l)}}{\sum_{p\in S^{(l)}} (\pi_{\mathrm{sJ}}^{+(p)} + \pi_{\mathrm{sJ}}^{-(p)}) + |\pi^l|}. \tag{6.55}$$

The previous expression is singular when there are no junction points at a particular point. However, our interest is in the junction point flux which can be seen, using 6.41, to take the simplified and worst case functional form of $\ln(1/\pi^+)\pi^+$. Use of L'Hopital's rule on $-\frac{\ln(\pi)}{\frac{1}{\pi}}$ yields a limit of zero as π approaches zero meaning that the flux is not singular. The final

form of the closed evolution equations for the positive junction point density and vector density are given as

$$
\begin{aligned}
\frac{\mathrm{d}}{\mathrm{dt}}\pi_J^{(pqr)+} &= -\operatorname{div}(\overline{\mathbf{v}}_{\mathrm{J}}^{(pqr)+}\pi_J^{(pqr)+}) \\
\frac{d}{dt}\boldsymbol{\rho}_{\mathrm{s}}^{(l)} &= \operatorname{curl}\left(\overline{\boldsymbol{v}}^{(l)} \times \boldsymbol{\rho}_{\mathrm{s}}^{(l)}\right) - \sum_{p,q:\,(lpq)\in S^l} \operatorname{sgn}^{(lpq,l)}\left(\overline{\boldsymbol{v}}_{\mathrm{J}}^{(lpq)+}\pi_{\mathrm{sJ}}^{(lpq)+} - \overline{\boldsymbol{v}}_{\mathrm{J}}^{(lpq)-}\pi_{\mathrm{sJ}}^{(lpq)-}\right) \\
\overline{\mathbf{v}}_{\mathrm{J}}^{(pqr)+} &= -\,\mathrm{M}\sum_{\mathrm{j}}^{3}\operatorname{sgn}^{(pqr,\mathrm{j})}\left(\overline{\mathrm{E}}_{\mathrm{j}}(\theta)\frac{\boldsymbol{\rho}_{\mathrm{s}}^{(\mathrm{j})}}{|\boldsymbol{\rho}_{\mathrm{s}}^{(\mathrm{j})}|} + \frac{d\overline{\mathrm{E}}_{\mathrm{j}}(\theta)}{\mathrm{d}\theta}\mathbf{n}^{(\mathrm{j})} \times \frac{\boldsymbol{\rho}_{\mathrm{s}}^{(\mathrm{j})}}{|\boldsymbol{\rho}_{\mathrm{s}}^{(\mathrm{j})}|}\right) \\
\overline{\mathrm{E}}_{\mathrm{j}}(\theta) &= \frac{\mu \mathrm{b}^2}{4\pi(1-\nu)}(1-\nu\cos(\theta)^2)\ln\left(\frac{4\overline{\mathrm{L}}_{\mathrm{o}}^{(\mathrm{j})}}{\mathrm{eb}}\right)
\end{aligned}
\tag{6.56}
$$

where $\rho = \mathrm{b}/4$ has been used, $\overline{\mathrm{L}}_{\mathrm{o}}^{(\mathrm{j})}$ is given by (6.55). For more details on the form of the transport equations, the reader is directed to [176] where the dislocation density transport equations have been derived. Similar expressions for the negative junction points may also be given.

6.7 Length scale considerations

In this section, an analysis of the previously made assumptions on the dislocation line's orientation at their endpoints is performed. We also analyze the assumptions that lead to the definition of the edge number density (6.47). These assumptions allowed us to obtain a closed-form expression for the evolution equations in (6.56) by writing the mean junction point flux in (6.37) in terms of a product of the mean velocity field and a mean junction point density . Different configurations and length scales that either defend or question these assumptions are analyzed.

The relation between the average line bundle orientation and the orientation of line tangents at the end points of the dislocation lines is highly dependent on the scale of the model. It is expected that there are regions on each dislocation line near the endpoints where the line orientations are strongly correlated to the average orientation of that line. Therefore, a length scale where the line tangent at the endpoints is correlated to the average line tangent is expected to exist. For instance, on the scale associated with the line bundle

approximation where the tangents of each line in an averaging volume is assumed to be similarly oriented. The size of this length scale would depend on the curvature of the lines. The idea that the endpoint orientations are strongly correlated, if not the same, to the line bundle orientation is consistent with the limiting case of analyzing infinitesimal averaging volumes.

The definition of the dislocation density vector field (6.49) suggests that the GND vector density field, $\boldsymbol{\rho}_{\mathrm{s}}^{(l)}$, is a line length weighted average of both open and closed lines. (6.49) is introduced here because it is expected that the orientation of the endpoints is more strongly correlated to the open dislocation lines compared to the closed dislocation lines due to the fact that the endpoints only exist with open dislocation segments. However, since the average line orientation consists of the average of both the open and closed segments, the average line bundle orientation may differ from the average orientation of the endpoints.

There are situations where the closed dislocation lines can heavily influence the average line orientation. This situation is depicted in Fig. 6.4. This situation may arise when two dislocations react to form a junction segment on the slip system of interest in Fig. 6.4. If the closed line orientations vary considerably from the endpoints, then the assumption that the endpoints share the average line bundle orientation is a poor approximation. This scenario is especially relevant in spatial regions where reactions have just started. However, there are

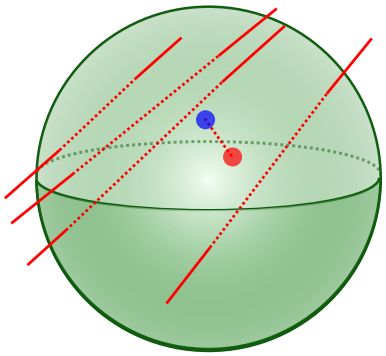

Fig.6.4. Dislocation configuration consisting of predominantly closed dislocation lines.

situations where the orientation of the endpoints is presumably highly correlated with the average line bundle orientation. For example, looking at a low energy dislocation structure in Fig. 6.5 it is easy to see that the orientation of the dislocation lines at their endpoints

is highly correlated to the average line orientation. In this case, the average line orientation is essentially all open dislocation line segments of the same orientation. Therefore, the assumption made in a previous section that the endpoint orientations are aligned with the average line bundle orientation is reasonable.

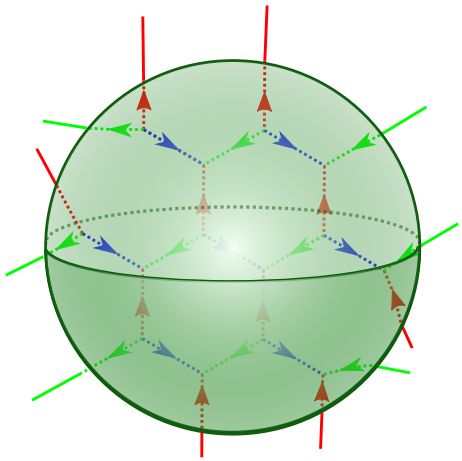

Fig.6.5. Low energy dislocation structure with many open dislocation line segments. Each slip system is denoted with a different color line. The orientation of the lines at their endpoints is strongly correlated to the line orientation in the bulk of the line.

At larger length scales, the curvature of the dislocation lines significantly impacts the average line bundle orientation. This orientation may differ considerably from the orientation at the endpoints of the dislocation line. An example depicting this scenario is given in Fig. 6.6. Two of the three slip systems involved have different endpoint line orientations than their respective line bundle averages in Fig. 6.6. This difference is partly due to the curvature of the lines and its effect on this scale. At scales where the line bundle approximation is used, it is expected that the line segments are approximately straight and therefore the line curvature issue is not a concern. A more thorough statistical analysis must be performed between the endpoint line orientation and the average line orientation to say anything more substantial about their relationship at different modeling scales.

The assumptions made in obtaining the average line length in (6.55) are now discussed. The average line length depends on the magnitude of the dislocation density and the edge number density as can be seen in (6.55). The reader is reminded that in deriving (6.55) it was

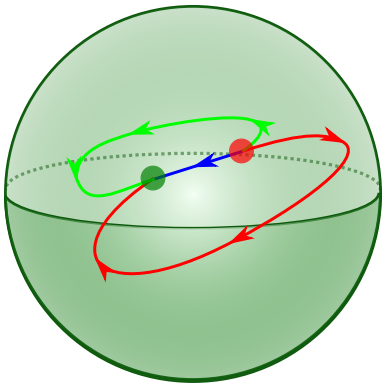

Fig.6.6. Junction formation process resulting in the line orientations of two of the three slip systems involved having different line orientations at their endpoints than their respective average line bundle orientations.

assumed that the dislocation density was predominantly composed of open dislocation line segments. This assumption may be a poor assumption in the initial stages of deformation (before there are many dislocation reactions) like in Fig. 6.4. As the crystal deforms, the error associated with this approximation is expected to decrease. However, when there is a lack of dislocation reactions, the average line length of the open segments may be skewed by the contribution of the closed dislocation segment's length to the dislocation density. This is problematic because the driving forces on junction nodes should only be proportional to the length of the connecting open dislocation line lengths.

A separate issue with the average line length is related to the fact that it was obtained from the magnitude of the dislocation vector density which only represents the geometrically necessary length of the dislocation lines. This is approximately equal to the total line length when the line bundle approximation is used to model on scales which are on the order of the annihilation distance.

In the previous section, an issue with the edge number density related to counting the number of dislocation segments that intersect the surface of the averaging volume was introduced. It was noted there that the edge number density only partially counted some of the surface segments after adding the magnitude of the endpoint density in (6.47). This problem can be best seen by comparing Fig. 6.3 and Fig. 6.5. The edge number density accurately counts the number of edges of all slip systems in the scenario depicted in Fig. 6.3. However, it is not able to capture any of the dislocation segments that intersect the surface of the ball in Fig. 6.5. Integrating the edge number density for the green slip system over the ball in this figure yields a total number of edges equal to 7 instead of the correct value of 10. The difference in these values is due to the fact that there are 6 edges that intersect the surface of the averaging volume. These values were not accounted for because 3 of the edges were oriented inward, and the other 3 were oriented outward from the volume, resulting in a zero value of the endpoint density. For this reason, the endpoint density could not provide any extra information about the edges intersecting the surface. The scenario depicted in Fig. 6.3 resulted in a non-zero endpoint density and therefore was able to contribute the net number of segments that intersected the surface. At increasing scales, the number of segments intersecting the surface is expected to grow slower than the number of segments

in the volume's interior. Therefore, the error associated with the edge number density from counting the net surface segments is expected to decrease as the averaging volume increases.

6.8 Conclusion

The discrete driving forces for junction point motion have been derived in this work. These forces were derived by taking the variational derivative of the elastic self-energy with respect to perturbations of the junction point locations. The line tension approximation was numerically validated in Section 6.4. In Section 6.5, the discrete driving forces in (6.14) were used along with a linear velocity mobility law for the junction points to derive the mean velocity field of the dislocation junction points. However, the mean velocity field depended on the average open dislocation segment length. By using the average edge number density and dislocation density, average open dislocation segment length was obtained for each slip system. An expression for the average edge number density on each slip system in terms of the junction point densities and the endpoint densities was derived in Section 6.6. Lastly, in Section 6.7, there was a discussion of various length-scale specific issues with the assumptions used to derive the mean junction driving force highlighting the influence of curvature of the dislocation lines and the closed dislocation segments on the orientation of the dislocations at the junction points. Also discussed the topic of how the edge number density only retains the net information of the dislocation segments that intersect with the surface of the averaging volume.

The resulting derived mean velocity field for the positive and negative junction points in (6.41) and (6.42), respectively, provide a closure for the continuum equations given in (6.38) in terms of the density variables used in the model. The model may now be treated as a physical theory of dislocations since the mean velocity field was derived considering dislocation physics. In this work, junction points that only have three dislocation arms were considered, but there may be more dislocation segments attached to each junction point. The driving forces derived in (6.35) can be easily extended to include these scenarios by increasing the summation from three to all the attached dislocation arms.

The resulting velocity field of the junction points is a nonlinear function of both the dislocation density and junction point density, making the solution of the final form (6.56) challenging to be solved analytically. Numerical methods will thus be needed to obtain the solution to the transport equations of the positive and negative junction point densities. Similarly, the discretization of the equations (6.56) and how to deal with the coupling of the transport equations for dislocation vector density and junction points requires special attention.

Moreover, it is also noted that Section 6.7 lacks a rigorous statistical analysis on the relationship between the endpoint orientation and average line bundle orientation on length scales consistent with the line bundle approximation (on the order of the annihilation distance of dislocations). It would also be of interest to study the average line length density of the open dislocation segments on this scale to help understand the limitations of the approximation (6.55).

In deriving the mean-field velocity of junction points, a velocity mobility law for the junction points was assumed [see (6.32)]. This assumption can be verified (or invalidated) by using molecular dynamics simulations where the driving forces on the junction nodes are known from the second set of equations in (6.14). The magnitude of the junction point velocity can also be measured and plotted against the magnitude of the driving force to obtain the mobility.

6.A Derivation of variation of self energy

In this appendix, details for the derivation of the variation of the self-energy term are given. The notation in this section is similar to the one used by [69]. The self-energy integral takes the form

$$F(c) = \int_c f(\theta) \mathrm{d}\ell. \tag{6.57}$$

Let $\boldsymbol{r}_c(\ell)$ be an arclength parameterization of one curve c and $\boldsymbol{u}_c$ be an arbitrary perturbation of the curve including arbitrary perturbations at the endpoints denoted by $\boldsymbol{u}_{\partial c} = \boldsymbol{u}_c(\partial c)$. The perturbed curve $c + \delta c$ is defined by

$$\boldsymbol{r}_{c+\delta cc}(\ell, t) = \boldsymbol{r}_c(\ell) + t\boldsymbol{u}_c(\ell). \tag{6.58}$$

Taking the variational derivative of the expression (6.57) amounts to computing

$$\delta F_c = \frac{d}{dt} \int_{c+\delta c} f(\theta) \mathrm{d}\ell|_{t=0}. \tag{6.59}$$

Using the transport identity (2D) in [69] yields

$$\begin{aligned} \delta F_c &= \int_{c+\delta c} \mathring{f(\theta)} - fk\boldsymbol{u}_{c_\mathrm{i}} \cdot \mathbf{n} \mathrm{d}\ell + \int_{\partial c} f\boldsymbol{u}_{\partial c} \cdot \mathbf{t} \\ &= \int_{c+\delta c} \frac{\mathrm{d}f(\theta)}{\mathrm{d}\theta} \mathring{\theta} - fk\boldsymbol{u}_c \cdot \mathbf{n} \mathrm{d}\ell + \int_{\partial c} f\boldsymbol{u}_{\partial c} \cdot \mathbf{t} \end{aligned} \tag{6.60}$$

where κ is the curvature of the curve. Noting that $\mathring{\theta} = V_s$, where V is the normal velocity of the curve (which is $\boldsymbol{u}_{c_\mathrm{i}} \cdot \boldsymbol{n}$ in the perturbed curve), and using integration by parts on the terms containing $\frac{\mathrm{d}f(\theta)}{\mathrm{d}\theta}\mathring{\theta}$, the above expression becomes

$$\delta F_c = \int_{c+\delta c} -\frac{\mathrm{d}}{\mathrm{d}s}\left(\frac{\mathrm{d}f(\theta)}{\mathrm{d}\theta}\right)\boldsymbol{u}_{c_\mathrm{i}} \cdot \mathbf{n} - f\kappa\boldsymbol{u}_{c_\mathrm{i}} \cdot \mathbf{n} \mathrm{d}\ell + \int_{\partial c} f\boldsymbol{u}_{\partial c} \cdot \mathbf{t} + \frac{\mathrm{d}f(\theta)}{\mathrm{d}\theta}\boldsymbol{u}_{\partial c} \cdot \mathbf{n} \tag{6.61}$$

$$= \int_{c+\delta cc} -\left(f + \frac{\mathrm{d}^2 f(\theta)}{\mathrm{d}\theta^2}\right)\kappa\boldsymbol{u}_c \cdot \mathbf{n} \mathrm{d}\ell + \int_{\partial c} f\boldsymbol{u}_{\partial c} \cdot \mathbf{t} + \frac{\mathrm{d}f(\theta)}{\mathrm{d}\theta}\boldsymbol{u}_{\partial c} \cdot \mathbf{n}$$

. (6.62)

where $\frac{\mathrm{d}\theta}{\mathrm{d}s} = \kappa$ was used in obtaining the last expression. Then, the final form for the variation of the functional (6.57) is given as

$$\delta F_c = \int_{c+\delta c} -\left(f + \frac{\mathrm{d}^2 f(\theta)}{\mathrm{d}\theta^2}\right)\kappa\boldsymbol{u}_c \cdot \mathbf{n} \mathrm{d}\ell + \int_{\partial c} f\boldsymbol{u}_{\partial c} \cdot \mathbf{t} + \frac{\mathrm{d}f(\theta)}{\mathrm{d}\theta}\boldsymbol{u}_{\partial c} \cdot \mathbf{n} \tag{6.63}$$

which is the form used in the main document.

7. SUMMARY AND OUTLOOK

The study of dislocations is imperative to further our understanding of plasticity in general. Their collective behavior gives rise to many emergent properties of the material. Discrete dislocation dynamics models have shown great promise in studying dislocation networks. However, due to the computational work scaling with the square of the number of segments, they quickly become infeasible on large spatial and time scales.

Continuum dislocation dynamics models have aided our understanding of complex dislocation interactions and overcome the scaling deficiency that the discrete models possess. A vector density mesoscale model at finite deformation has been derived in this work to understand . The transport relations for both the deformed and referential dislocation density measures have also been derived and are given in (3.71) and (3.73), respectively. The referential and deformed vector density transport equations are also given in (3.77) and (3.85), respectively. The two equations take a similar form. The only difference is that the material velocity is added to the transport relations for the density in the deformed configuration, and the derivative operators are taken in their respective frames. Referential and deformed vector density driving forces were also derived and obtained in (3.115) and (3.150), respectively.

The referential vector density transport equations are discretized in Section 4.6.1 along with a field dislocation mechanics update of the plastic distortion in Section 4.6.2. Updating the plastic distortion in this fashion results in fewer numerical errors [126]. A homogenization scheme is introduced to connect the mesoscale model to larger length scales using the deformation gradient. With this scheme introduced, the deformation is decomposed into mean and fluctuation components on the mesoscale. The discretized form of the crystal mechanics equations is written in terms of the fluctuation fields in (4.41). Solving the crystal mechanics field problem requires the computation of a tangent modulus in (4.43), and the stress update (4.39). A staggered solute scheme is implemented where the plastic distortion and mean deformation gradient are fixed during the mechanical field update. The whole algorithm is schematically shown in Fig. 4.1. A uniaxial tension test is simulated with

results shown in Fig. 4.14 along with the dynamic recovery of two oppositely oriented tilt boundaries whose results are shown in Fig. 4.13 and Fig. 4.12.

The current continuum dislocation literature lacks a fundamental derivation of dislocation reactions. When dislocations react, they form open dislocation lines on each slip system. The kinematics of the open dislocation lines were introduced in Chapter 5. An endpoint density was introduced in (5.32). The endpoint density was related to the junction point density in (5.44) by introducing the graph representing the dislocation network. In particular, the r-partite property of the dislocation network graph made this possible. This property was derived by considering the junction formation process and Frank's second rule. With the relationship between the endpoints and junction points, it was possible to write the transport equations for the dislocation density in terms of the junction points in (5.53). Transport equations for the junction point densities are also derived in (5.68) where source terms are added to account for topology changes of the network-related dislocation-dislocation reactions.

A study of the kinetics of the dislocation junction points is given in 6. The driving forces on individual junction points are derived here by taking the variational derivative of the self-energy of the dislocation network and are given in the second set of equations in (6.14). Introducing a velocity mobility law for the junction points provides a relationship for obtaining the velocity of each junction point. Then the mean velocity field for the junction point density is derived and given in (6.41) and (6.42) for the positive and negative junction point densities, respectfully. A mean junction segment length was also derived in (6.55) to account for the line length dependence of the junction forces. The final form for the transport equations, accounting for the kinetics of junction points, is given in (6.56) for the positive junction densities.

7.1 Future work

Looking forward it seem necessary to incorporate the work done in Chapter 5 and 6 into the finite deformation setting. Preliminary derivations suggest that the vector density

transport equations remain form invariant. The transport equations for the vector density are

$$\dot{\boldsymbol{\rho}}_{\mathrm{R}}^{(l)} = \mathrm{Curl}\Big(\mathbf{v}_{\mathrm{R}}^{(l)} \times \boldsymbol{\rho}_{\mathrm{R}}^{(l)}\Big) - \sum_{p,q:\,(lpq)\in S^l} \mathrm{sgn}^{(lpq,l)} \left(\boldsymbol{v}_{\mathrm{JR}}^{(lpq)+}\pi_{\mathrm{JR}}^{(lpq)+} - \boldsymbol{v}_{\mathrm{JR}}^{(lpq)-}\pi_{\mathrm{JR}}^{(lpq)-}\right) \tag{7.1}$$

$$\boldsymbol{\rho}'^{(l)}_{\mathrm{D}} = \mathrm{curl}\left((\mathbf{v}_{\mathbf{D}}^{(l)} + \mathbf{v}) \times \boldsymbol{\rho}_{\mathrm{D}}^{(l)}\right) - \sum_{p,q:\,(lpq)\in S^l} \mathrm{sgn}^{(lpq,l)} \left((\boldsymbol{v}_{\mathrm{JR}}^{(lpq)+} + \mathbf{v})\pi_{\mathrm{JR}}^{(lpq)+} - (\boldsymbol{v}_{\mathrm{JR}}^{(lpq)-} + \mathbf{v})\pi_{\mathrm{JR}}^{(lpq)-}\right).$$

A numerical solution to the coupled transport equations is now possible since we have obtained the mean velocity field for the junction points. However, the solution to these coupled transport equations will require discretization and linearization. In particular, the nonlinearities of the junction point velocity (6.56) will need to be addressed.

The mean-field theory derived in this work can also be enriched with correlation effects. Correlation terms will be important in establishing a relationship between the endpoint orientation and the line bundle orientation. Since the junction points grow along the intersections of two glide planes, it is expected that the negative and positive junction points will be correlated at orientations that correspond to intersections of glide planes.

The average line segment length depends on the GND vector density field. The GND vector density may provide an incorrect length measure at larger scales since it cannot accurately describe the line length information at increasing scales. Alternatively, the total dislocation line length can be used on these larger scales where the GND density does not represent the line length information accurately. The types of models that have the total line length as a state variable can be found in the works of the Hochrainer group [88]. In these models, the line orientation at the endpoints can also be related to the GND orientation using information about the curvature of the line. Assuming that all dislocation lines have the same curvature and line length, a relationship between the endpoint orientation and the line bundle orientation can be obtained using geometrical arguments on circular arcs.

There is still some exciting work that can be investigated related to the graph-theoretical representation of the dislocation network. As this work is generalized to include more than three junction arms, the complexity of the network will increase. In graph theory, measures of the complexity of a graph are related to the entropy of the graph. The idea of a tem-

perature and entropy of a graph has been explored for some time [206]. However, there are still unanswered questions related to defining the complexity of a graph in general [142, 206]. How these ideas connect to dislocation networks is an interesting topic for future study. In [199], the network entropy depends on the edge and nodal information, which further motivates the need for both nodal and edge information in dislocation models where graph entropy information may be needed.

8. BIBLIOGRAPHY

[1] A. Acharya. A model of crystal plasticity based on the theory of continuously distributed dislocations. *Journal of the Mechanics and Physics of Solids*, 49(4):761–784, 2001.

[2] A. Acharya. Constitutive analysis of finite deformation field dislocation mechanics. *Journal of the Mechanics and Physics of Solids*, 52(2):301–316, 2 2004.

[3] A. Acharya. Microcanonical entropy and mesoscale dislocation mechanics and plasticity. *Journal of Elasticity*, 104(1-2):23–44, 2011.

[4] A. Acharya and A. Roy. Size effects and idealized dislocation microstructure at small scales: Predictions of a Phenomenological model of Mesoscopic Field Dislocation Mechanics: Part I. *Journal of the Mechanics and Physics of Solids*, 54(8):1687–1710, 2006.

[5] A. Acharya, A. Roy, and A. Sawant. Continuum theory and methods for coarse-grained, mesoscopic plasticity. *Scripta Materialia*, 54(5):705–710, 3 2006.

[6] S. Akhondzadeh, N. Bertin, R. B. Sills, and W. Cai. Slip-free multiplication and complexity of dislocation networks in FCC metals. *Materials Theory*, 5(1):2, 12 2021.

[7] B. Alger, D. Andrš, R. W. Carlsen, D. R. Gaston, F. Kong, A. D. Lindsay, J. M. Miller, C. J. Permann, J. W. Peterson, A. E. Slaughter, and R. Stogner. {MOOSE} {W}eb page. \url{https://mooseframework.org}, 2019.

[8] J. P. Anderson and A. El-Azab. On the three-dimensional spatial correlations of curved dislocation systems. *Materials Theory*, 5(1):1, 2021.

[9] P. M. Anderson, J. P. Hirth, and J. Lothe. *Theory of dislocations*. Cambridge University Press, Cambridge, 3rd edition, 2017.

[10] M. Ardeljan, I. J. Beyerlein, and M. Knezevic. A dislocation density based crystal plasticity finite element model: Application to a two-phase polycrystalline HCP/BCC composites. *Journal of the Mechanics and Physics of Solids*, 66(1):16–31, 5 2014.

[11] R. Arora and A. Acharya. Dislocation pattern formation in finite deformation crystal plasticity. *International Journal of Solids and Structures*, 184:114–135, 12 2020.

[12] R. Arora, X. Zhang, and A. Acharya. Finite element approximation of finite deformation dislocation mechanics. *Computer Methods in Applied Mechanics and Engineering*, 367:113076, 2020.

[13] A. Arsenlis, W. Cai, M. Tang, M. Rhee, T. Oppelstrup, G. Hommes, T. G. Pierce, and V. V. Bulatov. Enabling strain hardening simulations with dislocation dynamics. *Modelling and Simulation in Materials Science and Engineering*, 15(6):553–595, 9 2007.

[14] R. Asaro and J. Rice. Strain localization in ductile single crystals. *Journal of the Mechanics and Physics of Solids*, 25(5):309–338, 10 1977.

[15] R. J. Asaro. Crystal plasticity. *Trans. ASME: J. Appl. Mech.*, 50(4b):921–934, 1983.

[16] T. Belytschko, K. Wing, B. Moran, and K. Elkhodary. *Nonlinear Finite Element for Continua and Structures*. John Wiley & Sons, 2014.

[17] B. A. Bilby, R. Bullough, L. R. T. Gardner, E. Smith, and J. M. Whittaker. Continuous distributions of dislocations IV. Single glide and plane strain. *Proceedings of the Royal Society of London. Series A. Mathematical and Physical Sciences*, 244(1239):538–557, 4 1958.

[18] B. A. Bilby, R. Bullough, E. Smith, L. Gardner, and E. Smith. Continuous distributions of dislocations: a new application of the methods of non-riemannian geometry. *Proceedings of the Royal Society A: Mathematical, Physical and Engineering Sciences*, 231(1185):263–273, 8 1955.

[19] D. N. Blaschke and B. A. Szajewski. Line tension of a dislocation moving through an anisotropic crystal. *Philosophical Magazine*, 98(26):2397–2424, 2018.

[20] J. Bonet and R. D. Wood. *Nonlinear Continuum Mechanics for Finite Element Analysis*, volume 9780521838. Cambridge University Press, Cambridge, 2008.

[21] R. Bott and L. W. Tu. *Differential forms in algebraic topology*, volume 82. Springer-Verlag New York, 1982.

[22] R. Brenner, A. J. Beaudoin, P. Suquet, and A. Acharya. Numerical implementation of static Field Dislocation Mechanics theory for periodic media. *Philosophical Magazine*, 94(16):1764–1787, 2014.

[23] L. M. Brown. The self-stress of dislocations and the shape of extended nodes. *The Philosophical Magazine: A Journal of Theoretical Experimental and Applied Physics*, 10(105):441–466, 9 1964.

[24] V. Bulatov and W. Cai. *Computer Simulations of Dislocations*. Oxford University Press, 11 2006.

[25] V. Bulatov, W. Cai, J. Fier, M. Hiratani, G. Hommes, T. Pierce, M. Tang, M. Rhee, K. Yates, and T. Arsenlis. Scalable line dynamics in ParaDiS. In *SC'04: Proceedings of the 2004 ACM/IEEE Conference on Supercomputing*, page 19, 2004.

[26] V. V. Bulatov and W. Cai. Nodal Effects in Dislocation Mobility. *Physical Review Letters*, 89(11):9–12, 2002.

[27] V. V. Bulatov, L. L. Hsiung, M. Tang, A. Arsenlis, M. C. Bartelt, W. Cai, J. N. Florando, M. Hiratani, M. Rhee, G. Hommes, T. G. Pierce, and T. D. De La Rubia. Dislocation multi-junctions and strain hardening. *Nature*, 440(7088):1174–1178, 4 2006.

[28] W. Cai. Computational Mechanics Forum, 2022.

[29] W. Cai, A. Arsenlis, C. R. Weinberger, and V. V. Bulatov. A non-singular continuum theory of dislocations. *Journal of the Mechanics and Physics of Solids*, 54(3):561–587, 2006.

[30] D. Caillard. Dynamic strain ageing in iron alloys: The shielding effect of carbon. *Acta Materialia*, 112:273–284, 2016.

[31] W. D. Callister Jr and D. G. Rethwisch. *Callister's materials science and engineering*. John Wiley & Sons, 2020.

[32] V. Capasso. *An Introduction to Random Currents and Their Applications*. SpringerBriefs in Mathematics. Springer International Publishing, Cham, 2018.

[33] P. Cermelli. Material symmetry and singularities in solids. *Proceedings of the Royal Society of London. Series A: Mathematical, Physical and Engineering Sciences*, 455(1981):299–322, 1 1999.

[34] P. Cermelli and M. E. Gurtin. On the characterization of geometrically necessary dislocations in finite plasticity. *Journal of the Mechanics and Physics of Solids*, 49(7):1539–1568, 7 2001.

[35] L. Y. Chen, M.-r. He, J. Shin, G. Richter, and D. S. Gianola. Measuring surface dislocation nucleation in defect-scarce nanostructures. *Nature Materials*, 14(7):707–713, 2015.

[36] J. Clayton, C. Hartley, and D. McDowell. The missing term in the decomposition of finite deformation. *International Journal of Plasticity*, 52:51–76, 1 2014.

[37] F. F. Csikor, I. Groma, T. Hochrainer, D. Weygand, and M. Zaiser. On the range of 3D dislocation pair correlations. 12 2008.

[38] G. de Rham. *Differentiable Manifolds*, volume 266 of *Grundlehren der mathematischen Wissenschaften*. Springer Berlin Heidelberg, Berlin, Heidelberg, 1984.

[39] R. de Wit. Relation between dislocations and disclinations. *Journal of Applied Physics*, 42(9):3304–3308, 1971.

[40] R. de Wit. Continuous distribution of disclination loops. *Physica Status Solidi (a)*, 18(2):669–681, 8 1973.

[41] R. de Wit. Theory of disclinations: II. Continuous and discrete disclinations in anisotropic elasticity. *Journal of Research of the National Bureau of Standards Section A: Physics and Chemistry*, 77A(3):359, 1973.

[42] R. de Wit. Theory of disclinations: IV. Straight disclinations. *Journal of Research of the National Bureau of Standards Section A: Physics and Chemistry*, 77A(5):607, 1973.

[43] J. Deng and A. El-Azab. Dislocation pair correlations from dislocation dynamics simulations. *Journal of Computer-Aided Materials Design*, 14(S1):295–307, 12 2007.

[44] J. Deng and A. El-Azab. Mathematical and computational modelling of correlations in dislocation dynamics. *Modelling and Simulation in Materials Science and Engineering*, 17(7):075010, 10 2009.

[45] J. Deng and A. El-Azab. Temporal statistics and coarse graining of dislocation ensembles. *Philosophical Magazine*, 90(27-28):3651–3678, 9 2010.

[46] B. Devincre, R. Madec, G. Monnet, S. Queyreau, R. Gatti, and L. Kubin. Modeling crystal plasticity with dislocation dynamics simulations: The 'microMegas' code. In *Mech. Nano-Objects*, pages 81–99. Presse des Mines, 1 2011.

[47] R. deWit. Theory of disclinations: III. Continuous and discrete disclinations in isotropic elasticity. *Journal of Research of the National Bureau of Standards Section A: Physics and Chemistry*, 77A(3):359, 5 1973.

[48] R. Diestel. *Graph Theory*, volume 173 of *Graduate Texts in Mathematics*. Springer Berlin Heidelberg, Berlin, Heidelberg, 2 2017.

[49] L. M. Dougherty, I. M. Robertson, and J. S. Vetrano. Direct observation of the behavior of grain boundaries during continuous dynamic recrystallization in an Al–4Mg–0.3Sc alloy. *Acta Materialia*, 51(15):4367–4378, 2003.

[50] L. Dupuy and M. C. Fivel. A study of dislocation junctions in FCC metals by an orientation dependent line tension model. *Acta Materialia*, 50(19):4873–4885, 2002.

[51] P. Eisenlohr, M. Diehl, R. Lebensohn, and F. Roters. A spectral method solution to crystal elasto-viscoplasticity at finite strains. *International Journal of Plasticity*, 46:37–53, 7 2013.

[52] A. El-Azab. Statistical mechanics treatment of the evolution of dislocation distributions in single crystals. *Physical Review B*, 61(18):11956–11966, 5 2000.

[53] A. El-Azab. Statistical mechanics of dislocation systems. *Scripta Materialia*, 54(5):723–727, 3 2006.

[54] A. El-Azab and G. Po. Continuum Dislocation Dynamics: Classical Theory and Contemporary Models. In W. Andreoni and S. Yip, editors, *Handbook of Materials Modeling*, pages 1–25. Springer International Publishing, Cham, 2018.

[55] M. Epstein and R. Segev. A unified geometric treatment of material defects. *arXiv: Mathematical Physics*, pages 1–14, 5 2013.

[56] M. Epstein and R. Segev. On the Geometry and Kinematics of Smoothly Distributed and Singular Defects. *arXiv: Mathematical Physics*, 2014.

[57] H. Federer and W. H. Fleming. Normal and Integral Currents. *The Annals of Mathematics*, 72(3):458, 11 1960.

[58] J. M. Finney and C. Laird. Strain localization in cyclic deformation of copper single crystals. *The Philosophical Magazine: A Journal of Theoretical Experimental and Applied Physics*, 31(2):339–366, 2 1975.

[59] M. Fivel. Discrete Dislocation Dynamics: Principles and Recent Applications. *Multiscale Modeling of Heterogenous Materials: From …*, pages 17–36, 2010.

[60] E. I. Galindo-Nava and P. E. J. Rivera-Díaz-del Castillo. Thermostatistical modelling of hot deformation in FCC metals. *International Journal of Plasticity*, 47:202–221, 2013.

[61] D. R. Gaston, C. J. Permann, J. W. Peterson, A. E. Slaughter, D. Andrš, Y. Wang, M. P. Short, D. M. Perez, M. R. Tonks, J. Ortensi, L. Zou, and R. C. Martineau. Physics-based multiscale coupling for full core nuclear reactor simulation. *Annals of Nuclear Energy*, 84:45–54, 2015.

[62] I. Groma. Link between the microscopic and mesoscopic length-scale description of the collective behavior of dislocations. *Physical Review B*, 56(10):5807–5813, 9 1997.

[63] I. Groma, F. F. Csikor, and M. Zaiser. Spatial correlations and higher-order gradient terms in a continuum description of dislocation dynamics. *Acta Materialia*, 51:1271–1281, 2003.

[64] I. Groma, M. Zaiser, and P. D. Ispánovity. Dislocation patterning in a two-dimensional continuum theory of dislocations. *Physical Review B*, 93(21):214110, 6 2016.

[65] V. Guillemin and P. Haine. *Differential Forms*. WORLD SCIENTIFIC, 6 2018.

[66] V. Guillemin and A. Pollack. Oriented intersection theory. In *Differential Topology*, pages 94–150. American Mathematical Society, Providence, Rhode Island, 8 2010.

[67] M. D. Gunzburger and P. B. Bochev. *Least-Squares Finite Element Methods*, volume 166 of *Applied Mathematical Sciences*. Springer New York, New York, NY, 2009.

[68] M. Gurtin. *Configurational Forces as Basic Concepts of Continuum Physics*, volume 137 of *Applied Mathematical Sciences*. Springer New York, New York, NY, 2000.

[69] M. E. Gurtin. *Thermomechanics of Evolving Phase Boundaries in the Plane*. Oxford University Press, 1993.

[70] M. E. Gurtin. The Burgers vector and the flow of screw and edge dislocations in finite-deformation single-crystal plasticity. *Journal of the Mechanics and Physics of Solids*, 54(9):1882–1898, 9 2006.

[71] M. E. Gurtin. A finite-deformation, gradient theory of single-crystal plasticity with free energy dependent on the accumulation of geometrically necessary dislocations. *International Journal of Plasticity*, 26(8):1073–1096, 8 2010.

[72] M. E. Gurtin, L. Anand, and S. P. Lele. Gradient single-crystal plasticity with free energy dependent on dislocation densities. *Journal of the Mechanics and Physics of Solids*, 55(9):1853–1878, 2007.

[73] M. E. Gurtin, E. Fried, and L. Anand. *The Mechanics and Thermodynamics of Continua*. Cambridge University Press, Cambridge, 2010.

[74] M. E. Gurtin and B. D. Reddy. Some issues associated with the intermediate space in single-crystal plasticity. *Journal of the Mechanics and Physics of Solids*, 95:230–238, 10 2016.

[75] N. Hansen and X. Huang. Microstructure and flow stress of polycrystals and single crystals. *Acta Materialia*, 46(5):1827–1836, 3 1998.

[76] W. Hauser. On the Fundamental Equations of Electromagnetism. *American Journal of Physics*, 38(1):80–85, 1 1970.

[77] R. Hill. Generalized constitutive relations for incremental deformation of metal crystals by multislip. *Journal of the Mechanics and Physics of Solids*, 14(2):95–102, 1966.

[78] P. B. Hirsch, R. W. Horne, and M. J. Whelan. LXVIII. Direct observations of the arrangement and motion of dislocations in aluminium. *Philosophical Magazine*, 1(7):677–684, 1956.

[79] J. P. Hirth, T. Jøssang, and J. Lothe. Dislocation energies and the concept of line tension. *Journal of Applied Physics*, 37(1):110–116, 1966.

[80] J. P. Hirth, J. Lothe, and T. Mura. Theory of Dislocations (2nd ed.). *Journal of Applied Mechanics*, 50(2):476–477, 6 1983.

[81] T. Hochrainer. *Evolving systems of curved dislocations:mathematical foundations of a statistical theory*. PhD thesis, Karlsruhe Institute of Technology, 2007.

[82] T. Hochrainer. Moving dislocations in finite plasticity: a topological approach. *ZAMM Zeitschrift fur Angewandte Mathematik und Mechanik*, 93(4):252–268, 4 2013.

[83] T. Hochrainer. Multipole expansion of continuum dislocations dynamics in terms of alignment tensors. *Philosophical Magazine*, 95(12):1321–1367, 2015.

[84] T. Hochrainer. Thermodynamically consistent continuum dislocation dynamics. *Journal of the Mechanics and Physics of Solids*, 88:12–22, 3 2016.

[85] T. Hochrainer, P. Gumbsch, and M. Zaiser. A Non-Linear Multiple Slip Theory in Continuum Dislocation Dynamics. In *Proceedings of the 4th Int. Conf. on Multiscale Materials Modelling*, pages 115–118, 2008.

[86] T. Hochrainer, S. Sandfeld, M. Zaiser, and P. Gumbsch. Continuum dislocation dynamics: towards a physical theory of crystal plasticity. *Journal of the Mechanics and Physics of Solids*, 63(1):167–178, 2 2014.

[87] T. Hochrainer and B. Weger. Is crystal plasticity non-conservative? Lessons from large deformation continuum dislocation theory. *Journal of the Mechanics and Physics of Solids*, 141:103957, 2020.

[88] T. Hochrainer, M. Zaiser, and P. Gumbsch. A three-dimensional continuum theory of dislocation systems: kinematics and mean-field formulation. *Philosophical Magazine*, 87(8-9):1261–1282, 3 2007.

[89] C. Hong, X. Huang, and G. Winther. Dislocation content of geometrically necessary boundaries aligned with slip planes in rolled aluminium. *Philosophical Magazine*, 93(23):3118–3141, 8 2013.

[90] X. Huang and N. Hansen. Grain orientation dependence of microstructure in aluminium deformed in tension. *Scripta Materialia*, 37(1):1–7, 7 1997.

[91] X. Huang and G. Winther. Dislocation structures. Part I. Grain orientation dependence. *Philosophical Magazine*, 87(33):5189–5214, 11 2007.

[92] D. Hughes, Q. Liu, D. Chrzan, and N. Hansen. Scaling of microstructural parameters: misorientations of deformation induced boundaries. *Acta Materialia*, 45(1):105–112, 1 1997.

[93] D. A. Hughes and N. Hansen. Deformation structures developing on fine scales. *Philosophical Magazine*, 83(31-34):3871–3893, 10 2003.

[94] D. A. Hughes and N. Hansen. The microstructural origin of work hardening stages. *Acta Materialia*, 148:374–383, 2018.

[95] D. Hull and D. J. Bacon. *Introduction to Dislocations*. Elsevier, 2011.

[96] P. D. Ispánovity, S. Papanikolaou, and I. Groma. Emergence and role of dipolar dislocation patterns in discrete and continuum formulations of plasticity. *Physical Review B*, 101(2), 2020.

[97] B. Jakobsen. Formation and subdivision of deformation structures during plastic deformation. *Science*, 312(5775):889–892, 5 2006.

[98] K. Kashihara, M. Tagami, and F. Inoko. Deformed Structure and Crystal Orientation at Deformation Bands in ⟨011⟩ Aluminum Single Crystals. *Materials Transactions, JIM*, 37(4):564–571, 1996.

[99] Y. Kawasaki and T. Takeuchi. Cell structures in copper single crystals deformed in the [001] and [111] axes. *Scripta Metallurgica*, 14(2):183–188, 2 1980.

[100] K. Kondo. On the geometrical and physical foundations of the theory of yielding. *2nd Japan National Congress for Applied Mechanics*, 2:41–47, 1952.

[101] S. Kondo, T. Mitsuma, N. Shibata, and Y. Ikuhara. Direct observation of individual dislocation interaction processes with grain boundaries. *Science advances*, 2(11):e1501926–e1501926, 11 2016.

[102] A. M. Kosevich. The deformation field in an anisotropic elastic medium containing moving dislocations. *Sov. Phys. JETP*, 15(1):108–115, 1962.

[103] A. M. Kosevich. Dynamical theory of dislocations. *New York*, 5(5):579–609, 1965.

[104] E. Kossecka and R. de Wit. Disclination Kinematics. *Arch Mech*, 29(5):633–651, 1977.

[105] E. Kröner. Continuum Theory of Dislocations and Self-Stresses. *Ergebnisse der Angewandten Mathematik*, 5:1–277, 1958.

[106] E. Kröner. Allgemeine Kontinuumstheorie der Versetzungen und Eigenspannungen. *Archive for Rational Mechanics and Analysis*, 4(1):273–334, 1 1959.

[107] E. Kröner. General Continuum Theory of Dislocations And Proper Stresses. *Arch. Rat. Mech. Anal*, 4:273–334, 1960.

[108] E. Kröner. Continuum Theory of Defects. In *Phsique des Defauts / Physics of Defects (Les Houches, Session XXXV, 1980)*, pages 215–315. North-Holland, 1981.

[109] E. Kröner. Benefits and shortcomings of the continuous theory of dislocations. *International Journal of Solids and Structures*, 38(6-7):1115–1134, 2001.

[110] L. P. Kubin, R. Madec, and B. Devincre. Dislocation Intersections and Reactions in FCC and BCC Crystals. *MRS Proceedings*, 779:W1.6, 2 2003.

[111] D. Kuhlmann-Wilsdorf. Chapter 59 The LES theory of solid plasticity. In F. R. N. Nabarro and M. S. Duesbery, editors, *Dislocations in Solids*, volume 11, pages 211–342. Elsevier, 2002.

[112] N. Langdon. Explicit expressions for stress field of a circular dislocation loop. *Theoretical and Applied Fracture Mechanics*, 33(3):219–231, 6 2000.

[113] B. C. Larson, A. El-Azab, W. Yang, J. Z. Tischler, W. Liu, and G. E. Ice. Experimental characterization of the mesoscale dislocation density tensor. *Philosophical Magazine*, 87(8-9):1327–1347, 3 2007.

[114] G. Le, A. Godfrey, N. Hansen, W. Liu, G. Winther, and X. Huang. Influence of grain size in the near-micrometre regime on the deformation microstructure in aluminium. *Acta Materialia*, 61(19):7072–7086, 11 2013.

[115] G. Le, A. Godfrey, C. Hong, X. Huang, and G. Winther. Orientation dependence of the deformation microstructure in compressed aluminum. *Scripta Materialia*, 66(6):359–362, 3 2012.

[116] E. H. Lee. Elastic-Plastic Deformation at Finite Strains. *Journal of Applied Mechanics*, 36(1):1–6, 3 1969.

[117] J. M. Lee. *Introduction to Smooth Manifolds*. Springer New York, second edition, 2013.

[118] E. Lehmann, S. Loehnert, P. Wriggers, S. Lohnert, and P. Wriggers. Computational homogenisation of polycrystalline elastoplastic microstructures at finite deformation. *Technische Mechanik*, 32(2):369–379, 2012.

[119] J. Lépinoux and L. Kubin. The dynamic organization of dislocation structures: A simulation. *Scripta Metallurgica*, 21(6):833–838, 6 1987.

[120] L. E. Levine, P. Geantil, B. C. Larson, J. Z. Tischler, M. E. Kassner, W. Liu, M. R. Stoudt, and F. Tavazza. Disordered long-range internal stresses in deformed copper and the mechanisms underlying plastic deformation. *Acta Materialia*, 59(14):5803–5811, 8 2011.

[121] D. Li, H. Zbib, X. Sun, and M. Khaleel. Predicting plastic flow and irradiation hardening of iron single crystal with mechanism-based continuum dislocation dynamics. *International Journal of Plasticity*, 52:3–17, 1 2014.

[122] N. Li and J. Wang. In-situ TEM Study of Dislocation-Interface Interactions. In *The Transmission Electron Microscope-Theory and Applications*. IntechOpen, 2015.

[123] K. K. Liang. Efficient conversion from rotating matrix to rotation axis and angle by extending Rodrigues' formula. 10 2018.

[124] F. X. Lin, A. Godfrey, D. J. Jensen, and G. Winther. 3D EBSD characterization of deformation structures in commercial purity aluminum. *Materials Characterization*, 61(11):1203–1210, 11 2010.

[125] P. Lin and A. El-Azab. Implementation of annihilation and junction reactions in vector density-based continuum dislocation dynamics. *Modelling and Simulation in Materials Science and Engineering*, 28(4), 2020.

[126] P. Lin, V. Vivekanandan, K. Starkey, B. Anglin, C. Geller, and A. El-Azab. On the computational solution of vector-density based continuum dislocation dynamics mod-

els: A comparison of two plastic distortion and stress update algorithms. *International Journal of Plasticity*, 138:102943, 3 2021.

[127] X. Ling, M. F. Horstemeyer, and G. P. Potirniche. On the numerical implementation of 3D rate-dependent single crystal plasticity formulations. *International Journal for Numerical Methods in Engineering*, 63(4):548–568, 5 2005.

[128] Q. Liu, D. Juul Jensen, and N. Hansen. Effect of grain orientation on deformation structure in cold-rolled polycrystalline aluminium. *Acta Materialia*, 46(16):5819–5838, 10 1998.

[129] Y. Lu, J. Song, J. Y. Huang, and J. Lou. Surface dislocation nucleation mediated deformation and ultrahigh strength in sub-10-nm gold nanowires. *Nano Research*, 4(12):1261–1267, 2011.

[130] R. Madec, B. Devincre, and L. Kubin. On the nature of attractive dislocation crossed states. *Computational Materials Science*, 23(1-4):219–224, 4 2002.

[131] R. Madec, B. Devincre, and L. P. Kubin. From Dislocation Junctions to Forest Hardening. *Physical Review Letters*, 89(25):255508, 12 2002.

[132] I. H. I. H. Madsen and J. Tornehave. *From calculus to cohomology: de Rham cohomology and characteristic classes*. Cambridge University Press, 1997.

[133] E. Martínez, J. Marian, A. Arsenlis, M. Victoria, and J. M. Perlado. Atomistically informed dislocation dynamics in fcc crystals. *Journal of the Mechanics and Physics of Solids*, 2008.

[134] Y. Matsukawa and G. S. Liu. In situ TEM study on elastic interaction between a prismatic loop and a gliding dislocation. *Journal of Nuclear Materials*, 425(1):54–59, 2012.

[135] Y. Matsukawa, Y. Osetsky, R. E. Stoller, and S. J. Zinkle. The collapse of stacking-fault tetrahedra by interaction with gliding dislocations. *Materials Science and Engineering: A*, 400-401:366–369, 2005.

[136] G. Maugin. *Material Inhomogeneities in Elasticity*. Chapman and Hall/CRC, 9 2020.

[137] S. Mazumder. *Numerical methods for partial differential equations: Finite difference and finite volume methods*. Elsevier, 12 2015.

[138] C. Miehe, S. Mauthe, and F. Hildebrand. Variational gradient plasticity at finite strains. Part III: Local–global updates and regularization techniques in multiplicative plasticity for single crystals. *Computer Methods in Applied Mechanics and Engineering*, 268:735–762, 1 2014.

[139] M. Monavari, S. Sandfeld, and M. Zaiser. Continuum representation of systems of dislocation lines: a general method for deriving closed-form evolution equations. *Journal of the Mechanics and Physics of Solids*, 95:575–601, 2016.

[140] M. Monavari and M. Zaiser. Annihilation and sources in continuum dislocation dynamics. *Materials Theory*, 2(1):30, 12 2018.

[141] A. Morro. Evolution equations and thermodynamic restrictions for dissipative solids. *Mathematical and Computer Modelling*, 52(9-10):1869–1876, 2010.

[142] M. Morzy, T. Kajdanowicz, and P. Kazienko. On measuring the complexity of networks: Kolmogorov complexity versus entropy. *Complexity*, 2017:1–12, 2017.

[143] H. Mughrabi. Dislocation wall and cell structures and long-range internal stresses in deformed metal crystals. *Acta Metallurgica*, 31(9):1367–1379, 9 1983.

[144] T. Mura. Continuous distribution of moving dislocations. *Philosophical Magazine*, 24(187):63–69, 5 1963.

[145] T. Mura and D. M. Barnett. Micromechanics of Defects in Solids. *Journal of Applied Mechanics*, 50(2):477, 1983.

[146] J. Nye. Some geometrical relations in dislocated crystals. *Acta Metallurgica*, 1(2):153–162, 3 1953.

[147] E. Olami and R. Kupferman. Homogenization of edge-dislocations as a weak limit of de-Rham currents. *arXiv: Mathematical Physics*, 2018.

[148] J. Oldroyd. On the formulation of rheological equations of state. *Proceedings of the Royal Society of London. Series A. Mathematical and Physical Sciences*, 200(1063):523–541, 1950.

[149] B. O'Neill. *Elementary Differential Geometry*. Elsevier, 2006.

[150] E. Orowan. Zur kristallplastizität. i. *Zeitschrift für Physik*, 89(9-10):605–613, 1934.

[151] M. Peach and J. S. Koehler. The forces exerted on dislocations and the stress fields produced by them. *Physical Review*, 80(3):436–439, 1950.

[152] G. Po. MoDELib : Mechanics Of Defect Evolution Library, 2022.

[153] G. Po, Y. Huang, and N. Ghoniem. A continuum dislocation-based model of wedge microindentation of single crystals. *International Journal of Plasticity*, 114:72–86, 2019.

[154] G. Po, M. S. Mohamed, T. Crosby, C. Erel, A. El-Azab, and N. Ghoniem. Recent Progress in Discrete Dislocation Dynamics and Its Applications to Micro Plasticity. *Jom*, 66(10):2108–2120, 10 2014.

[155] M. Polanyi. Über eine Art Gitterstörung, die einen Kristall plastisch machen könnte. *Zeitschrift für Physik*, 89(9):660–664, 1934.

[156] J. N. Reddy and Reddy J. *An Introduction to Continuum Mechanics*. Cambridge University Press, Cambridge, 2013.

[157] B. J. R. Rice. Inelastic constitutive relations for solids : theory and its application. *Journal of the Mechanics and Physics of Solids*, 19:433–455, 1971.

[158] I. M. Robertson. The effect of hydrogen on dislocation dynamics. *Engineering Fracture Mechanics*, 68(6):671–692, 2001.

[159] D. Rodney and R. Phillips. Structure and Strength of Dislocation Junctions: An Atomic Level Analysis. *Physical Review Letters*, 82(8):1704–1707, 2 1999.

[160] F. Roters, M. Diehl, P. Shanthraj, P. Eisenlohr, C. Reuber, S. Wong, T. Maiti, A. Ebrahimi, T. Hochrainer, H.-O. Fabritius, S. Nikolov, M. Friák, N. Fujita, N. Grilli, K. Janssens, N. Jia, P. Kok, D. Ma, F. Meier, E. Werner, M. Stricker, D. Weygand, and D. Raabe. DAMASK – The Düsseldorf Advanced Material Simulation Kit for modeling multi-physics crystal plasticity, thermal, and damage phenomena from the single crystal up to the component scale. *Computational Materials Science*, 158:420–478, 2 2019.

[161] F. Roters, P. Eisenlohr, T. R. Bieler, and D. Raabe. *Crystal Plasticity Finite Element Methods*. Wiley-VCH Verlag GmbH & Co. KGaA, Weinheim, Germany, 10 2010.

[162] F. Roters, P. Eisenlohr, L. Hantcherli, D. D. Tjahjanto, T. R. Bieler, and D. Raabe. Overview of constitutive laws, kinematics, homogenization and multiscale methods in crystal plasticity finite-element modeling: Theory, experiments, applications. *Acta Materialia*, 58(4):1152–1211, 2010.

[163] A. Roy, A. Acharya, and A. Roy. Size effects and idealized dislocation microstructure at small scales: predictions of a phenomenological model of mesoscopic field dislocation mechanics: part II. *Journal of the Mechanics and Physics of Solids*, 54(8):1687–1710, 8 2006.

[164] S. Saeb, P. Steinmann, and A. Javili. Aspects of Computational Homogenization at Finite Deformations: A Unifying Review From Reuss' to Voigt's Bound. *Applied Mechanics Reviews*, 68(5):050801, 9 2016.

[165] S. Sandfeld, T. Hochrainer, M. Zaiser, and P. Gumbsch. Continuum modeling of dislocation plasticity: Theory, numerical implementation, and validation by discrete dislocation simulations. *Journal of Materials Research*, 26(5):623–632, 2011.

[166] S. Sandfeld, E. Thawinan, and C. Wieners. A link between microstructure evolution and macroscopic response in elasto-plasticity: Formulation and numerical approxima-

tion of the higher-dimensional continuum dislocation dynamics theory. *International Journal of Plasticity*, 72:1–20, 2015.

[167] S. Sandfeld and M. Zaiser. Pattern formation in a minimal model of continuum dislocation plasticity. *Modelling and Simulation in Materials Science and Engineering*, 23(6):065005, 9 2015.

[168] E. Schmid and W. Boas. *Plasticity of Crystals: With Special Reference to Metals*. Chapman & Hall, 1968.

[169] J. Schröder. A numerical two-scale homogenization scheme: the FE2-method. In J. Schröder and K. Hackl, editors, *Plasticity and Beyond: Microstructures, Crystal-Plasticity and Phase Transitions*, pages 1–64. Springer Vienna, Vienna, 2014.

[170] K. Schulz, L. Wagner, and C. Wieners. A mesoscale continuum approach of dislocation dynamics and the approximation by a Runge-Kutta discontinuous Galerkin method. *International Journal of Plasticity*, 120:248–261, 9 2019.

[171] R. Sedláek, C. Schwarz, J. Kratochvíl, E. Werner, R. Sedláček, C. Schwarz, J. Kratochvíl, and E. Werner. Continuum theory of evolving dislocation fields. *Philosophical Magazine*, 87(8-9):1225–1260, 3 2007.

[172] B. Seeber and G. White. Materials at low temperatures. In *Handbook of Applied Superconductivity, Volume 2*, pages 1083–1093. American Society for Metals, 1998.

[173] V. B. Shenoy, R. V. Kukta, and R. Phillips. Mesoscopic analysis of structure and strength of dislocation junctions in fcc metals. *Physical Review Letters*, 84(7):1491–1494, 2 2000.

[174] R. B. Sills, N. Bertin, A. Aghaei, and W. Cai. Dislocation Networks and the Microstructural Origin of Strain Hardening. *Physical Review Letters*, 2018.

[175] R. B. Sills, W. P. Kuykendall, A. Aghaei, and W. Cai. Fundamentals of Dislocation Dynamics Simulations. In *Springer Series in Materials Science*, volume 245, pages 53–87. Springer, 2016.

[176] K. Starkey, T. Hochrainer, and A. El-Azab. Development of mean-field continuum dislocation kinematics with junction reactions using de Rham currents and graph theory. *Journal of the Mechanics and Physics of Solids*, 158:104685, 2022.

[177] K. Starkey, G. Winther, and A. El-Azab. Theoretical development of continuum dislocation dynamics for finite-deformation crystal plasticity at the mesoscale. *Journal of the Mechanics and Physics of Solids*, 139:103926, 6 2020.

[178] J. Steeds. Dislocation arrangement in copper single crystals as a function of strain. *Proceedings of the Royal Society of London. Series A. Mathematical and Physical Sciences*, 292(1430):343–373, 5 1966.

[179] M. Stricker, M. Sudmanns, K. Schulz, T. Hochrainer, and D. Weygand. Dislocation multiplication in stage II deformation of fcc multi-slip single crystals. *Journal of the Mechanics and Physics of Solids*, 119:319–333, 10 2018.

[180] M. Stricker and D. Weygand. Dislocation multiplication mechanisms - Glissile junctions and their role on the plastic deformation at the microscale. *Acta Materialia*, 99:130–139, 2015.

[181] M. Sudmanns, J. Bach, D. Weygand, and K. Schulz. Data-driven exploration and continuum modeling of dislocation networks. *Modelling and Simulation in Materials Science and Engineering*, 2020.

[182] M. Sudmanns, M. Stricker, D. Weygand, T. Hochrainer, and K. Schulz. Dislocation multiplication by cross-slip and glissile reaction in a dislocation based continuum formulation of crystal plasticity. *Journal of the Mechanics and Physics of Solids*, 132:103695, 11 2019.

[183] M. Tagami, K. Kashihara, T. Okada, and F. Inoko. Effect of Cross Slips on Multiple Slips and Recrystallization in ⟨111⟩ and ⟨001⟩ Al Single Crystals. *Journal of the Japan Institute of Metals*, 64(7):535–542, 2000.

[184] G. I. Taylor. The mechanism of plastic deformation of crystals. Part I.—Theoretical. *Proceedings of the Royal Society of London. Series A, Containing Papers of a Mathematical and Physical Character*, 145(855):362–387, 1934.

[185] P. Ván. Objective time derivatives in nonequilibrium thermodynamics. *Proceedings of the Estonian Academy of Sciences*, 57(3), 2008.

[186] N. P. van Dijk. Formulation and implementation of stress-driven and/or strain-driven computational homogenization for finite strain. *International Journal for Numerical Methods in Engineering*, 107(12):1009–1028, 9 2016.

[187] S. N. Varadhan, A. J. Beaudoin, A. Acharya, and C. Fressengeas. Dislocation transport using an explicit Galerkin/least-squares formulation. *Modelling and Simulation in Materials Science and Engineering*, 14(7):1245–1270, 10 2006.

[188] V. Vivekanandan, P. Lin, G. Winther, and A. El-Azab. On the implementation of dislocation reactions in continuum dislocation dynamics modeling of mesoscale plasticity. *Journal of the Mechanics and Physics of Solids*, 149:104327, 4 2021.

[189] B. Weger, S. Gupta, and T. Hochrainer. Analysing discrete dislocation data using alignment and curvature tensors. *Comptes Rendus Physique*, 2021.

[190] B. Weger and T. Hochrainer. Leaving the Slip System - Cross Slip in Continuum Dislocation Dynamics. *PAMM*, 19(1), 11 2019.

[191] D. Weygand, L. H. Friedman, E. V. d. Giessen, and A. Needleman. Aspects of boundary-value problem solutions with three-dimensional dislocation dynamics. *Modelling and Simulation in Materials Science and Engineering*, 10(4):306, 7 2002.

[192] D. Weygand and P. Gumbsch. Study of dislocation reactions and rearrangements under different loading conditions. *Materials Science and Engineering A*, 400-401(1-2 SUPPL.):158–161, 7 2005.

[193] L. K. Wickham, K. W. Schwarz, and J. S. Stölken. Rules for Forest Interactions between Dislocations. *Physical Review Letters*, 83(22):4574–4577, 11 1999.

[194] G. Winther, C. Hong, and X. Huang. Low-Energy Dislocation Structure (LEDS) character of dislocation boundaries aligned with slip planes in rolled aluminium. *Philosophical Magazine*, 95(13):1471–1489, 5 2015.

[195] S. Wulfinghoff and T. Böhlke. Gradient crystal plasticity including dislocation-based work-hardening and dislocation transport. *International Journal of Plasticity*, 69:152–169, 6 2015.

[196] S. Xia, J. Belak, and A. El-Azab. The discrete-continuum connection in dislocation dynamics: I. Time coarse graining of cross slip. *Modelling and Simulation in Materials Science and Engineering*, 24(7):075007, 10 2016.

[197] S. Xia and A. El-Azab. Computational modelling of mesoscale dislocation patterning and plastic deformation of single crystals. *Modelling and Simulation in Materials Science and Engineering*, 23(5), 7 2015.

[198] S. X. Xia and A. El-Azab. A preliminary investigation of dislocation cell structure formation in metals using continuum dislocation dynamics. *IOP Conference Series: Materials Science and Engineering*, 89(1), 8 2015.

[199] C. Ye, R. Wilson, L. Rossi, A. Torsello, and E. Hancock. Thermodynamic Analysis of Time Evolving Networks. *Entropy*, 20(10):759, 10 2018.

[200] S. Yeÿmov, I. Groma, E. V. D. Giessen, S. Yefimov, E. Van der Giessen, I. Groma, and E. Van der Giessen. A comparison of a statistical-mechanics based plasticity model with discrete dislocation plasticity calculations. *Journal of the Mechanics and Physics of Solids*, 52(2):279–300, 2004.

[201] T. H. Youssef. Dislocations in α-Brass single crystals fatigued at low stress amplitude. *physica status solidi (a)*, 3(3):801–810, 11 1970.

[202] M. Zaiser. Local density approximation for the energy functional of three-dimensional dislocation systems. *Physical Review B - Condensed Matter and Materials Physics*, 92(17):1–17, 2015.

[203] M. Zaiser and T. Hochrainer. Some steps towards a continuum representation of 3D dislocation systems. *Scripta Materialia*, 54(5):717–721, 3 2006.

[204] M. Zaiser, M. C. Miguel, and I. Groma. Statistical dynamics of dislocation systems: The influence of dislocation-dislocation correlations. *Physical Review B - Condensed Matter and Materials Physics*, 64:1–9, 2001.

[205] H. M. Zbib, T. Díaz De La Rubia, M. Rhee, and J. P. Hirth. 3D dislocation dynamics: Stress-strain behavior and hardening mechanisms in fcc and bcc metals. *Journal of Nuclear Materials*, 276(1):154–165, 1 2000.

[206] H. Zenil, N. Kiani, and J. Tegnér. A Review of Graph and Network Complexity from an Algorithmic Information Perspective. *Entropy*, 20(8):551, 7 2018.

[207] X. Zhang, X. Lu, J. Zhao, Q. Kan, Z. Li, and G. Kang. Temperature effect on tensile behavior of an interstitial high entropy alloy: Crystal plasticity modeling. *International Journal of Plasticity*, 150:103201, 3 2022.

[208] X. H. Zheng, H. W. Zhang, X. Huang, N. Hansen, and K. Lu. Influence of strain rate on the orientation dependence of microstructure in nickel single crystals. *Philosophical Magazine Letters*, 96(2):52–59, 2 2016.